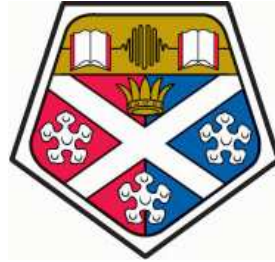


UNIVERSITY OF STRATHCLYDE

DEPARTMENT OF ELECTRONIC & ELECTRICAL ENGINEERING



**Channel Measurements
and
Modelling
for
Sensor Network Applications**

Konstantinos Sasloglou

A thesis presented in fulfilment of the requirements for the degree
of Doctor of Philosophy

to

Centre for Intelligent Dynamic Communications

University of Strathclyde in Glasgow

January 2010

Declaration

This thesis is the result of the author's original research. It has been composed by the author and has not been previously submitted for examination which has led to the award of a degree.

The copyright of this thesis belongs to the author under the terms of the United Kingdom Copyright Acts as qualified by University of Strathclyde Regulation 3.50. Due acknowledgement must always be made of the use of any material contained in, or derived from, this thesis.

Signed:

Date:

Abstract

Wireless sensor network (WSN) technology has evolved as a convergence of wireless communications and sensor technologies. WSNs are a category of ad-hoc networks used widely for condition monitoring applications.

Issues related to the physical layer of WSNs are of particular significance and can critically affect WSN reliability and performance. For this reason channel characterisation and modelling are important processes when designing WSNs. The diverse nature of the environment in which such networks are deployed means that these characteristics and models are sensitively dependent on application.

This thesis focuses on channel modelling for three particular WSN applications: gas-turbine engine monitoring, animal husbandry (in particular cattle monitoring in the beef industry) and WSNs for smart buildings.

The WSN transmission channel context has been presented and relevant channel measurement and modelling literature has been reviewed. Transmission loss statistics have been measured for WSN nodes deployed in each of the three applications. Channel models have been extracted from the resulting data-bases which allow accurate link budget estimations. In the gas-turbine application a system model incorporating interference and noise in addition to transmission loss has been implemented and in the animal husbandry application the practical benefits of antenna and base-station diversity have been assessed.

Acknowledgements

This section gives me the chance to thank all those people who in their way have provided support during my PhD.

I would like to thank my primary supervisor, Professor Ivan Andonovic, to whom I owe my presence in the Department. His guidance, support and advice was crucial and helped me to obtain research experience.

Special thanks go to Dr. Ian Andrew Glover, the technical advisor of this thesis. His expertise in this field was vital for its completion. The uncountable hours we spent on discussions gave me a unique opportunity to obtain technical and research experience.

Many thanks go to my colleagues and co-authors of some of my publications, Dr. Kae-Hsiang Kwong, Mr. Hock Guan Goh and Mr. Tsungta Wu, who have kindly provided me with measurement data from the cattle monitoring experiment and allowed me to apply further statistical analysis.

I would like to acknowledge Dr. Faisal Darbari, co-author in two of my publications, for his contribution on the measurement process and the analysis of the interior wall and the very short distance (0.1 to 1 m) chipboard measurements.

I would also like to thank Dr. Griogair Whyte for providing the antennas he has designed and Dr. Partha S. Dutta for the excellent co-operation and support during the measurements undertaken at Rolls-Royce premises in Derby.

Many thanks to Dr. David Harle and Dr. Craig Michie who they were always there when I needed their help, to Mr. Ioannis Kolovos, Dr. George Michalareas, Dr. Christos Tachtatzis, Dr. Michael P. Gilroy and Dr. Robert Atkinson for their moral support.

I would also like to thank my soul mate QiYing (Christine) Wu providing love and care all those years. Her moral support was vital during the difficulties I have been addressing.

Last but not least, this is my chance to express my deep gratitude to my beloved parents, Nikolaos and Stella, and my brother Michael who have given the most out of them to support, by any means, my prolonged studies.

Abbreviations

ACF	Autocorrelation Function
AP	Access Point
ASK	Amplitude Shift Keying
CW	Continuous Wave
dB	decibel
dBi	decibel with reference an isotropic antenna
dBm	decibel with reference to 1 milliwatt
dBV	decibel with reference to 1 volt
dBW	decibel with reference to 1 watt
DSPL	Dual Slope Path Loss
FSK	Frequency Shift Keying
FSPL	Free Space Path Loss
GFSK	Gaussian Frequency Shift Keying
GSM	Global System for Mobile communications
GUI	Graphical User Interface
HF	High Frequency
IEEE	Institute of Electrical and Electronics Engineers
ISI	Inter-Symbol Interference
ISM	Industrial, Scientific and Medical
ITU	International Telecommunication Union
kbps	Kilo bits per second
LOS	Line-of-Sight
Mbps	Mega bits per second
MSK	Minimum Shift Keying
NLOS	Non Line-of-Sight
OOK	On-Off Keying
O-QPSK	Offset QPSK
OSI	Open Systems Interconnection

PCB	Printed Circuit Board
PEPL	Plane Earth Path Loss
PHY	Physical Layer
PM	Pulse Modulation
PNA	Programmable Network Analyser
PVC	Polyvinyl Chloride
QPSK	Quadrature Phase Shift Keying
RF	Radio Frequency
RSSI	Received Signal Strength Indicator
SNR	Signal-to-Noise Ratio
SSPL	Single Slope Path Loss
SW	Square Wave
UCLA	University of California at Los Angeles
UHF	Ultra High Frequency
UWB	Ultra-wideband
VHF	Very High Frequency
WP	Work Package
WLAN	Wireless Local Area Network
WPAN	Wireless Personal Area Network
WSN	Wireless Sensor Network

Contents

Abstract	ii
Acknowledgements	iii
List of Figures	xvii
List of Tables	xviii
List of Publications	xx
1 Introduction	1
1.1 Motivation	1
1.2 Aims and Objectives	2
1.3 Thesis Organisation	2
1.4 Contributions and Publications	4
2 Transmission Channel Context	6
2.1 Wireless Sensor Networks	6
2.1.1 Introduction and Evolution	6
2.1.2 Wireless Sensor Network Technologies	8
2.1.2.1 RF Chipsets	8
2.1.2.2 Wireless Nodes	8
2.1.2.3 Comparison	11
2.2 Channel Implications for Higher Level Protocols	11
3 Literature Review - Channel Measurements and Modelling	15
3.1 Basic Propagation Mechanisms	15
3.1.1 Reflection and Transmission Coefficients	16
3.2 Modelling	18
3.2.1 Path Loss	18
3.2.1.1 Free Space (Friis) Model	20

3.2.1.2	Plane Earth Path Loss Model	21
3.2.1.3	Single Slope Path Loss Model	26
3.2.1.4	Dual Slope Path Loss Model	28
3.2.2	Fading	28
3.2.2.1	Fading based on multipath time delay spread . .	29
3.2.2.1.1	Flat Fading	30
3.2.2.1.2	Frequency Selective Fading	30
3.2.2.2	Fading based on Doppler spread	31
3.2.2.2.1	Fast Fading	31
3.2.2.2.2	Slow Fading	31
3.3	Diversity	31
4	Wireless Data Acquisition in Gas Turbine Engines	33
4.1	Motivation	33
4.2	Aims and Objectives	34
4.3	Measurements	34
4.3.1	ISM-band Measurements	36
4.3.1.1	Measurements without Cowling (Set 1)	41
4.3.1.2	Measurements with Cowling (Set 2)	42
4.3.2	UWB-band Measurements	43
4.3.2.1	Measurements without Cowling (Set 1)	47
4.3.2.2	Measurements with Cowling (Set 2)	47
4.4	Modelling	48
4.5	Results	49
4.6	Interference and Noise	63
4.6.1	Interference	63
4.6.2	Noise	63
4.7	System Model	66
4.7.1	System Platform	66
4.7.1.1	Transmission Gain Model	66
4.7.1.1.1	Transmission Gain Model Parameters . .	68
4.7.1.1.2	Transmission Gain Blocks	68
4.7.1.2	Interference Model	69
4.7.1.2.1	Interference Model Parameters	69
4.7.1.2.2	Interference Model Blocks	70
4.7.1.3	Noise Model	71
4.7.1.3.1	Noise Model Parameters	72
4.7.1.3.2	Noise Model Blocks	72

4.7.1.4	Downsampling	73
4.7.1.5	Model Output	73
4.7.2	Model Validation	73
4.8	Summary and Conclusions	73
5	Diversity Channels for Animal Husbandry	79
5.1	Motivation	80
5.2	Aims and objectives	80
5.3	Measurements and Modelling	80
5.3.1	Ceramic Patch Antenna	80
5.3.2	Measurements	82
5.3.2.1	Statistics	84
5.3.2.2	Diversity	92
5.3.2.2.1	Antenna Diversity	92
5.3.2.2.2	Base-station Diversity	93
5.3.2.2.3	Overall Diversity	93
5.4	Base-station Antenna Height	99
5.5	Summary and Conclusions	102
6	Wireless Sensor Networks Channels for Smart Building Appli-	
	cations	104
6.1	Motivation	104
6.2	Aims and Objectives	104
6.3	Surface Waves	105
6.4	Wall Measurements	108
6.4.1	Offset and Reduced Height	111
6.4.2	Transmission Loss	113
6.4.3	Gradients and Path Loss Index	113
6.5	Chipboard Measurements for Very Short Distance	116
6.5.1	Variations with Height and Distance	116
6.5.1.1	Vertical Polarisation	118
6.5.1.2	Horizontal Polarisation	120
6.6	Chipboard Measurements for Short Distance	126
6.6.1	Results	129
6.6.2	Gradients and Path Loss Indices	136
6.7	Summary and Conclusions	137

CONTENTS

7	Conclusions and Future Work	140
7.1	Conclusions	140
7.2	Discussion and Future Work	143
A	Complex Factor F (Equation Proof)	145
B	UWB-band Measurements and Modelling for Measurements without Cowling (3 GHz to 11 GHz)	147
C	UWB-band Measurements and Modelling for Measurements with Cowling (3 GHz to 11 GHz)	156
D	Rectaxial Antenna Radiation Pattern and Chipboard Reflection Coefficient	166
	Bibliography	168

List of Figures

1.1	Thesis overview.	3
2.1	High level description of sensor node.	7
2.2	Major key issues to be considered during the design of an ad-hoc WSN [4].	9
2.3	CC2420 by Chipcon (After [14]).	11
2.4	Comparison of the wireless devices available in the market.	13
2.5	Schematic diagram of OSI layers, including antennas and channel.	14
3.1	Schematic diagram of an electromagnetic wave reflected and transmitted at a medium interface.	16
3.2	Reflection and transmission coefficients for (a) average (dry) ground ($\epsilon_r = 7.0$, $\sigma = 0.001$) and (b) reflection magnitudes for vertical and horizontal polarisation.	19
3.3	Free space path loss versus distance for selected frequencies.	21
3.4	Two-ray propagation assumed for the PEPL model.	22
3.5	Free space (blue) and plane earth propagation models for vertical (black and dashed) and horizontal (red and solid) polarisations ($f = 2.45$ GHz, $\epsilon_r = 15$ and $\sigma = 0.005$).	25
3.6	Free space (blue) and plane earth propagation models for vertical polarization assuming typical ground (black dashed) and perfect conductor (red solid).	26
3.7	Variation of received power with receive antenna height for 50 m antenna separation, 2.45 GHz and transmit antenna height of 2 m.	27
3.8	Example single slope path loss models.	27
3.9	Example dual slope path loss model.	28
3.10	A wireless channel model [24].	29

3.11	The four types of fading [23]. T_s , T_c , B_s and B_c are transmitted symbol duration, coherence time, transmitted signal bandwidth and coherence bandwidth of the channel, respectively.	30
4.1	Wireless technologies operating within the spectrum of 2.4 - 11 GHz.	35
4.2	Schematic diagram of two-path geometry in a cylinder.	35
4.3	Maximum ISI "tolerable" symbol rate versus engine radius.	36
4.4	(a) Channel frequency response (S_{21}), (b) its ACF and (c) its ACF on an expanded scale.	38
4.5	50% correlation bandwidth for measurements (a) without and (b) with cowling and the corresponding cumulative distribution functions (c) and (d), respectively.	39
4.6	Rectaxial antenna.	39
4.7	Measured return loss (S_{11}) for rectaxial antennas.	40
4.8	Antenna positioners.	40
4.9	Gnome engine.	41
4.10	Schematic diagram of engine measurement points (set 1); black (or darker for black and white reproductions) points omitted. First and second digits indicate location on circumference and location of plane on engine axis, respectively.	41
4.11	Gnome engine with cowling.	42
4.12	Schematic diagram of engine measurement points (set 2); black (or darker points for black and white reproduction) omitted. First and second digits indicate location on circumference and location of plane on engine axis, respectively.	43
4.13	Spectral mask for UWB in (a) USA and (b) Europe (After [53]).	43
4.14	(a) Channel frequency response (S_{21}), (b) its ACF and (c) its ACF on an expanded scale.	44
4.15	50% correlation bandwidths for measurements (a) without and (b) with cowling and the corresponding cumulative distribution functions (c) and (d), respectively.	45
4.16	UWB antenna.	46
4.17	Antenna return loss (S_{11}).	46
4.18	Schematic diagram of path geometry.	48
4.19	Measurement data without cowling (set 1) and best-fit first-degree polynomial surface.	49
4.20	Measurement data with cowling (set 2) and best-fit first-degree surface.	50

4.21	Two dimensional projection of data without cowling (set 1) illustrating transmission gain versus path length.	50
4.22	Two dimensional projection of data with cowling (set 2) illustrating transmission gain versus path length.	51
4.23	Difference (ϵ) between measurement points and best-fit surface: measurements (a) without and (b) with cowling.	52
4.24	Projection of data in Figures 4.23 (a) and (b) illustrating dependence of ϵ on path length.	52
4.25	Histogram of error within a single s - κ quantization interval and corresponding normal distribution for measurements (a) without and (b) with cowling.	53
4.26	Normal probability plots corresponding to the histograms in Figure 4.25 (a) and (b).	54
4.27	Histogram of error for all s - κ quantization intervals and corresponding normal distribution for measurements (a) without and (b) with cowling.	54
4.28	Normal probability plots corresponding to the histograms in Figure 4.27 (a) and (b).	54
4.29	μ versus s , κ and σ versus s , κ for measurements without cowling (set 1).	55
4.30	μ versus s , κ and σ versus s , κ for measurements with cowling (set 2).	55
4.31	Transmission gain model.	56
4.32	Example of best-fit transmission gain model for measurements without cowling (6 GHz - 7 GHz).	56
4.33	Example of best-fit transmission gain model for measurements with cowling (6 GHz - 7 GHz).	57
4.34	Two dimensional projection of data (without cowling) illustrating transmission gain versus path length (6 GHz - 7 GHz).	57
4.35	Two dimensional projection of data (with cowling) illustrating transmission gain versus path length (6 GHz - 7 GHz).	58
4.36	Difference (ϵ) between measured data and model: measurements (a) without and (b) with cowling (6 GHz - 7 GHz).	58
4.37	Projection of data in Figures 4.36 (a) and (b) illustrating dependence of ϵ on path length (6 GHz - 7 GHz).	60

4.38	Error histograms and corresponding normal distribution for a single quantised pair of s - κ for measurements (a) without and (b) with cowling.	60
4.39	Normal probability plots corresponding to the histograms in Figure 4.38 (a) and (b).	61
4.40	μ versus s , κ and σ versus s , κ for measurements without cowling (6 GHz - 7 GHz).	61
4.41	μ versus s , κ and σ versus s , κ for measurements with cowling (6 GHz - 7 GHz).	63
4.42	Interference waveforms. (After [54].)	64
4.43	Example radiated susceptibility test levels. (After [54].)	65
4.44	High level description of the system model.	66
4.45	Simulink system model.	67
4.46	Transmission gain model.	68
4.47	Interference model.	69
4.48	Noise model.	72
4.49	Model validation with no channel fluctuation, no interference and no thermal noise.	74
4.50	Model validation with channel fluctuation only (no interference and no thermal noise).	74
4.51	Model validation with interference only (no channel fluctuation and no thermal noise).	75
4.52	Model validation with thermal noise only (no channel fluctuation, no interference). For this case only, the transmission power was set to -55 dBW (-25 dBm) which is the minimum transmission power for MICAz.	75
4.53	Model validation with channel fluctuation, interference and thermal noise.	76
5.1	Inset-fed microstrip patch with a ceramic element [64].	81
5.2	Radiation pattern of the patch antenna (After [64]).	81
5.3	The MICAz transceiver.	82
5.4	PCB carrying the MICAz module.	82
5.5	Schematic illustration of antenna arrangement on collar and trial area.	83
5.6	Trial area.	83
5.7	Base-station configuration.	83
5.8	Data received by base-station 1.	85

5.9	Data received by base-station 2.	85
5.10	Peak-to-peak fluctuation of the received power at each individual antenna. From left to right, BS1C1A1, BS1C1A2, BS1C2A1, BS1C2A2, BS2C1A1, BS2C1A2, BS2C2A1, BS2C2A2. (BSxCyAz denotes base-station, collar and antenna numbers, respectively.)	86
5.11	Pdfs of power (dBm) at BS1 for (a) A1 on C1 and (b) A2 on C1 and (c) A1 on C2 and (d) A2 on C2. (Smooth curve represents the best-fit normal distribution.)	88
5.12	Pdfs of power (dBm) at BS2 for (a) A1 on C1 and (b) A2 on C1 and (c) A1 on C2 and (d) A2 on C2. (Smooth curve represents the best-fit normal distribution.	89
5.13	Cdfs of power (dBm) at BS1 for (a) A1 on C1 and (b) A2 on C1 and (c) A1 on C2 and (d) A2 on C2. (Smooth curve represents the best-fit normal distribution.	89
5.14	Cdfs of power (dBm) at BS2 for (a) A1 on C1 and (b) A2 on C1 and (c) A1 on C2 and (d) A2 on C2. (Smooth curve represents the best-fit normal distribution.	90
5.15	CDFs of detected voltage (volts) at BS1 for (a) A1 on C1 and (b) A2 on C1 and (c) A1 on C2 and (d) A2 on C2. (Smooth curve represents the best-fit log-normal distribution.)	90
5.16	CDFs of detected voltage (volts) at BS2 for (a) A1 on C1 and (b) A2 on C1 and (c) A1 on C2 and (d) A2 on C2. (Smooth curve represents the best-fit log-normal distribution.)	91
5.17	Data received from A1 on C1 at (a) BS1 and (b) BS2, and data received from A2 on C1 at (c) BS1 and (d) BS2.	91
5.18	Received signal power (dBm) for antenna 1 and antenna 2, mean received signal (dBm), and selection diversity signal (dBm) for (a) C1 to BS1, (b) C2 to BS1, (c) C1 to BS2 and (d) C2 to BS2.	94
5.19	Antenna diversity gain for each instance: (a) C1 to BS1, (b) C2 to BS1, (c) C1 to BS2 and (d) C2 to BS2.	95
5.20	Received signal power (dBm) for BS1 and BS2, mean received signal (dBm), and selection diversity signal (dBm) for (a) A1 of C1 to BS1 and BS2, (b) A2 of C1 to BS1 and BS2, (c) A1 of C2 to BS1 and BS2 and (d) A2 of C2 to BS1 and BS2.	96
5.21	Base-station diversity gain for each instance: (a) A1 of C1 to BS1 and BS2, (b) A2 of C1 to BS1 and BS2, (c) A1 of C2 to BS1 and BS2 and (d) A2 of C2 to BS1 and BS2.	97

5.22	Overall selection and mean diversity for the first collar (two antennas and two base-stations).	97
5.23	Overall selection and mean diversity for the second collar (two antennas and two base-stations).	98
5.24	Overall antenna and base-station diversity using collar 1.	98
5.25	Overall antenna and base-station diversity gain collar 2.	99
5.26	Mean overall diversity gain of the two collars.	99
5.27	Variation of the received power (watts) as a function of base-station height.	101
5.28	Comparison of simulated and measured RSSI as a function of base-station height for (a) perfect conductor and (b) pasture.	101
5.29	Received power (dBm) as a function of distance for (a) perfect conductor and (b) grass.	102
6.1	Variation of surface-wave factor magnitude ($\epsilon_r = 3.55$, $\sigma = 0.02$ S/m and $f = 2.45$ GHz).	107
6.2	Rectaxial antenna (left) and ceramic patch antenna (right).	108
6.3	Vertically polarised rectaxial antennas with (a) 30 cm reduced height and (b) 0 cm reduced height (in contact with the ceiling).	109
6.4	Microstrip patch antenna located with a reduced height of (a) 30 cm and (b) 0 cm (in contact with the ceiling).	110
6.5	Rectaxial antennas with 0 cm reduced height (in contact with the ceiling) oriented (a) vertically and (b) horizontally.	111
6.6	Transmission gain (dB) versus node separation (Curves correspond to offsets of 0, 5 and 10 mm)	112
6.7	Mean transmission gain with 95% confidence intervals.	113
6.8	Measurement standard deviations.	114
6.9	Linear regression of transmission loss data.	115
6.10	Path loss indices for each individual measurement.	115
6.11	Measurement setup.	117
6.12	Vertically polarised measurements.	117
6.13	Horizontally polarised measurements.	118
6.14	Transmission gain versus antenna separation and height for vertical polarisation (Data separated in to sets V1 and V2 on the basis of antenna height dependence).	119
6.15	Transmission gain versus antenna height (Data set V1).	120

6.16	Transmission gain for vertical polarisation, with logarithmic best-fit line, compared to free space and two-ray model ($\epsilon_r = 3.55$ and $\sigma = 0.02$).	121
6.17	Measurement data and best-fit first-degree polynomial surface. . .	122
6.18	Measurement data and best-fit surface.	122
6.19	Transmission gain versus antenna separation and height for horizontal polarisation (Data separated in two sets H1 and H2 on the basis of antenna height dependence).	123
6.20	Transmission gain for vertical and horizontal polarisation (data set V1 and H1).	124
6.21	Transmission gain for horizontal polarisation, with logarithmic best-fit line, compared to free space and two-ray model ($\epsilon_r = 3.55$ and $\sigma = 0.02$).	125
6.22	Measurement data and best-fit first-degree polynomial surface. . .	127
6.23	Measurement data and best-fit surface.	127
6.24	Measurement surface.	128
6.25	Very short and short distance measurements for antenna height 0.65 cm with best-fit lines.	129
6.26	Measurements for antenna height 0.65 cm.	131
6.27	Very short and short distance measurements for antenna height 5.65 cm with best-fit lines.	132
6.28	Measurements for antenna height 5.65 cm.	133
6.29	Transmission gain (dB) for antenna height 10 cm.	134
6.30	Transmission gain (dB) for antenna height 15 cm	134
6.31	Transmission gain (dB) for antenna height 20 cm	135
6.32	Standard deviation of transmission gain (dB) in respect of path length and antenna height for short distance measurements. . . .	135
6.33	All available measurements for vertical polarisation.	136
6.34	Path loss indices for all measurements (both very short and short range measurements).	137
B.1	Transmission gain and error modelling of measurements without cowling within 3 GHz to 4 GHz.	148
B.2	Transmission gain and error modelling of measurements without cowling within 4 GHz to 5 GHz.	149
B.3	Transmission gain and error modelling of measurements without cowling within 5 GHz to 6 GHz.	150

B.4	Transmission gain and error modelling of measurements without cowl- ing within 6 GHz to 7 GHz.	151
B.5	Transmission gain and error modelling of measurements without cowl- ing within 7 GHz to 8 GHz.	152
B.6	Transmission gain and error modelling of measurements without cowl- ing within 8 GHz to 9 GHz.	153
B.7	Transmission gain and error modelling of measurements without cowl- ing within 9 GHz to 10 GHz.	154
B.8	Transmission gain and error modelling of measurements without cowl- ing within 10 GHz to 11 GHz.	155
C.1	Transmission gain and error modelling of measurements with cowl- ing within 3 GHz to 4 GHz.	157
C.2	Transmission gain and error modelling of measurements with cowl- ing within 4 GHz to 5 GHz.	158
C.3	Transmission gain and error modelling of measurements with cowl- ing within 5 GHz to 6 GHz.	159
C.4	Transmission gain and error modelling of measurements with cowl- ing within 6 GHz to 7 GHz.	160
C.5	Transmission gain and error modelling of measurements with cowl- ing within 7 GHz to 8 GHz.	161
C.6	Transmission gain and error modelling of measurements with cowl- ing within 8 GHz to 9 GHz.	162
C.7	Transmission gain and error modelling of measurements with cowl- ing within 9 GHz to 10 GHz.	163
C.8	Transmission gain and error modelling of measurements with cowl- ing within 10 GHz to 11 GHz.	164
D.1	Measured and simulated radiation pattern of rectaxial antenna. After [51].	167
D.2	Magnitude of the reflection coefficient for $\epsilon = 3.55$ and $\sigma = 0.02$	167

List of Tables

2.1	Some of the most popular available RF chipsets.	10
2.2	Some of the most popular wireless sensor devices available in the market.	12
4.1	ISM frequency band allocations (After [50]).	37
4.2	Transmission model polynomial coefficients.	51
4.3	Gradients (dB/m) of mean transmission gain \overline{G}_T with respect to s and κ for ISM-band measurements.	51
4.4	μ and σ values for each quantisation interval.	53
4.5	Transmission gain model coefficients.	59
4.6	Gradients of mean transmission gain \overline{G}_T with respect to s and κ for UWB-band measurements.	59
4.7	μ and σ values for each quantisation interval.	62
4.8	Available categories for the input. (After [54].)	64
5.1	Correlation coefficient of signals received by antennas on a single collar.	87
5.2	Correlation coefficient of signals received by different base-stations.	92
6.1	Gradients for V1 and V2.	119
6.2	Mean difference in transmission gain for vertical and horizontal polarisation (data set V1 and H1).	123
6.3	Average difference in transmission gain for horizontal polarisation (data set H1 and H2)	124
6.4	Standard deviation for horizontal polarisation measurements.	126
6.5	Gradients for H1.	126
6.6	Transmission gain level (dB) at 1 m.	132
6.7	Gradients of all measurements of Section 6.6.	136

List of Publications

- [1] K. Sasloglou, I. A. Glover, I. Andonovic, and S. A Bhatti. Measurements and Physical-layer Modelling of Transmission Loss for Gas Turbine Engine Sensor Networks. In *IET Festival of Radio Science, Birmingham, UK*, Dec. 2009.
- [2] K. Sasloglou, I. A. Glover, P. Dutta, R. Atkinson, I. Andonovic, and G. Whyte. Empirical Modelling and Simulation of Transmission Loss between Wireless Sensor Nodes in Gas Turbine Engines. In *The 7th International Conference on Information, Communications and Signal Processing (ICICS 2009), Macau*, Dec. 2009.
- [3] K. Sasloglou, I. A. Glover, H. G. Goh, K. H Kwong, M. P. Gilroy, C. Tachtatzis, C. Michie, and I. Andonovic. Antenna and Base-station Diversity for WSN Livestock Monitoring. *Scientific Research Journal on Wireless Sensor Network*, Volume 1:pages 383–396, Dec. 2009.
- [4] K. Sasloglou, I. A. Glover, P. Dutta, R. Atkinson, I. Andonovic, and G. Whyte. A Channel Model for Wireless Sensor Networks in Gas Turbine Engines. In *Proc. Loughborough Antennas & Propagation Conference (LAPC 2009), Loughborough, UK*, pages 761–764, Nov. 2009.
- [5] K. H. Kwong, T. T. Wu, K. Sasloglou, B. Stephen, D. Cao, H. G. Goh, S. K. Goo, M. Gilroy, C. Tachtatzis, I. A. Glover, C. Michie, and I. Andonovic. Implementation of Herd Management System with Wireless Sensor Networks. In *Joint International Agricultural Conference (JIAC 2009), Wageningen, Netherlands*, Jul. 2009.
- [6] K. H. Kwong, K. Sasloglou, H. G. Goh, T. T. Wu, B. Stephen, M. Gilroy, C. Tachtatzis, I. A. Glover, C. Michie, and I. Andonovic. Adaptation of Wireless Sensor Network for Farming Industries. In *The 6th International Conference on Networked Sensing Systems (INSS 2009), Carnegie Mellon University, Pittsburgh, USA*, Jun. 2009.

- [7] K. Sasloglou, F. Darbari, I. A. Glover, I. Andonovic, and R. W. Stewart. Some Preliminary Short-range Transmission Loss Measurements for Wireless Sensors Deployed on Indoor Walls. In *Proc. 11th IEEE Singapore International Conference on Communication Systems (ICCS 2008)*, pages 129–132, Guangzhou, China, Nov. 2008.
- [8] K. Sasloglou, I. A. Glover, K. H. Kwong, and I. Andonovic. Wireless Sensor Network for Animal Monitoring Using both Antenna and Base-station Diversity. In *Proc. 11th IEEE Singapore International Conference on Communication Systems (ICCS 2008)*, pages 27–33, Guangzhou, China, Nov. 2008.
- [9] F. Darbari, K. Sasloglou, R. W. Stewart, I. A. Glover, and I. Andonovic. Effect of Antenna Height and Polarisation on Short Wireless Links. In *16th European Signal Processing Conference (EUSIPCO 2008), Lausanne, Switzerland*, Aug. 2008.

CHAPTER 1

Introduction

This thesis deals with channel measurements and modelling for three sensor network applications: gas turbine engine monitoring, cattle monitoring and smart buildings.

1.1 Motivation

The motivations for this work are:

- At the time that the WIDAGATE (Wireless Data Acquisition for Gas Turbine Engines) project started no similar work was in the public domain. None of the existing work on diffraction around cylinders could be directly applied to the gas turbine WSN problem, since it dealt with smooth cylinders and antennas placed far from the surface. The WIDAGATE model is required to accommodate a cylinder with large random surface irregularities.
- Although many projects have addressed animal monitoring applications, none of them has incorporated any form of diversity.
- Existing indoor propagation models primarily address the loss expected due to propagation through different building materials (brick, stone, wood, plaster, glass etc.), their composite structures (e.g. walls, ceilings, floors, doors) and the expected loss and fading statistics for propagation within room interiors - as distinct from propagation over a rooms bounding plane surfaces. It is the latter which is of primary concern in smart building WSN applications.

All three applications areas have been components of larger collaborative projects (WIDAGATE [1], CBM [2] and SpeckNet [3]) with associated commercial and/or research council sponsorship.

1.2 Aims and Objectives

The principal aim of the thesis is to characterise the wireless channel for these sensor network applications and investigate those techniques that may be used to improve the channels' reliability and/or performance.

The more detailed objectives are:

- Transmission loss measurements in specific environments
 - around the surface of a Gnome gas turbine engine
 - in a cattle enclosure
 - over two important surfaces in the interior of buildings
- Extraction of empirical models and comparison with theoretical expectations
- Construction of physical layer channel simulator for gas-turbine WSN applications
- Investigation of practical WSN diversity techniques for cattle monitoring applications
- Investigation of the significance of surface waves and antenna's-surface offset for WSNs in smart building applications

1.3 Thesis Organisation

The organisation of the thesis is summarised in Figure 1.1.

Chapter 2 contains a brief review of the wireless sensor networks including the evolution, current technologies and comparison between wireless devices available on the market.

Chapter 3 is a review of fundamental theoretical concepts used in the thesis. These include basic mechanisms of electromagnetic wave propagation, path loss, fading and diversity methods.

Chapter 4 is an account of the WIDAGATE channel measurements and modelling for a gas turbine WSN. The channel model has been derived from measurements on a Gnome engine. The resulting channel model is part of a system model implemented in Simulink comprising transmission gain, interference and noise.

Chapter 5 describes channel measurements and modelling of a cattle condition monitoring WSN. Antenna and base-station diversity is investigated and a thorough statistical analysis of the resulting data is presented. The gain obtainable with antenna diversity, base-station diversity and combined antenna-base-station diversity is determined.

Chapter 6 contains channel measurements and modelling for smart building WSN applications. Measurements were undertaken on large vertical and horizontal surfaces for different ranges and antenna-surface displacements.

Chapter 7 draws together conclusions and makes suggestions for further work.

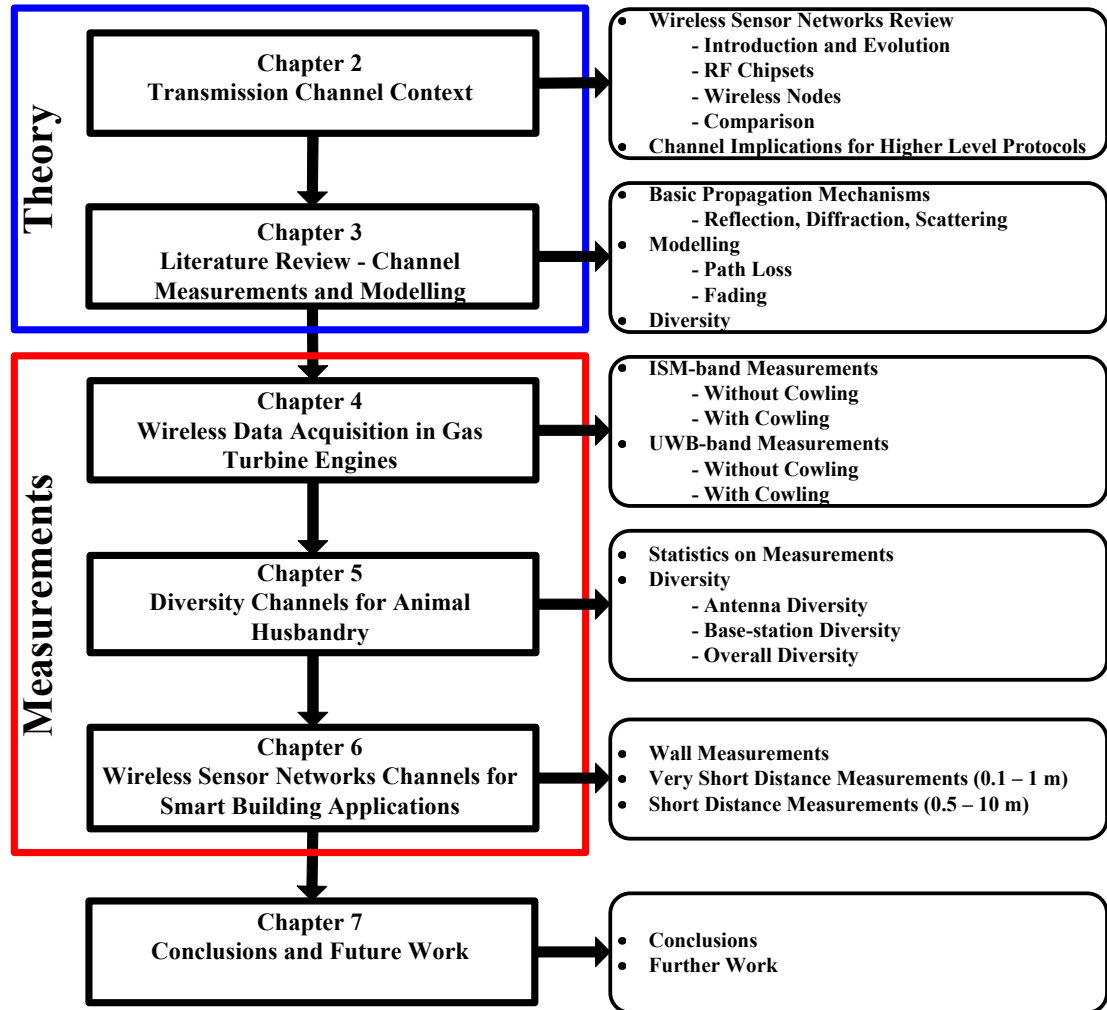


Figure 1.1: Thesis overview.

1.4 Contributions and Publications

The principal contributions associated with the work achieved in this thesis are:

- The first channel measurements ever reported for gas turbine engine WSN.
- The first antenna and base-station diversity study for cattle monitoring WSN applications.
- New transmission loss measurements for short range (1 - 2.5 m) and very short range (0.1 - 1 m) propagation over interior plane surfaces and extraction of new transmission gain models for smart building WSN applications.

Extracts of the work presented in this thesis have been described in the following journal and international conference proceedings:

1. K. Sasloglou, I. A. Glover, H. G. Goh, K. H. Kwong, M. P. Gilroy, C. Tachtatzis, C. Michie and I. Andonovic. Antenna and Base-station Diversity for WSN Livestock Monitoring. *Scientific Research Journal on Wireless Sensor Network*, Volume 1: p. 383-396, Dec. 2009.
2. K. Sasloglou, I. A. Glover, P. Dutta, R. Atkinson, I. Andonovic and G. Whyte. Empirical Modelling and Simulation of Transmission Loss between Wireless Sensor Nodes in Gas Turbine Engines. In *The 7th International Conference on Information, Communications and Signal Processing (ICICS 2009)*, Macau, Dec. 2009.
3. K. Sasloglou, I. A. Glover, P. Dutta, R. Atkinson, I. Andonovic and G. Whyte. A Channel Model for Wireless Sensor Networks in Gas Turbine Engines. In *Loughborough Antennas & Propagation Conference (LAPC 2009)*, Loughborough, UK, Nov. 2009.
4. K. Sasloglou, I. A. Glover, I. Andonovic and S. A. Bhatti. Measurements and Physical-layer Modelling of Transmission Loss for Gas Turbine Engine Sensor Networks. In *IET Festival of Radio Science*, Birmingham, UK, Dec. 2009.
5. K. Sasloglou, F. Darbari, I. A. Glover, I. Andonovic and R. W. Stewart. Some Preliminary Short-range Transmission Loss Measurements for Wireless Sensors Deployed on Indoor Walls. In *Proc. 11th IEEE Singapore International Conference on Communication Systems (ICCS 2008)*, p. 129-132, Guangzhou, China, Nov. 2008.

6. K. Sasloglou, I. A. Glover, K. H. Kwong and I. Andonovic. Wireless Sensor Network for Animal Monitoring Using both Antenna and Base-station Diversity. In Proc. 11th IEEE Singapore International Conference on Communication Systems (ICCS 2008), p. 27-33, Guangzhou, China, Nov. 2008.
7. F. Darbari, K. Sasloglou, R. W. Stewart, I. A. Glover and I. Andonovic. Effect of Antenna Height and Polarisation on Short Wireless Links. In 16th European Signal Processing Conference (EUSIPCO 2008), Lausanne, Switzerland, Aug. 2008.
8. K. H. Kwong, T. T. Wu, K. Sasloglou, B. Stephen, D. Cao, H. G. Goh, S. K. Goo, M. Gilroy, C. Tachtatzis, I. A. Glover, C. Michie and I. Andonovic. Implementation of Herd Management System with Wireless Sensor Networks. In Joint International Agricultural Conference (JIAC 2009), Wageningen, Netherlands, Jul. 2009.
9. K. H. Kwong, K. Sasloglou, H. G. Goh, T. T. Wu, B. Stephen, M. Gilroy, C. Tachtatzis, I. A. Glover, C. Michie and I. Andonovic. Adaptation of Wireless Sensor Network for Farming Industries. In The 6th International Conference on Networked Sensing Systems (INSS 2009), Carnegie Mellon University, Pittsburgh, USA, Jun. 2009.

CHAPTER 2

Transmission Channel Context

This chapter contains a brief introduction to wireless sensor networks (WSN), including evolution, current technologies and the available chipsets and wireless nodes. A brief discussion of the channel implications for higher level protocols is also included.

2.1 Wireless Sensor Networks

Wireless Sensor Networks (WSNs) are spatially distributed small, light, low-cost and low power consumption autonomous nodes communicating with each other through the wireless medium and monitoring parameters such as temperature, pressure, light intensity, vibration, acceleration etc [4].

Each node consists of three sub-systems, as shown in Figure 2.1. The sensor sub-system, which is usually transducers sensing physical quantities (such as temperature), the processing sub-system, which is a micro-controller for performing local computations on the sensed data, and the communication sub-system, which is an RF chipset for establishing communication between neighbouring nodes [4].

Many wireless devices are also equipped with (FLASH) memory elements, integrated in the processing subsystem, to store sensed data when there is no connection to the base-station.

2.1.1 Introduction and Evolution

Although wireless communication networks have a long history, which starts in 1921, Wireless Personal Area Networks (WPANs) and WSNs have evolved rapidly over the last three decades. They now have applications in industrial , commercial, domestic and personal environments [5].

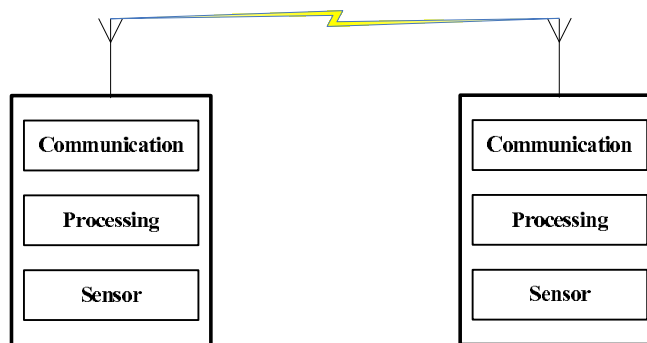


Figure 2.1: High level description of sensor node.

Wireless sensor network technology can be dated back to 1978 with a DARPA-sponsored project called Distributed Sensor Nets Workshop at Carnegie-Mellon University in Pittsburgh [5].

A number of WSN related projects are mentioned in [5]. Wireless Integrated Network Sensors (WINS) is dated back to 1993 and was a collaboration between UCLA and the Rockwell Science Center. It utilises the spread spectrum technique operating at either 900 MHz or 2.4 GHz. The PicoRadio program was started in University of California at Berkeley in 1999, an institute also known for the Smart Dust [6] program. The μ AMPS project started at MIT and resulted in the generation of the sensor network communication protocol LEACH (Low Energy Adaptive Clustering Hierarchy). Other projects include the Terminodes and the MANET (Mobile Ad-Hoc Networks) [5].

Depending on the application, the size of the sensor nodes can be very small. Transceivers in Specknet [3] have a volume of 1 mm^3 ($1 \text{ mm} \times 1 \text{ mm} \times 1 \text{ mm}$) for example. Wireless sensor networks appear in a range of applications including [5]:

- Industrial control and monitoring
- Home automation and consumer electronics
- Security and military sensing
- Asset tracking and supply chain management
- Intelligent agriculture and environmental sensing
- Health monitoring

The main characteristic that distinguish WSNs is their ad-hoc feature. In contrast with infrastructure networks, which need special nodes called Access Points (APs), no fixed infrastructure is required for ad-hoc networks. They offer

on-the-fly deployment at any desired location. The nodes may communicate either directly with each other (single-hop), or by forwarding messages through other accessible (multi-hop) nodes [4].

Some remarkable issues make sensor networks a distinct category of ad-hoc wireless networks, such as mobility of nodes, size of the network, density of deployment, power constraints, information fusion and traffic distribution [4].

Although ad-hoc wireless sensor networks can be deployed easily and conveniently, major key issues need to be taken into account during the design process [4]. A summary of these issues has been extracted from an analysis provided by Manoj and Murthy [4] and is presented in Figure 2.2.

2.1.2 Wireless Sensor Network Technologies

There are several standards currently available for deploying a WSN, including IEEE 802.15.1/ Bluetooth [7] and IEEE 802.11x (WLAN) [8]. However, the most common and widely used standard for WPANs to date is the IEEE 802.15.4/Zig-Bee standard [9]. UWB technology [10] [11] [12] is also used for WPANs when high data rates are required.

This section presents the RF chipsets and wireless sensor devices currently available.

2.1.2.1 RF Chipsets

Many RF chipsets are available in the wireless sensor market. Chipcon (acquired in 2006 by Texas Instruments [13]) dominates this market, as it is the main provider of one of the largest manufacturers of wireless nodes, such as Crossbow.

Figure 2.3 shows the popular CC2420, the chipset that MICAz wireless devices are equipped with.

The two main features that characterise RF chipset performance are data rate and power consumption. Table 2.1 summarises the characteristics of some of the dominant chipsets in the market.

2.1.2.2 Wireless Nodes

The selection of the appropriate wireless node (which corresponds to the appropriate chipset) is highly dependant on the target application. Data rate, range, power consumption and unit price are usually the crucial parameters which define the selection of the most suitable wireless device.

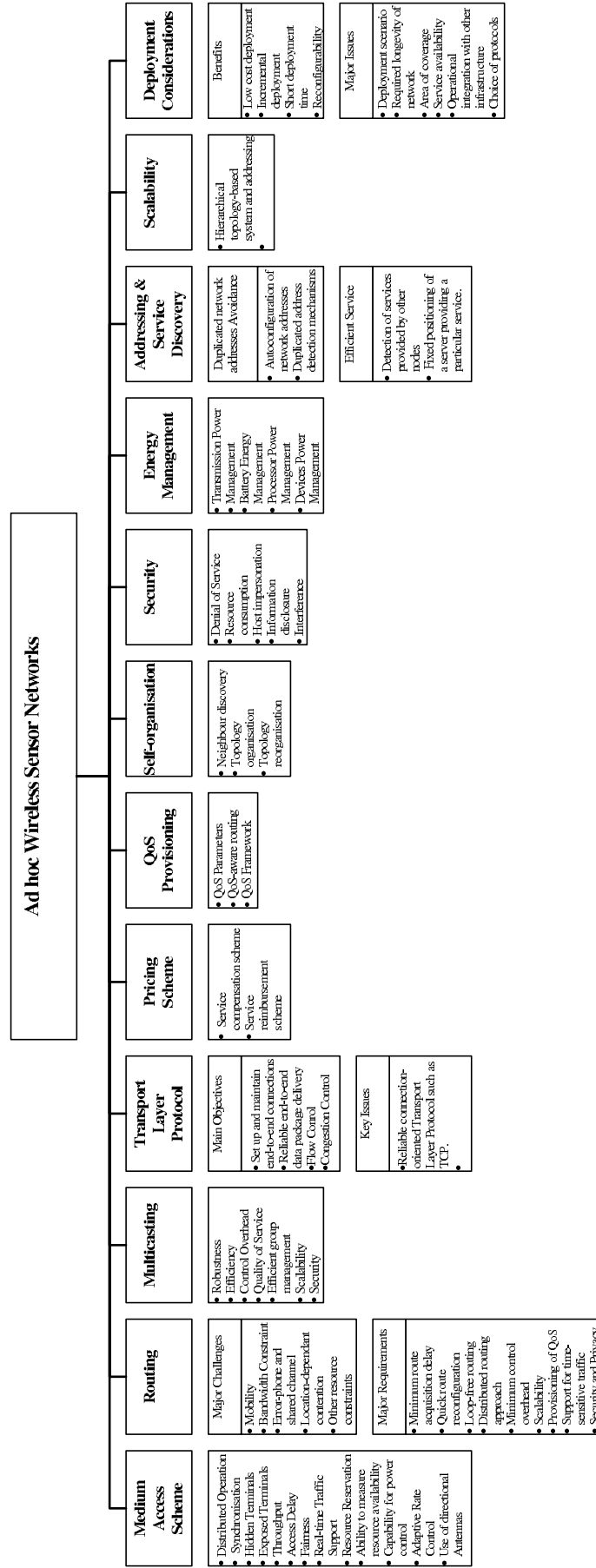


Figure 2.2: Major key issues to be considered during the design of an ad-hoc WSN [4].

Part Number	Manufacturer	Frequency Range (GHz)	TX Power (dBm)	Sensitivity (Max) (dBm)	Data Rate (kbps)	RX Current (Lowest) (mA)	Frequency (Min) (MHz)	Frequency (Max) (MHz)	Operating Voltage (Min) (V)	Modulation Techniques	Approx. Price (US\$)
CC1000	TI	< 1	12	-112	500	15.0	300	1000	2.1	FSK	4.75 (1kt)
CC1100E	TI	< 1	10	-118	153.6	19.9	470, 950	510, 960	1.8	2-FSK, GFSK, MSK, OOK, ASK	2.40 (100u)
CC1020	TI	< 1	10	-112	500	14.0	402, 804	470, 940	2.3	OOK, FSK, GFSK	4.35 (100u)
CC1101	TI	< 1	12	-112	500	14.0	300, 387, 779	348, 464, 928	1.8	N/A	2.35 (100u)
CC2400	TI	2.4	0	-101	1000	24.0	2400	2483	2	2-FSK, GFSK	3.40 (1kt)
CC2420	TI	2.4	0	-95	250	18.8	2400	2483.5	2.1	O-QPSK	4.15 (100u)
CC2500	TI	2.4	1	-104	500	13.3	2400	2483	3.6	2-FSK, GFSK, OOK, MSK	2.15 (100u)
CC2511F8	TI	2.4	1	-103	500	17.1	2400	2483.5	3.6	2-FSK, GFSK, MSK	4.40 (100u)
CC2520	TI	2.4	5	-98	250	22.3	2394	2507	1.8	O-QPSK	2.45 (100u)
RFW3M	VISHAY	2.4	8	-80	3000	18	2416	2464	2.5	ASK	N/A
RFW3M-PA	VISHAY	2.4	21	-78	3000	50	2400	2483.5	N/A	ASK	N/A
RFW8M	VISHAY	2.4	7	-76	8000	18	2426	2456	2.5	ASK	N/A
RFW122-M	VISHAY	2.4	7	-77	1000	7	2400	2483.5	2.4	ASK	N/A
DW44SS1000	Decawave	3.5 - 7	-14/-10	N/A	6800	2	3500	7000	2.5	BPSK	N/A

Table 2.1: Some of the most popular available RF chipsets.



Figure 2.3: CC2420 by Chipcon (After [14]).

Although Crossbow is the leading manufacturer of wireless sensor devices, there are other manufacturers that offer hardware with similar capabilities. The RF chipset of each device defines its performance, as the data rate and the majority of the power consumed depend on it. Table 2.2 summarises the wireless sensor devices currently available [15] [16] [17] [18].

2.1.2.3 Comparison

Advanced applications have forced manufacturers to develop chipsets that meet demanding standards in terms of data rate, range and power consumption.

Although Chipcon holds a large percentage of the market, their chipsets have rather limited data rate. VISHAY [19] offer high data rate RF chipsets which can reach 8 Mbps without compromising the power consumption.

One wireless device which is distinct from others is the ScenSor by Decawave [20] (equipped with the DW4aSS1000 chipset), based on the IEEE 802.15.4a [21] standard. This can achieve 6.8 Mbps, consuming very low currents (2 mA, 20 mA, 1 μ A and 100 nA for transmit, receive, watchdog timer and sleep mode respectively).

Figure 2.4 represents a comparison of the maximum data rates provided by the wireless devices currently available.

2.2 Channel Implications for Higher Level Protocols

The physical layer (PHY) is responsible for the transmission of the raw bit stream over the physical medium [22] [4]. It is the lowest level of the OSI reference model (Figure 2.5) and deals with all the mechanical (e.g. physical dimensions

Wireless Module	Manufacturer	RF Chipset	Max Data Rate (kbit/s)	Receiver Sensitivity (dBm)	Min/Max TX Power (dBm)	Freq. Band (MHz)	Max. Range (m)
Mica	Crossbow	TR1000	40	N/A	N/A	433/916	N/A
Mica2	Crossbow	CC1000	38.4	-98	-20/+5	868/916	160
Mica2Dot	Crossbow	CC1000	38.4	-101/-98	N/A	315/433/868/916	330/160
MicaZ	Crossbow	CC2420	250	-94	-24/0	2400-2480	100
TelosB	Crossbow	CC2420	250	-94	N/A	N/A	100
IMote 2.0	Crossbow	CC2420	250	-94	-24/0	2400-2480	N/A
Iris	Crossbow	N/A	250	-101	-24/+3	2405-2480	N/A
BTnode	ETH Zurich	CC1000	38.4	-98	-20/+5	433/868/915	N/A
FireFly 2.2	Carnegie Mellon University	CC2420	250	-94	-24/0	2400-2480	N/A
ScenSor	Decawave	DW44SS1000	6800	N/A	-14 or -10	3.5-7	70

Table 2.2: Some of the most popular wireless sensor devices available in the market.

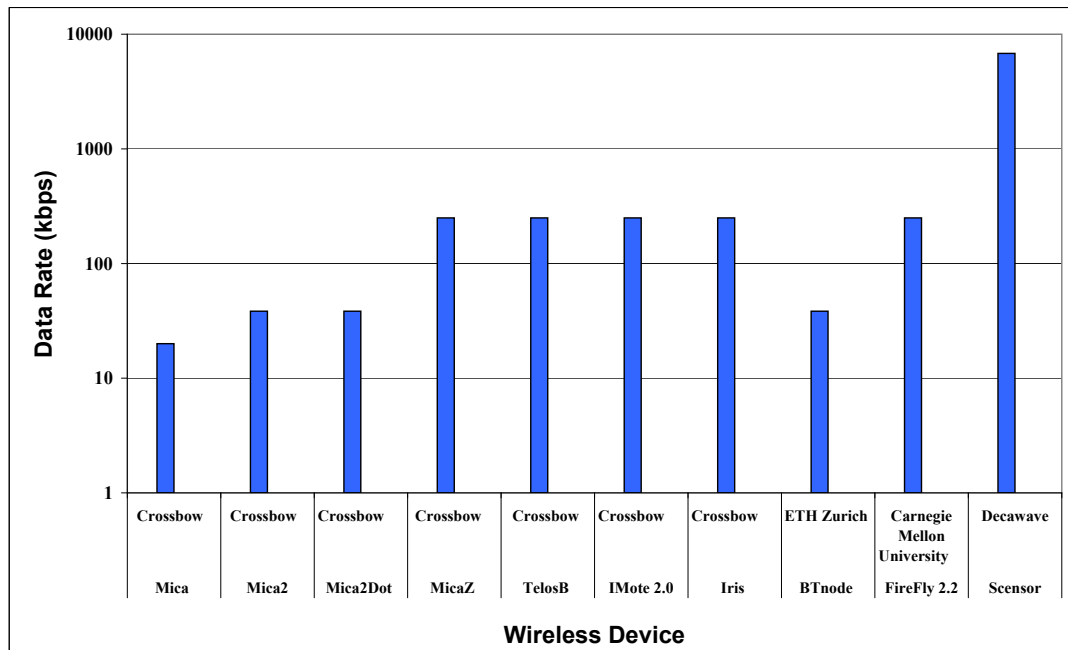


Figure 2.4: Comparison of the wireless devices available in the market.

cables, connectors and pins) and electrical (e.g. voltage levels, duration of each transmitting bit) specifications of the network hardware, as well as the physical medium which is used for transmitting those raw bits [4].

As the bottom OSI layer PHY has an impact on all the other layers of the protocol stack. This makes it vital to the overall communication system design.

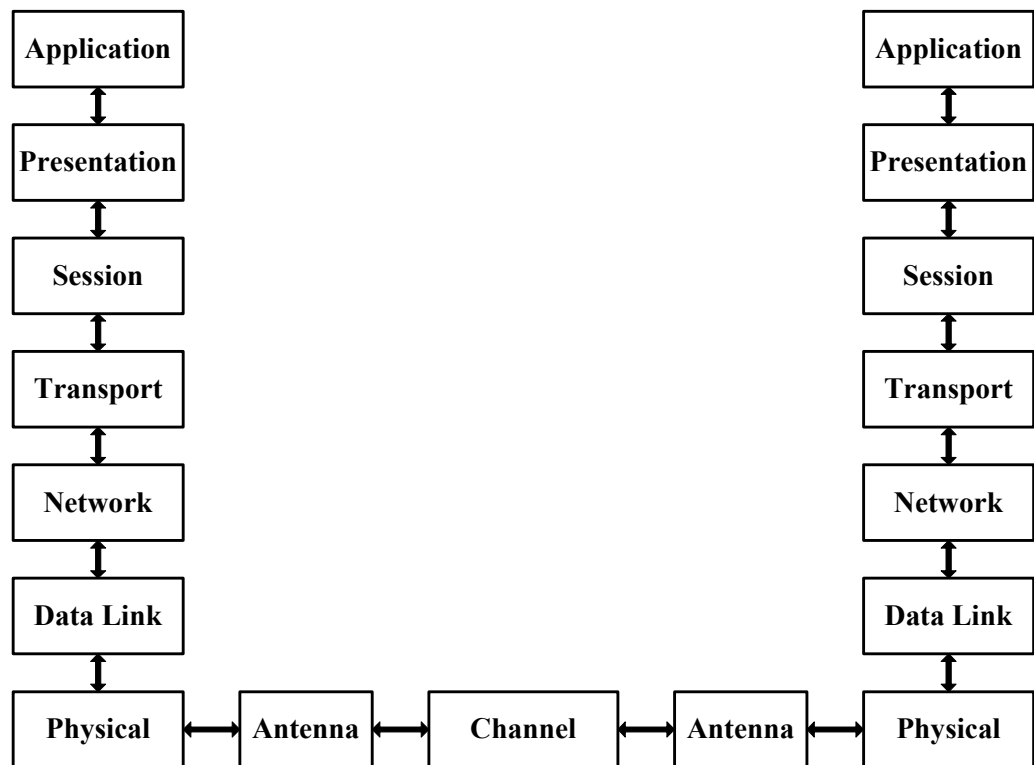


Figure 2.5: Schematic diagram of OSI layers, including antennas and channel.

CHAPTER 3

Literature Review - Channel Measurements and Modelling

In wireless communications, channel measurement refers to a method of quantifying the characteristics of the electromagnetic medium. Such characteristics include path loss and fading described in Sections 3.2.1 and 3.2.2, respectively.

Channel measurements are needed during the design process of a wireless communication system. They help in the estimation of the gain and loss factors which are crucial for link budget calculations. In this way, the system limits can be defined to ensure acceptable (relative to each application) performance (communication range, throughput and goodput) .

3.1 Basic Propagation Mechanisms

The five basic electromagnetic wave propagation mechanisms are reflection, transmission, absorption, diffraction and scattering [23].

When, during propagation, an electromagnetic wave impinges on a surface or object considerably larger in size than one wavelength, then part of the wave's energy is reflected, part is transmitted, and part (usually smaller) is absorbed by the material [23] [24].

When the communication link is obstructed by a large, opaque, obstacle there is no LOS link. The electromagnetic wave however may bend around the edge of the obstacle, and reach a transceiver located within the geometrical shadow. This effect is called diffraction.

When, during propagation, an electromagnetic wave impinges on objects smaller than one wavelength then scattering takes place [23]. Scattering also occurs due to rough surfaces [23].

3.1.1 Reflection and Transmission Coefficients

The propagation mechanisms associated with reflection are well described by the Fresnel equations. Assume that an electromagnetic wave is reflected on a plane surface with an incident angle θ_i , as shown in Figure 3.1.

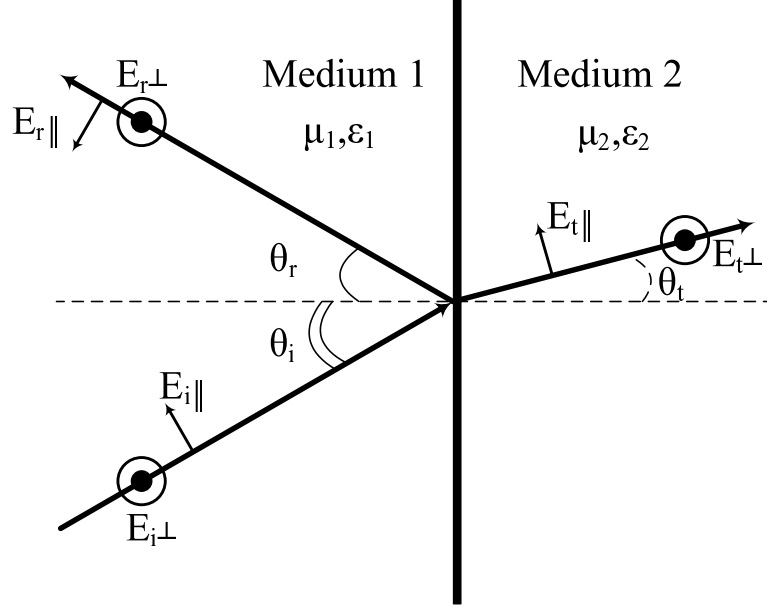


Figure 3.1: Schematic diagram of an electromagnetic wave reflected and transmitted at a medium interface.

In such a case, part of the energy is reflected at the surface with reflection angle θ_r equal to the incidence angle and part is transmitted into the second medium. The quantity of power reflected or transmitted through the medium is determined by reflection or transmission coefficients, respectively.

Both reflection and transmission coefficients are dependant on the polarisation of the wave. For parallel polarisation, the reflection coefficient (Γ_{\parallel}) is the ratio of the parallel polarised reflected electric field ($E_{r\parallel}$) to the parallel polarised incident field ($E_{i\parallel}$), given by Equations 3.1 and 3.2. Z_1 and Z_2 are the wave impedances of medium 1 and 2 respectively. For the measurements in this thesis medium 1 is always air with impedance 376.6Ω [24] [25].

$$\Gamma_{\parallel} = \frac{E_{r\parallel}}{E_{i\parallel}} \quad (3.1)$$

$$\Gamma_{\parallel} = \frac{Z_1 \cos \theta_i - Z_2 \cos \theta_t}{Z_2 \cos \theta_t + Z_1 \cos \theta_i} \quad (3.2)$$

For perpendicular polarisation, the reflection coefficient (Γ_{\perp}) is the ratio of the perpendicularly polarised reflected electric field to the perpendicularly polarised

3.1. BASIC PROPAGATION MECHANISMS

incident field, given by Equations 3.3 and 3.4 [24].

$$\Gamma_{\perp} = \frac{E_{r\perp}}{E_{i\perp}} \quad (3.3)$$

$$\Gamma_{\perp} = \frac{Z_2 \cos\theta_i - Z_1 \cos\theta_t}{Z_2 \cos\theta_i + Z_1 \cos\theta_t} \quad (3.4)$$

For parallel polarisation, the transmission coefficient (T_{\parallel}) is the ratio of transmitted to incident electric field, given by Equations 3.5 and 3.6 [24].

$$T_{\parallel} = \frac{E_{t\parallel}}{E_{i\parallel}} \quad (3.5)$$

$$T_{\parallel} = \frac{2Z_2 \cos\theta_i}{Z_2 \cos\theta_t + Z_1 \cos\theta_i} \quad (3.6)$$

For perpendicular polarisation, the transmission coefficient (T_{\perp}) is the ratio of reflected to incident electric field, given by Equation 3.7 and 3.8 [24].

$$T_{\perp} = \frac{E_{t\perp}}{E_{i\perp}} \quad (3.7)$$

$$T_{\perp} = \frac{2Z_2 \cos\theta_i}{Z_2 \cos\theta_i + Z_1 \cos\theta_t} \quad (3.8)$$

The impedance, Z , for any medium is given by Equation 3.9, where μ , σ , and ϵ are the medium's permeability, conductivity and permittivity, respectively, while $\omega = 2\pi f$.

$$Z = \sqrt{\frac{j\omega\mu}{\sigma + j\omega\epsilon}} \quad (3.9)$$

For dielectric materials with $\sigma_1 = \sigma_2 = 0$ and $\mu_1 = \mu_2$ the reflection and transmission coefficients are:

$$\Gamma_{\parallel} = \frac{Z_1 \cos\theta_i - Z_2 \sqrt{1 - \left(\frac{Z_2}{Z_1}\right)^2 \sin^2\theta_i}}{Z_2 \sqrt{1 - \left(\frac{Z_2}{Z_1}\right)^2 \sin^2\theta_i} + Z_1 \cos\theta_i} \quad (3.10)$$

$$\Gamma_{\perp} = \frac{Z_2 \cos\theta_i - Z_1 \sqrt{1 - \left(\frac{Z_2}{Z_1}\right)^2 \sin^2\theta_i}}{Z_2 \cos\theta_i + Z_1 \sqrt{1 - \left(\frac{Z_2}{Z_1}\right)^2 \sin^2\theta_i}} \quad (3.11)$$

$$T_{\parallel} = \frac{2Z_2 \cos\theta_i}{Z_2 \sqrt{1 - \left(\frac{Z_2}{Z_1}\right)^2 \sin^2\theta_i} + Z_1 \cos\theta_i} \quad (3.12)$$

$$T_{\perp} = \frac{2Z_2 \cos\theta_i}{Z_2 \cos\theta_i + Z_1 \sqrt{1 - \left(\frac{Z_2}{Z_1}\right)^2 \sin^2\theta_i}} \quad (3.13)$$

If the reflecting surface is horizontal then parallel polarised components are referred to as vertical and perpendicular polarised components are horizontal.

If the surface on which the electromagnetic wave impinges is a good conductor (essentially perfect) with high σ , most of the energy is reflected. However, in most cases the material is usually not a perfect conductor and some fraction of the energy is transmitted. The complex dielectric constant (which accounts for ohmic loss) for a lossy medium is given by Equation 3.14.

$$\epsilon = \epsilon_0 \epsilon_r - j \frac{\sigma}{2\pi f} \quad (3.14)$$

where ϵ_0 is 8.85×10^{-12} F/m, ϵ_r is relative permittivity and σ the conductivity (S/m) [23].

Figure 3.2 (a) shows an example of the reflection and transmission coefficients for average (dry) ground ($\epsilon_r = 7$ and $\sigma = 0.001$) at 2.45 GHz. It is apparent that for both vertical and horizontal polarisation, the reflection coefficients converge at -1, while the transmission coefficients converge at 0. It is also apparent that as the incident angle approaches 90 degrees (e.g. when antenna separation becomes small compared to antenna height) the reflection coefficients converge to -1.

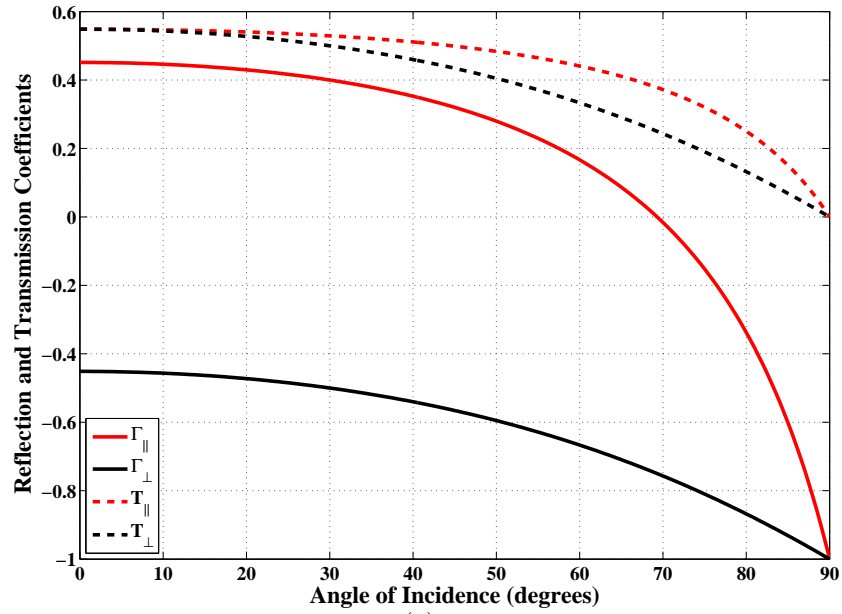
Figure 3.2 (b) shows the magnitude of the reflection and transmission coefficients. No reflection occurs for vertical polarisation at Brewster angle (θ_B) which may be calculated [23] using:

$$\sin(\theta_B) = \frac{\sqrt{\epsilon_r - 1}}{\sqrt{\epsilon_r^2 - 1}} \quad (3.15)$$

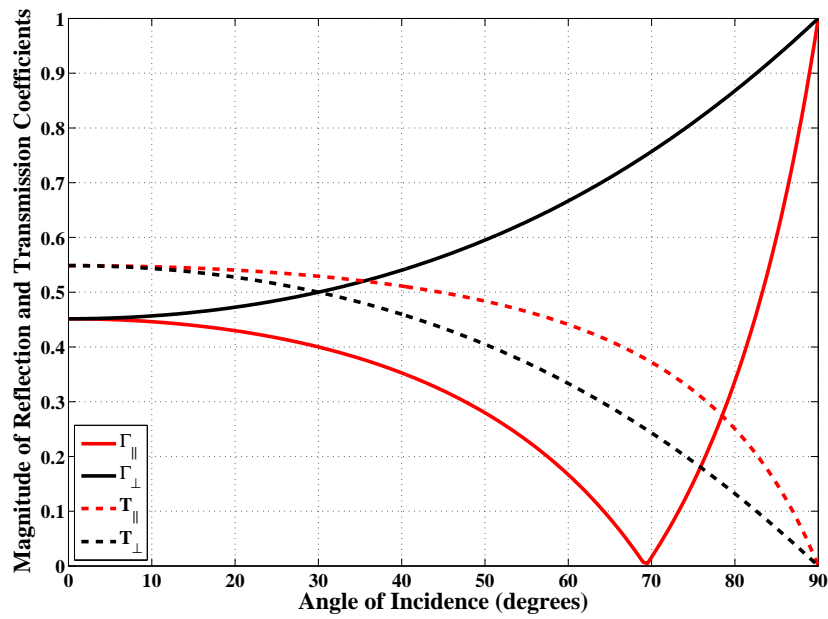
3.2 Modelling

3.2.1 Path Loss

In communications, path loss (PL) is defined as the ratio of transmitted power to received power assuming isotropic antennas [24].



(a)



(b)

Figure 3.2: Reflection and transmission coefficients for (a) average (dry) ground ($\epsilon_r = 7.0$, $\sigma = 0.001$) and (b) reflection magnitudes for vertical and horizontal polarisation.

Transmission loss (TL) is defined as the ratio of transmitted power to received power and includes gains introduced by receiving and transmitting antennas. Path loss is therefore the same as transmission loss for unity gain (0 dBi) antennas. Both PL and TL are usually expressed as positive dB values [23] [24].

Many theoretical and empirical models exist to predict path loss depending on the environment. The accuracy of the prediction usually increases with increasing complexity of the model.

Two of the simplest and most popular physical propagation models are the free space path loss (FSPL) model and the plane earth path loss (PEPL) model. These are described in Sections 3.2.1.1 and 3.2.1.2.

Two of the simplest and most popular empirical models are the single slope path loss (SSPL) and dual slope path loss (DSPL) models, respectively. These are described in Sections 3.2.1.3 and 3.2.1.4.

3.2.1.1 Free Space (Friis) Model

The free space path loss (FSPL) model, also known as Friis model, is the simplest of all propagation models.

In this case, only a direct LOS path is assumed, with no reflection and no diffraction.

The Friis path loss model is given by Equation 3.16, where P_T is transmission power, P_R is received power and G_T and G_R are transmitter and receiver antenna gains, respectively. The LOS distance between transmitter and receiver is d and the carrier wavelength is λ , where $\lambda = \frac{c}{f}$.

$$P_R = P_T G_T G_R \left(\frac{\lambda}{4\pi d} \right)^2 \quad (3.16)$$

Free space path loss (FSPL) is the ratio of transmitted to received power assuming isotropic antennas ($G_T = G_R = 1.0$) and therefore may be expressed as:

$$FSPL = \frac{P_T}{P_R} G_T G_R = \left(\frac{4\pi d}{\lambda} \right)^2 \quad (3.17)$$

Equation 3.17 when working in dB units is:

$$P_R[dBm] = P_T[dBm] + G_T[dBi] + G_R[dBi] - FSPL[dB] \quad (3.18)$$

3.2. MODELLING

and FSPL in dB is:

$$FSPL[dB] = 10\log_{10} \left(\frac{4\pi d}{\lambda} \right)^2 = 20\log_{10} \left(\frac{4\pi df}{c} \right) \quad (3.19)$$

Applying the properties of the logarithms, we get Equation 3.20:

$$FSPL[dB] = 20\log_{10} (f[Hz]) + 20\log_{10} (d[m]) + 20\log_{10} \left(\frac{4\pi}{c[m/s]} \right) \quad (3.20)$$

i.e.:

$$FSPL[dB] = 20\log_{10} (f[Hz]) + 20\log_{10} (d[m]) - 147.6 \quad (3.21)$$

Equation 3.21 is often expressed with different units (f in MHz and d in km),

i.e.:

$$FSPL[dB] = 20\log_{10} (f[MHz]) + 20\log_{10} (d[km]) + 32.4 \quad (3.22)$$

FSPL increases by increasing the frequency f or the antenna separation d .

Figure 3.3 shows the impact of frequency and distance on path loss.

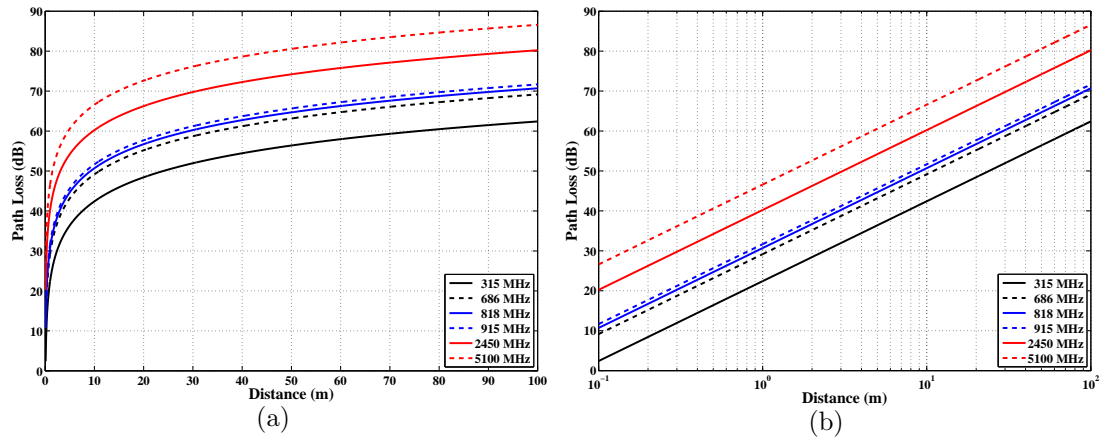


Figure 3.3: Free space path loss versus distance for selected frequencies.

FSPL increases at a rate of 6 dB per octave (20 dB per decade) due to the inverse square law, Figure 3.3 (b).

3.2.1.2 Plane Earth Path Loss Model

The Plane Earth Path Loss (PEPL) model is simple but more realistic than the free space model when a ground reflection is significant, Figure 3.4.

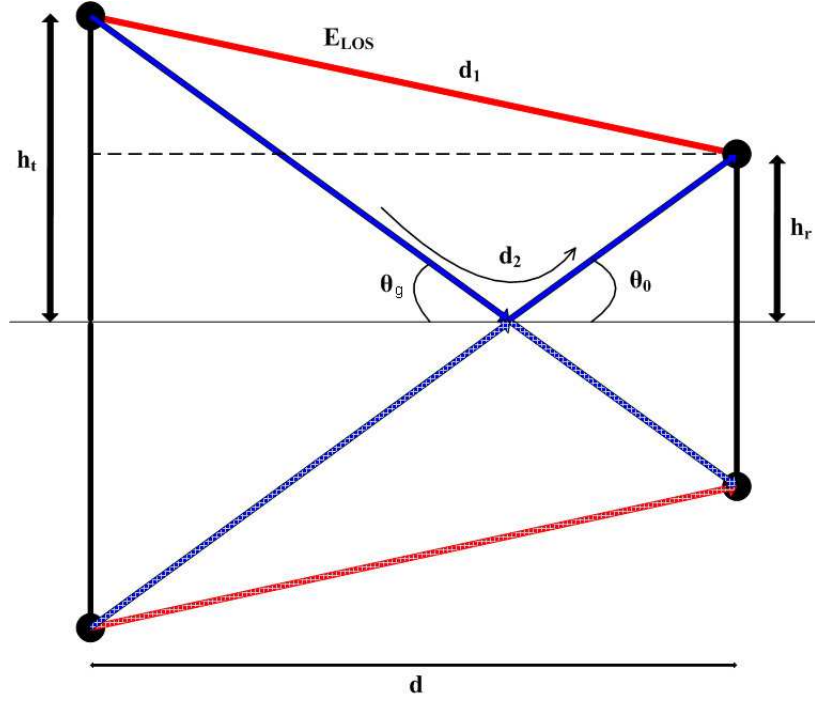


Figure 3.4: Two-ray propagation assumed for the PEPL model.

Following the method of images, the length of the two separate paths, d_1 and d_2 , may be estimated, as long as the heights of the transmitting (h_T) and receiving (h_R) antennas are known. From simple geometry:

$$d_1 = \sqrt{(h_T - h_R)^2 + d^2} \quad (3.23)$$

$$d_2 = \sqrt{(h_T + h_R)^2 + d^2} \quad (3.24)$$

The path length difference of these paths, Δ , is:

$$\Delta = d_2 - d_1 = d \left[\sqrt{\left(\frac{h_T + h_R}{d}\right)^2 + 1} - \sqrt{\left(\frac{h_T - h_R}{d}\right)^2 + 1} \right] \quad (3.25)$$

The phase difference of signals arriving via these two rays, θ_Δ , due to path length difference is therefore:

$$\theta_\Delta = \frac{2\pi\Delta}{\lambda} = \frac{\Delta\omega_c}{c} \quad (3.26)$$

while the time delay, τ_d , between signals arriving via the two rays is:

$$\tau_d = \frac{\Delta}{c} = \frac{\theta_\Delta}{2\pi f_c} \quad (3.27)$$

The total field arriving at the receiving antenna is the sum of the direct-wave field (A_{direct}) plus the reflected-wave field ($A_{reflected}$):

$$A_{TOTAL} = A_{direct} + A_{reflected} = A_{direct} + A_{direct}\Gamma e^{jk\Delta} \quad (3.28)$$

where Γ is the (complex) reflection coefficient. Simplifying:

$$A_{TOTAL} = A_{direct}|1 + \Gamma e^{jk\Delta}| \quad (3.29)$$

The ratio of received power P_R to direct power P_{direct} is therefore:

$$\frac{P_R}{P_{direct}} = \left(\frac{A_{TOTAL}}{A_{direct}} \right)^2 = |1 + \Gamma e^{jk\Delta}|^2 \quad (3.30)$$

Since the direct path is a LOS link it is described by the FSPL model, i.e.:

$$P_{direct} = P_T \left(\frac{\lambda}{4\pi d} \right)^2 \quad (3.31)$$

The PEPL ratio of transmitted to received power is therefore given by:

$$\frac{P_R}{P_T} = \left(\frac{\lambda}{4\pi d} \right)^2 |1 + \Gamma e^{jk\Delta}|^2 \quad (3.32)$$

Assuming that the antenna separation is large enough to yield very small grazing angles, and that the signal undergoes a phase change of 180 degrees ($\Gamma \approx -1$) then:

$$\frac{P_R}{P_T} = 2 \left(\frac{\lambda}{4\pi d} \right)^2 [1 - \cos(k\Delta)] \quad (3.33)$$

In the more general case [26], a complex factor F can be defined which is the (complex) ratio of field strength in the presence of the ground reflection to the free-space field strength:

$$F = 1 + |\Gamma| e^{j\phi} e^{-jk\Delta} \quad (3.34)$$

where ϕ is $\arg(\Gamma)$.

Assuming perfect reflection (i.e. $|\Gamma| e^{j\phi} = -1$) Equation 3.34 can be rewritten as follows (Proof in Appendix A).

$$|F| = 2\sin(k\Delta) \quad (3.35)$$

The power at the receiver is therefore given by:

$$P_R = EIRP \times FSPL \times |F|^2 \times G_R \quad (3.36)$$

where $EIRP = P_T G_T$ is the effective isotropic radiated power, i.e.:

$$P_R = P_T G_T \left(\frac{\lambda}{4\pi d} \right)^2 4\sin^2(k\Delta) G_R \quad (3.37)$$

In dB form Equation 3.37 becomes:

$$P_R(dBW) = P_T + G_T - FSPL + G_R + 6.0 + 20\log_{10} |\sin(k\Delta)| \quad (3.38)$$

The path difference, Δ , is often simplified using the binomial theorem ¹, as long as the antenna heights h_T and h_R are small compared with the antenna separation d ($h_T, h_R \ll d$) [24]:

$$\Delta = d_2 - d_1 \approx \frac{2h_T h_R}{d} = \Delta' \quad (3.39)$$

In this thesis, however, no such approximation is made and the accurate path difference Δ is normally assumed.

The furthest point of constructive interference between direct and reflected signals occurs for the smallest argument of $\sin(k\Delta')$ which is equal to 1.0, i.e.:

$$\frac{2\pi h_T h_R}{\lambda d} = \frac{\pi}{2} = 1 \quad (3.40)$$

The furthest point of constructive interference therefore occurs at distance R_{max} , given by:

$$R_{max} = \frac{4h_T h_R}{\lambda} \quad (3.41)$$

Figure 3.5 shows the free space (blue) and plane earth transmission gains for vertical (black dashed) and horizontal polarisation (red solid) for a typical ground ($\epsilon_r = 15$ and $\sigma = 0.005$) at 2.45 GHz. The vertical dashed line represents R_{max} .

Figure 3.6 shows the free space (blue) and plane earth transmission gains for typical ground (black dashed) and perfect conductor (red solid) vertical polari-

¹ $(1+x)^n \approx 1+nx$ for $x \ll 1$

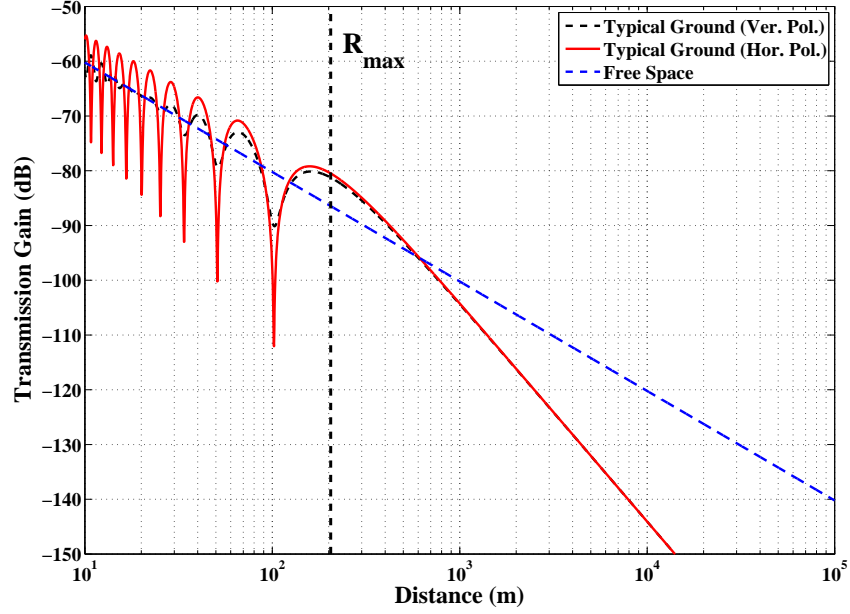


Figure 3.5: Free space (blue) and plane earth propagation models for vertical (black and dashed) and horizontal (red and solid) polarisations ($f = 2.45$ GHz, $\epsilon_r = 15$ and $\sigma = 0.005$).

sations.

The optimum receiver antenna height may be calculated by differentiating Equation 3.35 with respect to receive antenna height and setting the result to zero:

$$\frac{d|F|}{dh_R} = 2\cos\frac{2\pi h_T h_R}{\lambda d} \frac{2\pi h_T}{\lambda d} = 0 \quad (3.42)$$

i.e.:

$$\frac{2\pi h_T h_{R \text{ optimum}}}{\lambda d} = \frac{n\pi}{2} \quad (3.43)$$

where n is an odd integer (i.e. $n = 1, 3, 5, \dots$).

Thus:

$$h_{R \text{ optimum}} = n \frac{\lambda d}{4h_T} \quad (3.44)$$

Figure 3.7 shows the fluctuations of received power for a perfectly reflecting surface when the receiver antenna height changes, assuming a carrier frequency of 2.45 GHz, a transmitter antenna height (h_T) of 2 m and an antenna separation of 50 m. The maxima and minima are apparent. Knowing a separation distance,

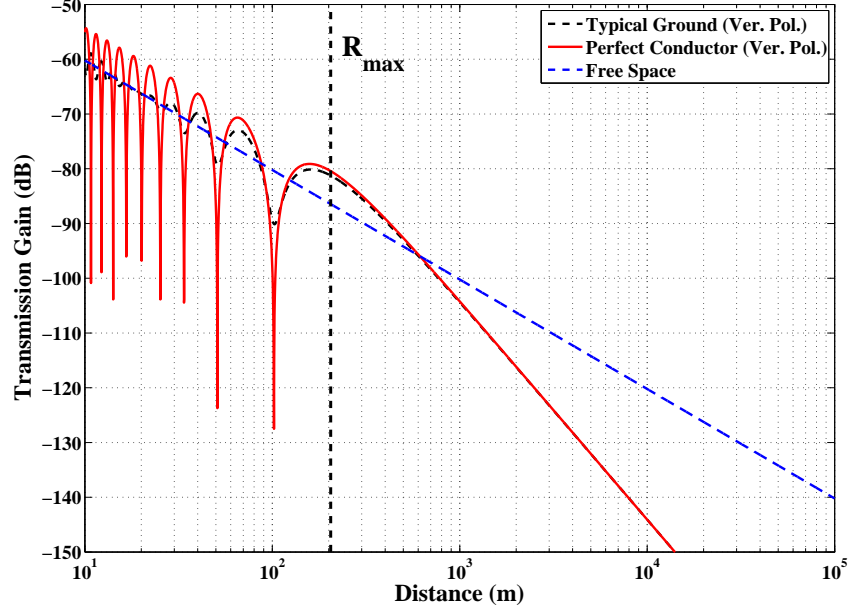


Figure 3.6: Free space (blue) and plane earth propagation models for vertical polarization assuming typical ground (black dashed) and perfect conductor (red solid).

an optimum antenna height for the receiver could be selected to minimise the transmission loss of the radio link. In this particular example, the optimum height is either at 0.75 m or 2.25 m. Such optimisation is only possible, however, if both amplitude and phase of the reflected wave are stable.

3.2.1.3 Single Slope Path Loss Model

The single slope path loss (SSPL) model is the simplest empirical model used for describing the propagation loss of a wireless communication link.

The SSPL model for median path loss ($L_{p,median}$) is given by Equation 3.45, where K is the offset, or intercept, at a reference distance d_0 , n is the path loss exponent [24] and d is antenna separation. For short links d_0 is usually 1 m.

$$L_{p,median} = K + 10n \log_{10} \left(\frac{d}{d_0} \right) \quad (3.45)$$

Received power, P_R , is therefore given by Equation 3.46:

$$P_R = P_T + G_T - L_{p,median} + G_R \quad (3.46)$$

Figure 3.8 shows an example of SSPL for $K = 20$ and $n = 2$ and 4. $P_T = 0$ dBm and the antenna gains are 0 dBi.

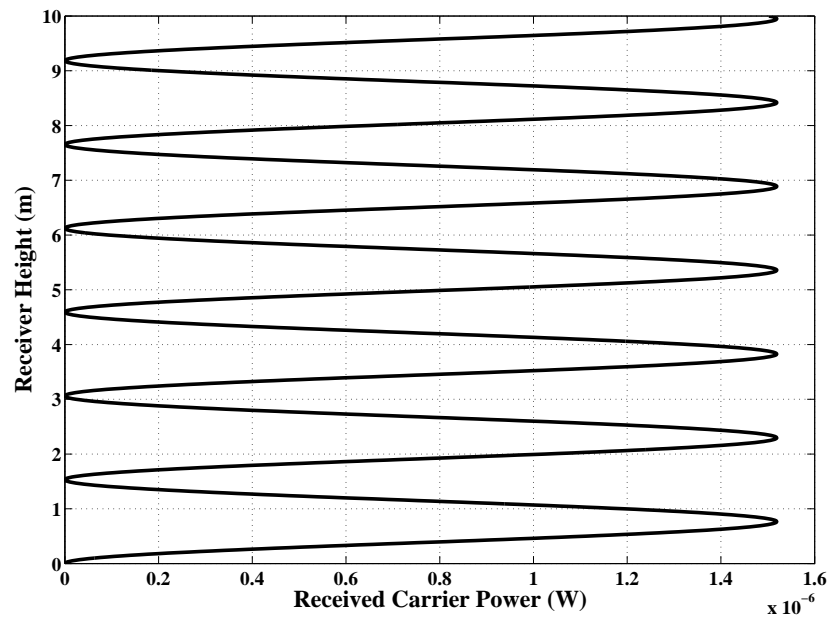


Figure 3.7: Variation of received power with receive antenna height for 50 m antenna separation, 2.45 GHz and transmit antenna height of 2 m.

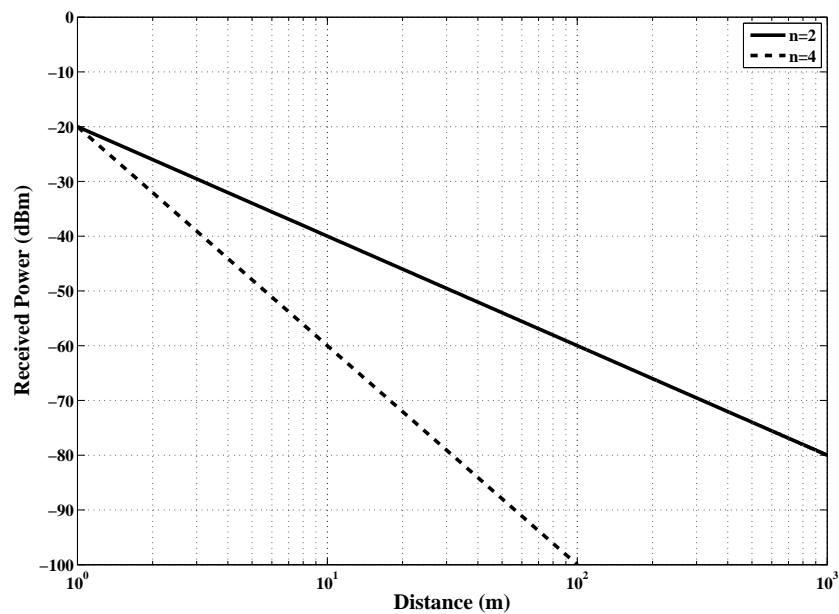


Figure 3.8: Example single slope path loss models.

3.2.1.4 Dual Slope Path Loss Model

Very often measurement data does not follow a single slope curve.

In this case, the propagation loss can be described by a piecewise linear curve with two slopes joining at a break point d_b .

The DSPL model is given by Equation 3.47, where n_1 and n_2 are the first and second curve segment gradients respectively, while d and d_b are distance and breakpoint distance, respectively.

$$L_{p,median} = \begin{cases} K + 10n_1 \log_{10} d, & \text{for } 0 \leq d \leq d_b \\ K + 10n_1 \log_{10} d_b + 10n_2 \log_{10} d - 10n_2 \log_{10} d_b, & \text{for } d_b \leq d \end{cases} \quad (3.47)$$

Received power is given by Equation 3.46 .

Figure 3.9 shows an example of DSPL assuming $K = 20$. The gradients of first and second line segments, n_1 and n_2 are 2 and 4, respectively. $P_T = 0$ dBm and the antenna gains are 0 dBi.

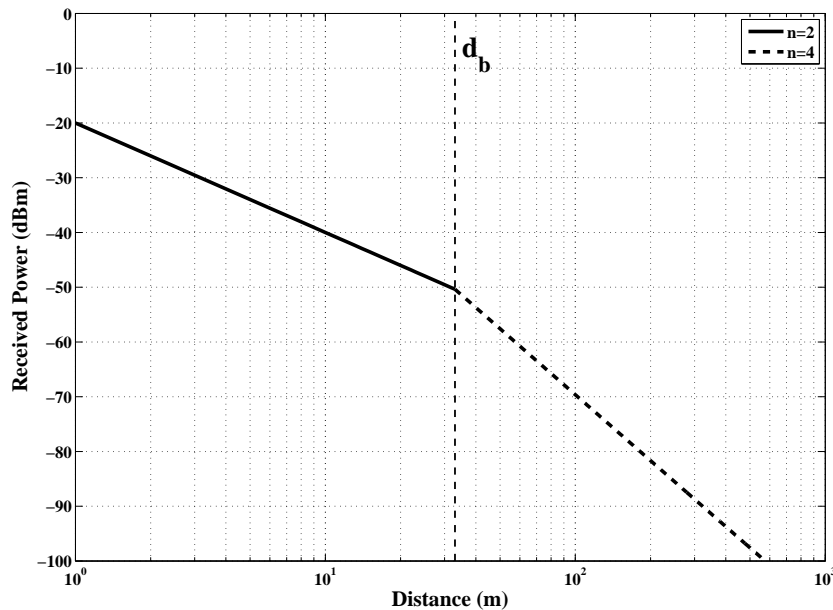


Figure 3.9: Example dual slope path loss model.

3.2.2 Fading

Taking into account only path loss, the received power would be constant at a specific distance. In practice, however, the signal is usually subject to fluctuations known as fading. Fading has been defined as follows [23]:

”Fading is used to describe the rapid fluctuations of the amplitudes, phases, or multipath delays of a radio signal over a short period of time or travel distance, so that large-scale path loss effects may be ignored”.

Multiple versions of a transmitted signal often arrive at the receiver at different time instances due to multipath effects. The interference between two or more versions of the same signal causes fading [23].

Figure 3.10 illustrates a wireless channel model including path loss, fading and noise.

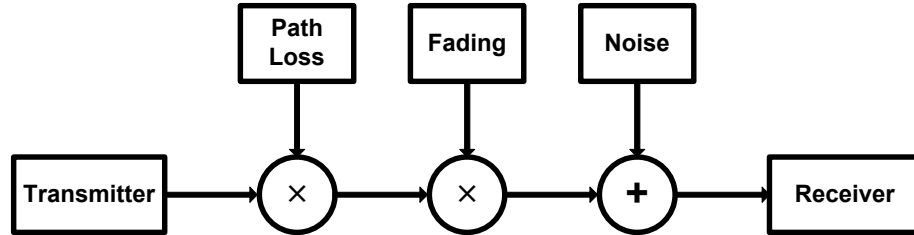


Figure 3.10: A wireless channel model [24].

The basic factors that affect fading are:

- Multipath propagation (resulting in spatial fading)
- Speed of the mobile station (resulting in temporal fading)
- Speed of surrounding objects (resulting in temporal fading)
- Transmission bandwidth of the signal (determining degree of frequency selective fading)

Fading can be categorised as four types as shown in Figure 3.11: flat, frequency selective, fast and slow. The first two are time dispersion effects (Section 3.2.2.1) and the latter two are frequency dispersion effects (Section 3.2.2.2).

The two parameters which determine the type of fading are the coherence time T_c and the coherence bandwidth B_c of the channel. Coherence time is a statistical measure of the time duration over which the channel impulse response is invariant, while coherence bandwidth is a statistical measure of the range of frequencies (bandwidth) over which the channel may be considered flat [23].

3.2.2.1 Fading based on multipath time delay spread

In multipath propagation, copies of the received signal (with different amplitude and phase) arrive at the receiver at different times. This is called time dispersion and as a result the duration of the signal received is larger than the one transmitted.

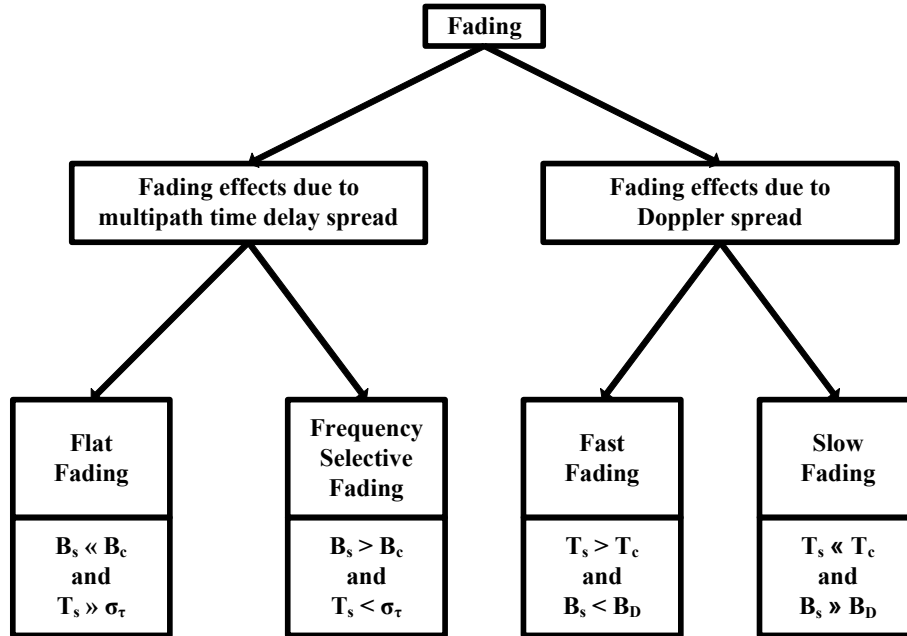


Figure 3.11: The four types of fading [23]. T_s , T_c , B_s and B_c are transmitted symbol duration, coherence time, transmitted signal bandwidth and coherence bandwidth of the channel, respectively.

When multipath propagation results in time dispersion, then the signal undergoes either flat or frequency selective fading [23].

Of particular interest are the delay spread measurements provided by [27], [28] and [29] for diverse frequencies (2, 5 and 17 GHz, 1.9 GHz and 915 MHz) and environments (indoor, Olympic Stadium of Athens and large train yard).

3.2.2.1.1 Flat Fading

When the coherence bandwidth of the channel B_c is larger than the bandwidth of the transmitted signal, then the signal undergoes flat fading. In such a case, the duration of the transmitted symbol T_s is larger than the rms delay spread σ_τ [23].

A flat fading simulator implemented in MatLab is presented in [30].

3.2.2.1.2 Frequency Selective Fading

When the coherence bandwidth of the channel B_c is smaller than the bandwidth of the transmitted signal, then the signal undergoes frequency selective fading. In such a case, the duration of the transmitted symbol T_s is smaller than the rms delay spread σ_τ [23].

The effect of frequency selectivity on multi-carrier wideband signals for indoor

and outdoor to indoor scenarios are studied in [31].

3.2.2.2 Fading based on Doppler spread

Although flat, and frequency selective, fading depends on the coherence bandwidth, fast and slow fading depends on the coherence time, which is inversely proportional to Doppler spread f_m [23]:

$$T_c \approx \frac{1}{f_m} \quad (3.48)$$

An interesting study of Doppler spread is presented in [32], concluded by indoor measurements at 2.4 GHz.

3.2.2.2.1 Fast Fading

In fast fading, the channel impulse response changes significantly within one symbol period. This corresponds to a high Doppler spread. In other words, the coherence time is shorter than the symbol period (i.e. $T_c < T_s$), which means that channel variations occur faster than baseband signal variations [23].

3.2.2.2.2 Slow Fading

In slow fading, the channel impulse response does not change significantly within one symbol period and therefore there is low Doppler spread. In other words, the coherence time is larger than the symbol period (i.e. $T_c > T_s$), which means that the channel variations occur slower than baseband signal variations [23].

3.3 Diversity

Multipath propagation is very common in practice and the received signal often therefore undergoes fading. Diversity techniques exist, however, which can reduce the impact of fading.

Diversity is based on the assumption that the probability of simultaneous deep fading at receivers separated spatially, in frequency, in polarisation or in time is low.

The most popular diversity techniques are [24] [23]:

- Spatial (Antenna) Diversity
 - Selection Diversity

3.3. DIVERSITY

- Feedback Diversity
- Maximal Ratio Diversity
- Equal Gain Diversity

- Polarisation Diversity

- Frequency Diversity

- Time Diversity

Selection diversity is used for data analysis in Section 5.3.2.2.

This is the simplest diversity technique and selects the strongest signal received from N antennas separated typically by a few wavelengths [33]. The signal received by each antenna is sampled and that with the highest instantaneous SNR is selected [23].

CHAPTER 4

Wireless Data Acquisition in Gas Turbine Engines

This chapter describes measurements and modelling undertaken during the collaborative WIDAGATE (Wireless Data Acquisition in Gas Turbine Engines) project. WIDAGATE addresses data acquisition in the context of instrumented gas turbine engines using wireless sensor network (WSN) and is being undertaken by a consortium comprising Rolls-Royce, Selex, University College London and the University of Strathclyde.

4.1 Motivation

Wireless sensing offers a potential step change in gas turbine engine testing by alleviating a number of significant disadvantages associated with the wired solution currently used. These disadvantages include lengthy, complicated and expensive wiring harnesses, complex set up processes and instrumentation, design flexibility, and inefficient data gathering. Currently the aerospace industry is assessing wireless sensor kits for test measurements.

At the time that the WIDAGATE project started no similar work on gas turbine engines had been published. Propagation around cylinders, and diffraction in particular, have been studied however. ITU-R P.526-10 Recommendation [34], for example, describes RF propagation by diffraction, including diffraction over cylindrical surfaces. In this document, and elsewhere [24] [35] [36] [37] [38] [39] [40] [41] [42], knife-edge diffraction approximation technique is used to model the propagation by diffraction around a cylindrical surface.

None of the existing studies is suitable however for a gas turbine engine, as such a model should accommodate a cylindrical surface with large random surface

irregularities.

4.2 Aims and Objectives

The aim of this study is to generate a physical layer wireless channel model derived from a set of channel measurements, in support of the WIDAGATE project to assess the potential of wireless sensor networks for the condition monitoring of gas turbine engines. The resulting model is being incorporated into a larger, multi-layer system model as part of the wider project. The physical layer channel model, incorporates interference and noise in addition to signal transmission characteristics.

The objectives can be summarised as follow:

- Measurements of channel frequency response (S_{21}) without and with engine cowling
- Generation of measurement database
- Extraction of transmission gain statistical model, scalable to engines of variable size
- Implementation of a simple noise model
- Identification of worst case interference model

4.3 Measurements

ISM-band and UWB-band frequency response measurements between pairs of points distributed on a grid over the cylindrical surface of a Gnome gas turbine engine have been made. The measurements, covering the range 2.4 - 2.5 GHz for ISM-band [43] and 3 - 11 GHz for UWB-band [44], have been made without (measurement set 1), and with (measurement set 2), an engine cowling. The corresponding measurement databases form the basis of an empirical transmission gain model.

The measurement frequency bands were selected based on the wireless devices currently available. Many WPAN (Section 2.1.2.2) or WLAN (Bluetooth [7], 802.11b/g/n [45] [46]) devices operate within 2.4 - 2.5 GHz ISM-band.

Some wireless transceivers operate in higher bands. Wireless USB, for example, uses the entire UWB-band for achieving high data rates [47]. IEEE 802.11y [48] operates within the 3.65 - 3.7 GHz band and IEEE 802.11a/n [49] operates in

4.3. MEASUREMENTS

the 5 GHz band. The bands occupied by a selection of technologies are illustrated in Figure 4.1.

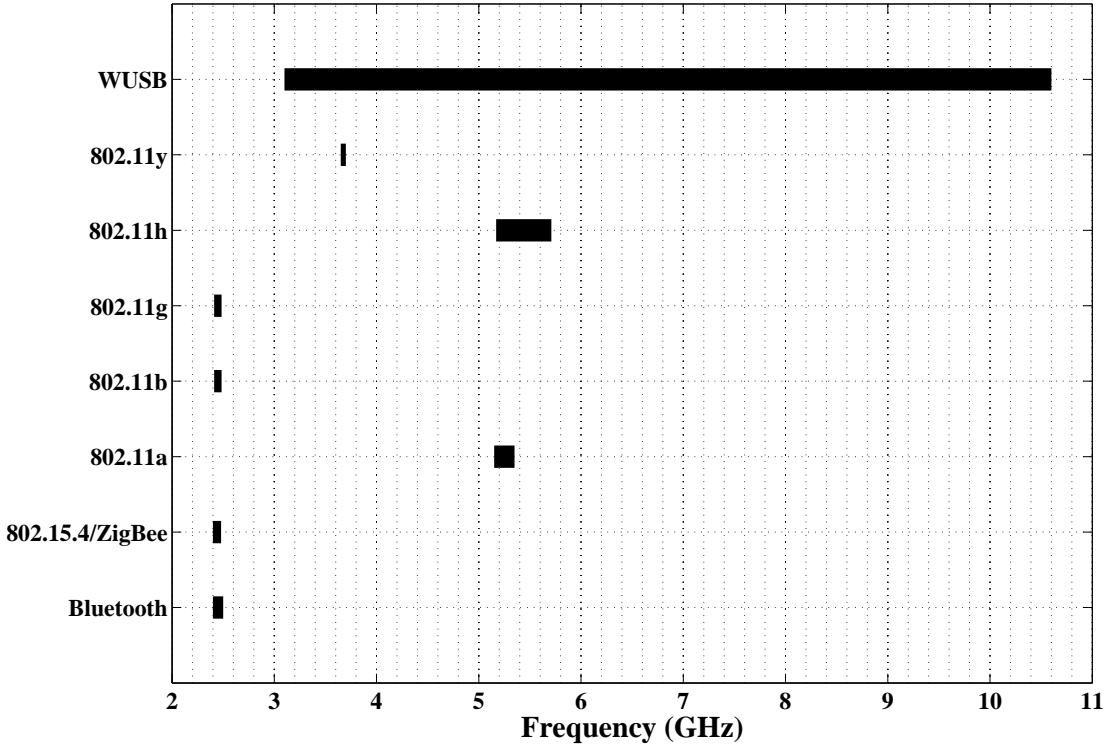


Figure 4.1: Wireless technologies operating within the spectrum of 2.4 - 11 GHz.

An estimate of the maximum data rate that can be accommodated assuming a narrowband channel model (i.e. flat fading without equalisation) is made by considering two path propagation between a pair of nodes located on the surface of a cylinder, Figure 4.2.

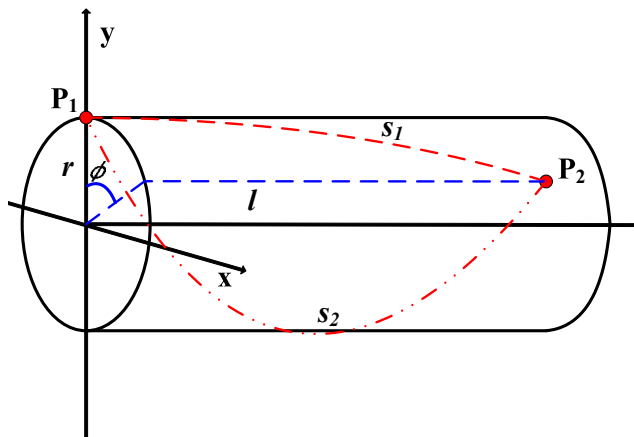


Figure 4.2: Schematic diagram of two-path geometry in a cylinder.

The maximum differential path length for the pair of nodes illustrated is:

$$\Delta s = s_2 - s_1 = \sqrt{(r(2\pi - \phi))^2 + l^2} - \sqrt{(r\phi)^2 + l^2} \quad (4.1)$$

The corresponding differential propagation delay for a propagation velocity c is:

$$\Delta T = \frac{\Delta s}{c} \quad (4.2)$$

Assuming a narrowband channel model is sufficient if inter-symbol interference is restricted to a symbol overlap 10% then the maximum symbol rate (assuming worst-case binary modulation) for which a narrowband channel model is adequate [26] is given by:

$$R_{symbol} \leq \frac{1}{10\Delta T} = \frac{c}{10 \left[\sqrt{(r(2\pi - \phi))^2 + l^2} - \sqrt{(r\phi)^2 + l^2} \right]} \quad (4.3)$$

For example with $r = 0.5$ m and $l = 1.0$ m then R_{symbol} is limited to 17.9 Mbit/s. Figure 4.3 shows the symbol rate limit of a narrowband model with respect to engine radius.

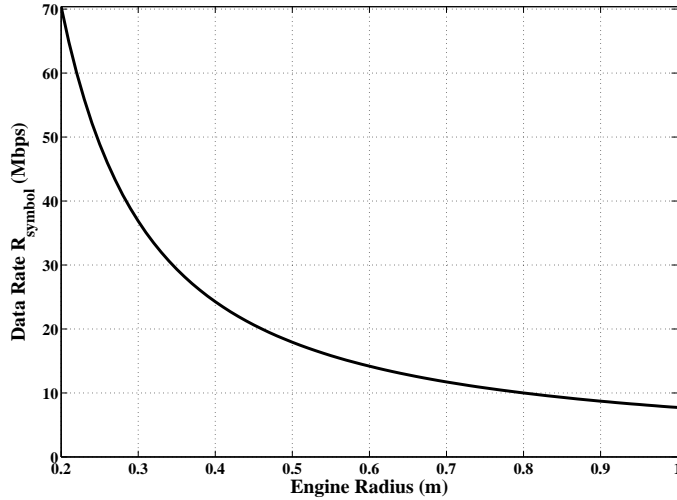


Figure 4.3: Maximum ISI "tolerable" symbol rate versus engine radius.

4.3.1 ISM-band Measurements

ISM bands occur at several frequencies, Table 4.1 [50]. The ISM-band used in WIDAGATE project is focused on the frequency range within 2.4 - 2.5 GHz.

A simple theoretical argument for the likely adequacy of a narrowband transmission model has already been given. This is now confirmed experimentally by examining the measurement data.

4.3. MEASUREMENTS

<i>Frequency Range</i>	<i>Center Frequency</i>	<i>Regions of Operation</i>
6.765 – 6.795 MHz	6.780 MHz	Subject to special authorisation
13.553 – 13.567 MHz	13.560 MHz	Subject to provisions of RR No.15.13
26.957 – 27.283 MHz	27.120 MHz	Subject to provisions of RR No.15.13
40.660 – 40.700 MHz	40.680 MHz	Subject to provisions of RR No.15.13
433.050 – 434.790 MHz	433.920 MHz	Region 1
902.000 – 928.000 MHz	915.000 MHz	Region 2
2.400 – 2.500 GHz	2.450 GHz	Subject to provisions of RR No.15.13
5.725 – 5.875 GHz	5.800 GHz	Subject to provisions of RR No.15.13
24.000 – 24.250 GHz	24.125 GHz	Subject to provisions of RR No.15.13
61.000 – 61.500 GHz	61.250 GHz	Subject to special authorisation
122.000 – 123.000 GHz	122.500 GHz	Subject to special authorisation
244.000 – 246.000 GHz	245.000 GHz	Subject to special authorisation

Table 4.1: ISM frequency band allocations (After [50]).

Figures 4.4 (a) and (b) show the channel frequency response and its autocorrelation function (ACF), respectively.

Figures 4.5 (a) and (b) summarise an analysis of the correlation bandwidth B_c , with the B_c values obtained for the ISM-band measurement sets 1 and 2.

Since half of the 50% correlation bandwidths exceed 5.5 MHz in both ISM-band measurements, we conclude that a narrowband model of the channel is adequate for most of the wireless devices currently available in the market (Table 2.2).

The ISM-band measurements were made between a pair of rectaxial antennas [51], Figure 4.6, using an Agilent N5230A network analyser. Figure 4.7 shows the return loss (S_{11}) of the antennas. Each antenna was connected to the network analyser using 10 m of high-quality, low-loss, RF cable [52].

The antennas were mounted on a PVC rod to minimise the effect of scattering from the metallic antenna positioners. The antenna positioners were shrouded with RF absorber, Figure 4.8.

The Gnome engine was mounted on a tubular steel framework, Figure 4.9, which was also shrouded with RF absorber to minimise unwanted reflections. For both measurement sets, the span of the network analyser was set to 100 MHz with a centre frequency of 2.45 GHz. The number of samples within the span (2.4 - 2.5 GHz) was 6401. The frequency sampling interval was therefore 15.62 kHz. The sweep time was 174.747 ms. The transmission power was -5 dBm. Before the measurements the system, including the cables, was calibrated.

The Gnome engine is approximately cylindrical, Figure 4.9. The length of the engine is 78 cm and its mean radius is 18 cm.

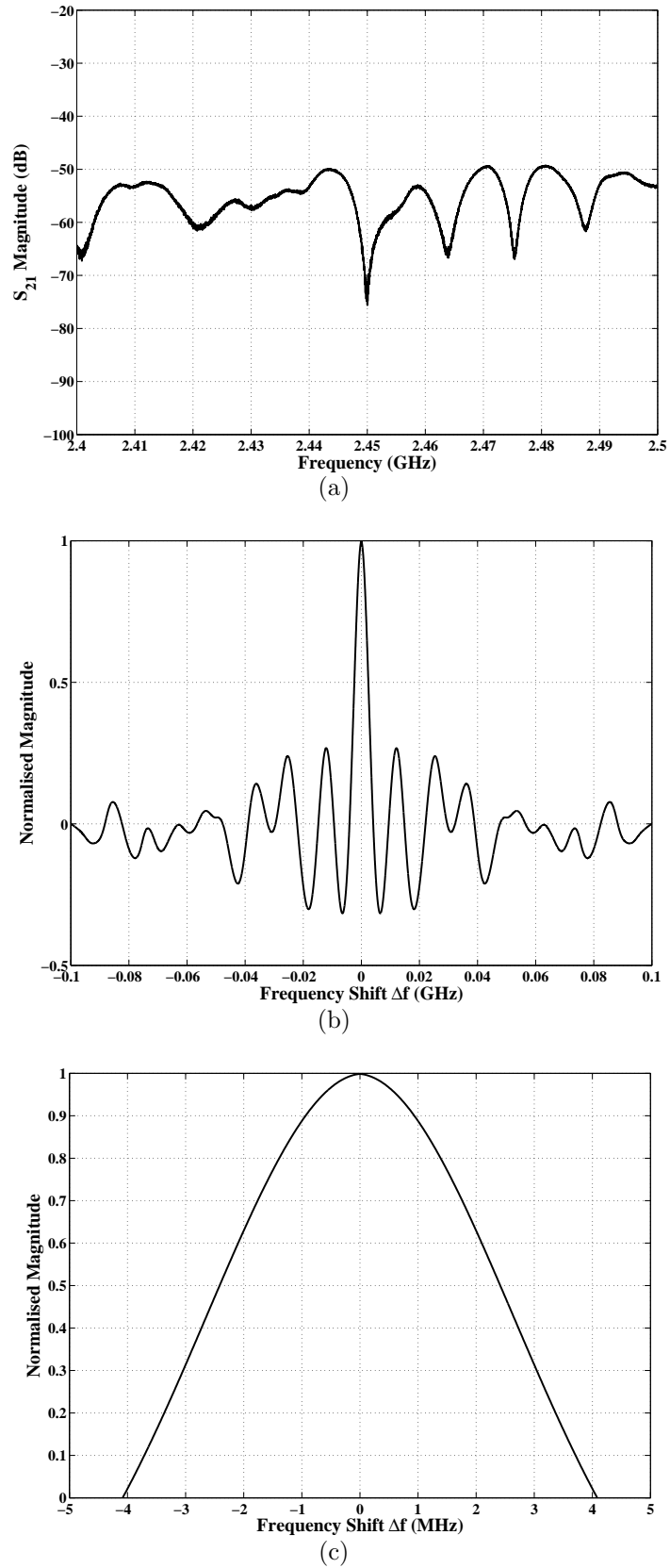


Figure 4.4: (a) Channel frequency response (S_{21}), (b) its ACF and (c) its ACF on an expanded scale.

4.3. MEASUREMENTS

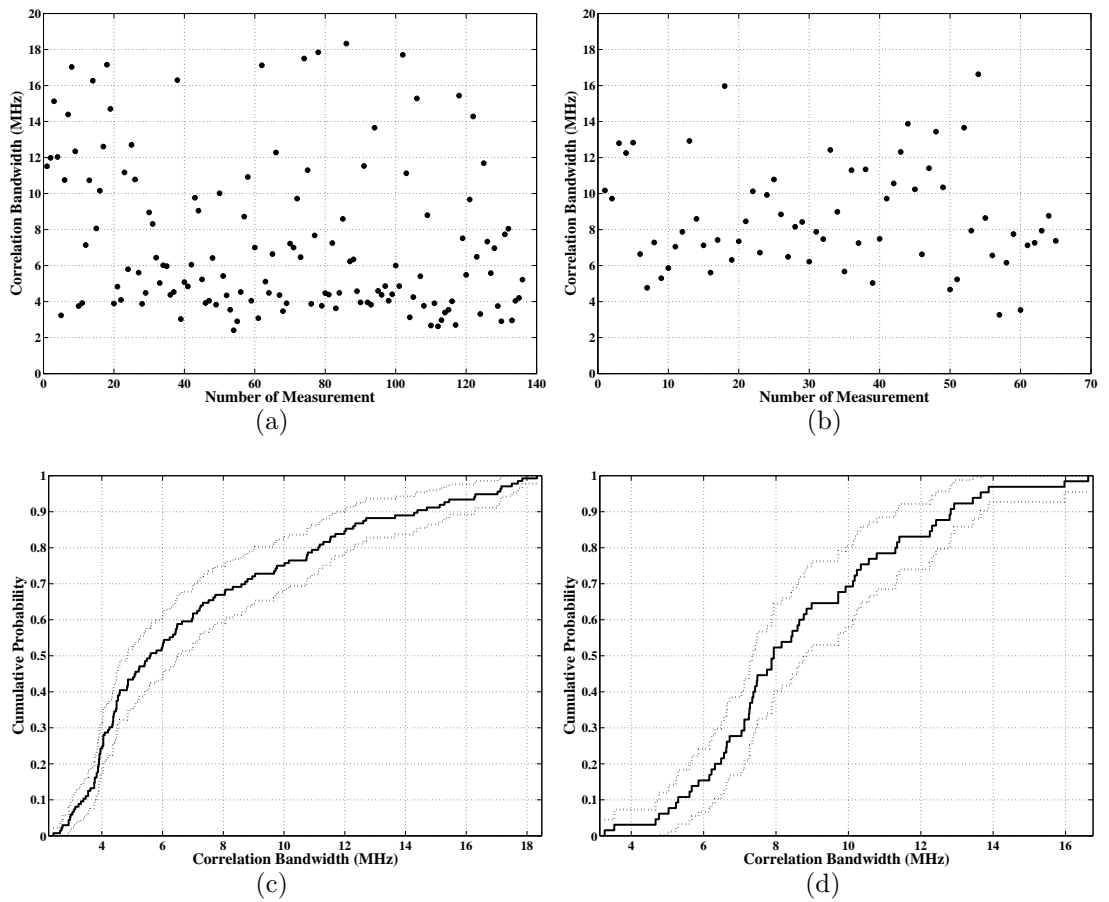


Figure 4.5: 50% correlation bandwidth for measurements (a) without and (b) with cowling and the corresponding cumulative distribution functions (c) and (d), respectively.

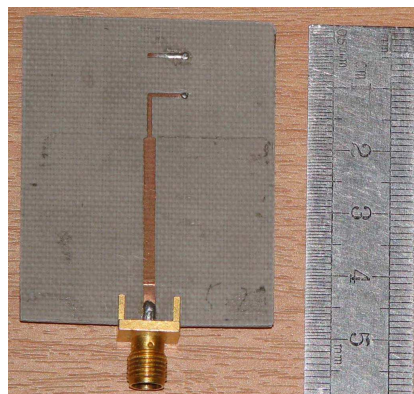


Figure 4.6: Rectaxial antenna.

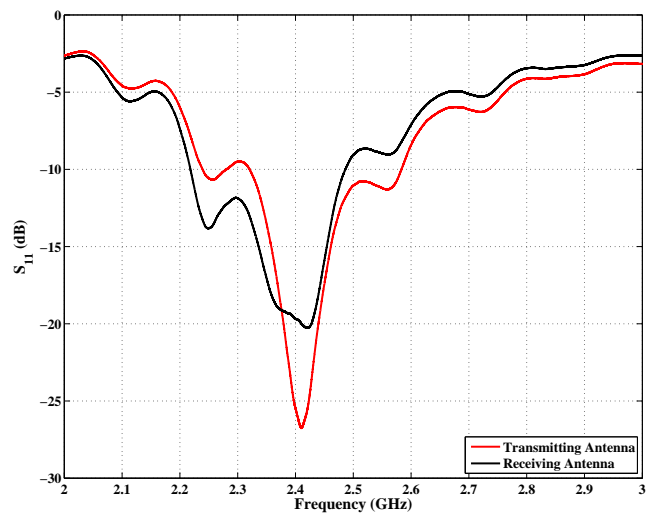


Figure 4.7: Measured return loss (S_{11}) for rectaxial antennas.



Figure 4.8: Antenna positioners.

4.3. MEASUREMENTS

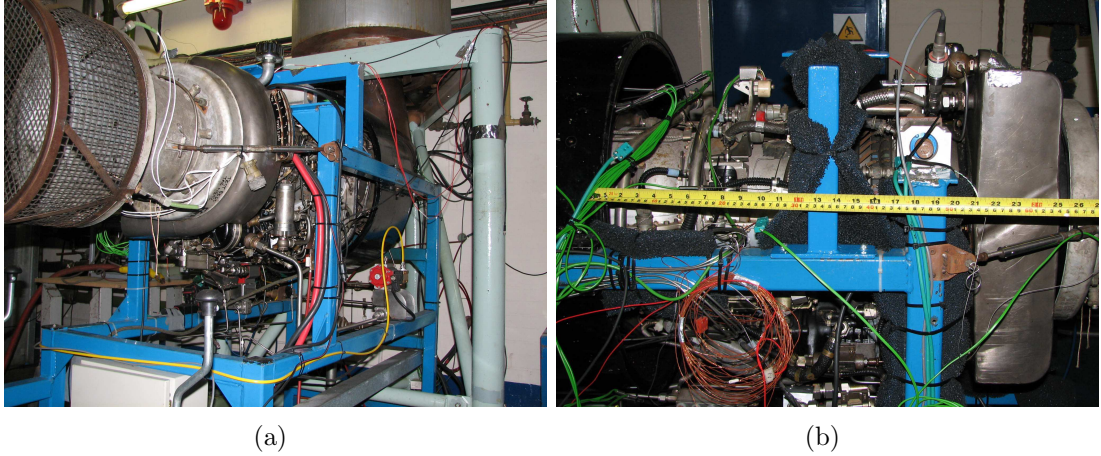


Figure 4.9: Gnome engine.

4.3.1.1 Measurements without Cowling (Set 1)

Measurement set 1 was undertaken in the Gnome Test Laboratory at Rolls-Royce in Derby, UK. The engine for these measurements had no cowling. The geometry of the measurements is illustrated schematically, in Figure 4.10. Six potential measurement points were distributed evenly around the circumference of the engine in five planes perpendicular to the engine axis along the length of the engine. The separation between adjacent planes was 28 cm, 24 cm, 6 cm and 20 cm.

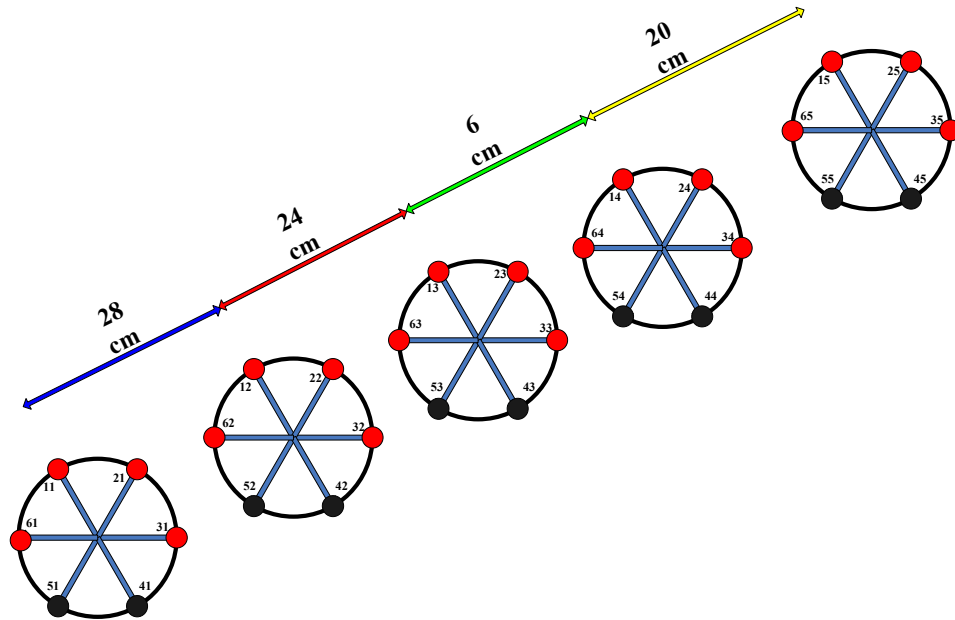


Figure 4.10: Schematic diagram of engine measurement points (set 1); black (or darker for black and white reproductions) points omitted. First and second digits indicate location on circumference and location of plane on engine axis, respectively.

4.3. MEASUREMENTS

There were, therefore, 30 potential measurement points in total. Since measurement time was limited and since measurements between all pairs of potential points includes redundant geometries two points on each plane were omitted from the measurement process. These are represented by black (darker) points in Figure 4.10. The total number of planned measurements between all pair of points was thus 190. The actual number of measurements made was 136; the balance of 54 measurements being omitted due to the limited time available in the Gnome engine laboratory. The residual redundancy in measurement geometries, however, means that all geometries are satisfactorily represented in the measurement database.

4.3.1.2 Measurements with Cowling (Set 2)

Measurement set 2 was undertaken in the Wireless Communications Laboratory at the University of Strathclyde. The Gnome engine used was identical in type but a different instance to that used for measurement set 1. The surface detail of the two engines was similar but not identical. Since the surface detail represents an essentially random distribution of scatterers the use of two engines is not thought to materially reduce the usefulness of the resulting statistical model. The engine for these measurements were made in the presence of an engine cowling manufactured by SCITEK Consultants Ltd. from stainless steel mesh, Figure 4.11.



Figure 4.11: Gnome engine with cowling.

Six potential measurement points were distributed evenly around the circumference of the engine in three planes perpendicular to the engine axis along the length of the engine. The separation between adjacent planes was 25 cm and 26 cm. This is illustrated schematically in Figure 4.12. Two points in each plane

4.3. MEASUREMENTS

(black in Figure 4.12) was again omitted. The total number of planned measurements was therefore 66. The number of measurements actually made was 65.

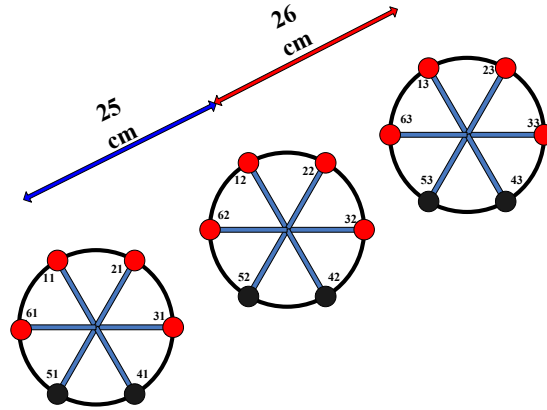


Figure 4.12: Schematic diagram of engine measurement points (set 2); black (or darker points for black and white reproduction) omitted. First and second digits indicate location on circumference and location of plane on engine axis, respectively.

4.3.2 UWB-band Measurements

The UWB-band in the USA is 3.1 - 10.6 GHz. In Europe the high spectral density regions of the spectral template is 6 - 8.5 GHz. The corresponding spectral masks are shown in Figure 4.13 [53].

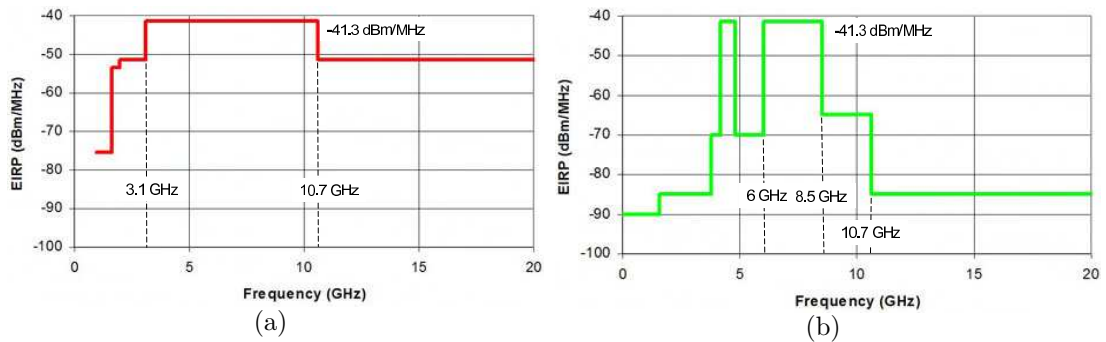


Figure 4.13: Spectral mask for UWB in (a) USA and (b) Europe (After [53]).

Section 4.3 gives a simple theoretical argument for the adequacy of a narrow-band transmission model. This is now confirmed experimentally by examining the measurement data.

Figures 4.14 (a) and (b) show the channel frequency response and its auto-correlation function (ACF), respectively.

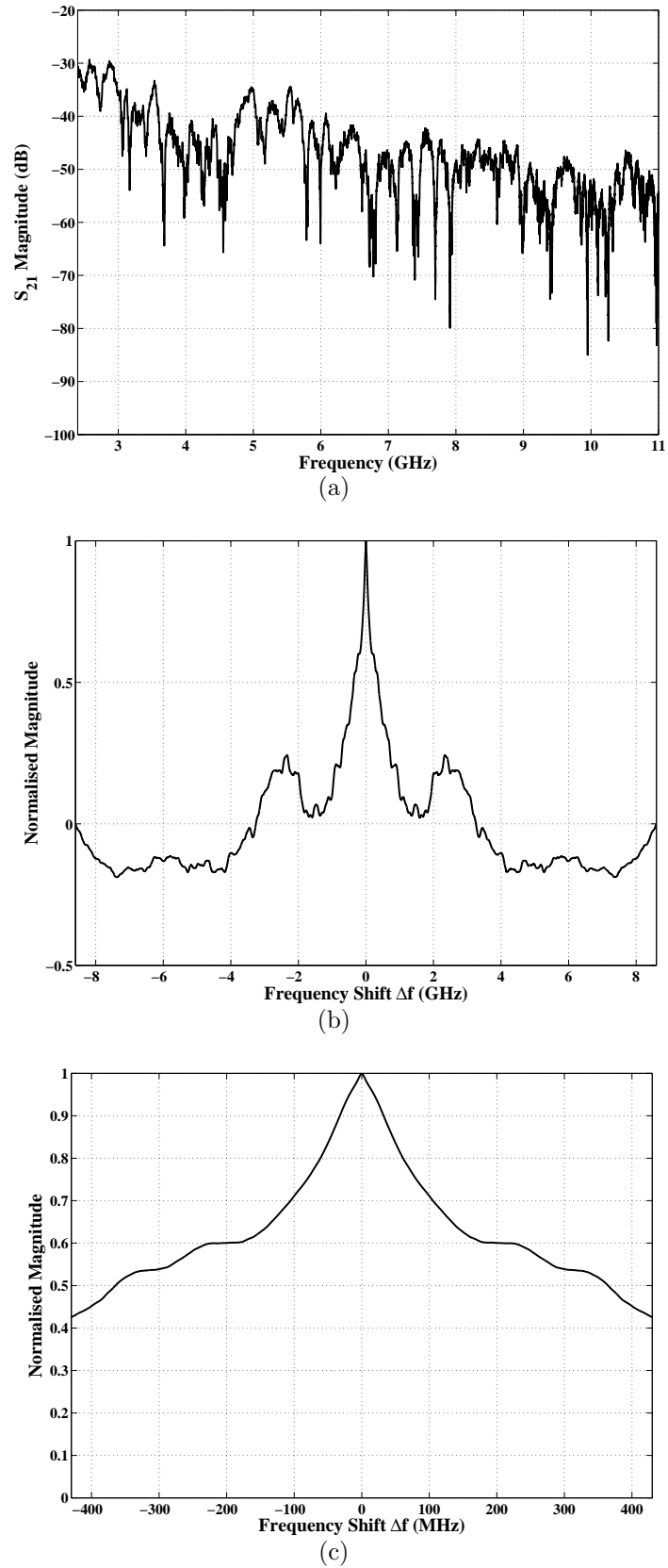


Figure 4.14: (a) Channel frequency response (S_{21}), (b) its ACF and (c) its ACF on an expanded scale.

4.3. MEASUREMENTS

Figures 4.15 (a) and (b) represent the correlation bandwidth, B_c , obtained from the UWB-band measurement sets 1 and 2, the same procedure as described in Section 4.3.1 being repeated over a much wider frequency band using a pair of UWB antennas [44].

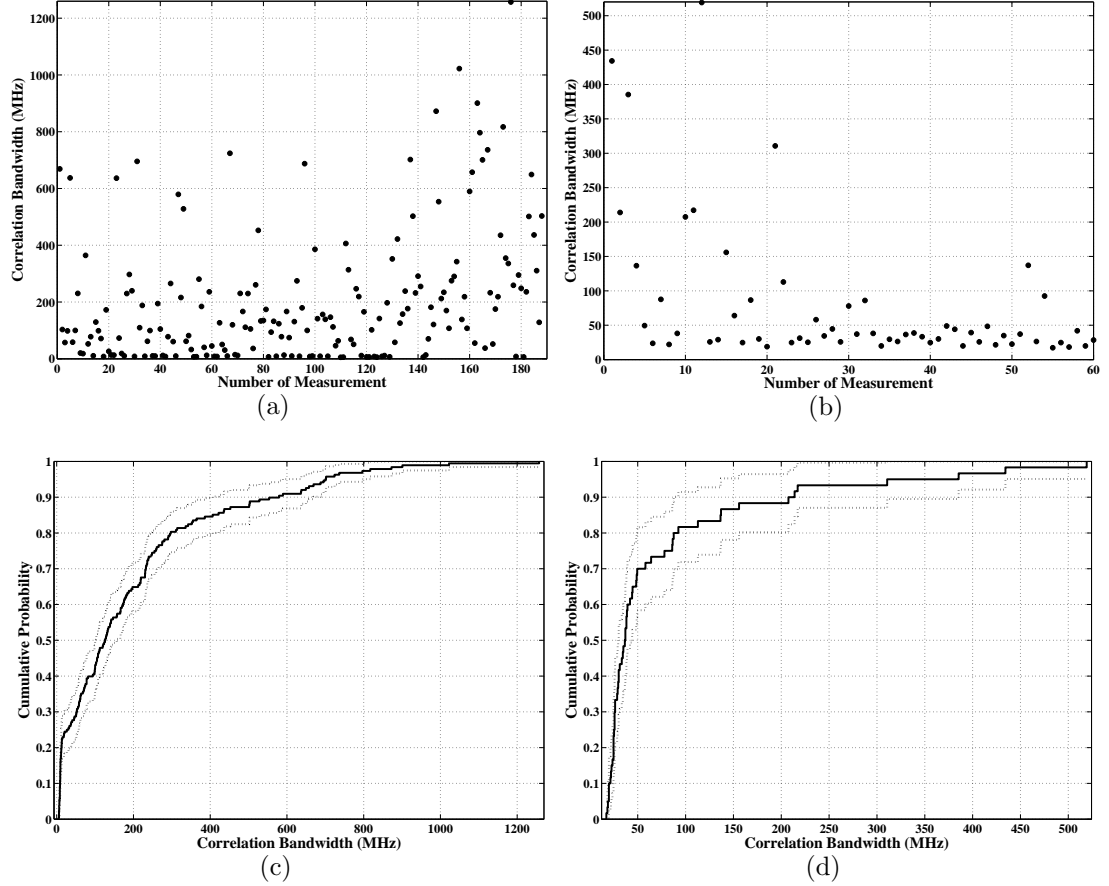


Figure 4.15: 50% correlation bandwidths for measurements (a) without and (b) with cowling and the corresponding cumulative distribution functions (c) and (d), respectively.

The UWB-band measurements were made between a pair of UWB, omnidirectional, antennas using an Agilent N5230A network analyser. Figure 4.16 shows one of the antennas.

Figure 4.17 shows the measured return loss (S_{11}) of the antennas used.

Similarly to the ISM-band measurements, transmission loss has been measured between pairs of points forming a grid over the cylindrical surface of the Gnome gas turbine engine, Figure 4.9.

The steel cradle in which the engine was mounted was shrouded, as far as possible, using flexible microwave absorber to reduce unwanted electromagnetic scattering. The measurements were made using an Agilent N5230A network

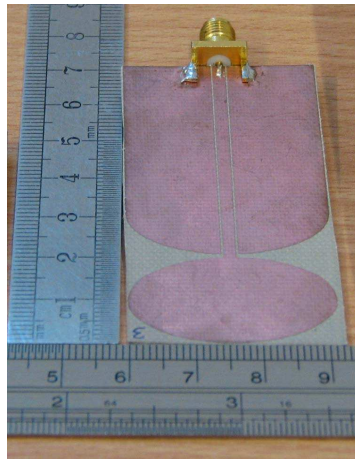


Figure 4.16: UWB antenna.

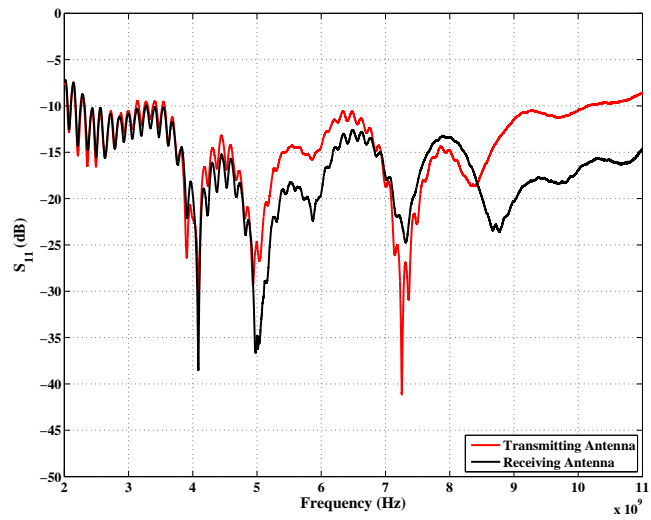


Figure 4.17: Antenna return loss (S_{11}).

analyser to obtain the frequency response over the range 2.4 - 11.0 GHz using the UWB antennas, Figure 4.16.

The measurements have been made both in the absence, Figure 4.9, and presence, Figure 4.11, of the engine cowling. These measurements are referred to here as set 1 and 2 respectively.

The measurement databases have been used to derive an empirical narrow-band transmission gain model for frequencies within the UWB band (3.1 - 10.6 GHz).

Each antenna was connected to the network analyser using 10 m of low-loss, high-quality coaxial cable [52].

The antennas were end-mounted on dielectric rods to keep the metallic structure of the antenna positioners as far as possible from the measurement volume. Like the engine cradle, the antenna positioners were shrouded in microwave absorber to further reduce the effect of unwanted scattering on the measurements.

The resolution of the measured discrete frequency response was 537.5 kHz, within 2.4 GHz to 11 GHz. The corresponding sweep time for those measurements is 436.827 msec. The transmission power was -5 dBm. The measurement system including cables was calibrated prior to the measurements.

4.3.2.1 Measurements without Cowling (Set 1)

The measurements of transmission loss for the engine without cowling (measurement set 1) were made in the Gnome Test Laboratory at Rolls-Royce in Derby, UK. Figure 4.10 shows the nominal topology of the measurement points (representing hypothetical nodes). Nominal node locations are assumed at 0° , 60° , 120° , and 180° on the engine circumference in each of five planes resulting in 20 node locations and 190 potential measurements. (Points at 240° and 300° are not represented since these give rise to redundant link geometries.) The planes, which were perpendicular to the axis of the engine, are separated by 28 cm, 24 cm, 6 cm and 20 cm. Two of the 190 measurements were lost due to an error when saving the relevant files.

4.3.2.2 Measurements with Cowling (Set 2)

The measurements of transmission loss for the engine with cowling (measurement set 2) were made in the University of Strathclyde Wireless Communications Laboratory.

The engine used was of the same (Gnome) type as that used for measurement set 1 but was not the same engine. The surface detail of the engine was therefore

different. Figure 4.12 shows the nominal topology of the measurement points. Similarly to the measurements in set 1, nominal node locations are assumed at 0° , 60° , 120° , and 180° on the engine circumference in each of three planes resulting in 12 node locations and 66 potential measurements. The planes, which were perpendicular to the axis of the engine, are separated by 25 cm and 26 cm.

Six of the 66 measurements were lost due to measurement error or corruption of data during saving.

4.4 Modelling

An empirical transmission gain (i.e. ratio of received to transmitted power) model has been derived from the measurement database. In order to make the model generic, such that it can be applied to engines of arbitrary size, the model is parameterised in terms of path length, s , and path curvature, κ . Figure 4.18 shows a schematic diagram of the path geometry, which defines these parameters.

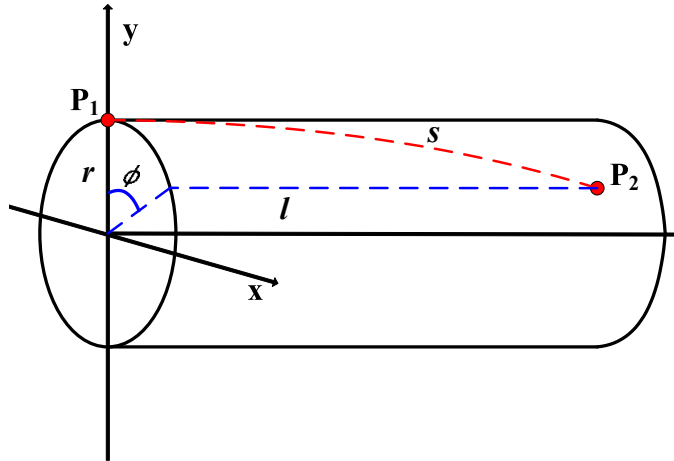


Figure 4.18: Schematic diagram of path geometry.

The path length of each measurement is that of a helical segment connecting transmitter (P_1) and receiver (P_2). The arc length s is given by:

$$s = \sqrt{(r\phi)^2 + l^2} \quad (4.4)$$

where r is engine radius, ϕ is angular separation between P_1 and P_2 projected onto a plane perpendicular to the engine axis and l is the separation of the planes perpendicular to the engine axis containing P_1 and P_2 .

The path curvature, reciprocal of radius of curvature, is given by:

$$\kappa = \frac{r}{r^2 + \left(\frac{l}{\phi}\right)^2} \quad (4.5)$$

It is a fundamental assumption of the generic model that s and κ are sufficient to predict transmission loss and that the effect of path torsion on loss is small. It is also assumed that narrowband modelling of transmission loss is adequate for practical engineering purposes. The rationale for this assumption is outlined in Section 4.3. Examination of the measured data (see Section 4.3.2) confirms the validity of this assumption.

4.5 Results

Analysis of the measurement database has been undertaken and the best-fit first-degree polynomial, $As + B\kappa + C\overline{G}_T + D = 0$, where \overline{G}_T is mean transmission gain in dB (< 0), has been derived. The resulting best-fit surface for measurement sets 1 and 2 are shown in Figures 4.19 and 4.20 respectively. Each point is the mean of the 6401 spot frequencies within the span. (The mean has been calculated using linear ratios, not dBs.)

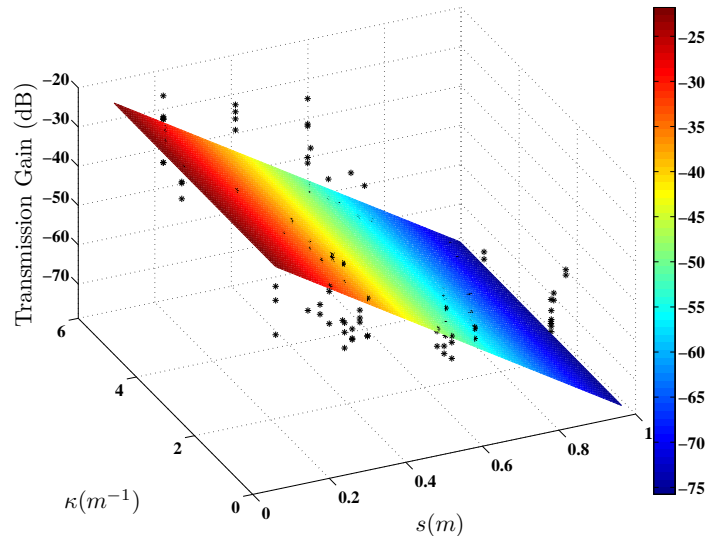


Figure 4.19: Measurement data without cowling (set 1) and best-fit first-degree polynomial surface.

Figures 4.21 and 4.22 show the projection of Figures 4.19 and 4.20, respectively, chosen to illustrate the influence of path length. In both cases, the transmission gain \overline{G}_T decreases when the path length s increases.

Table 4.2 contains the best-fit polynomial coefficients derived for each measurement set, emphasising the high dependence of the mean transmission gain

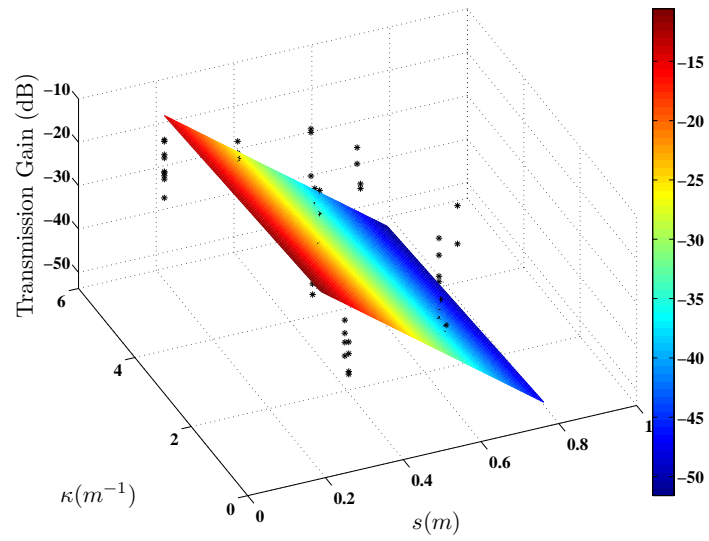


Figure 4.20: Measurement data with cowling (set 2) and best-fit first-degree surface.

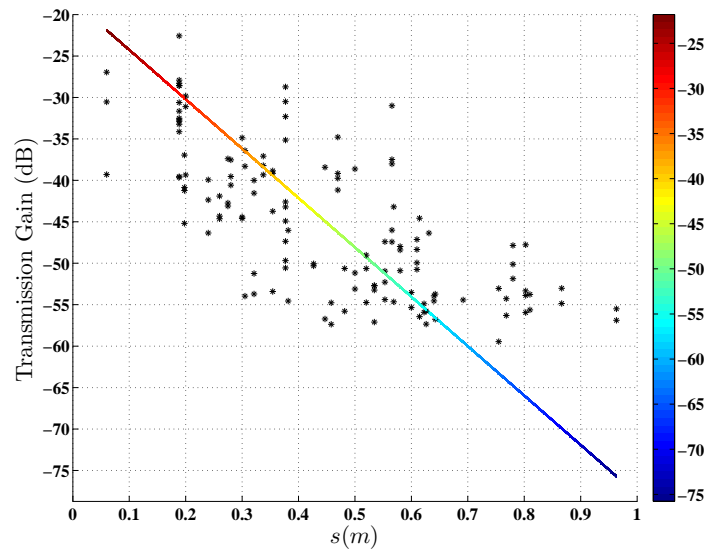


Figure 4.21: Two dimensional projection of data without cowling (set 1) illustrating transmission gain versus path length.

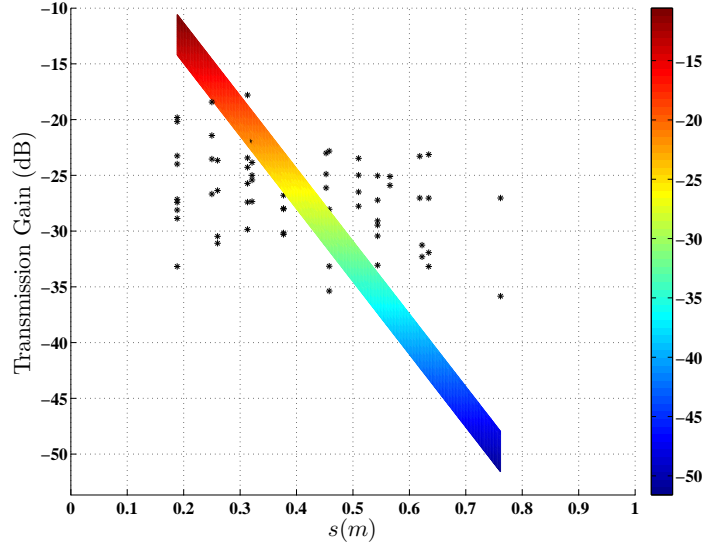


Figure 4.22: Two dimensional projection of data with cowling (set 2) illustrating transmission gain versus path length.

\overline{G}_T on path length s .

	Polynomial Coefficients			
	A	B	C	D
Meas. Set 1	-0.99986	0.00043	-0.01678	-0.30833
Meas. Set 2	-0.99983	-0.010042	-0.01532	0.02659

Table 4.2: Transmission model polynomial coefficients.

The gradients for the ISM-band measurements are summarised in Table 4.3. ISM-band measurements without cowling (set 1) appear to have lower gradient, with respect to s , than the one with cowling (set 2). However, both gradients are very close. Relative insensitivity of the mean transmission gain to the path curvature, κ , is apparent in both sets. The offset of the measurements with a cowling is higher (1.74), than those without a cowling (-18.37), which is shown by the \overline{G}_T levels in Figures 4.19 and 4.20.

\overline{G}_T	Gradient		
	s	κ	<i>Offset</i>
Meas. Set 1	-59.58	0.03	-18.37
Meas. Set 2	-65.26	-0.66	1.74

Table 4.3: Gradients (dB/m) of mean transmission gain \overline{G}_T with respect to s and κ for ISM-band measurements.

The error between the measured data and the first-degree model, Equation

4.5. RESULTS

4.6, has been modelled in the same way as the original data, Figure 4.23.

$$\epsilon_{dB} = G_{T_{measured}} - G_{T_{model}} \quad (4.6)$$

Figure 4.24 shows a projection of Figure 4.23 chosen to illustrate the influence of path length.

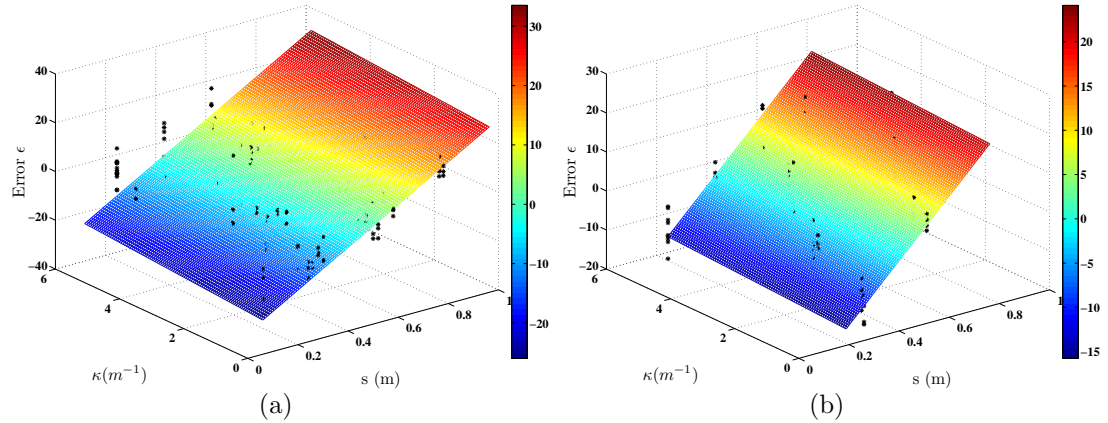


Figure 4.23: Difference (ϵ) between measurement points and best-fit surface: measurements (a) without and (b) with cowling.

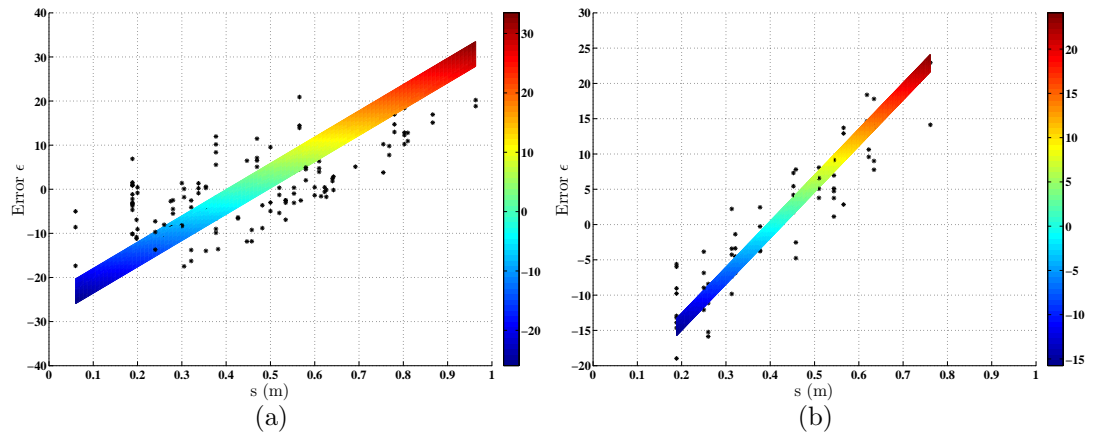


Figure 4.24: Projection of data in Figures 4.23 (a) and (b) illustrating dependence of ϵ on path length.

The 2-dimensional space spanned by s and κ is quantised in a 4 (s) by 3 (κ) grid and the histogram of ϵ within each 2-dimensional quantisation interval is constructed. The mean and standard deviation of the histogram data have been calculated.

Figures 4.25 (a) and (b) show example histograms for measurements set 1 and 2, respectively, and the normal distribution corresponding to the data's mean, μ ,

4.5. RESULTS

and standard deviation, σ . It is not convincing that the difference (ϵ) follows a normal distribution within each quantisation interval, however the available samples are closer to the normal distribution line in the probability plot (Figures 4.26 (a) and (b)) than any other commonly occurring distribution.

Table 4.4 contains the means and standard deviations for all the quantisation intervals for both measurements set 1 and 2.

		Intervals											
		1	2	3	4	5	6	7	8	9	10	11	12
Meas. Set 1	μ	-7.9	-5.5	0.9	15.4	-5.8	-2.9	-0.9	9.2	-4.1	-2.1	5.5	8.0
	σ	5.7	5.5	4.4	3.1	7.7	8.4	1.1	3.1	5.7	8.0	6.9	4.4
Meas. Set 2	μ	-23.3	-7.9	7.3	22.6	-9.9	-0.5	9.3	18.5	-11.6	-1.4	11.8	25.0
	σ	4.8	4.6	4.3	4.1	5.4	5.7	5.3	6.2	4.3	2.3	4.9	7.4

Table 4.4: μ and σ values for each quantisation interval.

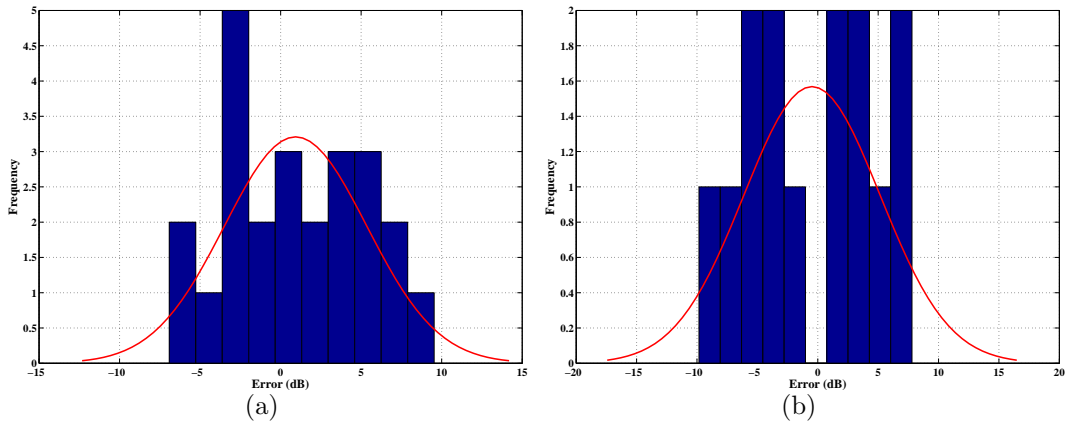


Figure 4.25: Histogram of error within a single s - κ quantization interval and corresponding normal distribution for measurements (a) without and (b) with cawling.

Figures 4.26 (a) and (b) show normal distribution probability plots corresponding to Figures 4.25 (a) and (b). The data appear to follow the normal distribution. All the points are within the 10% probability error (distance of the point from the distribution line). This is the case for most of the quantisation intervals.

Figures 4.27 (a) and (b) show the histograms of the error data (dB) for all 12 quantisation intervals for measurement set 1 and 2, respectively.

Figures 4.28 (a) and (b) show the probability plots for all 12 quantisation intervals for normal distribution corresponding to Figures 4.27 (a) and (b) for measurement set 1 and 2, respectively. The error data for all 12 quantisation intervals are close to the normal distribution (as might be expected from the central limit theorem).

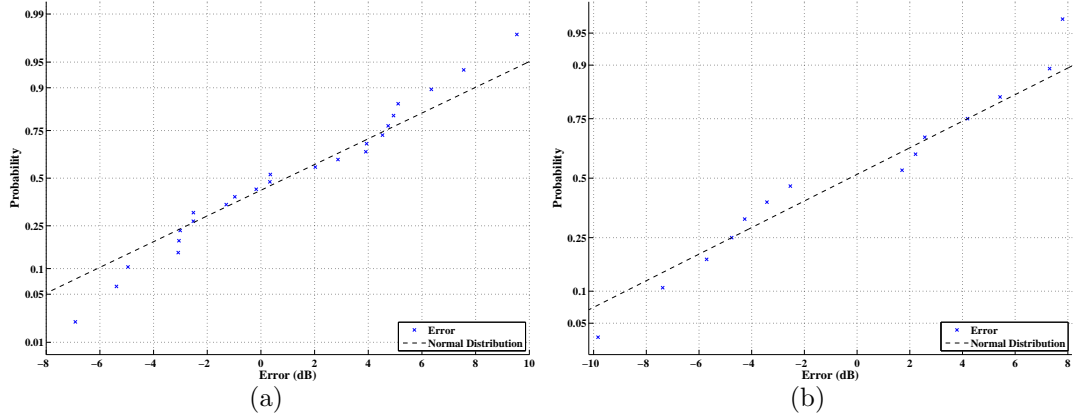


Figure 4.26: Normal probability plots corresponding to the histograms in Figure 4.25 (a) and (b).

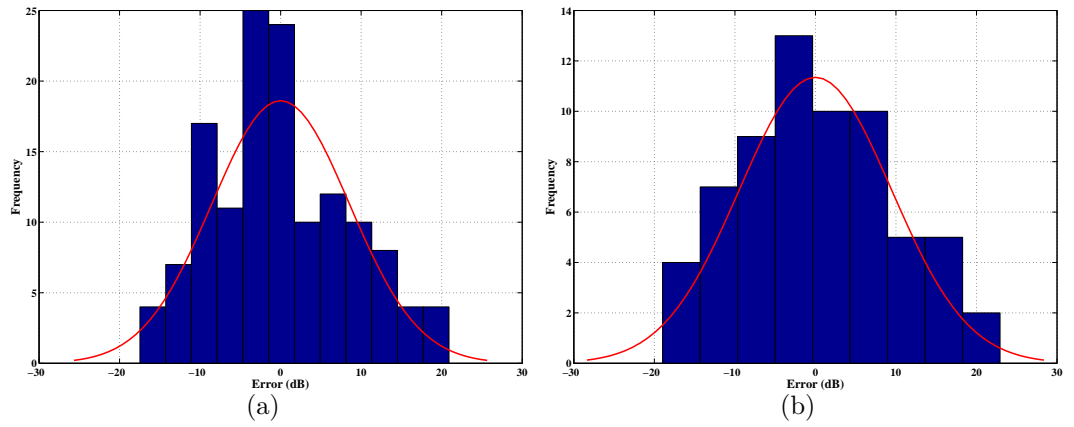


Figure 4.27: Histogram of error for all s - κ quantization intervals and corresponding normal distribution for measurements (a) without and (b) with cowling.

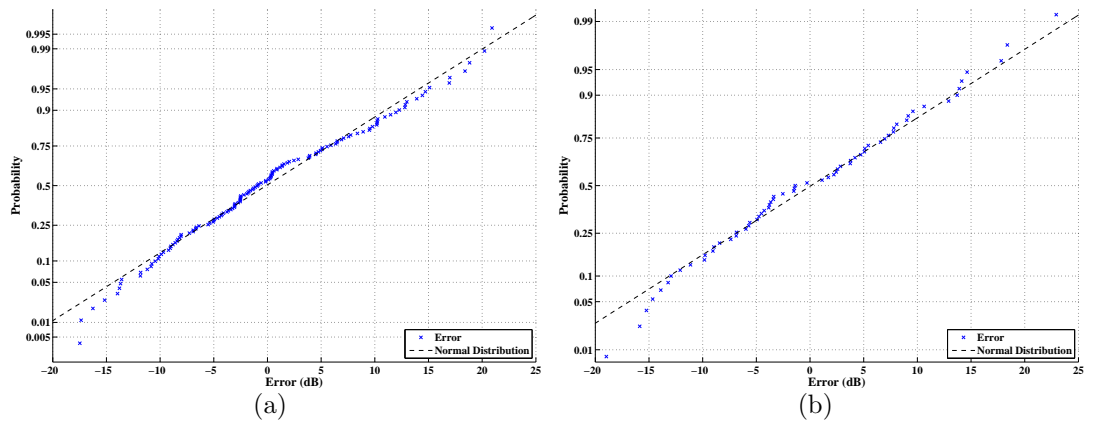


Figure 4.28: Normal probability plots corresponding to the histograms in Figure 4.27 (a) and (b).

4.5. RESULTS

The dependence of μ and σ is again modelled on s and κ using a first-degree polynomial surface, Figures 4.29 and 4.30.

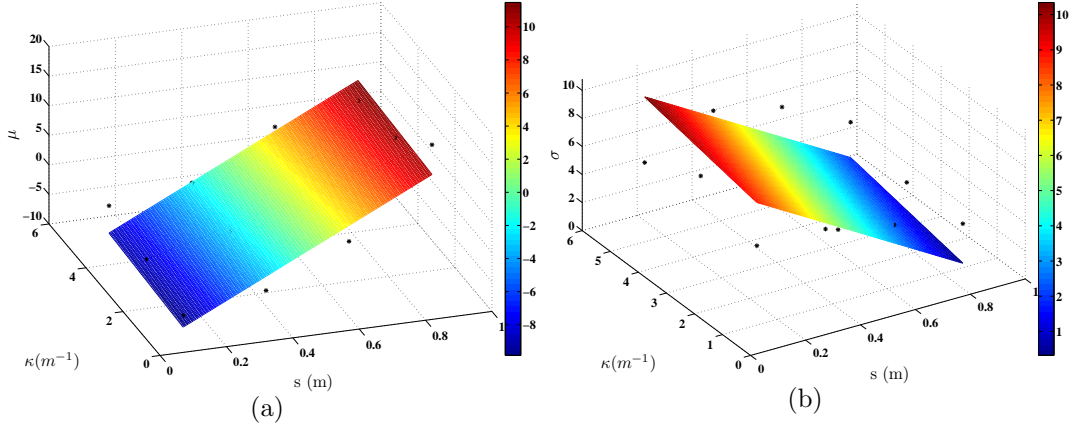


Figure 4.29: μ versus s , κ and σ versus s , κ for measurements without cowling (set 1).

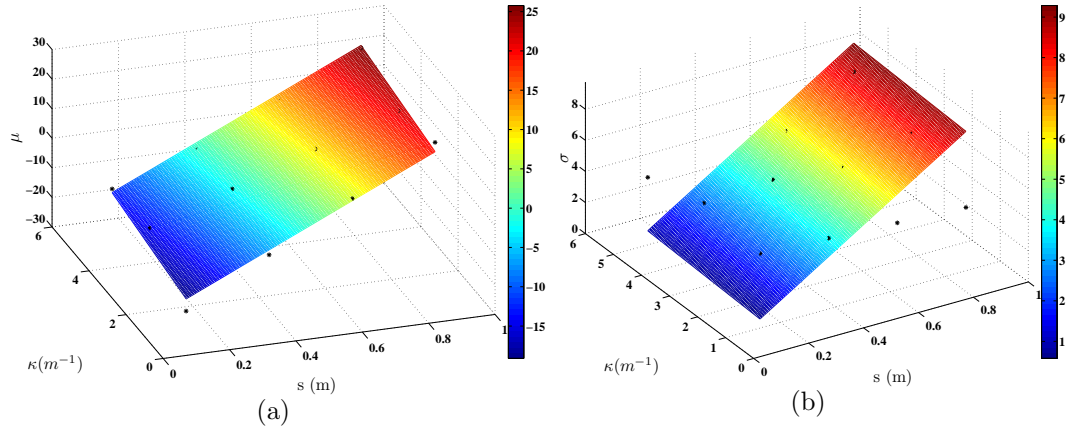


Figure 4.30: μ versus s , κ and σ versus s , κ for measurements with cowling (set 2).

The random surface detail of the gas turbine engine means that path loss must be modelled statistically. The transmission gain model proposed therefore comprises a deterministic component, $\overline{G}_T(s, \kappa)$, and a random component $e(s, \kappa)$ where e is a Gaussian random variable with mean and standard deviation that depend on s and κ , i.e.:

$$G_T(s, \kappa) = \overline{G}_T(s, \kappa) + e[\mu(s, \kappa), \sigma(s, \kappa)] \quad (4.7)$$

A block diagram of the transmission gain model is shown in Figure 4.31 in which $g_i(t)$ is the transmitted signal.

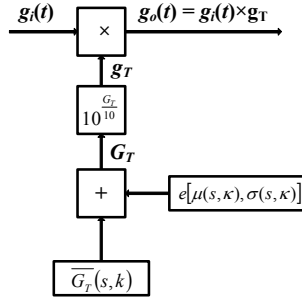


Figure 4.31: Transmission gain model.

Since half of the 50% correlation bandwidths exceed 25 MHz in both UWB-band measurements, a narrowband model of the channel is adequate.

Similar to the ISM-band measurements, a first-degree polynomial, $As + B\kappa + C\bar{G}_T + D = 0$, where \bar{G}_T (< 0) is mean transmission gain in dB, which best fits the empirical data in each 1 GHz frequency band has been obtained. Examples are shown in Figures 4.32 and 4.33, respectively, for measurements without, and with, a cowling for the 6 - 7 GHz band. The results for each 1 GHz interval between 3 and 11 GHz are shown in Appendices B and C.

Each measurement point is the mean within each 1 GHz interval. (The mean has been calculated using linear ratios, not decibels.)

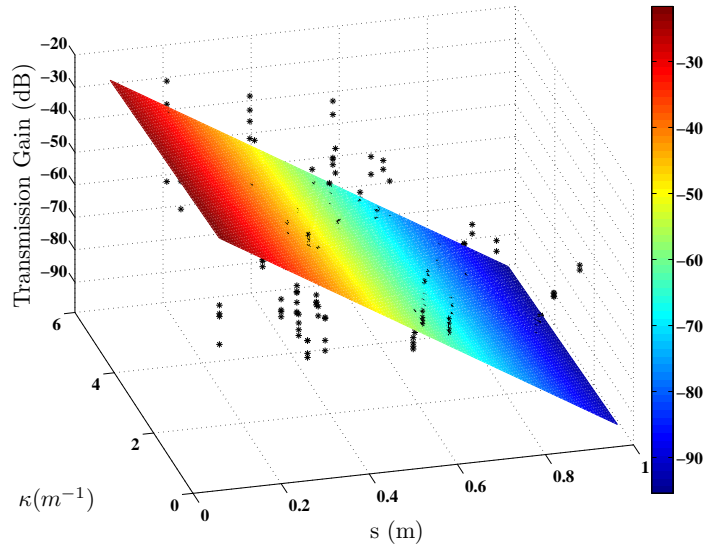


Figure 4.32: Example of best-fit transmission gain model for measurements without cowling (6 GHz - 7 GHz).

Figures 4.34 and 4.35 show the projection of Figures 4.32 and 4.33, respectively, chosen to illustrate the influence of path length. In both cases, the transmission gain \bar{G}_T decreases when the path length s increases.

Table 4.5 shows the best-fit polynomial coefficients derived for each measure-

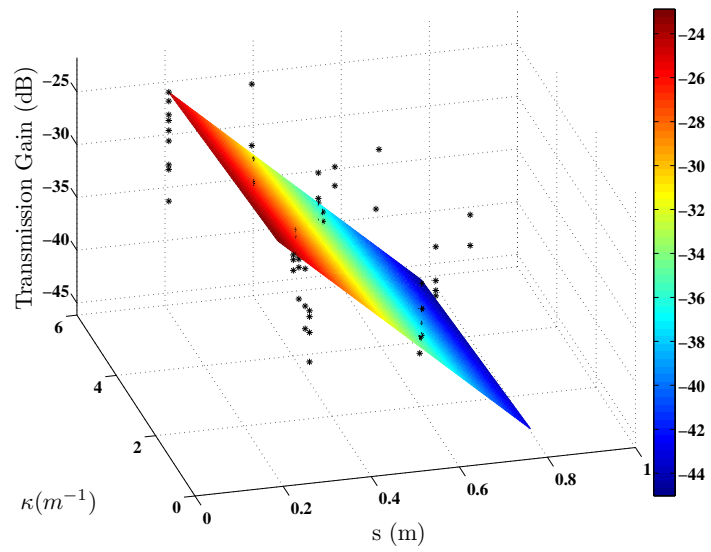


Figure 4.33: Example of best-fit transmission gain model for measurements with cowling (6 GHz - 7 GHz).

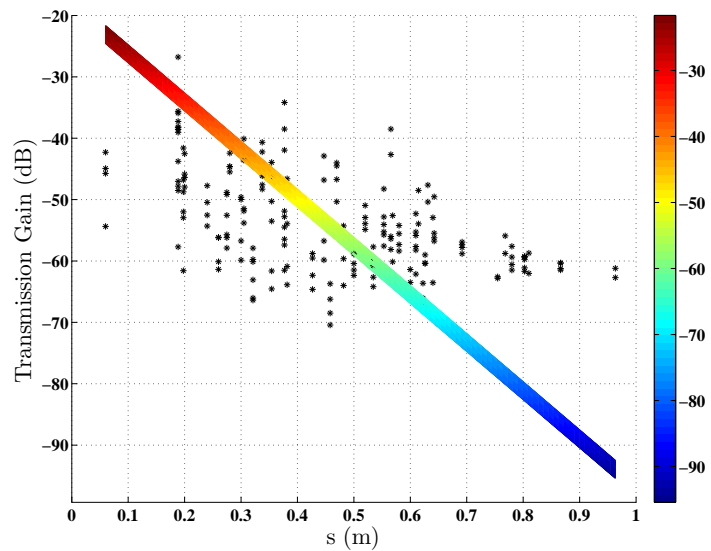


Figure 4.34: Two dimensional projection of data (without cowling) illustrating transmission gain versus path length (6 GHz - 7 GHz).

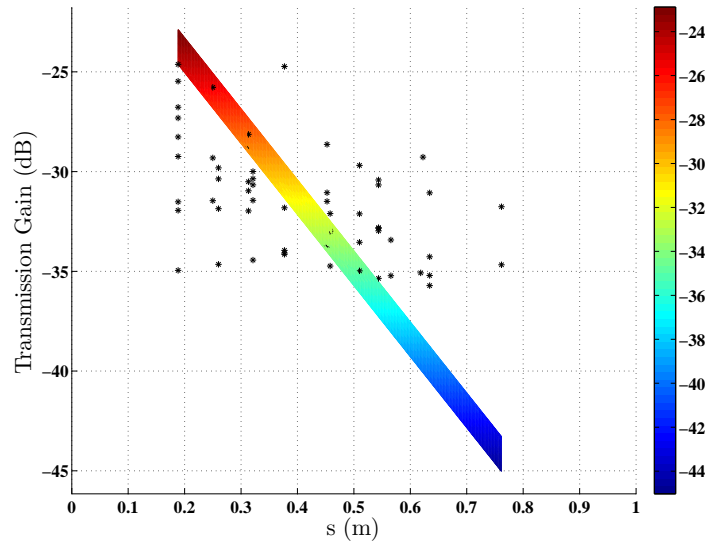


Figure 4.35: Two dimensional projection of data (with cowling) illustrating transmission gain versus path length (6 GHz - 7 GHz).

ment set in each frequency band. The predominant dependence of \overline{G}_T on path length s is clear.

The gradients and offset for the UWB sub-band measurements are summarised in Table 4.6. In general, the measurement without cowling (set 1) have larger gradients, with respect to s , than those with cowling (set 2). Relative insensitivity of the transmission gain to path curvature, κ , is also apparent. The offset of the measurements with cowling is higher, than the one without cowling.

The error between the measured data and the model, Equation 4.6, has been calculated and itself modelled using the same process as described above, Figure 4.36 and 4.37.

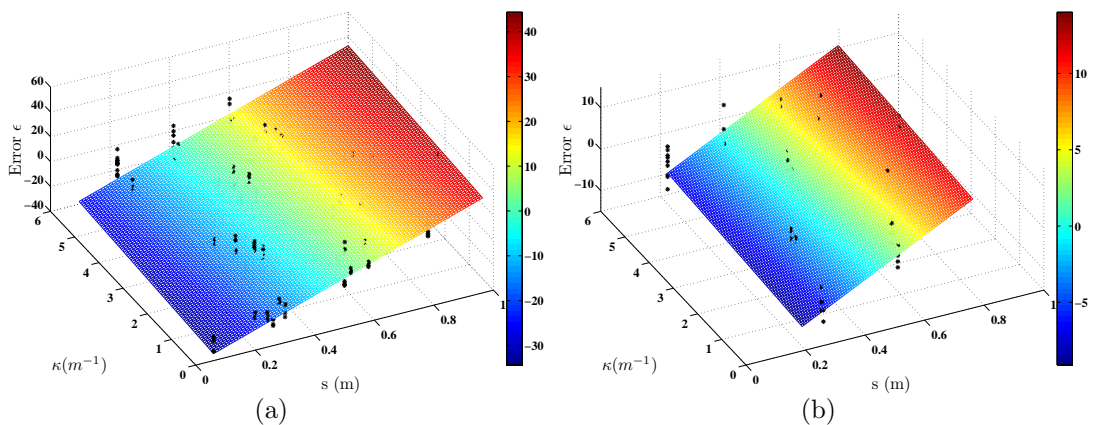


Figure 4.36: Difference (ϵ) between measured data and model: measurements (a) without and (b) with cowling (6 GHz - 7 GHz).

		<i>Polynomial Coefficients</i>			
	f	A	B	C	D
Meas. Set 1	3.0–4.0	-0.9997	-0.0203	-0.0139	-0.1972
(without cowling)	4.0–5.0	-0.9998	-0.0125	-0.0134	-0.1925
	5.0–6.0	0.9999	0.0049	0.0131	0.2044
	6.0–7.0	0.9999	0.0066	0.0127	0.2161
	7.0–8.0	-0.9998	-0.0080	-0.0139	-0.2953
	8.0–9.0	0.9998	0.0073	0.0157	0.4091
	9.0–10.0	0.9998	0.0039	0.0160	0.4500
	10.0–11.0	0.9998	0.0037	0.0163	0.4846
Meas. Set 2	3.0–4.0	-0.9994	-0.0084	-0.0327	-0.4314
(with cowling)	4.0–5.0	-0.9997	-0.0029	-0.0202	-0.1315
	5.0–6.0	-0.9996	0.0018	-0.0258	-0.3390
	6.0–7.0	0.9995	0.0088	0.0280	0.4536
	7.0–8.0	-0.9997	-0.011	-0.0201	-0.2219
	8.0–9.0	-0.9997	-0.0116	-0.0189	-0.1825
	9.0–10.0	-0.9997	-0.0116	-0.0182	-0.1842
	10.0–11.0	-0.9998	-0.0083	-0.0150	-0.0947

Table 4.5: Transmission gain model coefficients.

	Gradient			
\overline{G}_T	f	s	κ	<i>Offset</i>
Meas. Set 1	3-4	-71.53	-1.45	-14.11
(without cowling)	4-5	-74.34	-0.93	-14.32
	5-6	-75.86	-0.38	-15.51
	6-7	-78.41	-0.52	-16.95
	7-8	-71.86	-0.58	-21.23
	8-9	-63.53	-0.46	-26.00
	9-10	-62.20	-0.25	-27.99
	10-11	-60.99	-0.23	-29.56
Meas. Set 2	3-4	-30.47	-0.26	-13.16
(with cowling)	4-5	-49.46	-0.15	- 6.51
	5-6	-38.65	0.07	-13.11
	6-7	-35.62	-0.31	-16.16
	7-8	-49.59	-0.55	-11.01
	8-9	-52.69	-0.61	- 9.62
	9-10	-54.65	-0.64	-10.07
	10-11	-66.22	-0.55	- 6.27

Table 4.6: Gradients of mean transmission gain \overline{G}_T with respect to s and κ for UWB-band measurements.

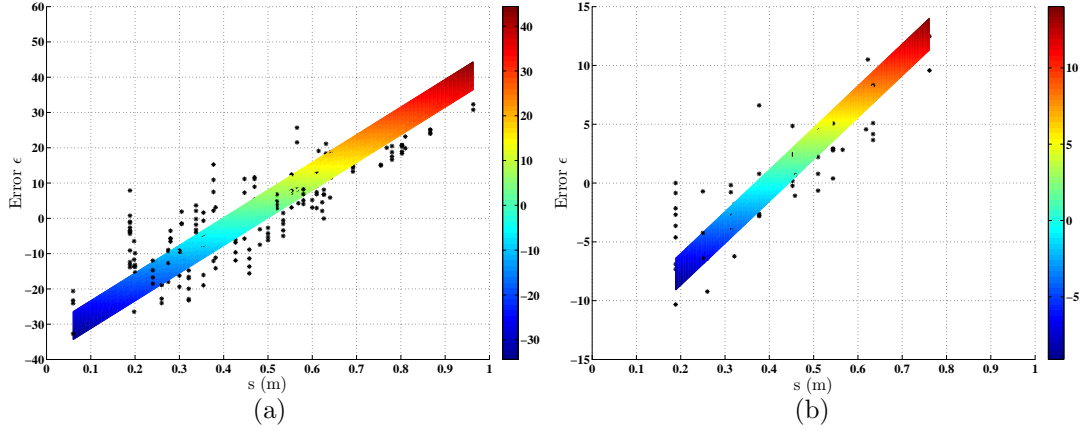


Figure 4.37: Projection of data in Figures 4.36 (a) and (b) illustrating dependence of ϵ on path length (6 GHz - 7 GHz).

The error as a function of s and κ is quantised (four intervals for s , three intervals for κ and a two-dimensional histogram of ϵ is constructed. The mean and standard deviation of the error for each pair of s and κ intervals has been calculated. Figure 4.38 is an example illustration of the best-fit normal distribution curve (i.e. with identical mean and standard deviation to the data). Finally, μ and σ are again regressed on s and κ using a first-degree polynomial surface as before, Figures 4.40 and 4.41. Similar to ISM-band measurements, for the difference (ϵ) a normal distribution is not very convincing. The samples, however, are closer to a straight line on a normal probability plot than any other simple model, Figure 4.39 .

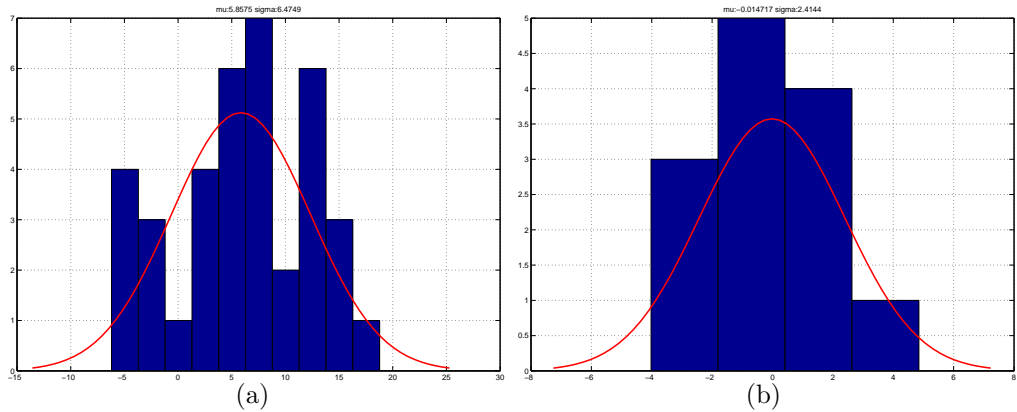


Figure 4.38: Error histograms and corresponding normal distribution for a single quantised pair of s - κ for measurements (a) without and (b) with cowling.

The histograms with the corresponding probability plots for all 12 quantisation intervals for normal distribution for each 1 GHz band are presented in

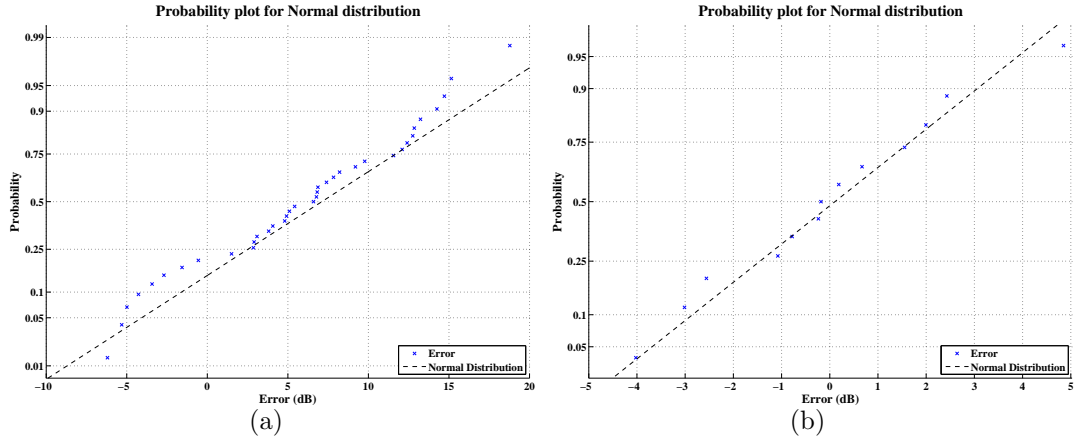


Figure 4.39: Normal probability plots corresponding to the histograms in Figure 4.38 (a) and (b).

detail in Appendices B and C and it seems that they are very close to the normal distribution, as expected from the central limit theorem.

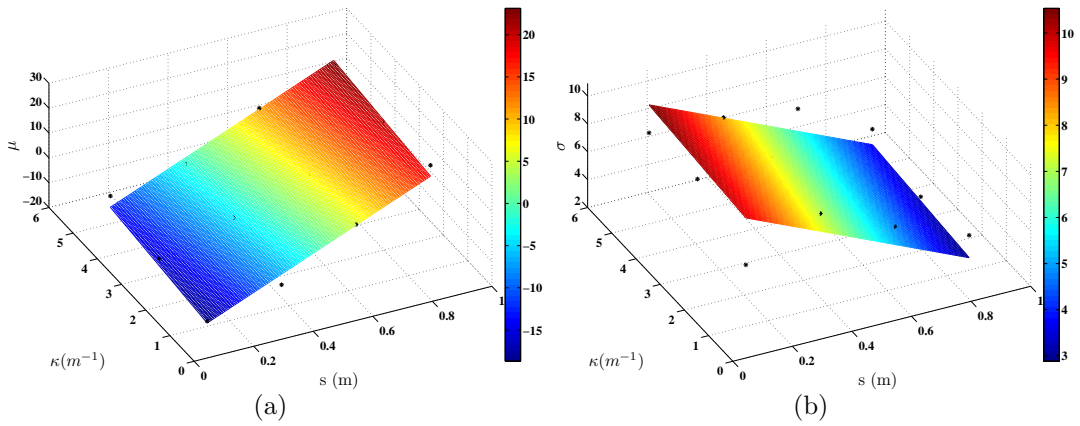


Figure 4.40: μ versus s , κ and σ versus s , κ for measurements without cowling (6 GHz - 7 GHz).

Table 4.7 contains the means and standard deviations for all quantisation intervals within each 1 GHz frequency band.

Appendices B and C include all the resulting graphs for error model, histograms and probability plots with regards to all the 1 GHz intervals within 3 - 11 GHz.

A system transmission gain model has been implemented using Simulink as a deliverable to the WIDAGATE project. The model includes deterministic and random components, i.e. $\overline{G}_T(s, \kappa)$, and $e(s, \kappa)$, respectively. e is a Gaussian random variable with mean and standard deviation that depend on s and κ (Equation 4.7).

		Frequency Band (GHz)	Intervals												
			1	2	3	4	5	6	7	8	9	10	11	12	
Meas. Set 1 (Without cowling)	μ	3-4	-16.1	-8.7	4.7	20.0	-11.5	-4.3	2.4	18.1	-7.3	-3.5	10.0	19.8	
		4-5	-17.0	-9.9	5.5	20.5	-11.6	-3.5	2.3	16.9	-7.5	-3.0	9.5	17.6	
		5-6	-16.0	-10.4	5.4	20.7	-11.5	-3.8	2.7	17.9	-7.5	-2.5	9.2	18.0	
		6-7	-18.0	-10.8	5.9	22.2	-13.5	-4.4	5.4	19.3	-8.8	-3.5	11.5	21.5	
		7-8	-16.9	-9.7	5.1	20.5	-12.1	-3.5	4.2	17.2	-7.9	-3.1	10.0	18.4	
		8-9	-13.9	-8.8	4.5	17.9	-10.1	-3.5	4.1	15.0	-5.8	-2.5	7.6	14.9	
		9-10	-13.3	-8.7	4.4	17.3	-9.9	-3.6	4.2	14.2	-5.9	-1.9	7.7	14.2	
		10-11	-13.1	-8.7	4.3	17.2	-9.8	-3.3	4.1	14.3	-6.1	-2.2	8.2	15.1	
		σ	3-4	3.9	7.6	5.9	4.6	6.6	8.6	7.0	3.0	7.4	7.9	8.0	4.7
			4-5	4.9	8.2	6.4	4.5	7.5	7.9	5.2	4.2	8.6	7.1	8.2	6.6
			5-6	7.5	8.6	6.8	4.6	9.0	8.2	4.3	4.1	9.0	6.9	7.8	6.1
			6-7	6.4	8.7	6.5	4.5	8.9	9.1	3.7	3.6	8.5	8.3	7.6	4.8
		7-8	7.0	7.5	5.8	3.9	8.7	8.1	3.2	3.0	8.3	8.0	7.5	4.5	
		8-9	5.0	6.6	4.4	3.7	7.3	6.3	2.9	2.2	8.3	8.3	6.1	2.3	
		9-10	6.0	6.3	4.4	4.1	7.7	5.8	1.4	2.8	7.9	8.1	6.2	3.0	
		10-11	5.3	6.1	4.4	3.8	7.4	5.7	0.7	2.4	7.9	7.6	6.7	3.4	
Meas. Set 2 (With cowling)	μ	3-4	-10.4	-3.7	3.0	9.7	-4.7	-0.1	4.6	9.0	-4.4	-0.2	6.3	12.8	
		4-5	-19.8	-7.1	5.7	18.4	-8.6	-0.0	8.1	17.2	-7.5	0.1	9.6	19.1	
		5-6	-14.8	-5.2	4.4	14.1	-6.9	-0.6	5.4	11.9	-4.4	-0.0	6.0	12.0	
		6-7	-12.1	-4.4	3.4	11.1	-5.5	-0.0	5.0	11.0	-4.3	-0.2	5.6	11.5	
		7-8	-18.9	-6.7	5.5	17.7	-7.8	0.2	8.2	16.3	-8.2	-0.2	10.8	21.8	
		8-9	-22.1	-7.9	6.4	20.7	-7.8	0.7	8.9	17.8	-8.6	-0.8	10.7	22.1	
		9-10	-22.1	-7.9	6.3	20.4	-8.7	0.7	9.3	19.6	-9.4	0.0	10.8	21.5	
		10-11	-27.1	-9.7	7.7	25.1	-11.1	0.4	11.6	23.4	-10.9	-0.9	14.8	30.5	
		σ	3-4	2.2	2.3	2.3	2.4	2.8	2.2	1.9	1.1	2.3	2.6	2.1	1.6
			4-5	1.5	2.2	2.9	3.6	5.1	3.7	2.8	0.9	3.3	4.5	3.6	2.7
			5-6	2.6	2.2	1.9	1.5	4.1	3.0	2.2	1.0	3.9	3.6	3.1	2.6
			6-7	2.6	2.4	2.3	2.2	2.6	2.4	2.5	2.1	3.4	3.6	3.4	3.1
		7-8	3.3	3.2	3.1	3.0	6.0	4.2	2.7	0.6	2.6	3.3	2.7	2.2	
		8-9	2.5	3.2	3.8	4.4	6.4	4.3	2.7	0.0	2.0	2.2	2.7	3.3	
		9-10	2.4	2.9	3.5	4.0	7.6	5.0	3.2	0.8	2.0	1.8	3.3	4.9	
		10-11	3.1	3.5	3.9	4.3	7.7	5.2	3.3	0.3	3.6	2.2	3.9	5.5	

Table 4.7: μ and σ values for each quantisation interval.

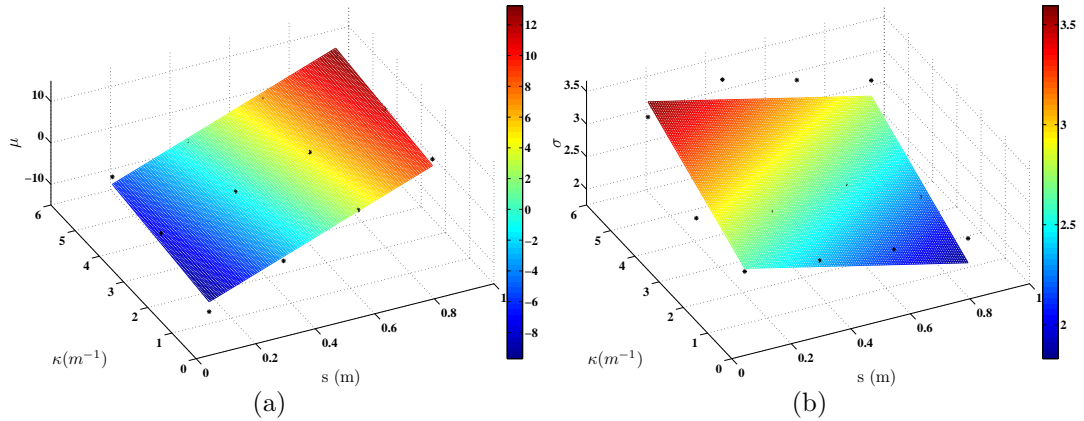


Figure 4.41: μ versus s , κ and σ versus s , κ for measurements with cowling (6 GHz - 7 GHz).

A block diagram of the system transmission gain model is shown in Figure 4.31.

4.6 Interference and Noise

4.6.1 Interference

An interference model has been extracted from ED-14 RTCA DO-160E Environmental Conditions and Test Procedures for Airborne Equipment [54]. This document specifies interference models in terms of the modulation and field strengths to be used in testing aircraft mounted devices in various equipment categories. The interference waveforms specified in this document include unmodulated continuous wave (CW) transmissions, square wave (SW) modulated transmissions and pulse modulated (PM) transmissions, see Figure 4.42.

The interference level specific to a certain equipment category is specified in a series of tables and graphs, e.g. Table 4.8 and Figure 4.43. This data has been incorporated in the interference model and can be selected. The field strengths specified are large however. The interference model developed therefore allows the interference level to be set manually.

4.6.2 Noise

A noise model has been developed incorporating components both external and internal to the receiver. The external component is specified by an antenna equivalent noise temperature. The internal component is specified by the receiver

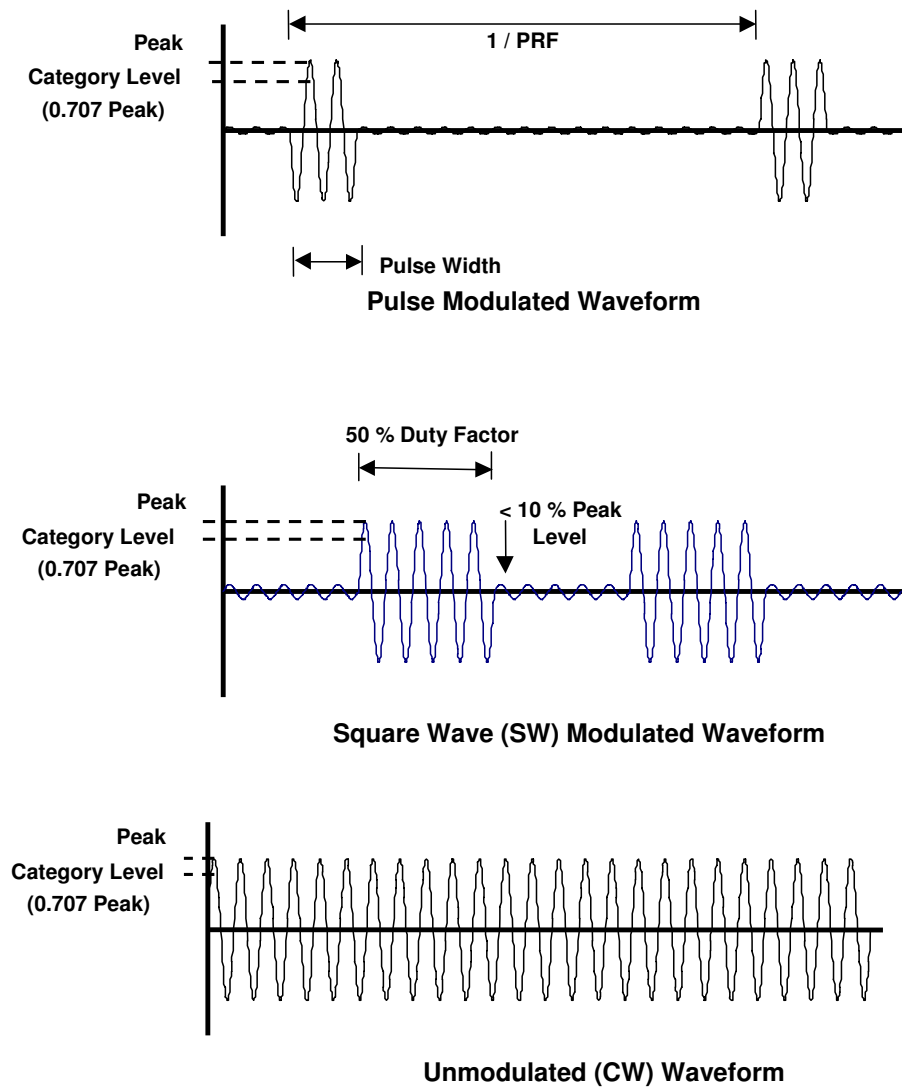


Figure 4.42: Interference waveforms. (After [54].)

<i>Category</i>	<i>Corresponding Number</i>	<i>Category</i>	<i>Corresponding Number</i>
Cat A	1	Cat J	10
Cat B	2	Cat K	11
Cat C	3	Cat L	12
Cat D	4	Cat R	13
Cat E	5	Cat S	14
Cat F	6	Cat T	15
Cat G	7	Cat W	16
Cat H	8	Cat Y	17
Cat I	9		

Table 4.8: Available categories for the input. (After [54].)

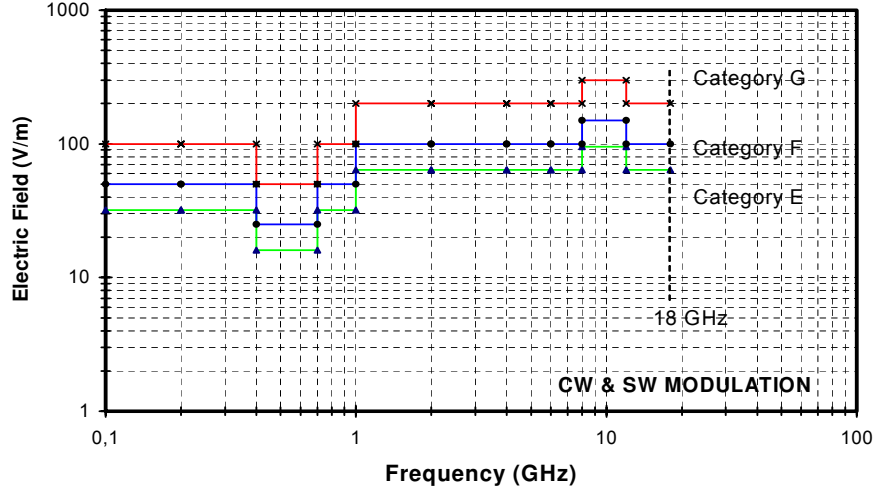


Figure 4.43: Example radiated susceptibility test levels. (After [54].)

ing WSN noise figure. Both components are assumed to be additive, white and Gaussian. The total noise power referred to the WSN input terminals is therefore given by:

$$n = k [T_a + (10^{(F/10)} - 1)290] B_N \quad (4.8)$$

where k is Boltzmann's constant (1.381×10^{-23} J/K), T_a is antenna equivalent noise temperature (K), F is WSN noise figure (dB) and B_N is the receiver noise bandwidth [26].

The antenna noise temperature is the noise power available at the receiving antenna terminals divided by kB_N .

Noise figure, F , is quoted in decibels and is related to the more fundamental quantity noise factor, f , by:

$$F = 10 \log_{10}(f)(dB) \quad (4.9)$$

Noise factor is defined as SNR (expressed as a power ratio) at the device input divided by SNR (expressed as a power ratio) at the device output when the input noise correspond to a temperature of 290 K [26].

$$f = \frac{(S/N)_i}{(S/N)_o} \Big|_{N_i=k290B} \quad (4.10)$$

4.7 System Model

A block diagram of the system model comprising (i) the transmission gain model, (ii) the interference model and (iii) the noise model, is shown in Figure 4.44. Red blocks denote input parameters.

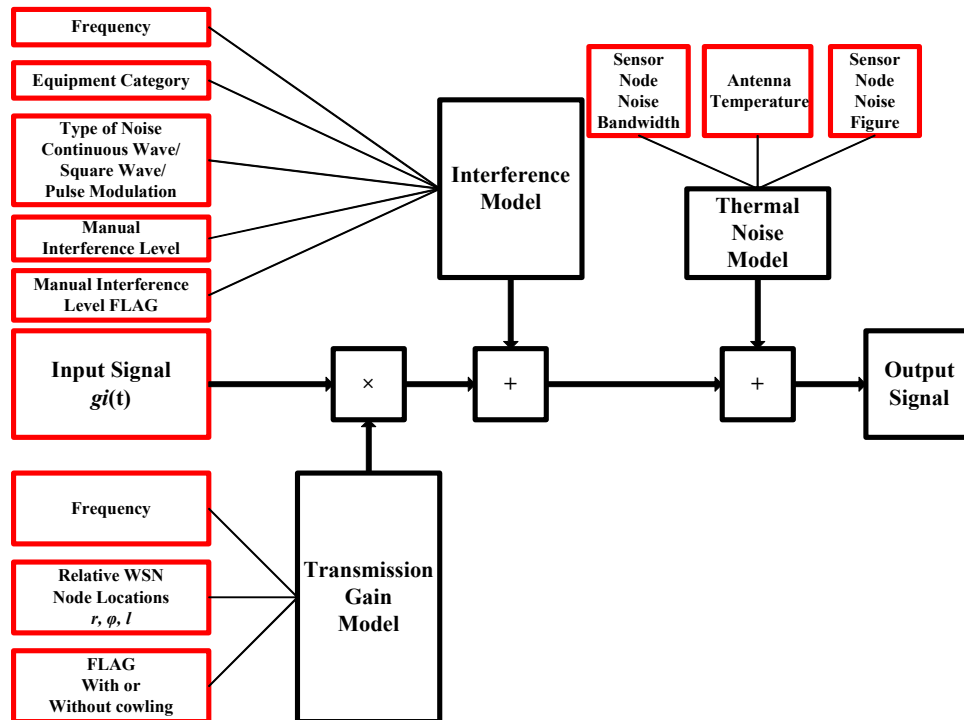


Figure 4.44: High level description of the system model.

4.7.1 System Platform

The system model has been implemented using Simulink. Figure 4.45 shows the complete Simulink block diagram.

4.7.1.1 Transmission Gain Model

Figure 4.46 shows the transmission gain model.

The transmission model specifies the transmission gain GT of the channel. This is the sum of the mean transmission gain GT_{bar} (dB) and a random variation (E_{dB}).

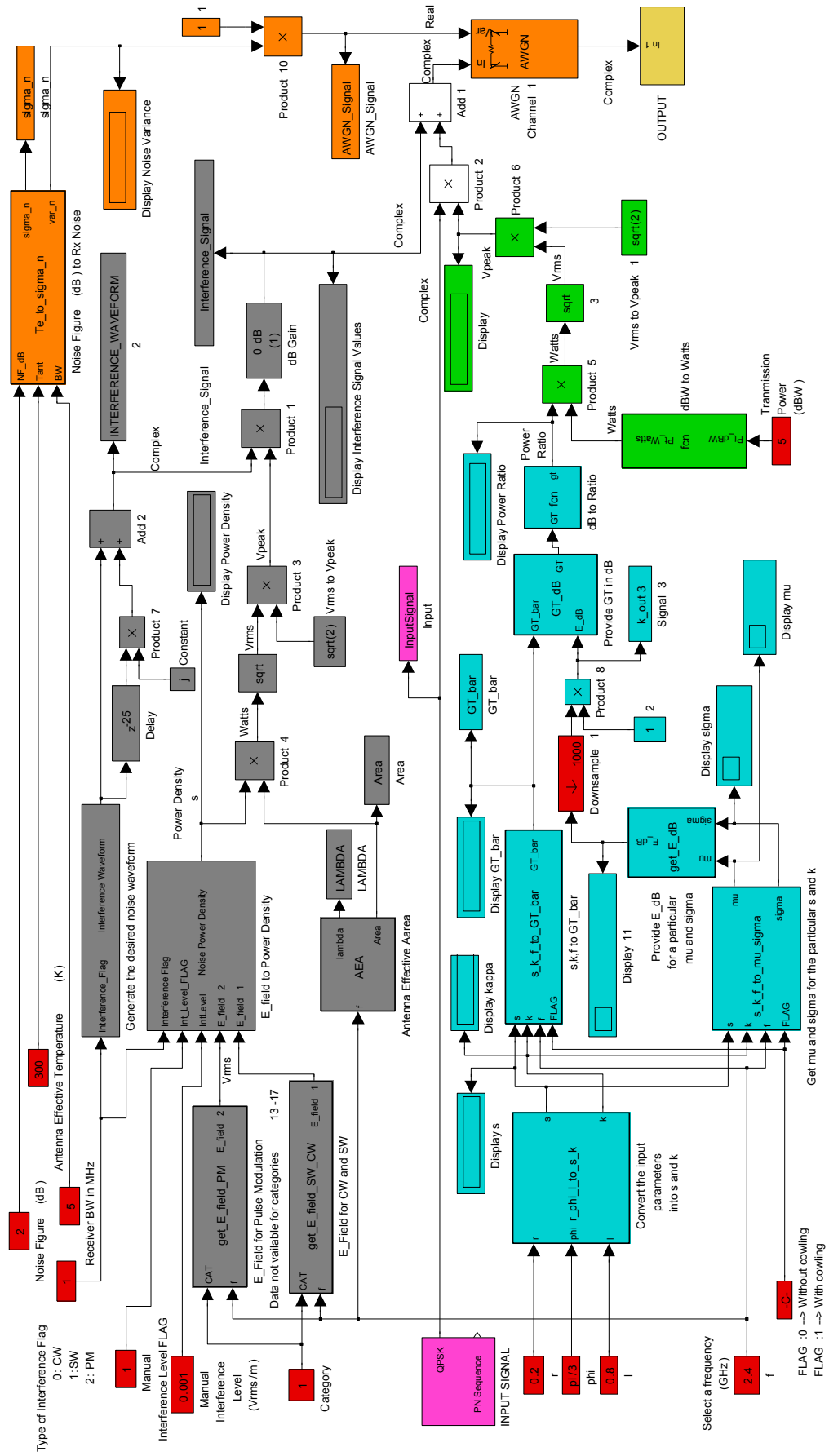


Figure 4.45: Simulink system model.

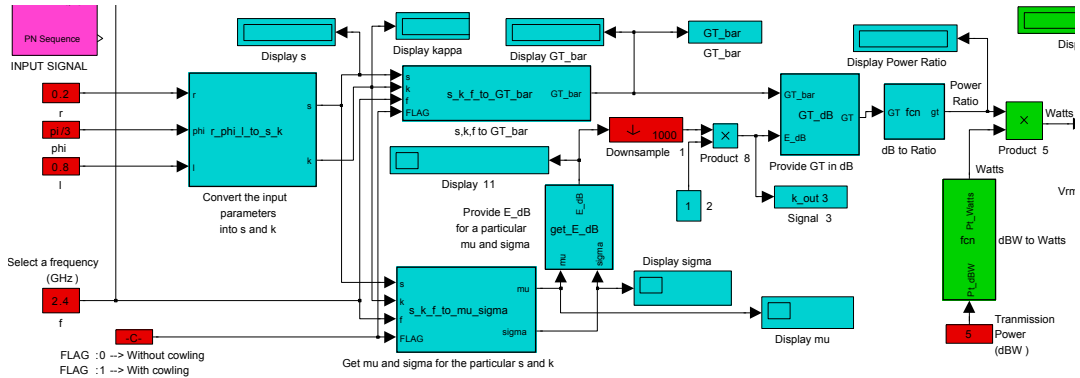


Figure 4.46: Transmission gain model.

4.7.1.1.1 Transmission Gain Model Parameters

The five parameters of the transmission model are:

Engine Radius (r)

This is the radius of the engine in metres. The value set as default is 0.2, which applies to the Gnome engine.

Angle (ϕ)

This is the angular separation in radians between two WSNs projected into a plain perpendicular to the engine axis. The value set as default is $\pi/3$ rad.

Length (l)

This is the lateral separation in metres between the planes perpendicular to the engine axis containing the WSNs. The value set as default is 0.8.

Transmission Frequency (f)

This is the transmission frequency in GHz. This automatically selects the appropriate polynomial from the transmission gain model. The valid range for this input is 2.4 to 11 (GHz). The value set as default is 2.4.

FLAG:0 without FLAG:1 with cowling

This flag is passed to the transmission gain model to select underlining measurements without (FLAG:0) or with (FLAG:1) cowling.

4.7.1.1.2 Transmission Gain Blocks

The transmission gain model consists of six blocks in total, which are implemented using Matlab embedded functions. These are:

$r_phi_l_to_s_k$

This function converts the engine radius r , and WSN relative coordinates ϕ and l into path length s and path curvature κ .

4.7. SYSTEM MODEL

s - κ - f - to - GT - bar

This function exports the mean transmission gain \bar{GT} corresponding to the particular values of s , κ and f values.

s - κ - f - to - mu - sigma

This function exports the values of μ and σ (the mean and standard deviation of the normal pdf from which the random component of transmission gain is derived) corresponding to the quantisation interval centred on s and κ , for the selected frequency.

get - E - dB This function generates the random component of transmission gain.

GT - dB This function adds the mean transmission gain \bar{GT} and the random variation E - dB.

dB - to - ratio

This function converts the dB value of transmission gain into the power gain of the channel as a dimensionless ratio.

4.7.1.2 Interference Model

Figure 4.47 shows the interference model.

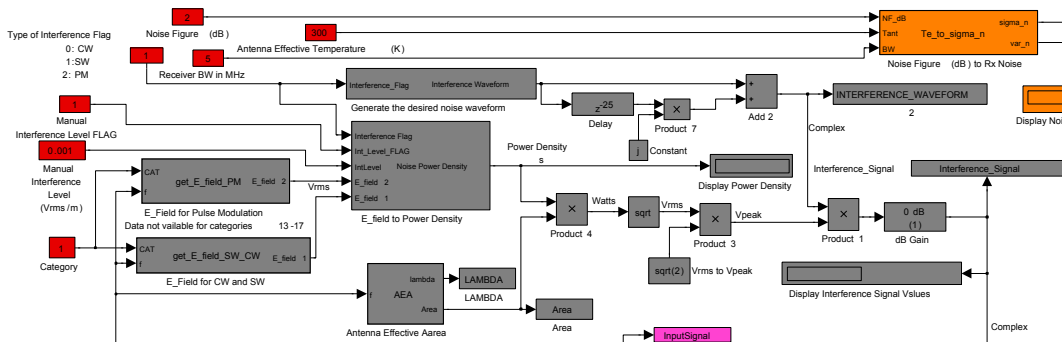


Figure 4.47: Interference model.

4.7.1.2.1 Interference Model Parameters

The four parameters of the interference model are:

Type of Interference Flag

This selects a CW, SW or PM interfering signal as defined below.

CW (Continuous Wave Unmodulated Carrier)

This is an unmodulated sinusoid derived from the block "Generate the desired noise waveform/SineWave".

SW (Square Wave Modulated Carrier)

This generates an Amplitude Shift Keyed (ASK) waveform with two non-zero amplitude levels. The waveform is generated from the sum of two baseband pulses with different amplitudes but the same, duty factor (50%). The passband ASK waveform is obtained by multiplying this sum with a sinusoid generated by the block SineWave. The relative amplitudes of the two signal states as delivered are 1.0 and 0.09. This is consistent with a requirement specified by [54].

PM (Pulse Modulated Carrier)

This generates an Amplitude Shift Keyed (ASK) waveform with one non-zero amplitude level. The waveform is generated from a baseband pulse train with arbitrary duty cycle. The passband ASK waveform is obtained by multiplying the baseband pulse train with a sinusoid generated by the block "SineWave". The non-zero amplitude of the pulse train as delivered is 1.0. The default value for duty-factor of the pulse train is 20%.

Manual Interference Level FLAG

When this flag is set to zero, the electric field strength (E - field) of the interfering signal at the receiving WSN is derived from the relevant table or graph in [54]. This is conditional on the selected equipment category. When this flag is set to 1, the electric field strength (E - field) of the interfering signal at the receiving WSN is set manually using the manual interference level parameter block.

Manual Interference Level (Vrms/m)

This parameter block sets the electric field strength E - field at the receiving WSN when the manual interference level flag is set to 1.

Category

This model parameter selects the appropriate equipment category as defined in [54]. The parameter is entered as an integer. The integers map to the equipment category letters as given in [54].

Transmission Frequency (f)

See Section 4.7.1.1.1.

4.7.1.2.2 Interference Model Blocks

get - E - field - PM

This block exports the electric field (V - rms/m) of a pulse modulated interfering signal conditional on equipment category and transmission frequency.

get - E - field - SW - CW

This block exports the electric field (V - rms/m) of a continuous wave or a square wave modulated interfering carrier conditional on equipment category and trans-

mission frequency.

Interference - Flag to Interference Waveform

This block generates the real passband interfering signal. The type of interference (CW, SW or PM) is conditional on the Interference_ Flag. The parameters of the interference signal as delivered are set to generate a waveform with peak amplitude 1.0 V/m and carrier frequency 62.5 kHz irrespective of interference type. (Note this carrier frequency has been chosen to be half of the symbol duration for the QPSK transmitted signal corresponding to a bit rate of 250 kbps. This ensures that the carrier frequency of the interference lies half-way between the peak and first null of the QPSK signal spectrum.)

Real passband interference to complex equivalent baseband conversion

The real interfering signal(CW, SW or PM) is converted to an equivalent complex baseband signal using the delay block, the "Product7" block, the "Constant j" block and the "Add2" block. The number of the parameter delay samples set by double clicking the delay block must be set to one quarter of the number of samples per period set in the Sine Wave generator within the "Interference - Flag to Interference Waveform" block.

E - field - to - Power Density

This block exports the power density (W/m^2) of the interfering signal at the receive WSN.

AEA (Antenna Effective Area)

This block calculates the effective area of an isotropic antenna from the specified WSN transmission frequency.

Power Density to Received Voltage conversion

Power density is multiplied by antenna effective area to give received power in watts. (The power density is a maximum if the interference is an SW or PM signal) The received maximum rms voltage is calculated as the square root of the maximum power density. The received peak voltage is calculated by multiplying the received maximum rms voltage by $\sqrt{2}$. The peak amplitude of the received interfering signal is set by multiplying the unit peak amplitude by the received peak voltage.

dB - Gain

This block can be used to attenuate or amplify the received interference by an arbitrary factor. The value as delivered is 0 dB.

4.7.1.3 Noise Model

Figure 4.48 shows the noise model.

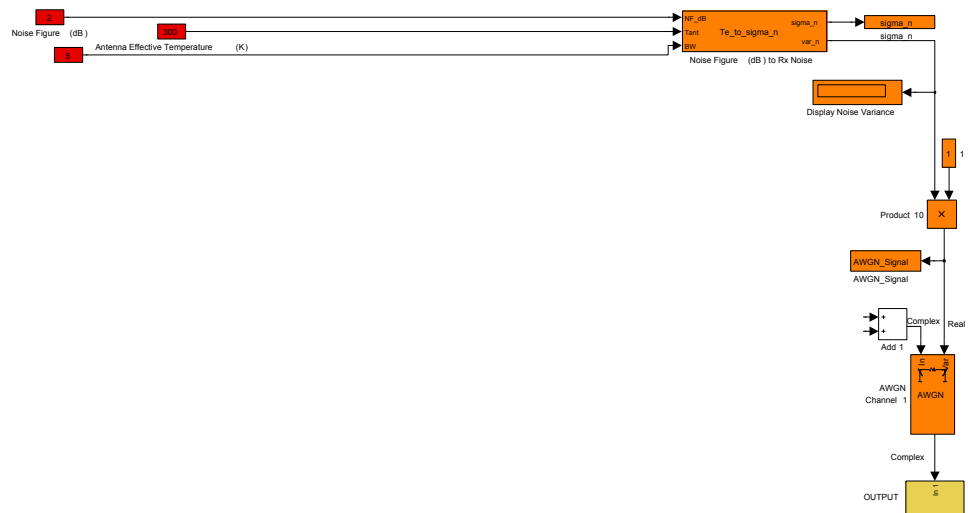


Figure 4.48: Noise model.

4.7.1.3.1 Noise Model Parameters

The three parameters of the noise model are:

Noise Figure (dB)

This is the WSN noise figure in dB. The value set on delivery is 2 dB.

Antenna Effective Temperature (K)

This is the antenna effective temperature in kelvin. The value set on delivery is 300. (This corresponds to the thermal noise temperature expected for an antenna whose radiation pattern illuminates a black body at a physical temperature of 300 K. In the context of thermal noise it is therefore a worst plausible case antenna temperature.)

Receiver Bandwidth in MHz

This is the bandwidth of the receiver. The value set on delivery is 5 MHz. This is the typical bandwidth of a WSN node transceiver (e.g. MICAz wireless node manufactured by Crossbow [15])

4.7.1.3.2 Noise Model Blocks

Te_to_sigma_n

This block imports the three parameters of the noise model and exports the variance var_n of the noise which is passed to the AWGN block.

AWGN

This block gets the variance of the noise σ_n and adds additive white Gaussian noise to the signal.

4.7.1.4 Downsampling

The value of E_{dB} changes with each single simulation step and therefore the channel fluctuates extremely fast during the simulation. To avoid such an effect and allow the user to perform a more realistic simulation, a sub-sampling feature of the E_{dB} parameter has been added. The user can double click the red block "Downsample1", shown in Figure 4.45, and enter the sub-sampling factor (integer). The value set on delivery is 1000, which means that the E_{dB} parameter keeps the same value for 1000 simulation steps (then receives the 1001st simulation value and keeps it for the next 1000 simulation steps).

4.7.1.5 Model Output

The output of the system model is the final sub-system block of Figure 4.45 (yellow). This sub-system includes the scope to visualise the constellation points, the demodulator and the final export of the signal to workspace for further process.

4.7.2 Model Validation

This section describes the validation of the Simulink system model. Channel fluctuations refer to the statistical deviation E_{dB} , signal interference to an interference source of 0.015 V/m, thermal noise to a noise source with noise figure 7 dB and transmission power to -20 dBW (+10 dBm), respectively, unless otherwise stated. The combinations for validating the system model are shown in Figures 4.49 to 4.53.

4.8 Summary and Conclusions

A comprehensive set of transmission loss measurements for wireless sensor nodes deployed around the surface of a gas turbine engine have been reported. ISM-band measurements have been made using a pair of omni-directional rectaxial antennas, as well as measurements covering the UWB frequency band, using appropriate antennas. The measurements have been made both in the presence of, and in the absence of, an engine cowling.

A simple empirical model comprising best-fit planar regression in path length s and path curvature κ has been derived for both the ISM-band and for each

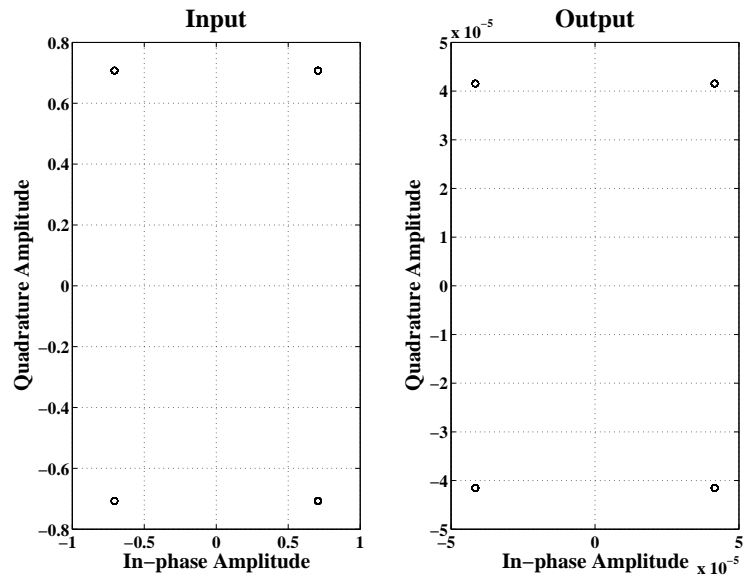


Figure 4.49: Model validation with no channel fluctuation, no interference and no thermal noise.

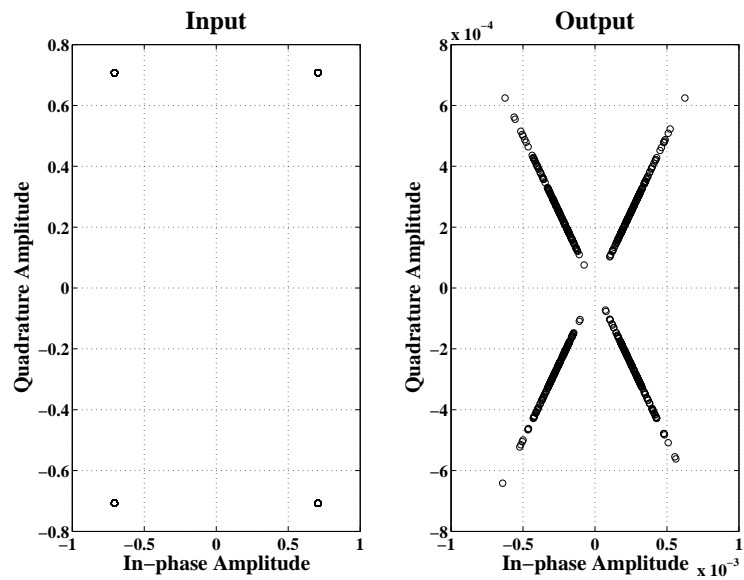


Figure 4.50: Model validation with channel fluctuation only (no interference and no thermal noise).

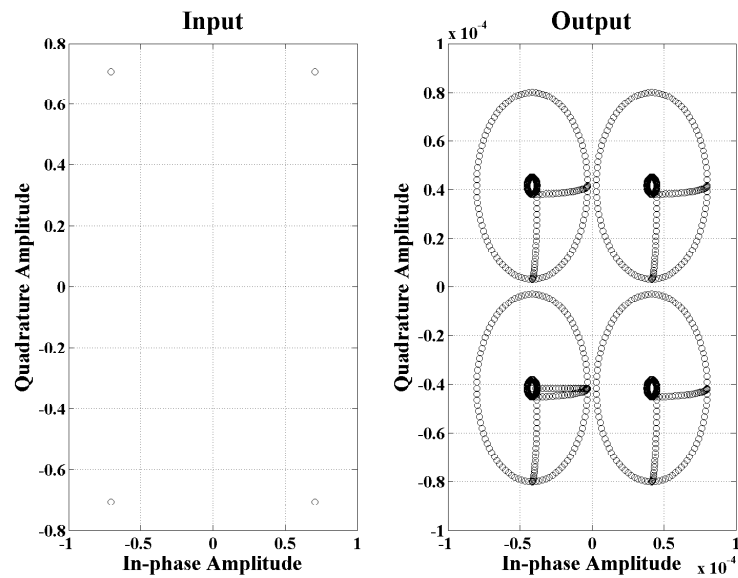


Figure 4.51: Model validation with interference only (no channel fluctuation and no thermal noise).

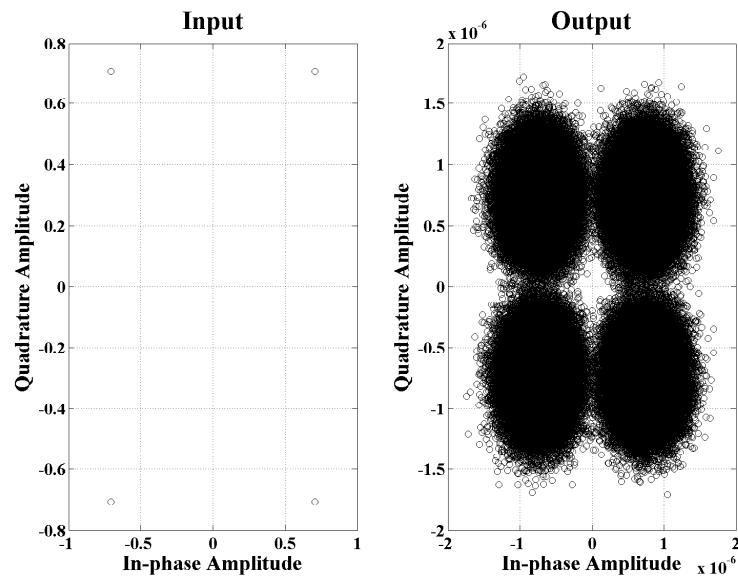


Figure 4.52: Model validation with thermal noise only (no channel fluctuation, no interference). For this case only, the transmission power was set to -55 dBW (-25 dBm) which is the minimum transmission power for MICAz.

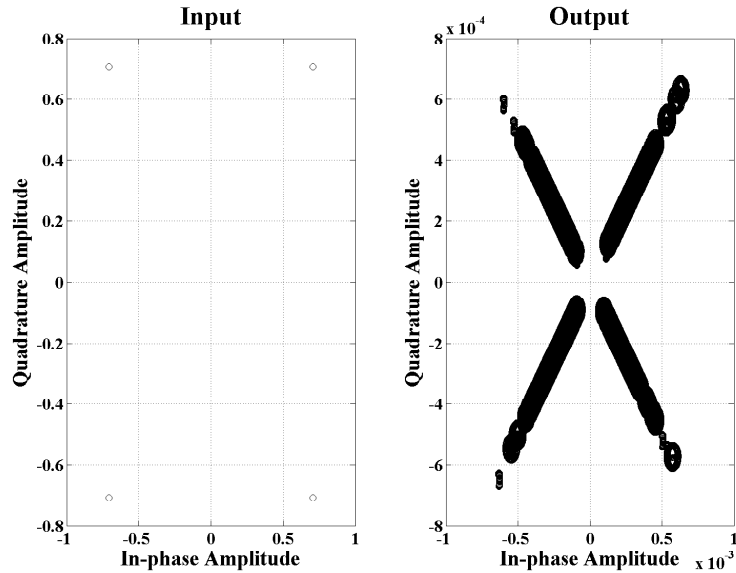


Figure 4.53: Model validation with channel fluctuation, interference and thermal noise.

1 GHz frequency interval within the UWB-band. The difference, ϵ , between model and measurements as a function of path length and curvature has been characterised. The resulting transmission gain model has been incorporated into a simulator along with both an interference and noise model. The simulator is currently being used within a larger project concerned with the investigation of the potential of WSNs for gas turbine engine testing.

The following conclusions are drawn:

- A simple theoretical model suggests that the maximum symbol rate (R_{symbol}) for which a narrowband propagation model is adequate for a gas turbine is dependent on engine radius r . As engine radius increases symbol rate decreases. For a Gnome engine, with mean radius 0.2 m, the maximum symbol rate is 70 Mbaud (Figure 4.3).
- The 50% exceedance of 50% correlation bandwidth derived from the measurements is 5.5 MHz and 8 MHz for ISM-band set 1 and set 2, respectively.
- The 50% exceedance of 50% correlation bandwidth derived from the measurements is 120 MHz and 25 MHz for UWB-band set 1 and set 2, respectively.
- Mean transmission gain \overline{G}_T is sensitively dependant on path length s .
- Mean transmission gain \overline{G}_T is relatively insensitive to path curvature κ .

- Mean transmission gain \overline{G}_T without cowling appears to be lower than with cowling. This is due to the cavity formed by the engine and cowling.
- Specific transmission gain $\left(\frac{d\overline{G}_T}{ds}\right)$ for ISM-band measurements without cowling (set 1), is lower than that with cowling (set 2). However, the converse is true for the UWB-band measurements for all 1 GHz intervals. The latter is anti-intuitive and no definitive (experimentally verified) explanation can be given at the time of writing. The hypothesis offered, however, is that the radiation impedance (and therefore the input impedance) of the UWB antennas is more sensitive to being enclosed by a conducting cavity than that of the ISM antennas. That the radiation impedance must be changed by a conducting enclosure becomes evident by considering the extreme case of an antenna excited inside a perfectly conducting (and therefore lossless) cavity. In this case no radiation can occur; the antenna necessarily being completely mismatched to its transmission line feed. This corresponds to the real part of the radiation impedance of the antenna becoming zero or infinity (depending on whether a series or parallel equivalent circuit for the antenna is being considered.) The reflection coefficient will then be slightly less than unity due only to the finite losses in the antenna. (A lossless antenna in a lossless cavity would result in a reflection coefficient magnitude of precisely 1.0.) There are thus two counterbalancing effects on the transmission-loss change going from the engine without cowling to the engine with cowling. The presence of the cowling reduces path loss due to the wave-guiding effect of the resulting cavity but increases antenna mismatch (at both transmitter and receiver) due to a change of radiation impedance. The hypothesis is thus that the reduced path-loss effect outweighs the impedance mismatch effect in the case of the narrowband (100 MHz) ISM antenna measurements at 2.4 GHz but the impedance mismatch effect outweighs the reduced path-loss effect in the case of the higher frequency (2.4 - 11 GHz), broader-band (8.6 GHz), measurements.
- Specific transmission gain $\left(\frac{d\overline{G}_T}{d\kappa}\right)$ is less than unity in all cases.
- The gradient of the mean difference with respect to path length $\left(\frac{d\epsilon}{ds}\right)$, is positive (for both ISM-band and UWB-band measurements without and with cowling). Its value is zero for $s = 0.43$ m. The transmission gain model has greatest accuracy, therefore, at path lengths close to 0.43 m.

- The distribution of mean difference ϵ within a single quantisation interval is closer to a normal distribution than any other common analytical distribution. Nevertheless, the fit is rather unconvincing.
- The distribution of mean difference ϵ for all 12 quantisation intervals is close to normal as might be expected from the central limit theorem.

CHAPTER 5

Diversity Channels for Animal Husbandry

WSNs are widely used in many applications, among them the monitoring of livestock and particularly cattle.

One of the early projects relating to habitat monitoring [55] was conducted at Great Duck Island; a 237-acre island located 15 km south of Mount Deset Island, Maine. 43 sensor nodes were deployed to monitor the microclimate in, and around, nesting burrows used by the Leachs Storm Petrel. The system was operated for something over four months and more than 1.1 million readings were collected. Each node incorporated a micro-controller, a low-power radio transmitter, memory and a battery. The node sensors measured light intensity, temperature and humidity. The sensor outputs were periodically sampled and the samples relayed to a base-station computer which acted as an Internet gateway, thus allowing real-time data access.

ZebraNet [56] used a WSN for tracking and monitoring zebras in Kenya. GPS-enabled sensor nodes were incorporated in collars and geographical location data was passed to a base-station using, where necessary, other network nodes as repeaters. The system hardware comprised a 16-bit Texas Instruments micro-controller, 4 Mbit of off-chip flash memory, a 900 MHz radio transceiver, and a low-power GPS chip.

'Wired Pigs' [57] used a wireless sensor network to monitor the movement of pigs.

Several trials using WSNs for cattle monitoring have been reported including [58] [59]. One trial [60] [61] equipped 45 animals with collars incorporating two batteries, a GPS receiver (including antenna), a communications transceiver and a communications antenna. The antennas were subject to damage, however, due to animals rubbing them on scratching posts and biting them [61].

5.1 Motivation

Although many projects have addressed animal monitoring applications, none have incorporated any form of diversity.

In mammal monitoring and tracking applications a single antenna is traditionally attached to a collar worn around the animal's neck. As the animal moves the line-of-sight (LOS) path between collar-antenna and base-station (or collar-antenna and another node in the WSN) might be obscured, either by fixed obstacles or by other animals. The latter is the more likely in the context of animals with a herding instinct on open grassland such as might be expected in the dairy and beef industries.

The incorporation of two antennas at the sensor node (spatial diversity) combined with two widely separated base-stations (base-station diversity) must clearly increase the probability of LOS conditions. It is the degree to which signal fading statistics are improved that is the focus of this work.

5.2 Aims and objectives

This particular research concerns the deployment of a real-time WSN which benefits from both base-station and antenna diversity. By real-time we mean that raw data are not stored on the wireless mote, but are transmitted directly to the base-stations after the sampling.

The primary objective is the measurements of the performance of a particular WSN in a realistic environment and the statistical analysis of the resulting data [62] [63].

5.3 Measurements and Modelling

5.3.1 Ceramic Patch Antenna

Each antenna is an inset-fed microstrip patch with a ceramic element attached to the radiating surface, Figure 5.1. The radiation pattern of the antenna is shown in Figure 5.2 at three frequencies, for two orthogonal linear polarisations in three orthogonal planes [64].

5.3.2 Measurements

The transceiver used was the MICAz [15] shown in Figure 5.3. It operates in the ISM-band between 2.4 GHz and 2.48 GHz. The transmitted power was set to -10 dBm.



Figure 5.3: The MICAz transceiver.

The transceiver is mounted on a PCB, Figure 5.4, which also includes an RF switch that connects the MICAz RF input/output to two microstrip antennas.

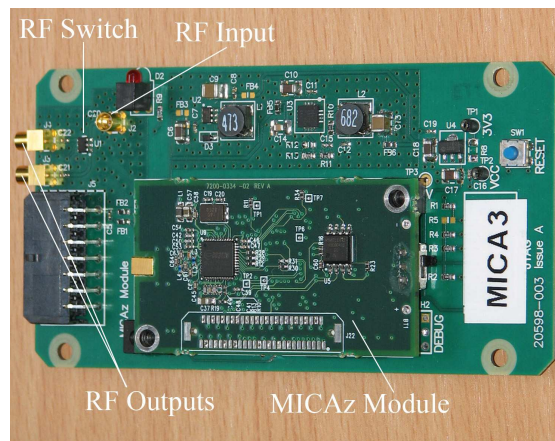


Figure 5.4: PCB carrying the MICAz module.

The entire configuration was attached to the collar, which was oriented on the animal such that one antenna was located on the left side of the neck and one on the right side as shown in Figure 5.5.

The measurement area was a large shed, approximately 20 m \times 12 m, enclosed by thick brick walls, a concrete floor and a pitched metallic roof, Figure 5.6.

The base-station comprised a transceiver (identical to those attached to the animal collars) interfaced to an MIB600 programming board. A block diagram is shown in Figure 5.7. The antenna used at the base-station was close to omnidirectional with a gain of 6 dBi [65].

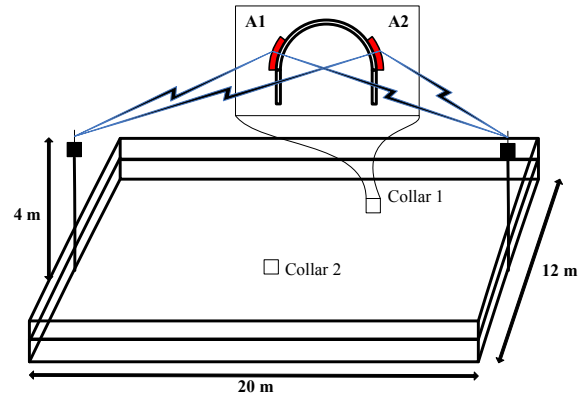


Figure 5.5: Schematic illustration of antenna arrangement on collar and trial area.



Figure 5.6: Trial area.

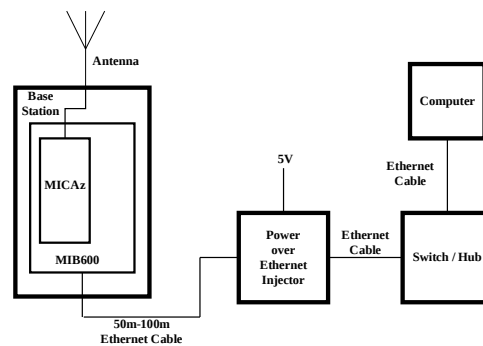


Figure 5.7: Base-station configuration.

Two test animals were released into the test area along with seven others and the received power was recorded for 75 minutes at both base-stations. The two antennas at each animal-mounted node were alternately connected to the transceiver for 1 s using the RF switch. The complete switching cycle therefore has a period of 2 s. The sampling frequency for a particular antenna was thus 0.5 Hz.

The movement of animals was sufficiently slow such that each 1 s block of contiguous data received from a given antenna can be assumed to originate from a single location.

The resulting data was smoothed by calculating the moving average of 15 samples representing a time window of 30 s.

5.3.2.1 Statistics

The raw data¹ (0.5 Hz samples) received from base-station 1 (BS1) and base-station 2 (BS2) are shown in the upper plots of Figures 5.8 (a), (b), (c) and (d) and Figures 5.9 (a), (b), (c) and (d), respectively. Figures (a) and (b) correspond to the data transmitted from antenna 1 (A1) and antenna 2 (A2), respectively, mounted on collar 1 (C1). Figures (c) and (d) correspond to the data transmitted from A1 and A2, respectively, mounted on C2.

¹For MICAz, the RSSI is an estimate of the received signal strength calculated over an 8-symbol period. [15]

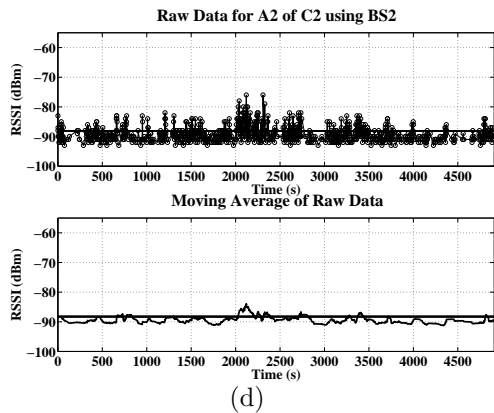
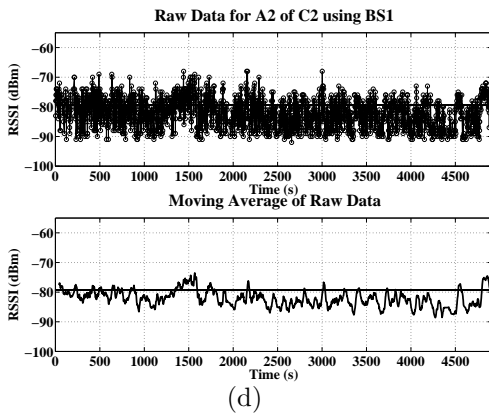
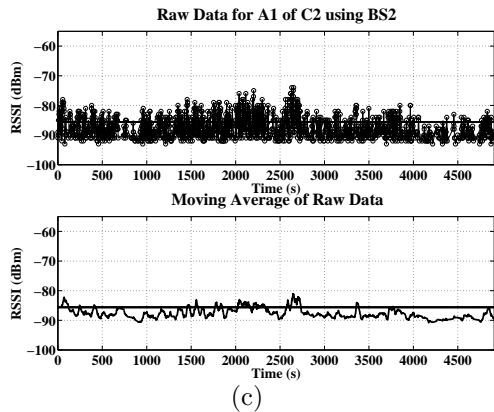
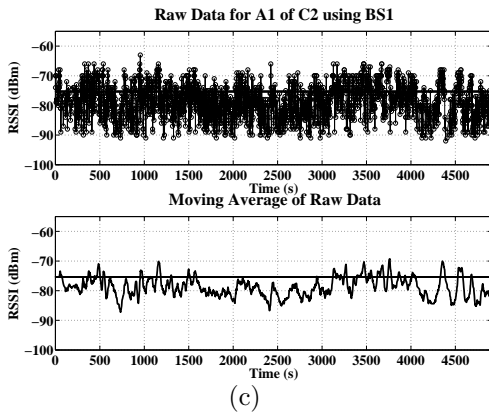
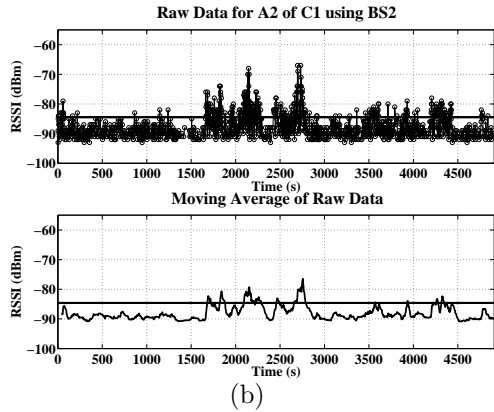
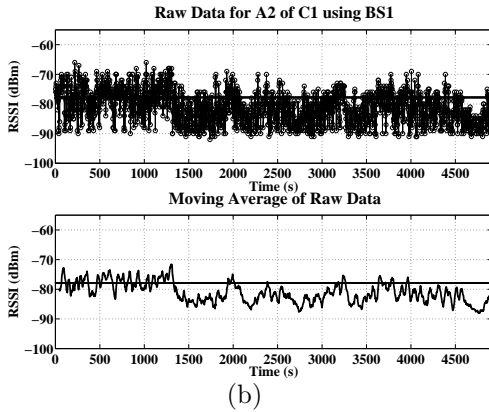
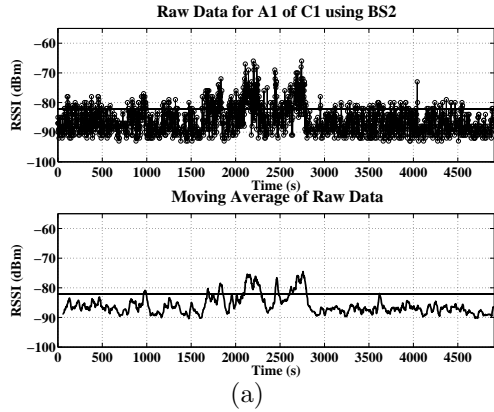
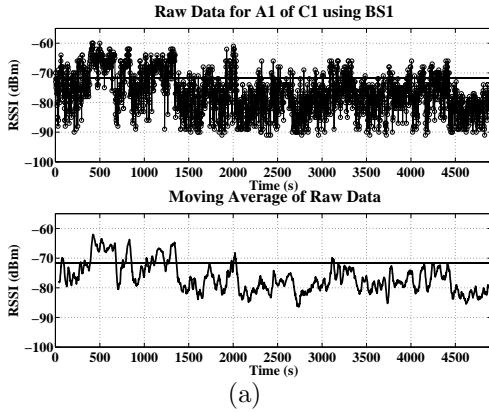


Figure 5.8: Data received by base-station 1.

Figure 5.9: Data received by base-station 2.

The fluctuation of power is large (up to 20 dB). The corresponding lower plots show the 15-sample moving average. The horizontal line in the figures represents the mean power for each measurement set.

The peak-to-peak variation of received power recorded for each antenna on each collar to each base-station over the total observation time is shown in Figure 5.10.

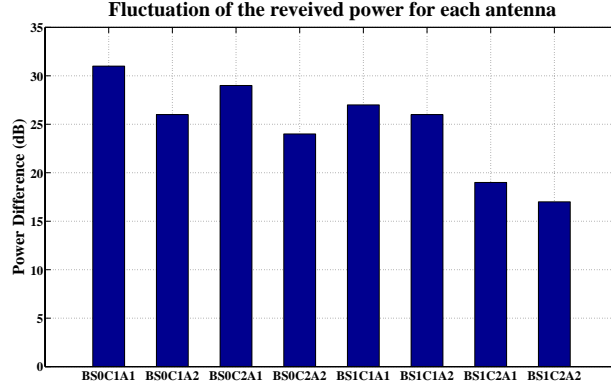


Figure 5.10: Peak-to-peak fluctuation of the received power at each individual antenna. From left to right, BS1C1A1, BS1C1A2, BS1C2A1, BS1C2A2, BS2C1A1, BS2C1A2, BS2C2A1, BS2C2A2. (BSxCyAz denotes base-station, collar and antenna numbers, respectively.)

For diversity advantage to be realised the fluctuation of received power in the two channels must be decorrelated.

The correlation coefficient $\rho_{X,Y}$ between two random variables X and Y with expected values μ_X and μ_Y and standard deviations σ_X and σ_Y is defined as:

$$\rho_{X,Y} = \frac{\text{cov}(X, Y)}{\sigma_X \sigma_Y} = \frac{E((X - \mu_X)(Y - \mu_Y))}{\sigma_X \sigma_Y} \quad (5.1)$$

where E denotes expectation and cov denotes covariance [66].

The correlation coefficients between the antennas mounted on the same collar are presented in Table 5.1. From the definition of correlation (Equation 5.1), the LOS component (which is essentially constant) is excluded which explains the very low values of correlation.

The probability distribution of the received signal from a particular mobile antenna to a particular base-station might be expected to be close to Ricean as a result of multipath propagation with a strong LOS component. The Ricean distribution is given by:

<i>Base-station</i>	<i>Collar</i>	<i>Correlation Coefficient between A1 and A2</i>
BS 1	Collar 1	0.2407
	Collar 2	0.0414
BS 2	Collar 1	-0.0733
	Collar 2	0.0158

Table 5.1: Correlation coefficient of signals received by antennas on a single collar.

$$p(r) = \begin{cases} \frac{r}{\sigma^2} e^{-\frac{(r^2+A^2)}{2\sigma^2}} I_0\left(\frac{Ar}{\sigma^2}\right) & \text{for } (A \geq 0, r \geq 0) \\ 0 & \text{for } (r < 0) \end{cases} \quad (5.2)$$

where A denotes the peak amplitude of the dominant signal and I_0 is the modified zero order Bessel function of the first kind [23]. The K -factor of a Ricean distribution is the power ratio between the (constant) component of signal power due to the LOS path and the (fluctuating) component of signal power due to all other paths, i.e.:

$$K = \frac{A^2}{2\sigma^2} \quad (5.3)$$

As the LOS component becomes smaller K -factor decreases and the probability density function (pdf) becomes more skewed. As K tends to zero the Ricean distribution approaches a Rayleigh distribution. As the LOS component becomes larger, K increases and the distribution becomes less skewed. As K tends to infinity, the Ricean distribution approaches a normal distribution.

Figure 5.11 shows the pdfs of the power received at BS1. Figures 5.11 (a) and (b) represent the pdfs of the data obtained from A1 and A2, respectively, regarding C1. Similarly, Figures 5.11 (c) and (d) refer to A1 and A2 on C2.

A normal distribution of power in dBm (i.e. a log-normal distribution of power in watts) appears to be the best fit to the data. If fading is due predominantly to multipath propagation this suggests the presence of a strong LOS component. An alternative, but less likely, interpretation would be that the log-normal fading reflects cascaded independent shadowing processes.

Figure 5.12 shows the pdf of the power received at BS2. In a similar way to Figure 5.11, Figures 5.12 (a) and (b) represent the data transmitted by C1 (for A1 and A2 respectively) and Figures 5.12 (c) and (d) the data transmitted from C2 (for A1 and A2 respectively).

Superficially this distribution appears to be closer to Rayleigh (in dBm) than

normal. The mean signal level is significantly lower than that for BS1 (due to the larger distance), however, and is approaching the receiver sensitivity which is -94 dBm. Since no signal is recorded when the received power falls below -94 dBm the pdf is effectively truncated at this level. It seems likely, therefore, that the pdf of the underlying signal is normal (in dBm) even though the pdf of the recorded (truncated) signal is skewed.

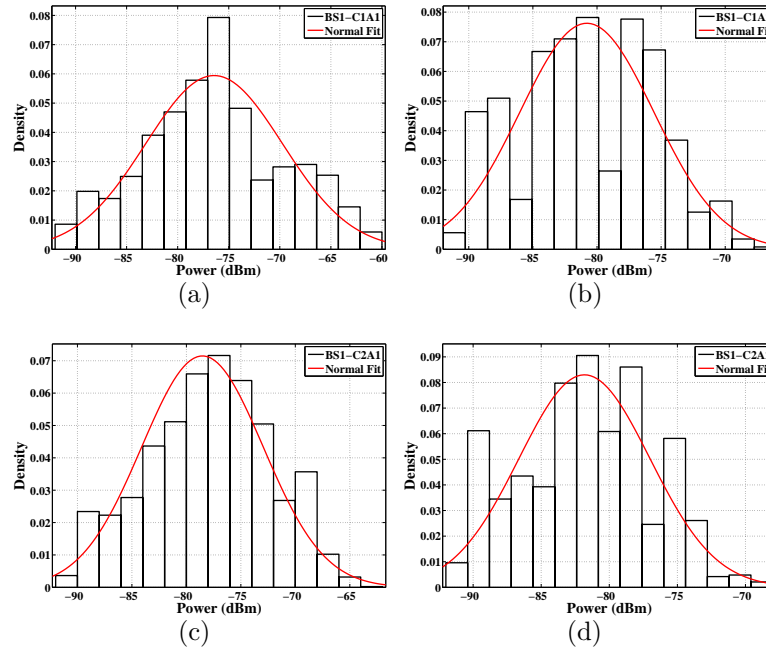


Figure 5.11: Pdfs of power (dBm) at BS1 for (a) A1 on C1 and (b) A2 on C1 and (c) A1 on C2 and (d) A2 on C2. (Smooth curve represents the best-fit normal distribution.)

The corresponding cumulative distribution functions (cdfs) are presented in Figures 5.13 and 5.14. The best-fit normal curves along with 95% confidence bounds are superimposed.

The close fit of the normal distribution to the data logged at BS1 is apparent. The fit is less good for the data obtained from BS2.

Figures 5.15 and 5.16 show similar plots for received voltage.

Figure 5.17 represents similar data to that presented in Figures 5.8 and 5.9 but of shorter time duration (approximately 40 minutes). The advantage of the use of base-station diversity is especially apparent in this data. Figures 5.17 (a) and (b) represent the power received at BS1 and BS2, respectively, from the signal transmitted from A1 on C1. Figures 5.17 (c) and (d) represent the power received at BS1 and BS2, respectively, from the signal transmitted from A2 on C1.

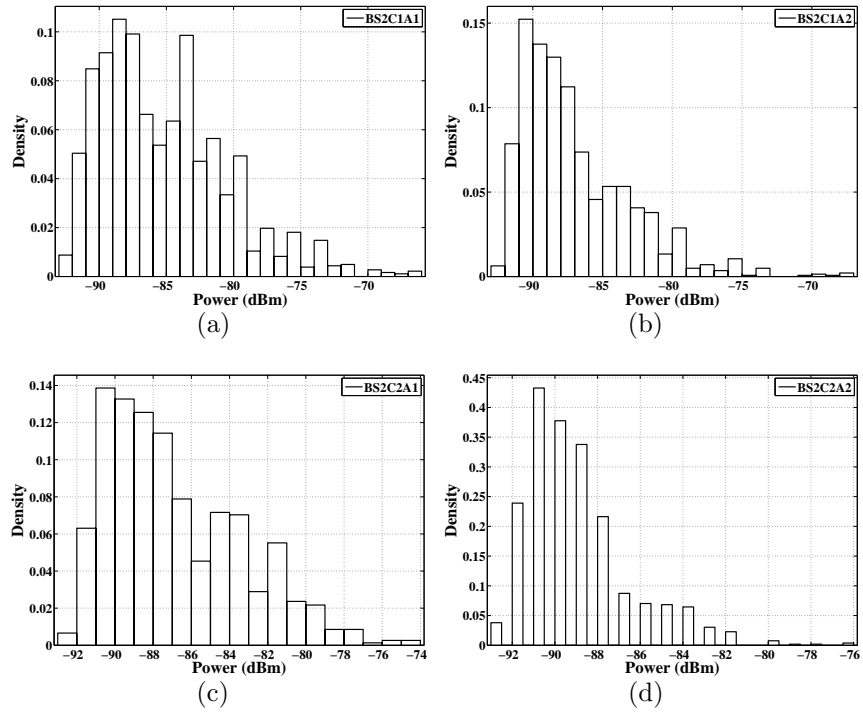


Figure 5.12: Pdfs of power (dBm) at BS2 for (a) A1 on C1 and (b) A2 on C1 and (c) A1 on C2 and (d) A2 on C2. (Smooth curve represents the best-fit normal distribution).

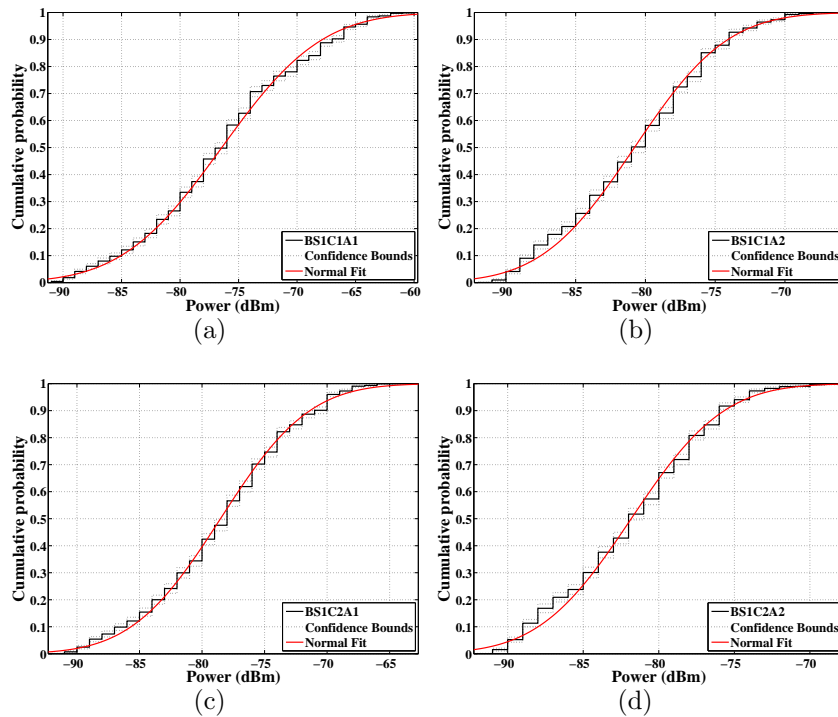


Figure 5.13: Cdfs of power (dBm) at BS1 for (a) A1 on C1 and (b) A2 on C1 and (c) A1 on C2 and (d) A2 on C2. (Smooth curve represents the best-fit normal distribution).

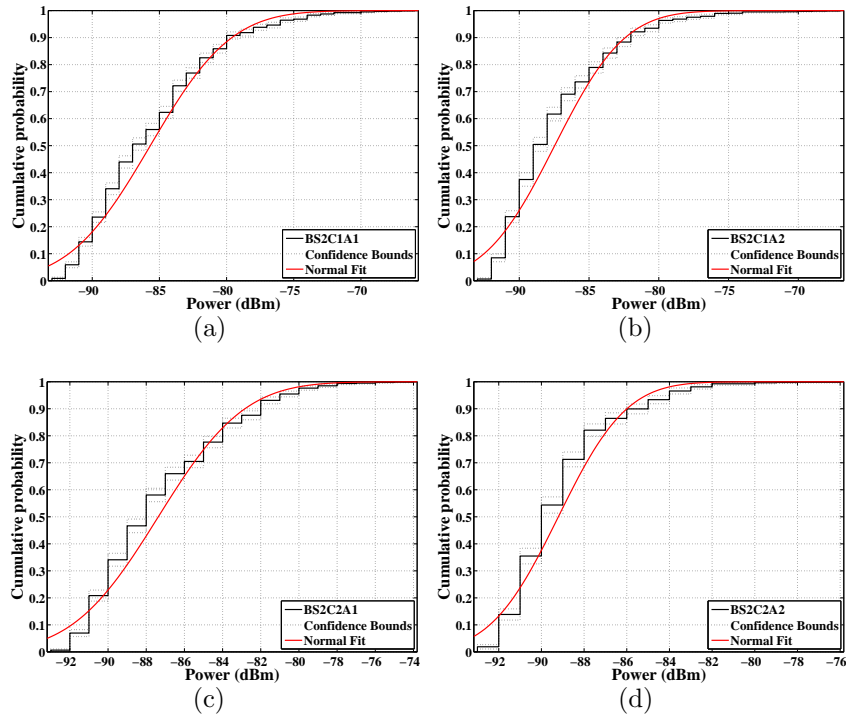


Figure 5.14: Cdfs of power (dBm) at BS2 for (a) A1 on C1 and (b) A2 on C1 and (c) A1 on C2 and (d) A2 on C2. (Smooth curve represents the best-fit normal distribution.)

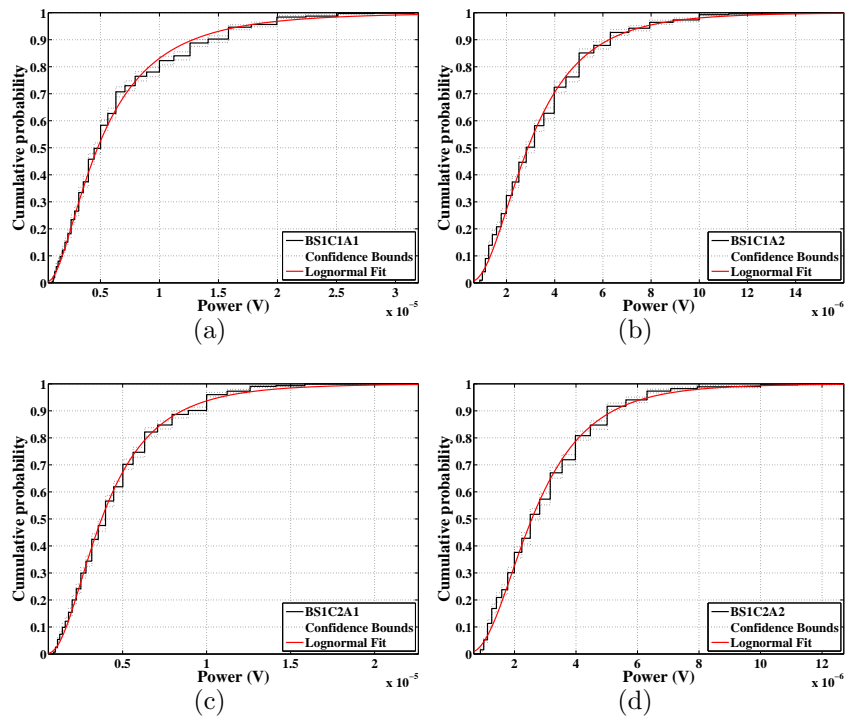


Figure 5.15: CDFs of detected voltage (volts) at BS1 for (a) A1 on C1 and (b) A2 on C1 and (c) A1 on C2 and (d) A2 on C2. (Smooth curve represents the best-fit log-normal distribution.)

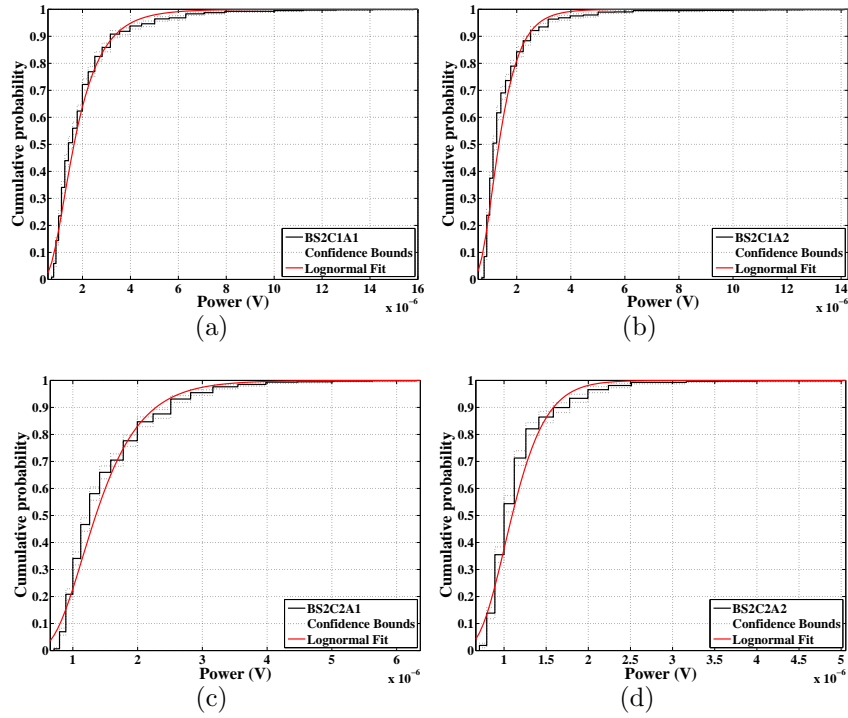


Figure 5.16: CDFs of detected voltage (volts) at BS2 for (a) A1 on C1 and (b) A2 on C1 and (c) A1 on C2 and (d) A2 on C2. (Smooth curve represents the best-fit log-normal distribution.)

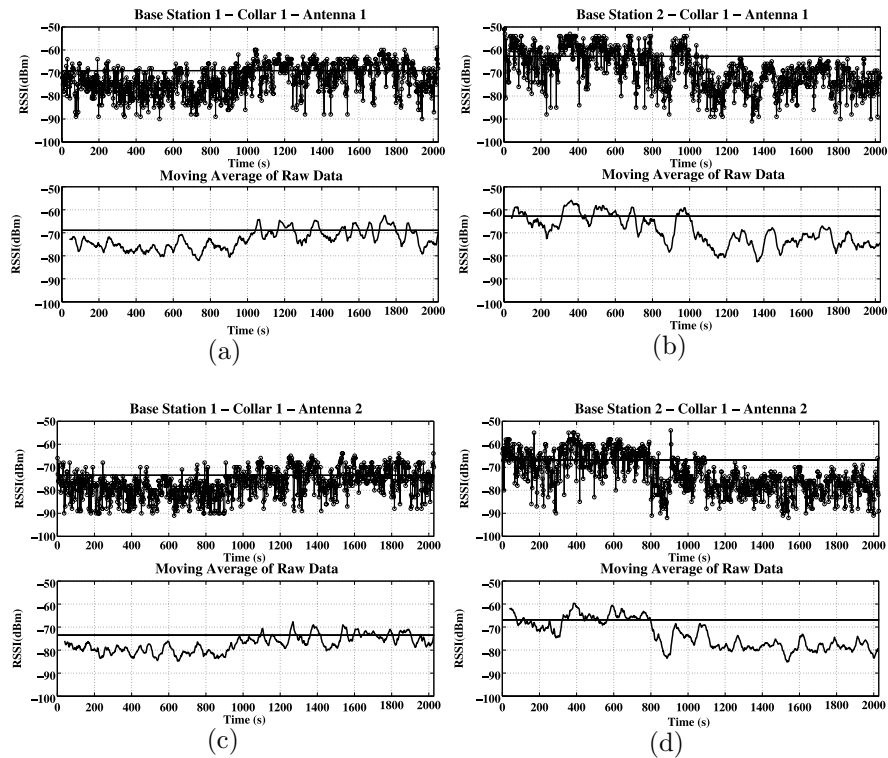


Figure 5.17: Data received from A1 on C1 at (a) BS1 and (b) BS2, and data received from A2 on C1 at (c) BS1 and (d) BS2.

The horizontal lines in Figure 5.17 represent the mean power for each measurement. The correlation coefficients between BS1 and BS2 signals are presented in Table 5.2.

<i>Collar</i>	<i>Antenna</i>	<i>Correlation Coefficient between BS1 and BS2</i>
C1	A1	-0.2646
	A2	-0.3062
C2	A1	-0.0212
	A2	-0.2217

Table 5.2: Correlation coefficient of signals received by different base-stations.

Base-station diversity clearly offers advantage. The consistently small negative correlation is interpreted as being due to essentially zero short-term correlation due to the physically independent multipath propagation structure experienced by the base-stations, and a longer term negative correlation due to the changes in distance between collar and base-stations as the animal moves.

5.3.2.2 Diversity

Two types of diversity gain have been evaluated. Antenna diversity relates to the advantage obtained by having two antennas on one collar. Base-station diversity relates to the advantage obtained by having two base-stations.

5.3.2.2.1 Antenna Diversity

Since there are two collars each with two antennas and two base-stations, the trial contains four independent instances of antenna diversity. These are: (i) diversity collar 1 to BS1, (ii) diversity collar 2 to BS1, (iii) diversity collar 1 to BS2 and (iv) diversity collar 2 to BS2.

Figure 5.18 shows the cdfs corresponding to each of these antenna diversity instances. In each sub-figure, there are four curves: the base-station signal received from A1, the base-station signal received from A2, the mean base-station signal received (calculated using A1 and A2), and the maximum base-station signal received (selected from A1 and A2). The mean base-station signal is adopted as the reference with which to calculate diversity gain. This is because either of the diversity antennas could be adopted as the reference. Taking the mean therefore reduces statistical noise to give a better estimate of expected value. The mean value is calculated from the received powers in dBm. This results in a

final diversity gain (in dB) corresponding to the geometric mean of the diversity gains expressed as ratios obtained using A1 and A2 references.

Figure 5.19 shows the cdfs of the expected diversity gain for (a) C1 to BS1, (b) C2 to BS1, (c) C1 to BS2 and (d) C2 to BS2.

The expected diversity gain (dB) is the difference between the selected diversity signal power (dBm) and the mean signal power (dBm).

The median diversity gain averaged over all four instances is 2.8 dB. The 10% and 90% diversity gain exceedances averaged over all four instances are 7.4 dB and 1.2 dB, respectively.

5.3.2.2.2 Base-station Diversity

There are four instances of base-station diversity gain. These are A1 on C1 to BS1 and BS2, A2 on C1 to BS1 and BS2, A1 on C2 to BS1 and BS2, and A2 on C2 to BS1 and BS2. The base-station diversity cumulative distributions are calculated in an identical way to the antenna diversity cumulative distributions. The results are shown in Figures 5.20 and 5.21.

The median diversity gain averaged over all four instances is 4.8 dB. The 10% and 90% diversity gain exceedances averaged over all four instances are 8.4 dB and 1.1 dB, respectively.

5.3.2.2.3 Overall Diversity

There are four instances of antenna and base-station diversity gain with regards to each collar. These are A1 to BS1, A2 to BS1, A1 to BS2 and A2 to BS2.

Figure 5.22 shows the four curves for each instance, the mean received signal (dBm) and the maximum signal received for the first collar.

Figure 5.23 shows the four curves for each instance, the mean received signal (dBm) and the maximum signal received for the second collar.

The overall diversity gain (i.e. the diversity gain available from the combined antenna diversity and base-station diversity) for the first and second collar is shown in Figure 5.24 and 5.25, respectively.

The median diversity gain averaged over all four instances for the first and second collar is 8.1 dB and 7 dB, respectively. The 10% exceedances averaged over all four instances are 14.3 and 11.2 dB for the first and second collar, respectively. The 90% exceedances are 4.1 dB for the first and 3.5 dB for the second collar respectively.

The mean overall diversity gain is shown in Figure 5.26. This is the mean value

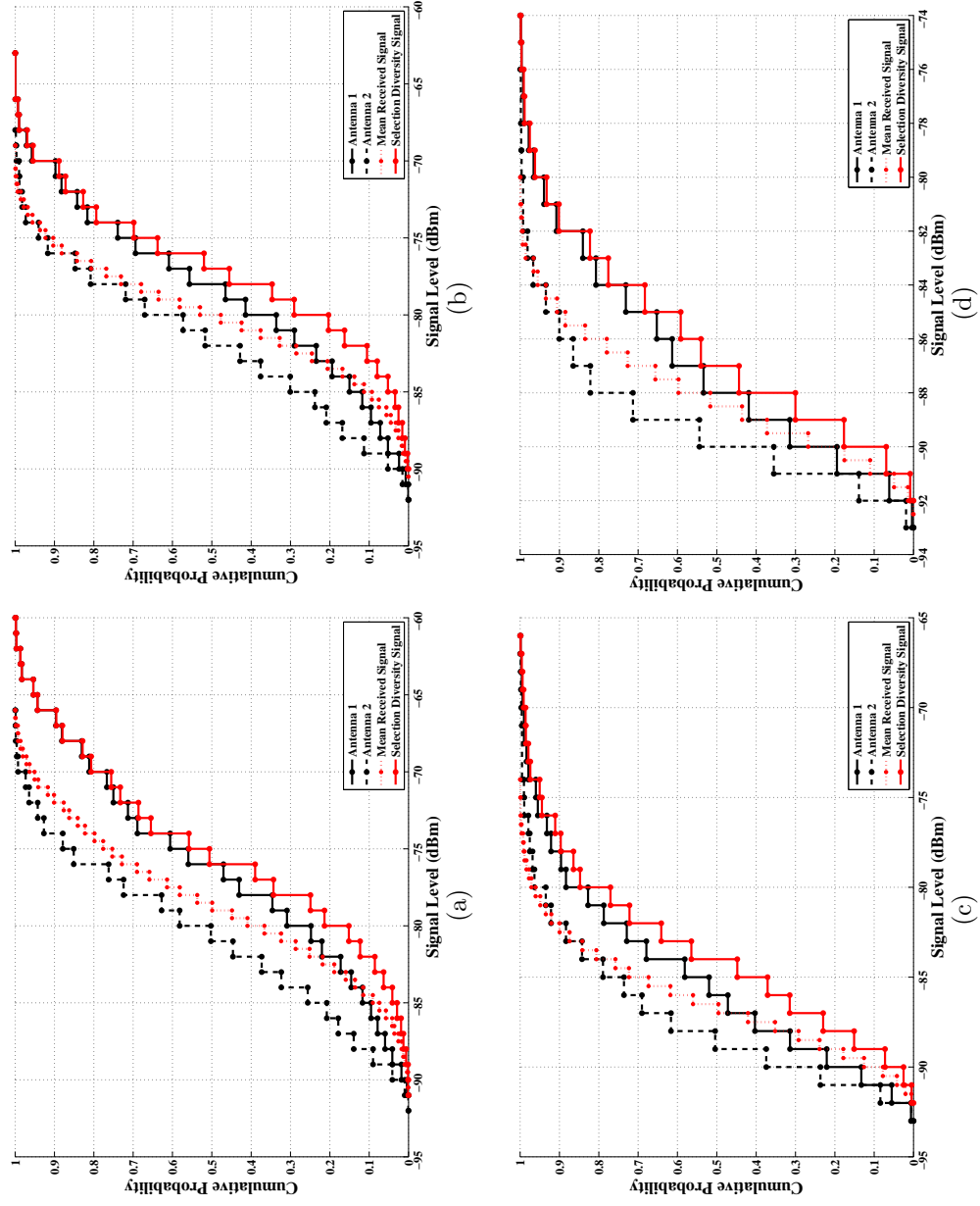


Figure 5.18: Received signal power (dBm) for antenna 1 and antenna 2, mean received signal (dBm), and selection diversity signal (dBm) for (a) C1 to BS1, (b) C2 to BS1, (c) C1 to BS2 and (d) C2 to BS2.

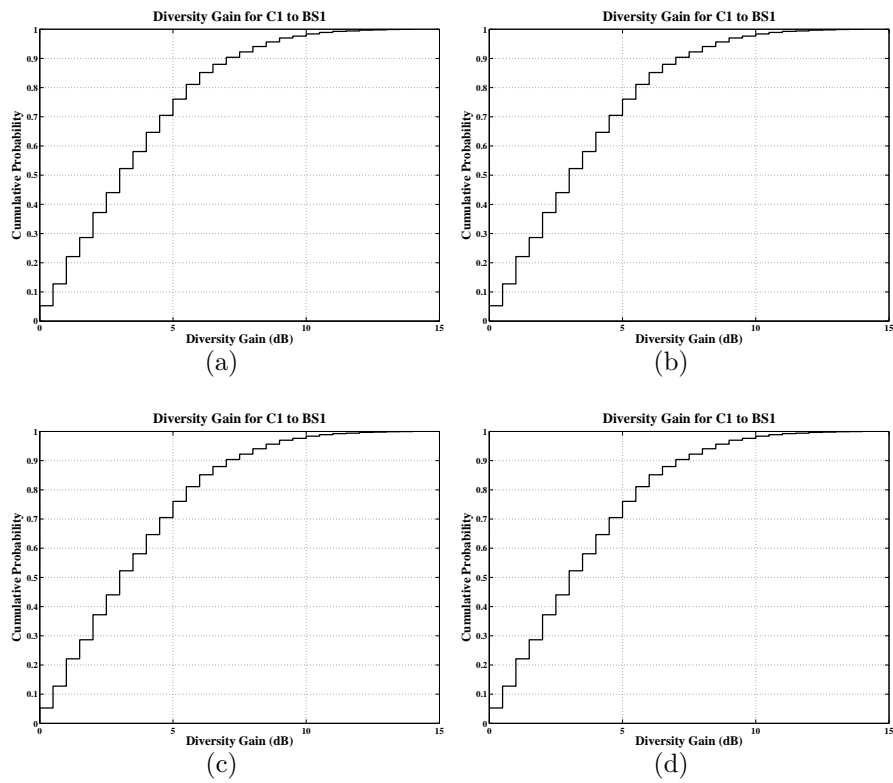


Figure 5.19: Antenna diversity gain for each instance: (a) C1 to BS1, (b) C2 to BS1, (c) C1 to BS2 and (d) C2 to BS2.

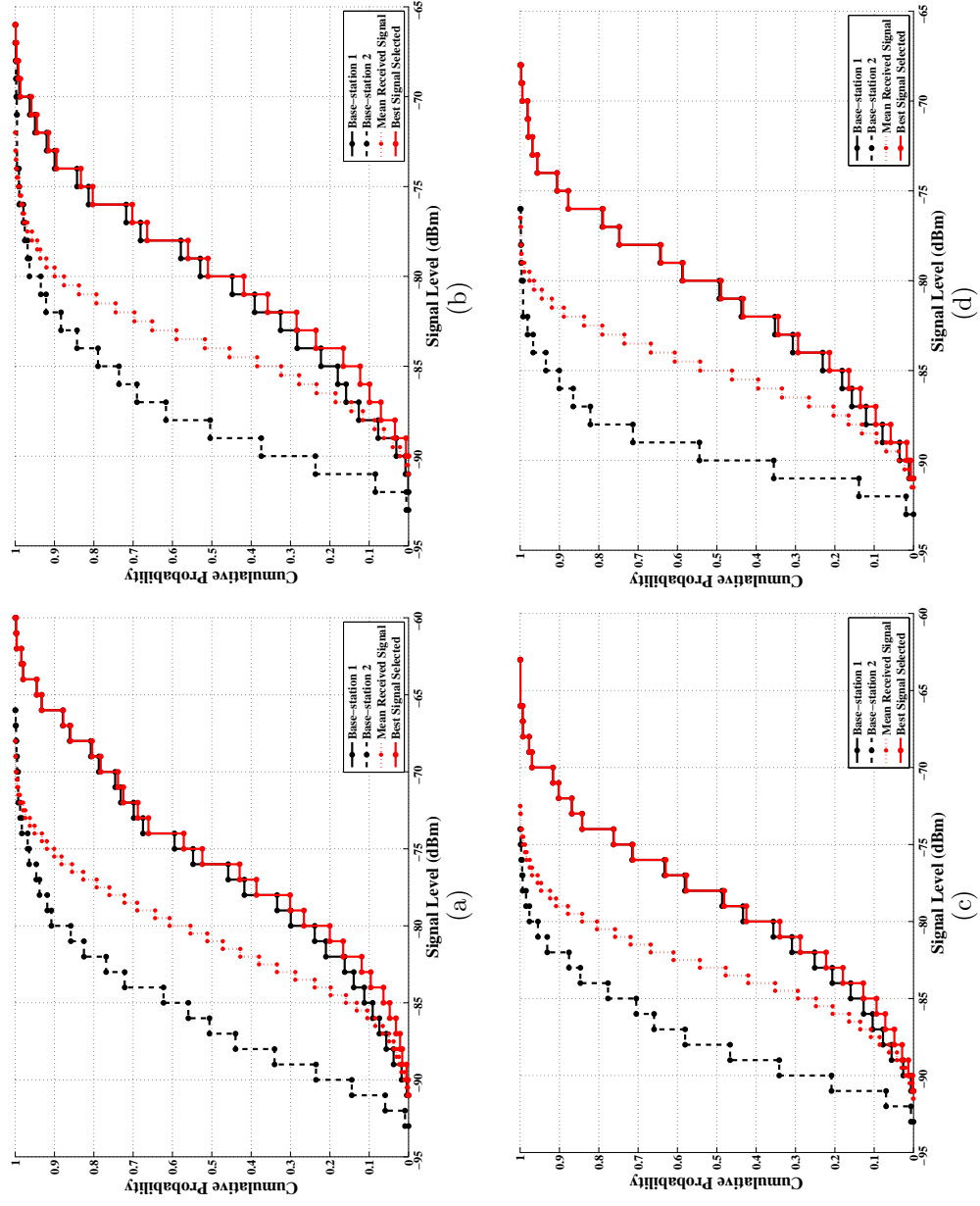


Figure 5.20: Received signal power (dBm) for BS1 and BS2, mean received signal (dBm), and selection diversity signal (dBm) for (a) A1 of C1 to BS1 and BS2, (b) A2 of C1 to BS1 and BS2, (c) A1 of C2 to BS1 and BS2 and (d) A2 of C2 to BS1 and BS2.

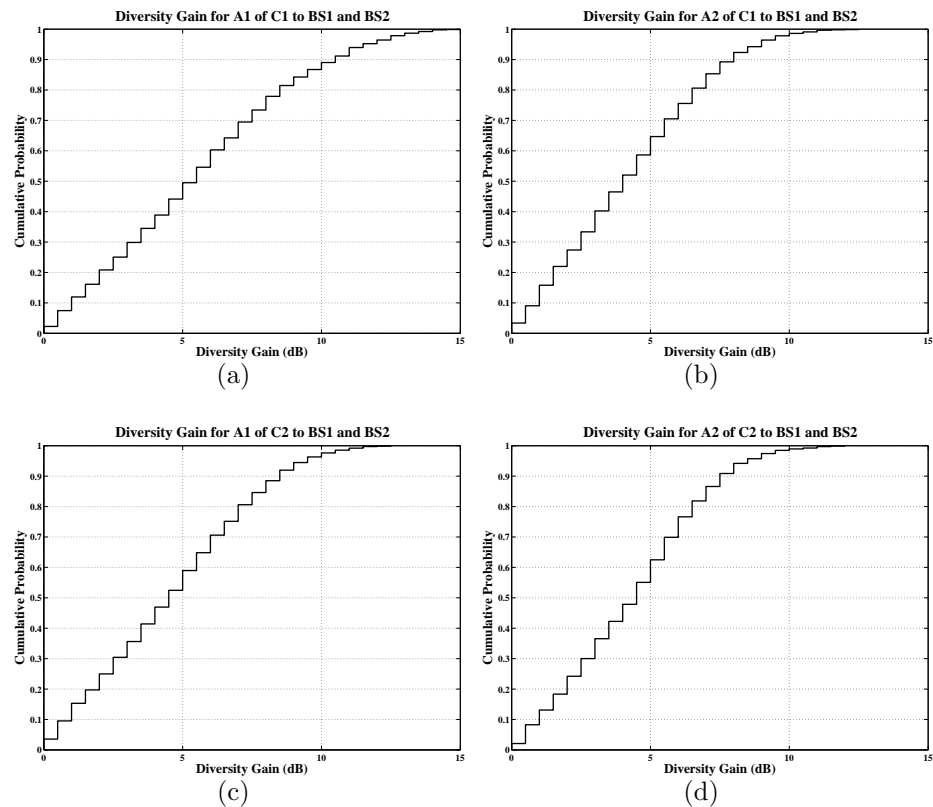


Figure 5.21: Base-station diversity gain for each instance: (a) A1 of C1 to BS1 and BS2, (b) A2 of C1 to BS1 and BS2, (c) A1 of C2 to BS1 and BS2 and (d) A2 of C2 to BS1 and BS2.

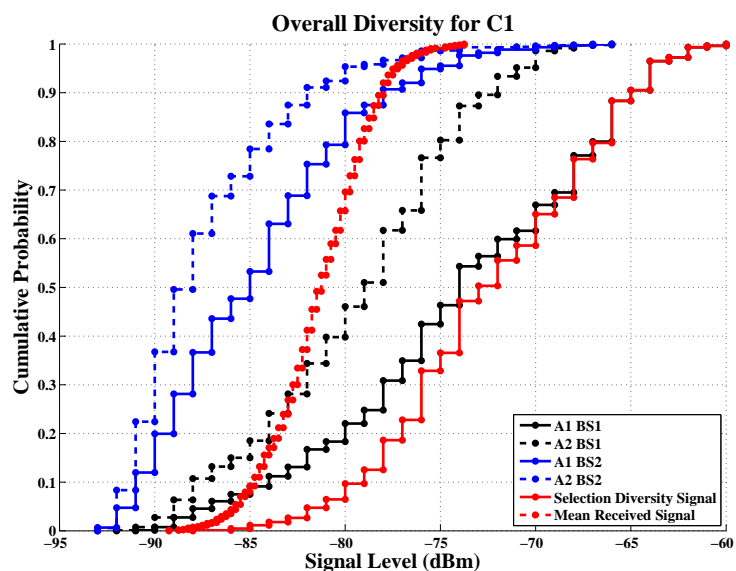


Figure 5.22: Overall selection and mean diversity for the first collar (two antennas and two base-stations).

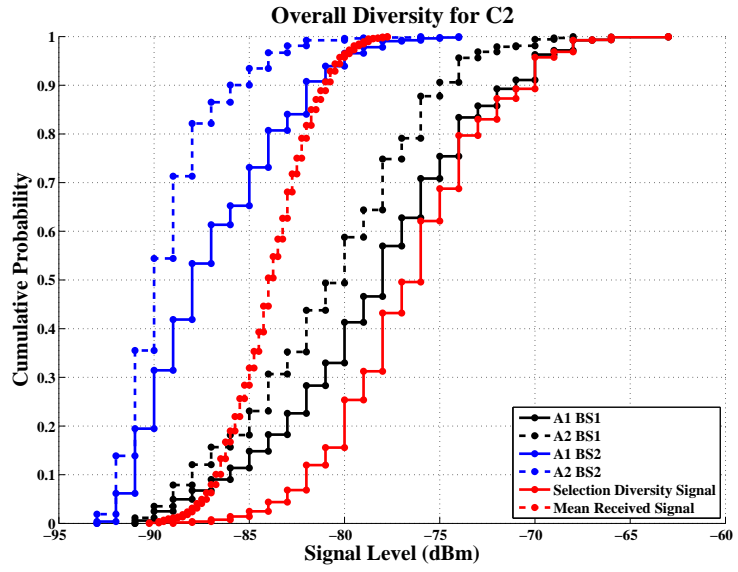


Figure 5.23: Overall selection and mean diversity for the second collar (two antennas and two base-stations).

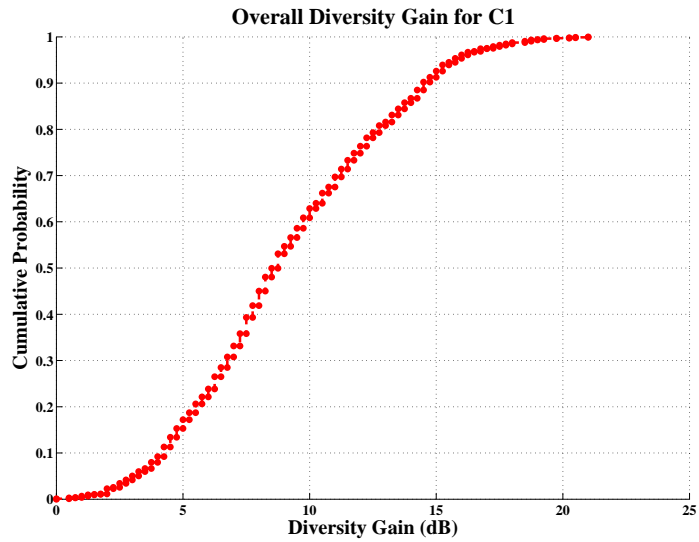


Figure 5.24: Overall antenna and base-station diversity using collar 1.

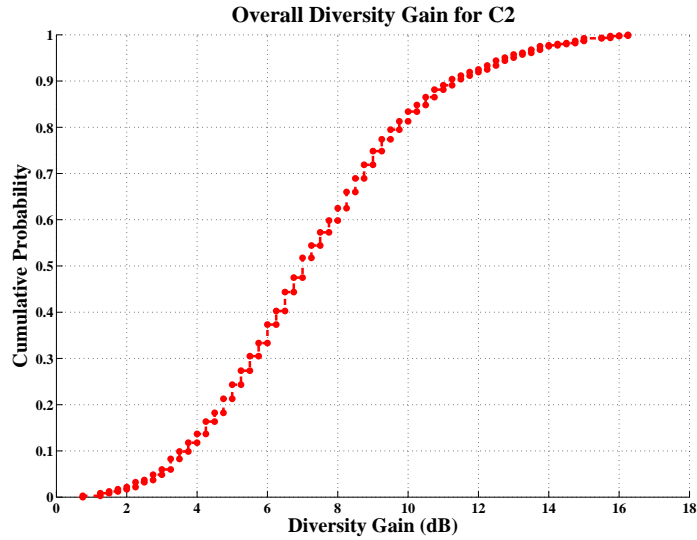


Figure 5.25: Overall antenna and base-station diversity gain collar 2.

calculated from the two individual collar diversity gains. The median overall mean diversity is 7.9 dB. The 10% and 90% diversity gain exceedances are 11.6 dB and 5 dB, respectively.

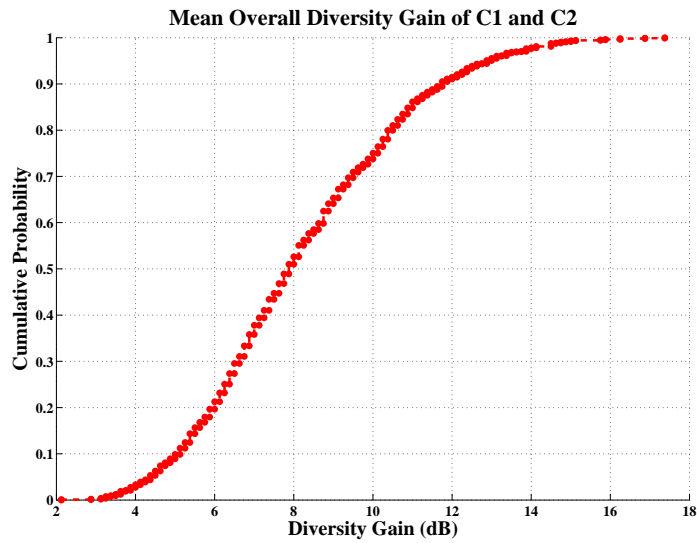


Figure 5.26: Mean overall diversity gain of the two collars.

5.4 Base-station Antenna Height

In an open environment received signal strength may be especially sensitive to the strength of the ground reflected propagation path. In the case of a strong ground reflection receive, and transmit, antenna heights (above ground level) will have a significant impact on received signal strength depending on whether

interference between direct and reflected paths is constructive or destructive. A simple two-path model can be used to describe (and predict) this effect (Section 3.2.1.2).

On a dairy farm the transmit antenna height is approximately 1.2 m (for a standing animal of average height). In principle the height for the base station (h_R) antenna could be optimised (for the expected value range of d providing this range is not too large) to ensure close to constructive interference between direct and ground reflected signals. This optimum height would be calculated by differentiating the factor $|F|$ (Equation 3.34) with respect to h_R and setting the result equal to zero [26].

$$\frac{d|F|}{dh_R} = 2\cos\left(\frac{2\pi h_T h_R}{\lambda d}\right) \frac{2\pi h_T}{\lambda d} = 0 \quad (5.4)$$

where λ , h_T , h_R and d are wavelength, transmitter height, receiver height and distance, respectively. The optimum base-station antenna height is therefore given by:

$$h_{Roptimum} = n \frac{\lambda d}{4h_T} \quad (5.5)$$

where n is an odd integer which would normally be chosen to 1. Choosing a value of $n > 1$ would mean a taller and therefore more expensive antenna tower. The value of n should, therefore, be chosen as to be as small as possible (thereby minimising the cost of the antenna tower) consistent with an acceptable cumulative distribution of fading due to shadowing [26].

Figure 5.27 shows the variation of the received power (in watts) as a function of base-station height for 2.4 GHz at 40 m distance [26].

Measurements of received power have been made at a distance of 40 m and compared with the power predicted by Equation 3.32 in Figure 5.28 [67]. The transmit antenna height was 1.2 m. This is consistent with Equation 5.5.

The terrain, on which the experiments were conducted, was open pasture. The length of the grass was approximately 5 cm.

Figures 5.28 (a) and (b) compare the two-ray model and measurements, assuming reflection from perfect conductor and pasture (with relative permittivity $\epsilon_r = 6$ and conductivity $\sigma = 0.1$). The measurements follow the simple two-ray model closely.

Figure 5.29 shows the received power with respect to the distance for these two cases (perfect conductor and pasture). The transmitter and receiver antenna

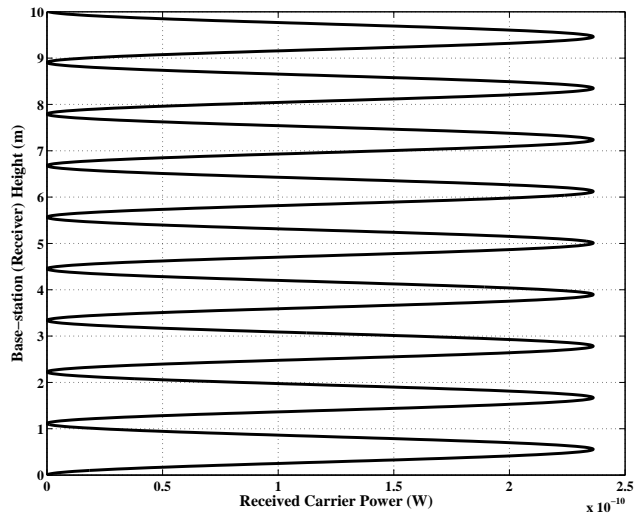


Figure 5.27: Variation of the received power (watts) as a function of base-station height.

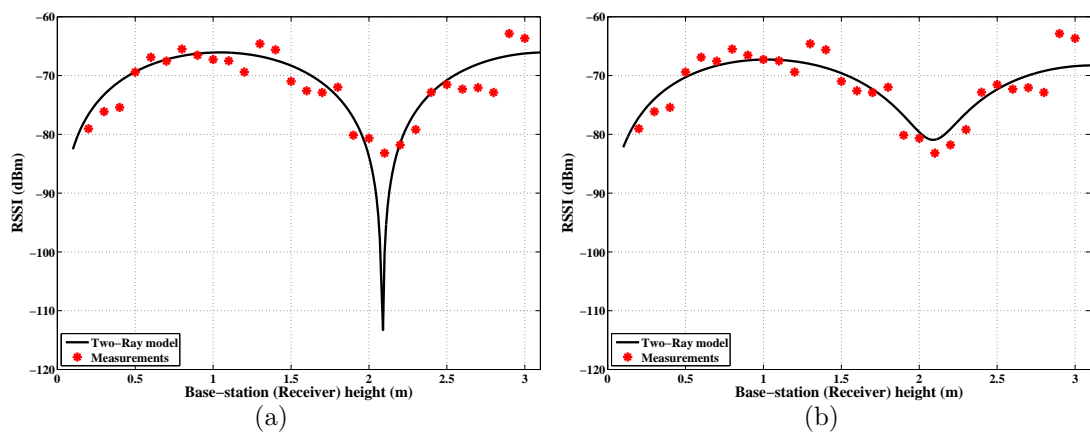


Figure 5.28: Comparison of simulated and measured RSSI as a function of base-station height for (a) perfect conductor and (b) pasture.

height is 1.2 m and 1 m, respectively. The transmission power is 0 dBm.

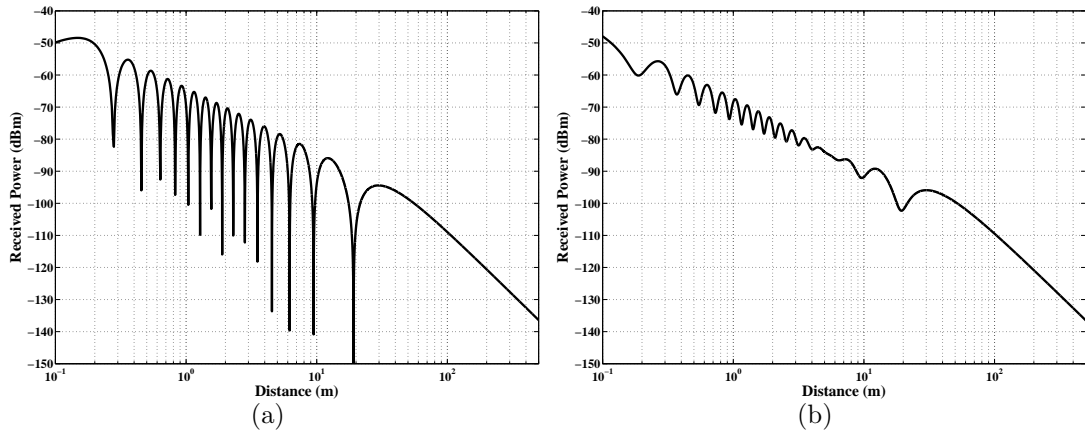


Figure 5.29: Received power (dBm) as a function of distance for (a) perfect conductor and (b) grass.

5.5 Summary and Conclusions

Antenna and base-station diversity has been applied to the wireless monitoring of farm animals. The statistical distributions of received signals and antenna/base-station signal correlations have been summarised. The advantage offered by selection diversity has been evaluated and the practicality of optimising base-station height has been investigated.

The following conclusions are drawn:

- Fluctuation of transmission loss is large (17 - 32 dB).
- The correlation between the signals received by two antennas on the same collar is low.
- The correlation between the signals received by two base-stations with respect to a single antenna on a collar is low (≤ 0.3).
- RSSI (dBm) is approximately normally distributed. (RSSI (volts) is therefore log-normally distributed).
- Antenna diversity and base-station diversity yield significant advantage for animal husbandry applications.
- Median antenna diversity gain (averaged over four experiment instances) is 2.8 dB. The 10% and 90% diversity gain exceedances averaged over the four instances are 7.4 dB and 1.2 dB, respectively.

- Median base-station diversity gain (averaged over four experiment instances) is 4.8 dB. The 10% and 90% diversity gain exceedances averaged over the four instances are 8.4 dB and 1.1 dB, respectively.
- Median diversity gain (averaged over four experiment instances) for two collars are 8.1 dB and 7 dB, respectively. The 10% exceedances averaged over all four instances are 14.3 and 11.2 dB for the first and second collar, respectively. The 90% exceedances are 4.1 dB for the first, and 3.5 dB for the second, collar.
- Median overall mean diversity is 7.9 dB. The 10% and 90% diversity gain exceedances are 11.6 dB and 5 dB, respectively.
- Optimising base-station height can offer significant signal enhancement.

This study shows that base-station diversity is advantageous over antenna diversity. In addition, it is more cost effective because the cost of installing an additional base-station is aggregated over the whole herd, whereas additional RF-switches and antennas in the collar represent an incremental cost.

CHAPTER 6

Wireless Sensor Networks Channels for Smart Building Applications

This chapter deals with measurements for dense sensor networks deployed in the interior of buildings such as those proposed in the project SpeckNet [3].

6.1 Motivation

The need for accurate modelling for very short (<1 m) or short (1 - 50 m) range communications comes, in part, from the increased uptake of WSNs in smart building applications.

Wireless sensor networks are being widely deployed for building monitoring and control resulting in multiple devices deployed over flat surfaces, especially walls and ceilings. (A similar situation exists for autonomous, but information sharing, robots travelling across an open floor space.)

Many indoor measurements of transmission loss exist in the literature (e.g. [68], [69], [70], [71], [72]). These, however, primarily address the transmission loss expected due to propagation through different building materials (brick, stone, wood, plaster, glass etc.), their composite structures (walls, ceilings, floors, doors etc.) and the expected loss and fading statistics for propagation within room interiors (as distinct from propagation over a room's bounding plane surfaces).

6.2 Aims and Objectives

The aim of this study is to develop transmission loss models for short, and very short, wireless links such as those required for indoor sensor networks applications.

Those models are focused on very low antenna heights (0.5 - 20 cm) or, more strictly, displacement from the plane surface over which they are deployed.

The objectives are:

- Short range measurements on a plasterboard interior wall and chipboard furniture surfaces
- Statistical analysis and extraction of empirical models
- Assessment of the significance of surface-wave propagation

6.3 Surface Waves

Electromagnetic waves may be classified as sky-waves, space-waves and surface-waves (e.g. [73], [74]). Surface-waves are sometimes referred to as ground-waves (although this term has also been used to describe the combination of direct and surface-reflected space waves.) Sky-waves are reflected from the ionosphere (at HF frequencies and below) and can be used for long range communication. Here we are concerned with very short range communication, such as may be encountered in sensor networks, at microwave frequencies where only space and surface-waves are plausible.

Space waves travel, essentially unbound, via the direct LOS path, reflected paths and (sometimes) refracted paths. Surface waves are (at least loosely) bound to the surface over which they propagate. There are various stages of transition between space and surface waves, and in practical wireless communication problems a clear division between the two is often difficult to draw [75].

The presence of a surface in close proximity to a transmitting or receiving antenna potentially modifies both wave generation and propagation mechanisms. It has been suggested [75] that in most situations surface-wave effects can be neglected if both transmitting and receiving antennas are elevated more than one wavelength above the surface. Conversely, and again in [75], it has been shown that surface waves can be significant if VHF antennas are located within less than one wavelength of the surface. Much existing work on surface wave propagation (e.g. [75], [76]) relates to long-range and relatively low-frequency communications. It is asserted in [73], for example, that surface wave effects are negligible for frequencies above 100 MHz and can be ignored for both horizontal and vertical polarisations provided accuracies of the order of 1 dB are acceptable.

Transceiver nodes in future, densely-packed, wireless sensor networks (e.g. Specknets [3]) will be small and are expected to be deployed close to (effectively

on) the ground or other surfaces (e.g. walls, floors, ceilings etc.). With node elevation above the surface measured in centimetres, or even millimetres, it is possible that surface-wave propagation will be significant.

In addition to link geometry (antenna heights and link length) and surface characteristics (permittivity, conductivity and roughness), polarisation might also affect the proportion of power carried by a surface-wave.

A simple, but fundamental, model [73] of propagation that accounts for the LOS space-wave, the surface reflected space-wave and the surface-wave is given by:

$$l_P = \left| \frac{e^{-jkd}}{2kd} [F_d + F_r [\Gamma + (1 - \Gamma)A] e^{-j\phi} + \dots] \right|^2 \quad (6.1)$$

Here l_P is the ratio of received to transmitted power between unity gain antennas, d is the path length from transmitter to receiver, k is wave number, F_d represents the direct (LOS) field-strength and F_r the reflected wave field-strength (which includes amplitude correction for the additional distance travelled). Γ is the (frequency-dependent) surface reflection coefficient which depends on incident wave polarisation and surface permittivity and conductivity. ϕ is the additional phase delay for the reflected ray.

The remaining unspecified terms (...) in Equation 6.1 represent the difference between a full electromagnetic field solution and this two-ray approximation which includes induction fields.

A is the (complex) surface-wave factor (with magnitude less than unity) given by [73]:

$$A = \frac{-1}{1 + jkd(jkd(\Gamma + \sin(\theta)))^2} \quad (6.2)$$

where θ is the reflected ray incidence angle determined by node height and separation.

The surface-wave factor depends on incident wave polarisation, frequency and surface properties. Figure 6.1 illustrates its dependence on several of these parameters for propagation over chipboard, with $\epsilon_r = 3.55$ and $\sigma = 0.02$ [77].

Surface-waves are significant for devices operating close to a surface. For small grazing angles the reflection coefficient Γ is approximately -1 and the LOS and reflected waves approximately cancel leaving the surface-wave to dominate. $|A|$ decreases with increasing node separation and antenna height (the incidence angle and the reflection coefficient therefore changes with antenna height). The

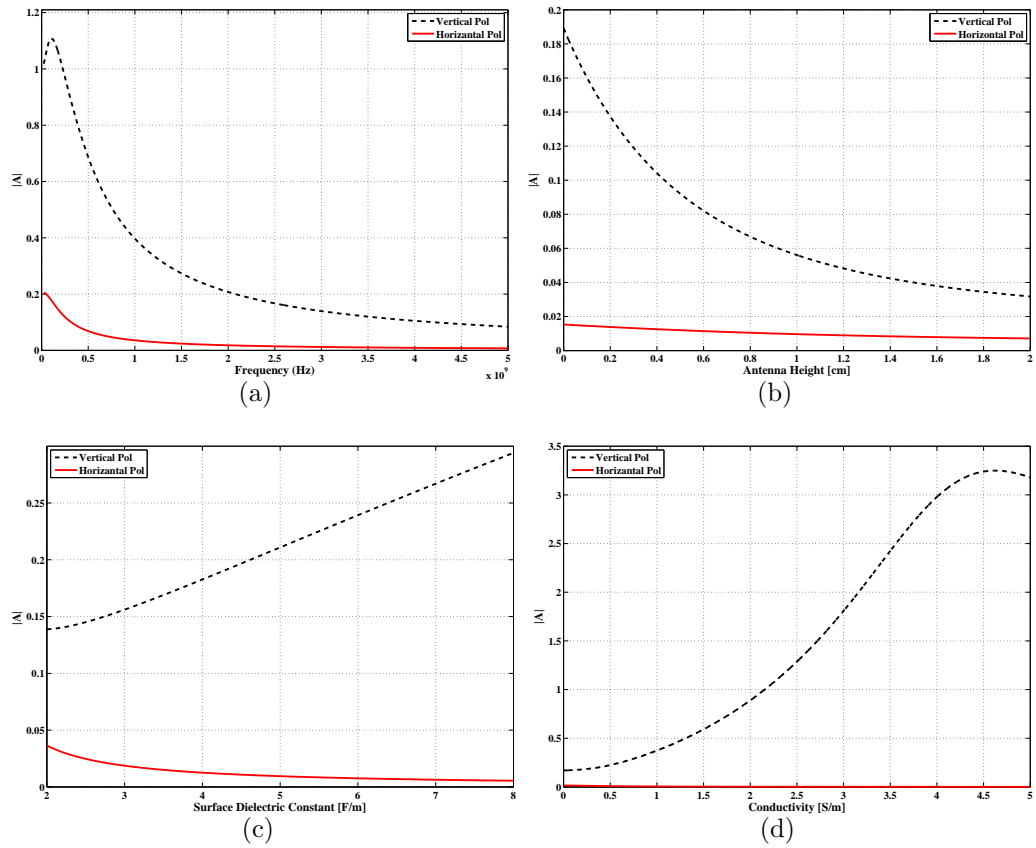


Figure 6.1: Variation of surface-wave factor magnitude ($\epsilon_r = 3.55$, $\sigma = 0.02$ S/m and $f = 2.45$ GHz).

following observations are made with respect to Figures 6.1 (a)-(d).

- $|A|$ decreases with increasing frequency (Figure 6.1 (a)).
- $|A|$ is larger for vertical polarisation than for horizontal polarisation (Figure 6.1 (a)).
- $|A|$ decreases with antenna height for vertical polarisation and is small, and approximately constant, for horizontal polarisation (Figure 6.1 (b)).
- $|A|$ increases with increasing surface permittivity for vertical polarisation and is small, and approximately constant, for horizontal polarisation (Figure 6.1 (c)).
- $|A|$ increases with increasing surface conductivity for vertical polarisation and is small, and approximately constant, for horizontal polarisation (Figure 6.1 (d)).

6.4 Wall Measurements

Measurements of transmission loss have been made at 2.445 GHz using a pair of ceramic patch antennas and a pair of linearly polarised rectaxial antennas [78], Figure 6.2. Partial pattern information for these antennas is available in [64] and [51]. The transmitted signal was an unmodulated carrier.

The return losses of the rectaxial and ceramic patch antennas were measured using a network analyser and found to be better than -15 dB between 2.40 and 2.50 GHz [51] and better than -6 dB between 2.4 and 2.485 GHz respectively [64]. Their respective gains are 2.2 dBi and 2 dBi.

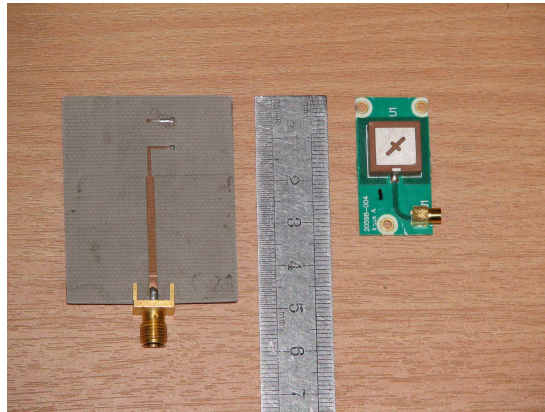


Figure 6.2: Rectaxial antenna (left) and ceramic patch antenna (right).

6.4. WALL MEASUREMENTS

All the measurements were made with the antennas flat against the wall surface.

Initially, the linearly polarised rectaxial antennas were oriented to radiate vertically ($\pm 2^\circ$). (Note that vertical here is interpreted in the conventional sense, i.e. defined with respect to the gravity; it does not imply perpendicular to the surface over which propagation is taking place.) The transmit and receive antennas were initially located 220 cm (17.93 wavelengths) from the floor and 30 cm (2.445 wavelengths) from the ceiling, Figure 6.3 (a). The distance between transmit and receive antennas (i.e. the path length) was initially set to 100 cm and the antennas were placed close to the wall (wall offset nominally 0 mm). Path length was then increased in steps of 25 cm up to a maximum distance of 250 cm (20 wavelengths) and received power recorded at each step.

The wall offset was then increased to 10 mm in steps of 5 mm and the received power was recorded for each pair of antenna offset and separation distance. Path length, antenna heights and power were measured with accuracies better than ± 1 mm, ± 0.5 mm and ± 1 nW, respectively.

A second series of measurements was repeated with the antenna height increased to 2.50 m (i.e. just at the intersection of the wall and ceiling) and the received power was recorded for each antenna-offset and antenna-separation pairs (Figure 6.3 (b)).

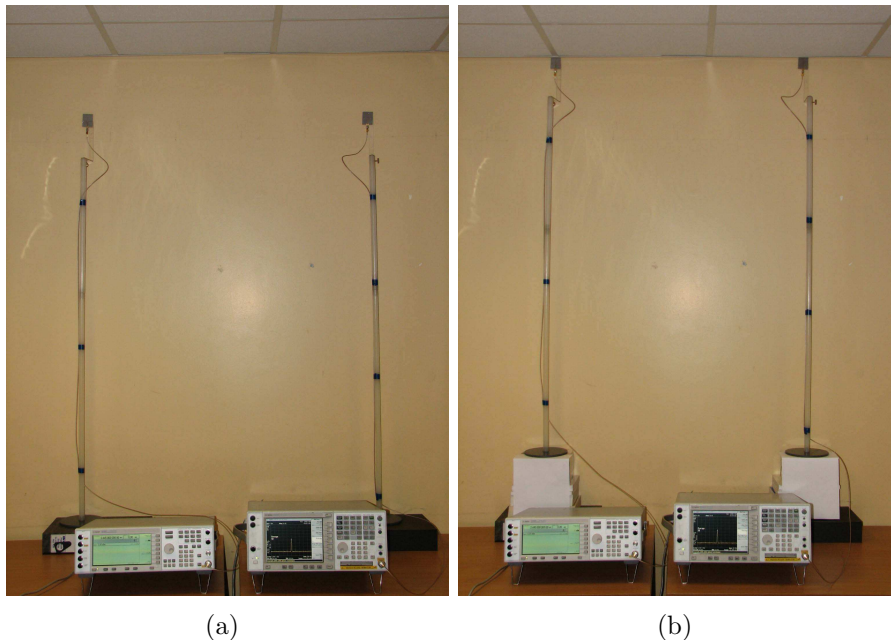


Figure 6.3: Vertically polarised rectaxial antennas with (a) 30 cm reduced height and (b) 0 cm reduced height (in contact with the ceiling).

6.4. WALL MEASUREMENTS

The transmit and receive rectaxial antennas were also oriented horizontally $\pm 2^\circ$ to radiate a horizontally polarised wave. The received power was recorded for each antenna reduced height, wall-offset and separation distance.

The measurement procedure was repeated using the pair of identical microstrip patch antennas [64] with the longer aperture dimension oriented horizontally $\pm 2^\circ$, Figure 6.4.

In all measurements the plane surface of the antennas was parallel to the wall surface.

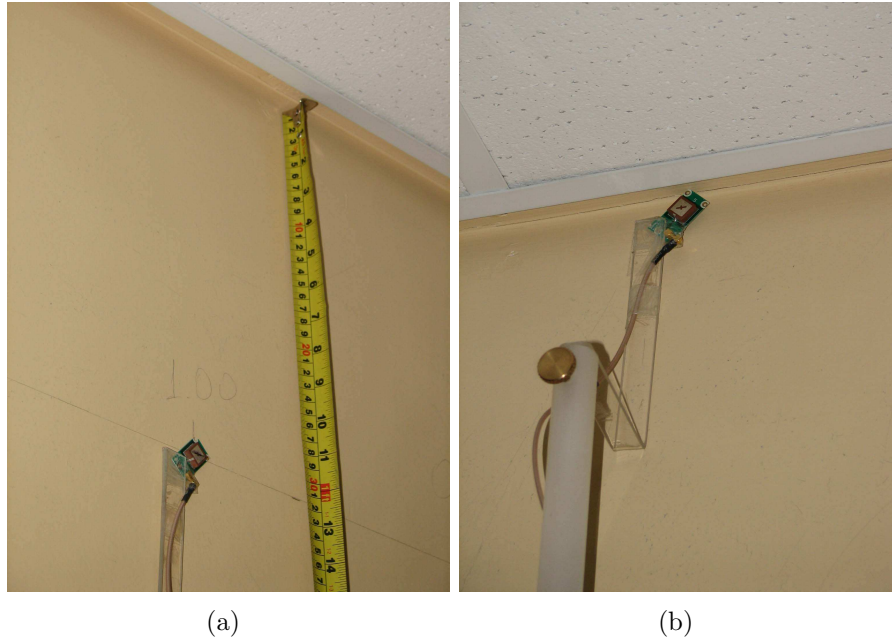


Figure 6.4: Microstrip patch antenna located with a reduced height of (a) 30 cm and (b) 0 cm (in contact with the ceiling).

In total, therefore, six sets of measurements have been made, four sets for the rectaxial antennas and two for the patch antennas.

An Agilent E4438C ESG vector signal generator was used as a source to generate a 2.445 GHz unmodulated 0 dBm carrier. Received power was measured using an Agilent E4440A spectrum analyser.

Significant fluctuation of the received power was observed and 50 independent measurements were therefore time-averaged. Power fluctuation was thereby reduced to less than ± 1 nW. The pair of antennas was then relocated on the wall but retaining the same offset, reduced height and node separation and a further measurement (including time averaging) was taken. This process was repeated several times. The final estimates of received power (and thus transmission loss) were then calculated by averaging these spatially separated measurements.

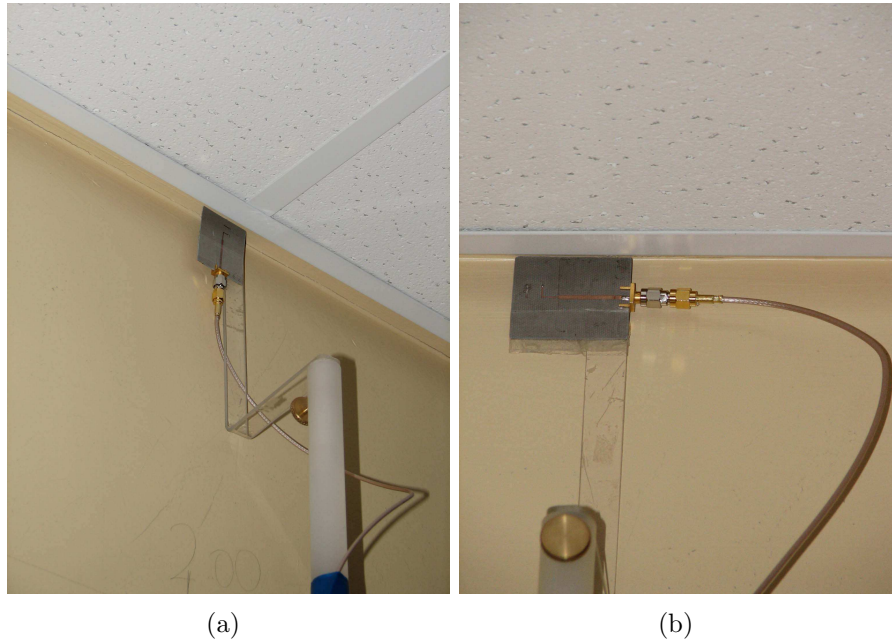


Figure 6.5: Rectaxial antennas with 0 cm reduced height (in contact with the ceiling) oriented (a) vertically and (b) horizontally.

The total measurement loss (including that due to cables, connectors and adaptors) was 9.3 dB. This loss has been removed during data analysis.

6.4.1 Offset and Reduced Height

The three curves in each plot of Figure 6.6 correspond to antenna-wall offsets of 0 mm, 5 mm and 10 mm. No significant dependence of received power on antenna-wall offset is apparent with the exception of the results for the microstrip antenna with a reduced height of 30 cm. In this case the difference reaches a maximum of 5 dB for a link length of 1.25 m.

In the case of the vertically polarised rectaxial antennas the loss is lower for a reduced height of 30 cm compared to a reduced height of 0 cm. (In fact, not only are the signal levels lower for each particular value of separation, but the gradients are higher.)

When the rectaxial antennas are horizontally polarised reduced height has no significant impact on transmission loss.

In the case of the patch antennas transmission loss is lower for a reduced height of 0 cm than for a reduced height of 30 cm. This is especially so for node separations less than 2 m.

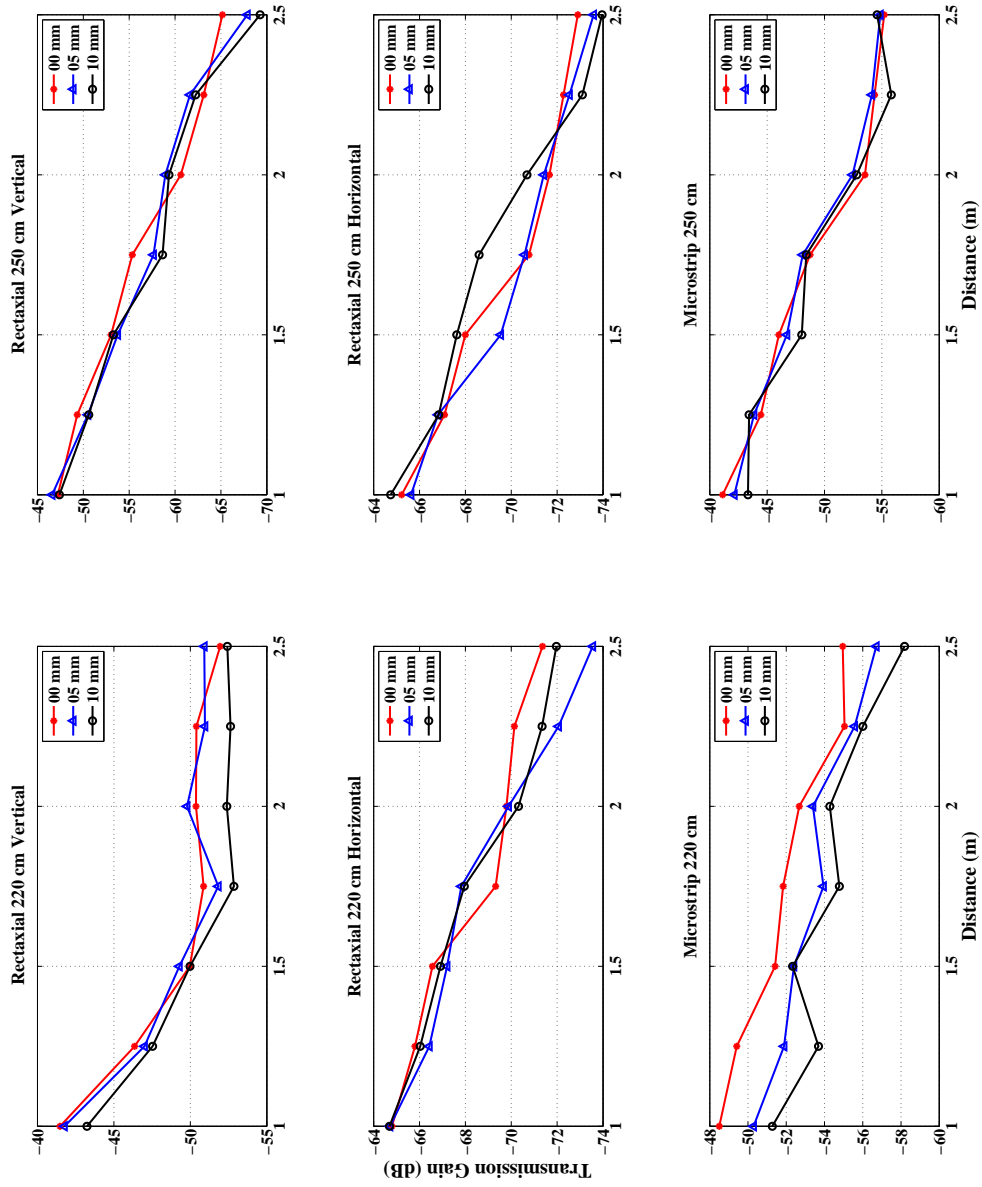


Figure 6.6: Transmission gain (dB) versus node separation (Curves correspond to offsets of 0, 5 and 10 mm)

6.4.2 Transmission Loss

95% confidence intervals for mean transmission power have been calculated using the three values of offset. These confidence limits are shown in Figure 6.7.

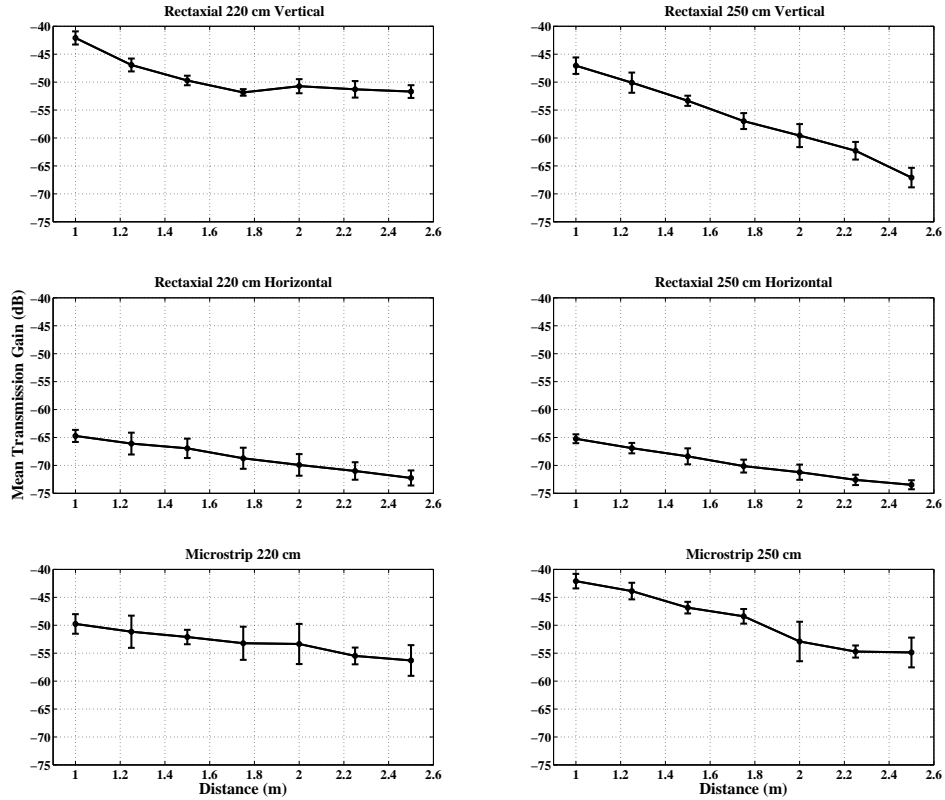


Figure 6.7: Mean transmission gain with 95% confidence intervals.

Figure 6.8 shows the standard deviation of the data for each set of measurements (subplot) and for each individual offset (bar).

The mean standard deviation of all the data for each set of measurements is represented by the horizontal line in each bar chart and is between 2 dB and 5.5 dB.

6.4.3 Gradients and Path Loss Index

The best-fit straight lines for the transmission loss data have been calculated using a minimum mean square error criterion [79] [23], Figure 6.9. The path-loss indices are summarised in Figure 6.10. They appear to be consistent across (i.e. largely independent of) antenna-wall offsets.

The path-loss index for the patch antennas with 0 cm reduced height is between 2.9 and 3.6 and for a 30 cm reduced height is between 1.4 and 1.6 representing, at least approximately, an inverse cube law and an inverse 3/2 law

6.4. WALL MEASUREMENTS

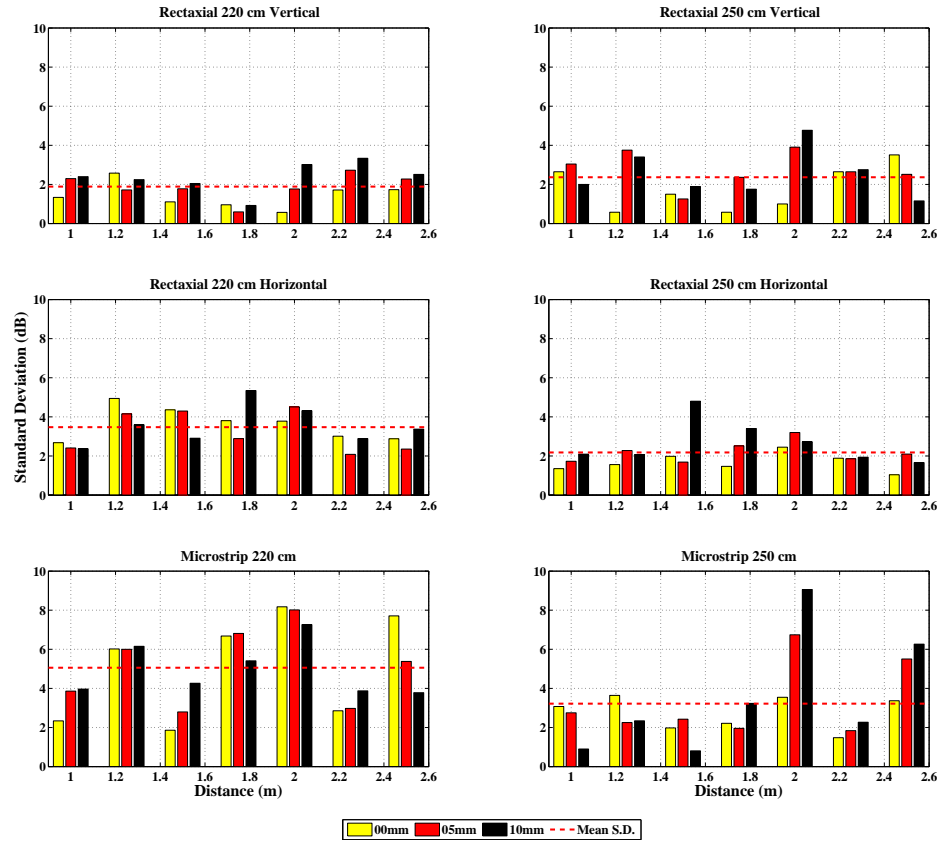


Figure 6.8: Measurement standard deviations.

respectively. This is counter-intuitive since it might be expected that close to the intersection between wall and ceiling (i.e. for a reduced height of 0 cm) spreading loss would be reduced over that for a larger reduced height by the guiding effect of the two perpendicular surfaces.

The path-loss index for the vertically polarised rectaxial antenna with 0 cm reduced height is between 4.2 and 4.6. This is close to the classical value for two-ray propagation over a plane reflecting surface. This may be coincidence, however, since the environment comprises two perpendicular plane surfaces (i.e. the wall and ceiling).

The path-loss index for the horizontally polarised rectaxial antenna lies between 2.0 and 2.1 for 0 cm reduced height and between 1.6 and 1.9 for 30 cm reduced height. Perversely, a free-space like path index appears to apply when the antennas are closest to the ceiling.

6.4. WALL MEASUREMENTS

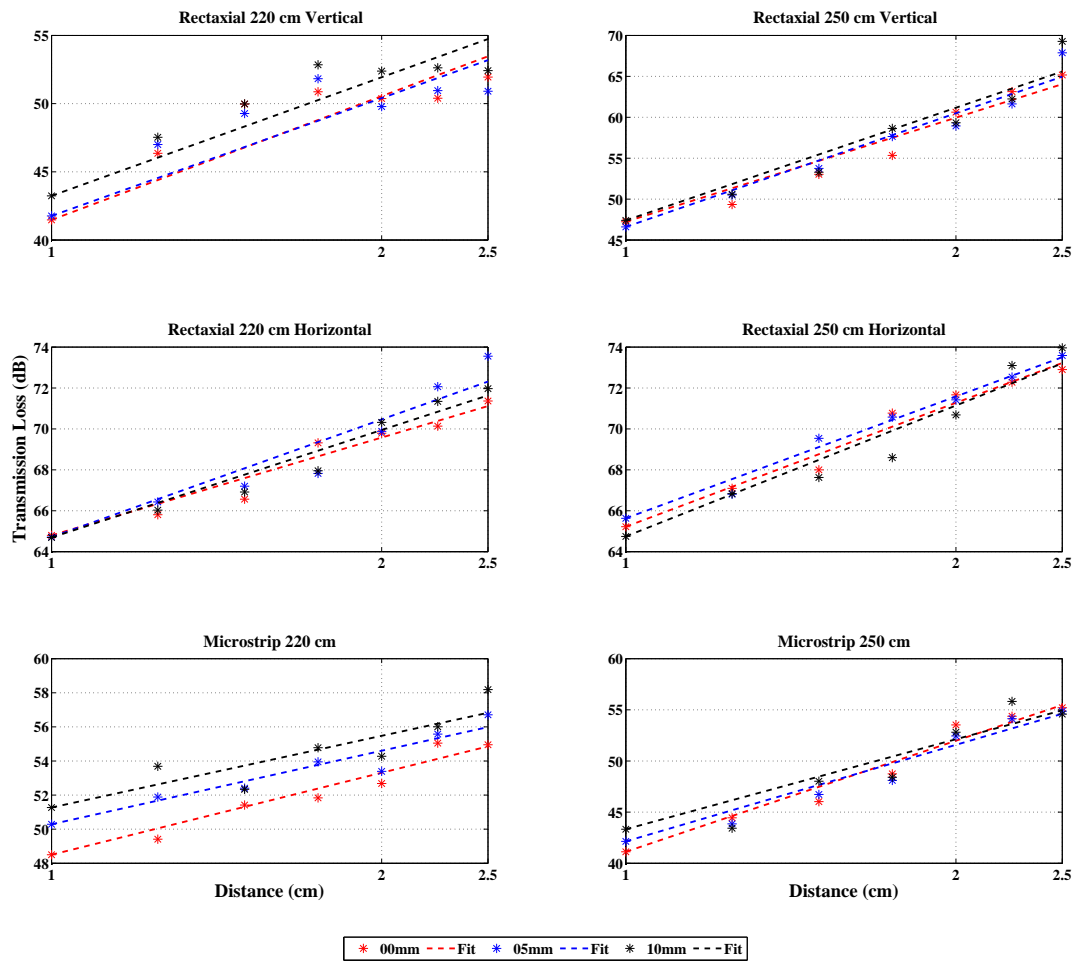


Figure 6.9: Linear regression of transmission loss data.

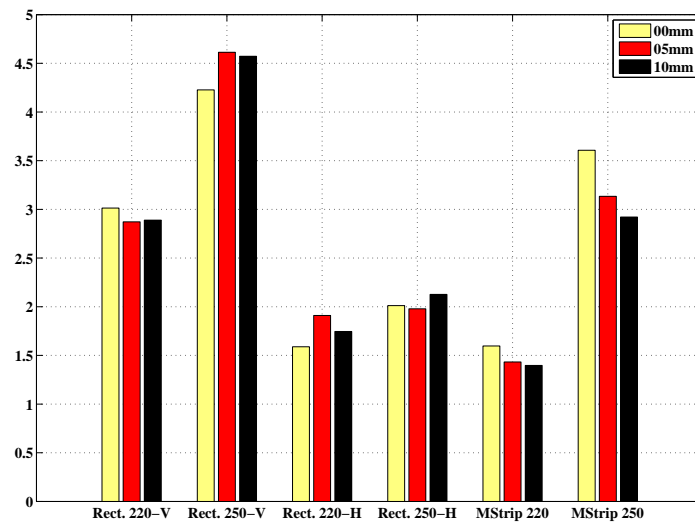


Figure 6.10: Path loss indices for each individual measurement.

6.5 Chipboard Measurements for Very Short Distance

A characterisation of the short range (< 100 cm) narrowband wireless channel between a pair of antennas with millimetric clearance over a plane surface is presented in this section, appropriate to a dense network of wireless transceivers operating in the 2.4 GHz ISM-band. Transmission loss measurements have been made in vertical and horizontal polarisations using rectaxial antennas for a range of antenna heights and separation distances for an initial assessment of the impact of surface waves [80]. Interpretation of the results suggests that surface wave propagation may be significant for very short WSN links.

6.5.1 Variations with Height and Distance

The effect of antenna height has been investigated using a pair of identical rectaxial antennas [51]. An Agilent E4438C ESG vector signal generator was used as a source to generate a 2.45 GHz unmodulated carrier with a power of 0 dBm. Received power was measured using an Agilent E4440A spectrum analyser. The measurements were carried on a plane, horizontal, surface (Figure 6.11) of laminated chipboard (thickness, length and width 2.5 cm, 180 cm and 160 cm respectively) with relative permittivity $\epsilon_r = 3.55$ and conductivity $\sigma = 0.02$ [77].

The linearly polarised antennas were oriented to radiate vertically $\pm 2^\circ$, Figure 6.12. The largest dimension of the radiating element is 13 mm and the antenna's nominal phase-centre is assumed to be located at this element's mid point. The height (h) of the antenna above the surface is defined as that of the nominal phase-centre, Figure 4.6. The distance between transmit and receive antennas was set to 10 cm with the antenna fed from above.

The antenna heights were increased from 0.65 cm to 5.65 cm (since the antenna nominal phase centre is 6.5 mm from the end as in Figure 4.6), in increments of 1 cm. (The heights of both transmit and receive antennas were the same for all measurements.) Antenna separation was increased from 10 cm to 50 cm in increments of 10 cm. Received power was recorded for each distance-height pair. For each distance-height combination ten measurements were recorded, the test-bench being displaced by at least one wave-length between measurements allowing averaging to reduce random errors. (Displacement allows any weak spatial fading due to multipath propagation to be treated as a component of random error.)

Additional measurements were carried out for the same range of antenna

6.5. CHIPBOARD MEASUREMENTS FOR VERY SHORT DISTANCE

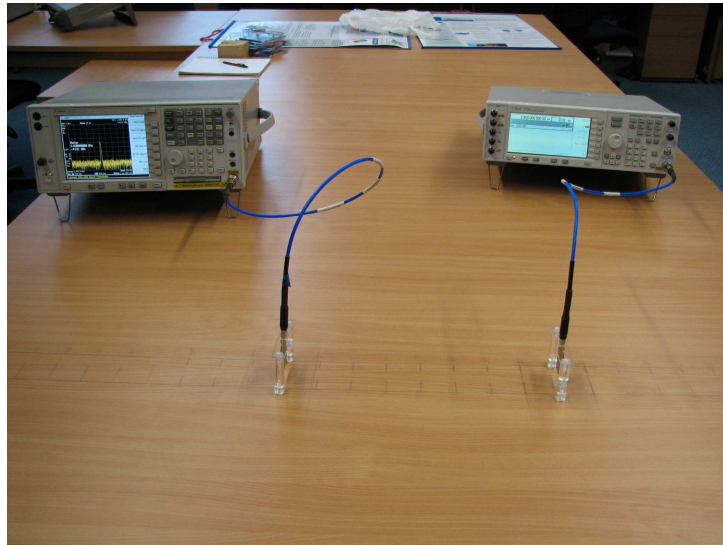


Figure 6.11: Measurement setup.

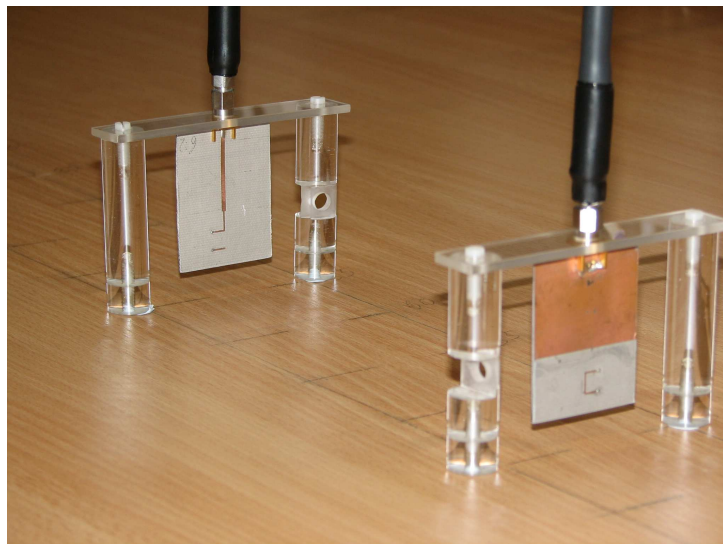


Figure 6.12: Vertically polarised measurements.

heights with transmit-receive antenna spacing of 75 cm and 100 cm. Path length, antenna height and transmission gain were measured with accuracies better than ± 1 mm, ± 0.5 mm and ± 1 dBm, respectively.

The above procedure was then repeated with antennas oriented to radiate horizontally ($\pm 2^\circ$), Figure 6.13.

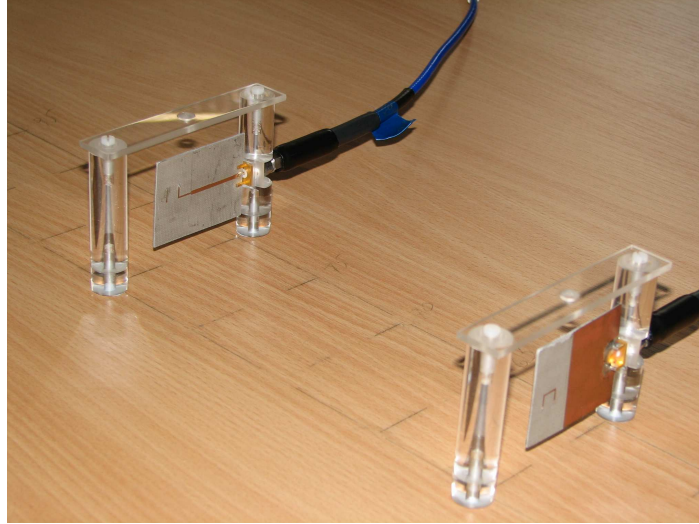


Figure 6.13: Horizontally polarised measurements.

6.5.1.1 Vertical Polarisation

Transmission gain measured (after averaging) for vertical polarisation as a function of antenna separation and antenna height is shown in Figure 6.14.

The measurements have been divided into two sets. Set V1 contains measurements satisfying $h \leq 2.65$ cm. Set V2 contains measurements satisfying $h \geq 3.65$ cm. The data for each set are shown in Figure 6.14.

The following observations are made with respect to data set V1.

- Transmission gain decreases with increasing antenna height, see also Figure 6.15. (A decrease in antenna height from 2.65 cm to 1.65 cm yields a power increase, averaged over all antenna separations, of 2.02 dB. A decrease in height from 1.65 cm to 0.65 cm yields a further improvement of 2.63 dB.) This might be explained by a dominant surface-wave component of coupling between the antennas which gets weaker as the antennas move farther from the surface. This interpretation is consistent with Figure 6.1 (b).
- Mean specific transmission loss is 14.5 dB/decade between 10 cm and 100 cm. This suggests that for data set V1, the measured data follows, at least approximately, a free space law, i.e. 20 dB/decade, see Figure 6.16.

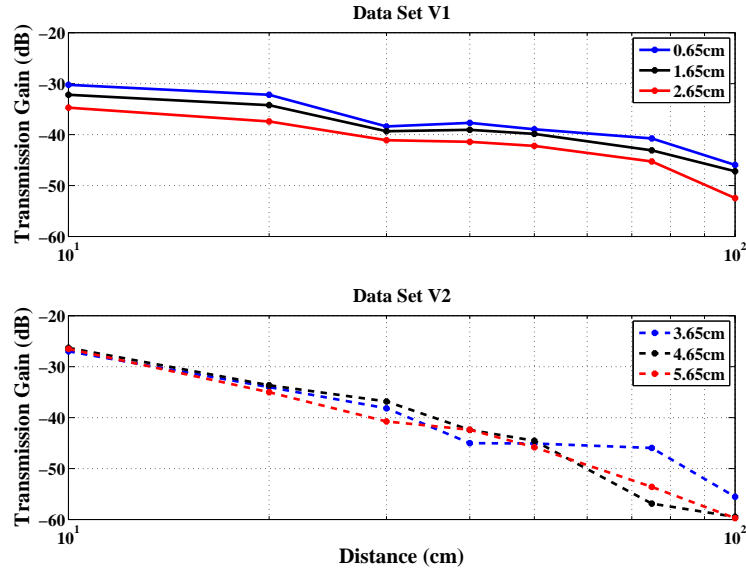


Figure 6.14: Transmission gain versus antenna separation and height for vertical polarisation (Data separated in to sets V1 and V2 on the basis of antenna height dependence).

<i>Antenna Height (cm)</i>	<i>Gradient (dB/decade)</i>
0.65	-14.72
1.65	-14.30
2.65	-15.64
3.65	-26.48
4.65	-34.37
5.65	-32.14

Table 6.1: Gradients for V1 and V2.

The following observation is made with respect to data set V2.

- Increasing antenna height above 2.65 cm has no significant effect on received power. This suggests that any surface-wave effect has decayed to a negligible level leaving only space-wave (LOS plus surface reflection) coupling between the antennas.
- For antenna height greater than 2.65 cm the gradient of the measured data (mean specific transmission loss) is approximately 31 dB/decade, further suggesting two-ray behaviour for separations greater than the distance R_{max} , see Figure 6.16.

Figure 6.17 shows transmission gain versus antenna separation and antenna height for all data available from the very short distance, vertical polarisation

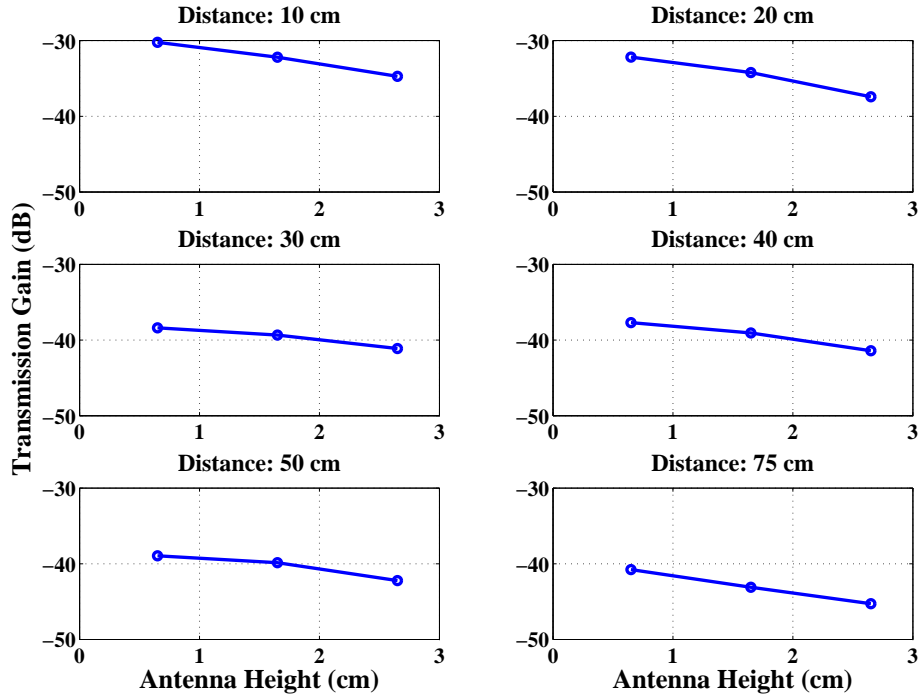


Figure 6.15: Transmission gain versus antenna height (Data set V1).

measurements. A best-fit first degree polynomial is extracted from the measurement points.

The polynomial has large offset from the measurement points. Triangle-based cubic interpolation has therefore also been applied, Figure 6.18.

6.5.1.2 Horizontal Polarisation

Transmission gain measured (after averaging) for horizontal polarisation as a function of antenna separation and antenna height is shown in Figure 6.19. The measurements have been divided into two sets. Set H1 contains measurements satisfying $h \leq 2.65$ cm. Set H2 contains measurements satisfying $3.65 \text{ cm} \leq h$.

The following observations are made with respect to data set H1.

- There is no clear, systematic, dependence of transmission gain for antenna height ≤ 2.65 cm. Also the propagation loss is greater for horizontal polarisation (for $h \leq 2.65$ cm, data set H1) than for vertical polarisation (data set V1), see also Figure 6.20. The mean difference between vertical and horizontal polarisation (data set V1 and H1) for three different antenna heights is given in Table 6.2. Since the horizontally polarised electric field is parallel to the surface the induced surface currents are higher than those for a vertically polarised field. This might be expected, therefore, to give

6.5. CHIPBOARD MEASUREMENTS FOR VERY SHORT DISTANCE

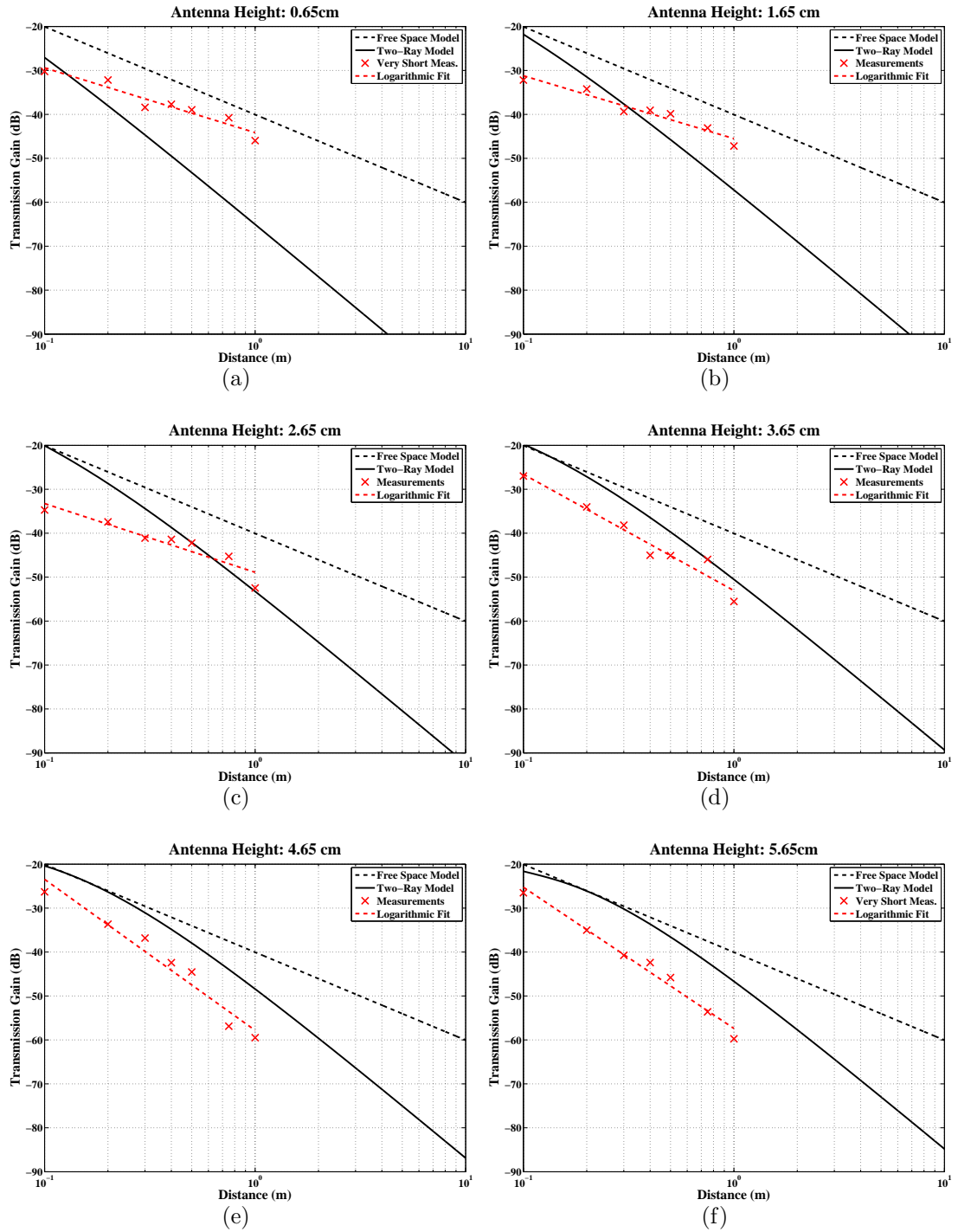


Figure 6.16: Transmission gain for vertical polarisation, with logarithmic best-fit line, compared to free space and two-ray model ($\epsilon_r = 3.55$ and $\sigma = 0.02$).

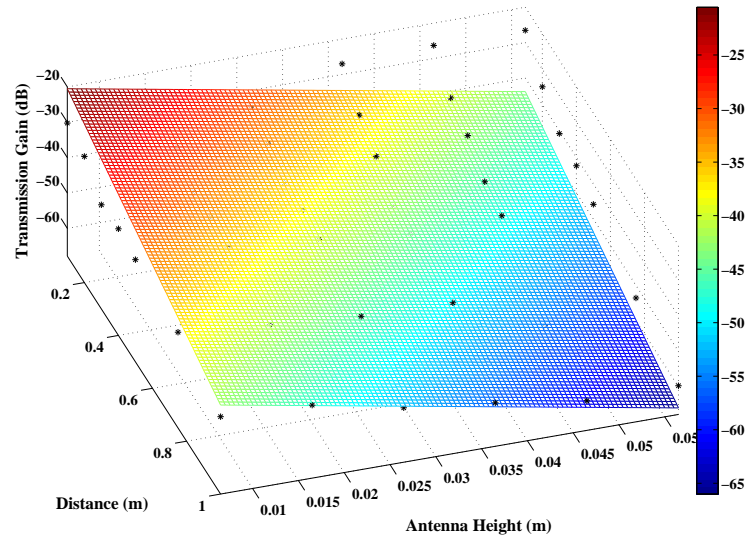


Figure 6.17: Measurement data and best-fit first-degree polynomial surface.

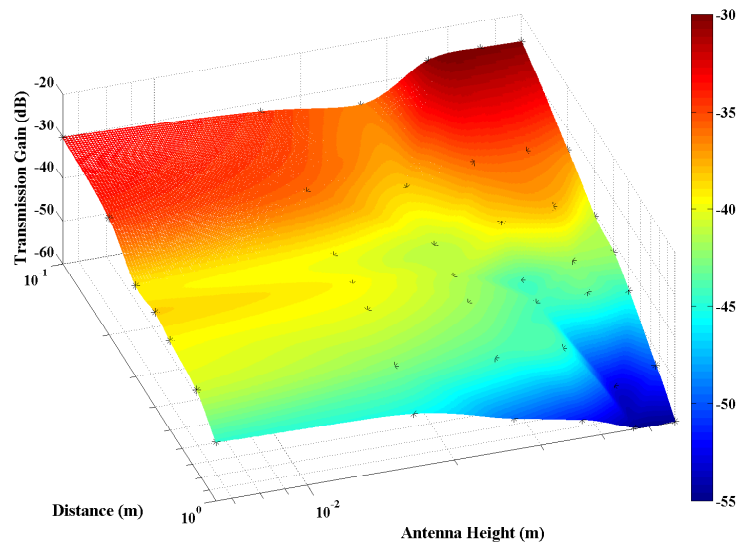


Figure 6.18: Measurement data and best-fit surface.

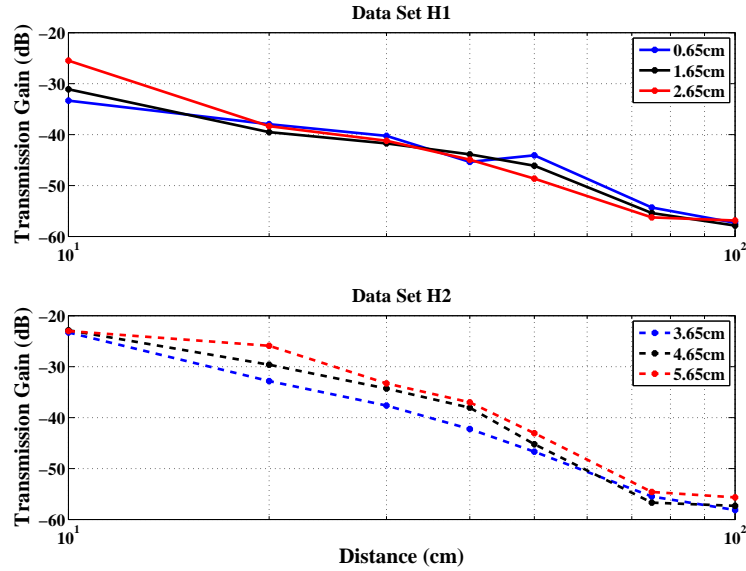


Figure 6.19: Transmission gain versus antenna separation and height for horizontal polarisation (Data separated in two sets H1 and H2 on the basis of antenna height dependence).

rise to greater attenuation due to higher conduction and/or displacement current losses.

<i>Height (cm)</i>	<i>Power Difference (dB)</i>
0.65	8.64
1.65	7.77
2.65	5.43

Table 6.2: Mean difference in transmission gain for vertical and horizontal polarisation (data set V1 and H1).

- In Figure 6.21, at low antenna heights ($h \leq 2.65$ cm) the mean gradient is 25.3 dB/decade. The gradient is larger (more negative) than that for vertical polarisation indicating greater attenuation.

The following observations are made with respect to data set H2.

- Loss generally increases as transmit and receive antenna heights are reduced until height of 3.65 cm. (This is not true for the shortest path length, i.e. 10 cm.)
- For antenna heights ≥ 2.65 cm, the gradient for separations greater than the distance R_{max} (35.4 dB/decade) suggests a two-ray model.

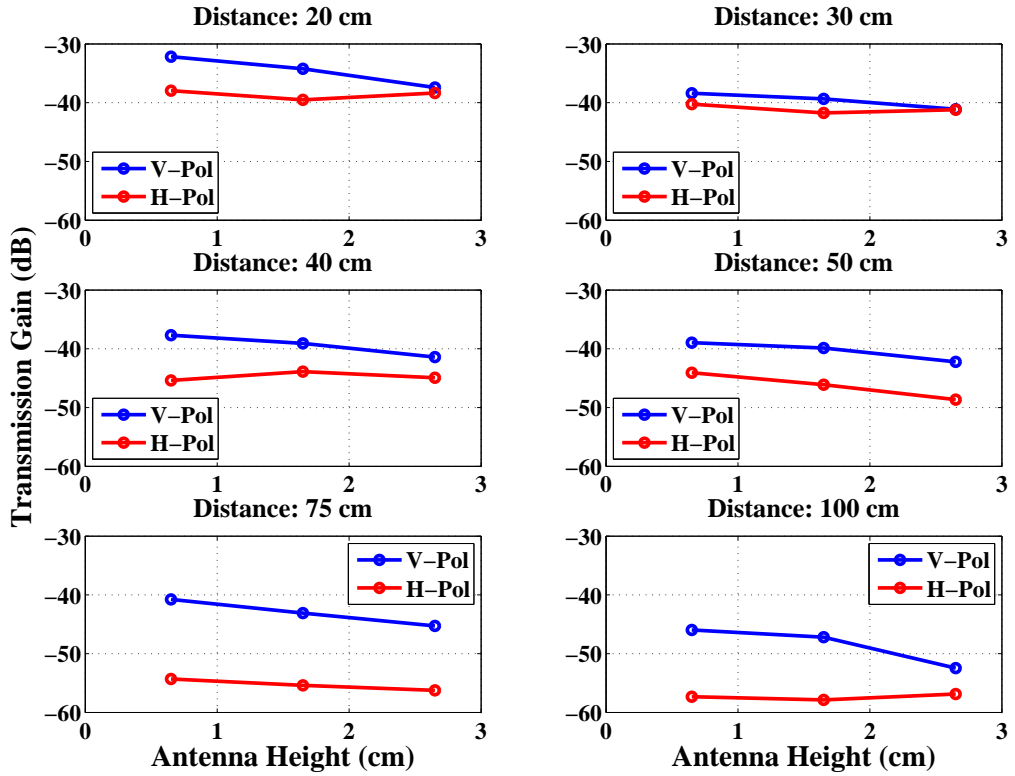


Figure 6.20: Transmission gain for vertical and horizontal polarisation (data set V1 and H1).

- Transmission gain averaged over antenna height is less for data set H1 than for data set H2. This suggests an increasing propagation loss with decreasing height for horizontal polarisation.

	Average Transmission gain (dB)					
	10 cm	20 cm	30 cm	40 cm	50 cm	100 cm
H1	-30.9	-38.3	-41.2	-44.6	-45.8	-57.3
H2	-23.0	-28.5	-30.6	-38.5	-44.7	-56.9
Diff	7.9	9.8	10.2	6.1	1.2	0.4

Table 6.3: Average difference in transmission gain for horizontal polarisation (data set H1 and H2)

- The spread of received power for various antenna heights decreases with increasing antenna separation (Table 6.4). This may reflect the diminishing surface-wave effect with distance. If this interpretation is correct then for antenna separations greater than 50 cm, the surface-wave effect could be neglected, see Figure 6.19.

6.5. CHIPBOARD MEASUREMENTS FOR VERY SHORT DISTANCE

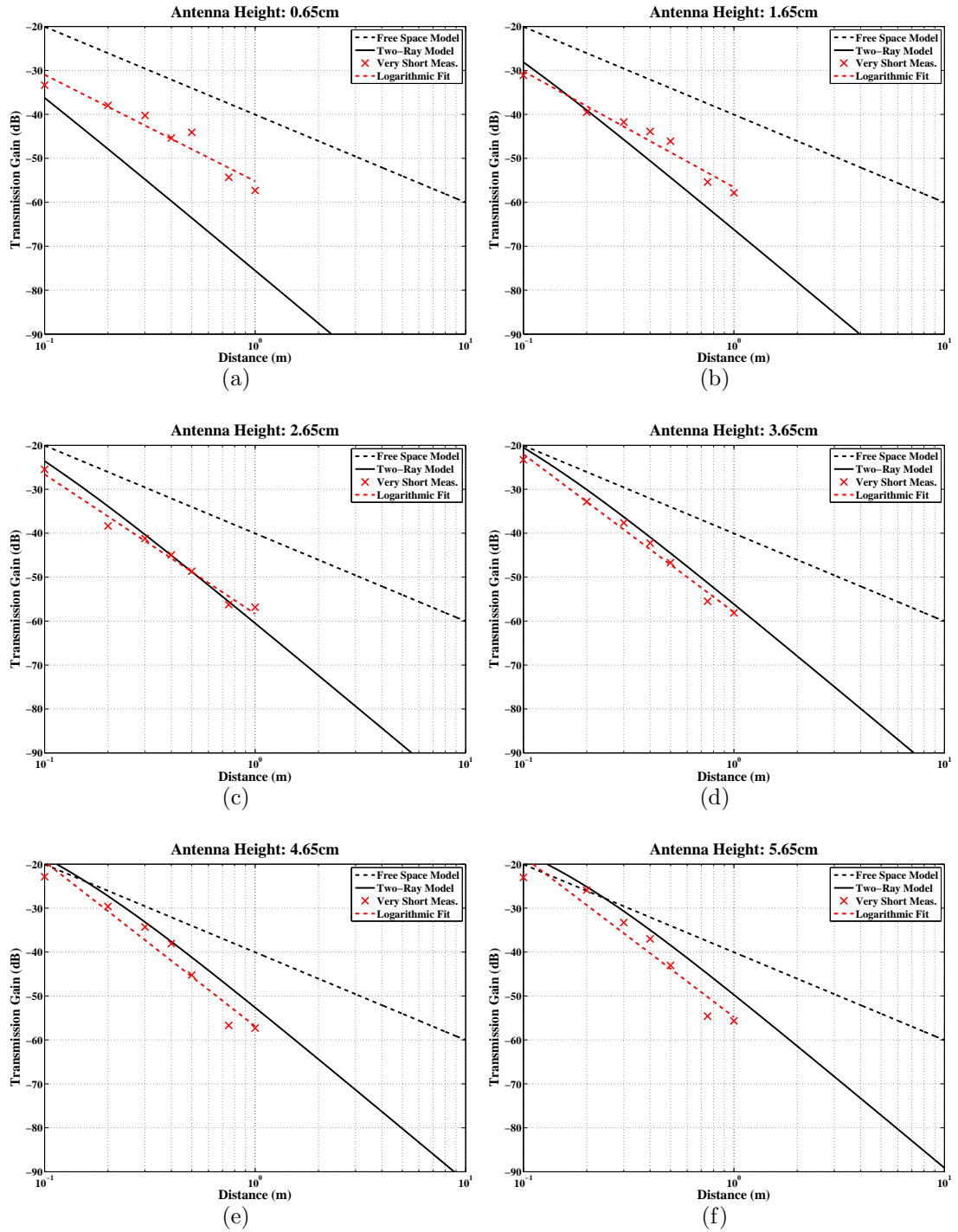


Figure 6.21: Transmission gain for horizontal polarisation, with logarithmic best-fit line, compared to free space and two-ray model ($\epsilon_r = 3.55$ and $\sigma = 0.02$).

<i>Antenna Height (cm)</i>	<i>Separation Distance (cm)</i>	<i>Standard Deviation (dB)</i>
0 - 5	10	4.67
0 - 5	20	5.49
0 - 5	30	3.61
0 - 5	40	3.57
0 - 5	50	1.98
0 - 5	75	0.92
0 - 5	100	0.87

Table 6.4: Standard deviation for horizontal polarisation measurements.

<i>Antenna Height (cm)</i>	<i>Gradient (dB/decade)</i>
0.65	-24.24
1.65	-26.39
2.65	-31.73
3.65	-35.95
4.65	-37.46
5.65	-36.42

Table 6.5: Gradients for H1.

Figure 6.22 shows transmission gain versus distance and antenna height for all data available from the very short distance, horizontal polarisation measurements. A best-fit first degree polynomial is extracted from the measurement points.

The polynomial fits the data points better than is the case for the vertical polarisation measurements. A triangle-based cubic interpolation has also been applied for completeness, however, Figure 6.23.

6.6 Chipboard Measurements for Short Distance

Measurements of transmission gain have been made at 2.45 GHz using a pair of linearly polarised rectaxial antennas, described in Section 4.3.1.

An Agilent E4438C ESG vector signal generator was used as a source to generate a 2.45 GHz unmodulated carrier with transmission power of 0 dBm. Received power was measured using an Agilent E4440A spectrum analyser.

The measurements were carried on a plane, horizontal, surface (Figure 6.24) of laminated chipboard, identical to the one used for the very short measurements (Section 6.5) with thickness, length and width 2.5 cm, 14.5 m and 4 m, respectively.

The rectaxial antennas were oriented to radiate vertically ($\pm 2^\circ$), i.e. aligned

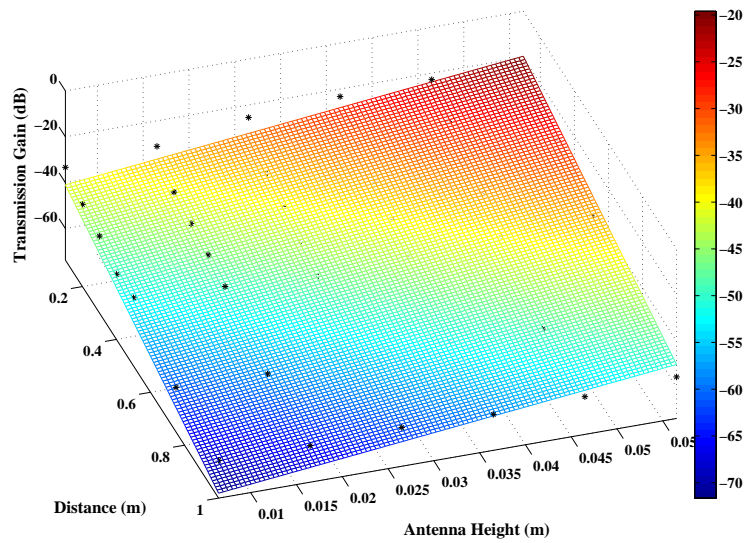


Figure 6.22: Measurement data and best-fit first-degree polynomial surface.

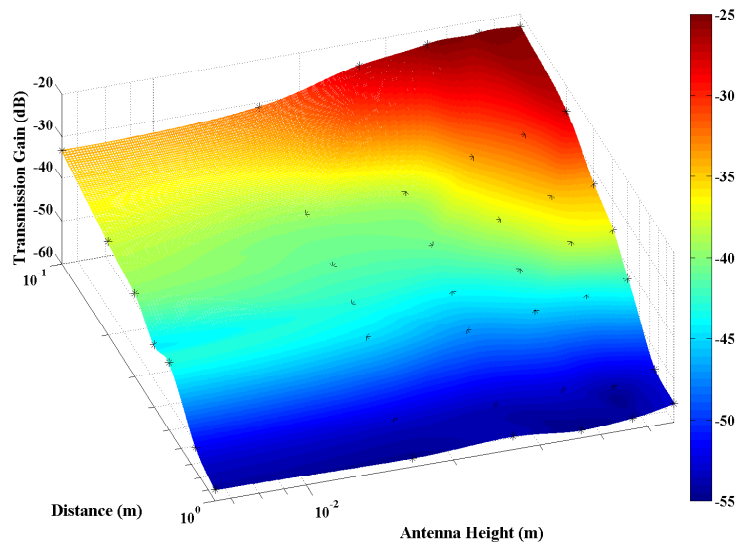


Figure 6.23: Measurement data and best-fit surface.



Figure 6.24: Measurement surface.

with gravity.

Initially, the antennas were placed on the surface with their phase centres at a height of approximately 0.65 cm.

The transmitting antenna was placed 1 m from the edge of the surface and, keeping this antenna static, the receiving antenna was placed at a range of 0.5 m to 10 m from the transmit antenna in steps of 0.5 m.

This procedure was repeated placing the static antenna at a distance of 1.5, 2, 2.5, 3, 3.5, 4 and 4.5 m from the edge of the surface, thus obtaining eight spatial samples.

This process was repeated placing both antennas at heights of 5, 10, 15 and 20 cm above the surface. For heights of 0.65 cm and 5.65 cm, the antennas were inverted (i.e. feed from above) to accommodate the low phase centre measurements.

The loss introduced by the RG-316 RF coaxial cable and the SMA connectors was measured to be 9.3 dB by connecting the signal generator to the spectrum analyser. This loss has been compensated.

Path length, antenna heights and power were measured with accuracies better than ± 1 mm, ± 0.5 mm and ± 1 nW, respectively.

The antenna stands used were made of either PVC or perspex (plexiglas) to minimise the effect of scattering close to the antennas.

Each transmission gain measurement point is the mean (using linear ratios, not dBs) of all (usually eight) spatial samples.

6.6.1 Results

Figure 6.25 shows the results obtained with an antenna height of 0.65 cm for very short range (red), and short range (green) measurements. The gradients of the data for both measurements are consistent and the deviation of the data from the logarithmic best-fit line is small. However, an unexplained offset between those measurements exists. This may have been caused by a systematic measurement error such as a wrong setting of the apparatus used (e.g. signal generator power level or spectrum analyser attenuation), but it is most likely caused by not properly tightening one of the connectors. In any event this error will affect the whole set of data.

For this reason, 12 dB compensation of the short distance measurements has been applied (shown in blue) justified by the measurement points at 0.5 m and 1 m.

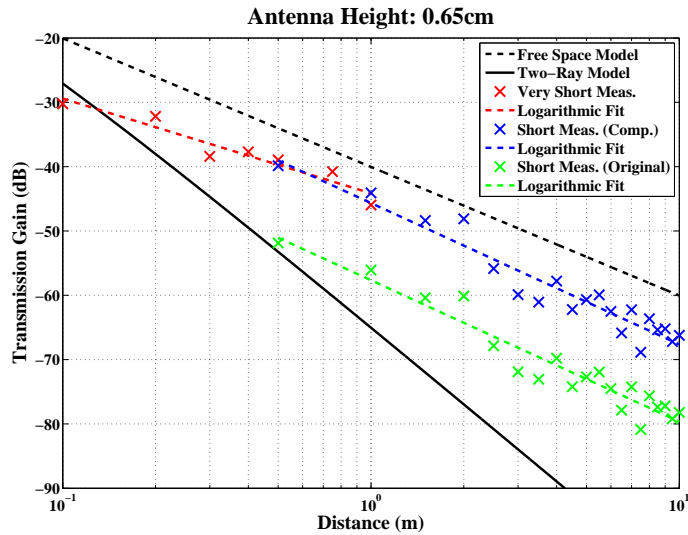


Figure 6.25: Very short and short distance measurements for antenna height 0.65 cm with best-fit lines.

Complimentary frequency response measurements were undertaken using the network analyser to obtain the transmission loss of particular distance points (0.5 m, 1 m, 1.5 m and 2 m) and thus validate the previous measurements. The validation measurements were made using the same equipment as used for the WIDAGATE measurements (Chapter 4). Each validation measurement point has been extracted by averaging the transmission gain over a 10 MHz span centred at 2.45 GHz.

Figures 6.26 (a), (b) and (c) show all measurements obtained for an antenna height of 0.65 cm for the entire span of ranges (0.1 to 10 m). The very short range (red triangles), the short range (blue triangles) and the network analyser

measurements (circles) are closely matched (difference less than 1 dB) at a range of 0.5 m and reasonably close to each other (difference less than 4 dB) at a range of 1 m. The short distance measurements are also close to the network analyser measurements (difference less than 2 dB) at 1.5 m. The only exception is the large difference (approximately 9 dB) between those measurements at 2 m.

The geometric mean of the measurements obtained at each range was calculated. These are denoted by red circles in Figure 6.26 (b) and a logarithmic best-fit curve was plotted, Figure 6.26 (c). This graph suggests that the logarithmic curve follows closely the free space law (a path loss index close to 2), but offset by approximately 7 dB. This is unexpected since a simple two-ray model would suggest an index closer to 4.

The same procedure was repeated for an antenna height of 5.65 cm. Figure 6.27 shows the measurements obtained for very short and short distance, with the logarithmic best-fit line for each case. This figure is of particular interest, as it shows that the gradient for ranges less than 1 m is 32 dB/decade, while the gradient for ranges greater than 1 m is 11 dB/decade.

Figures 6.28 (a), (b) and (c) show all measurements obtained for an antenna height of 5.65 cm for the entire span of ranges (0.1 to 10 m). The short path measurements (blue triangles) and the network analyser measurements (open circles) are closely matched (difference less than 1 dB) for a range of 0.5 m. The very short path measurements (red triangles) are different by 5 dB for the same range.

The short distance (blue triangles) and the network analyser (not shadowed circles) measurements are at similar levels (≈ 2 dB) for 1 m and 1.5 m, while the difference is approximately 3 dB for 2 m. The very short distance (red triangles) measurements are less than 5 dB lower than the rest at 1 m.

Similarly to the measurements for an antenna height of 0.65 cm antenna height, the overall gradient shown in Figure 6.28 (c) follows the free space model.

Figures 6.29, 6.30 and 6.31 show the results obtained for antenna heights of 10 cm, 15 cm and 20 cm, respectively. (These measurements were undertaken with the antennas oriented such that they were fed from below.)

The transmission gain is affected most by the rectaxial antenna radiation pattern at shorter distance and higher antenna height. In such cases the reflection coefficient is low, therefore the LOS path is dominant. Details of the rectaxial antenna radiation pattern and the magnitude of the reflection coefficient over the chipboard are available in Appendix D.

The logarithmic best-fit lines in all three cases suggest a gradient close to free

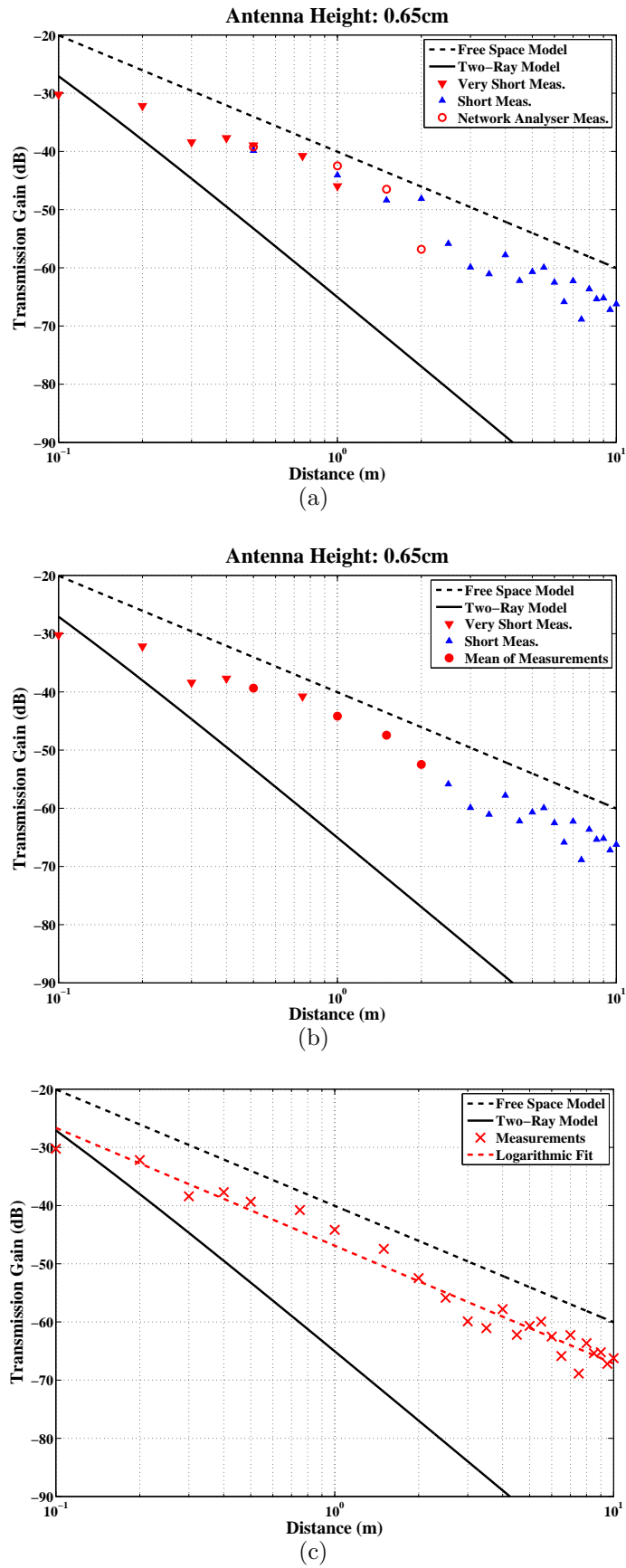


Figure 6.26: Measurements for antenna height 0.65 cm.

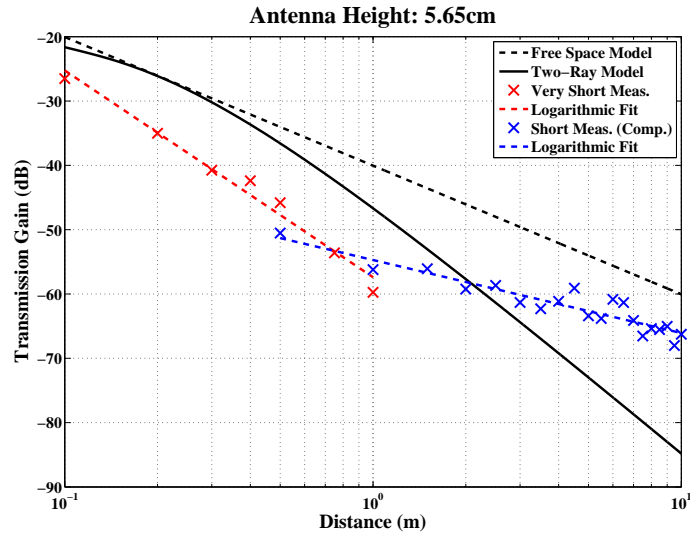


Figure 6.27: Very short and short distance measurements for antenna height 5.65 cm with best-fit lines.

space (20 dB/decade).

An interesting observation is that transmission gain generally increases, as antenna height increases, Table 6.6. The only exception is the level at 0.65 cm antenna height, which may be explained by the presence of a surface-wave.

<i>Antenna Height (cm)</i>	<i>Transmission Gain Level (dB) at 1 m</i>
0.65	-46.90
5.65	-50.54
10.00	-50.76
15.00	-46.62
20.00	-44.62

Table 6.6: Transmission gain level (dB) at 1 m.

The transmission gain standard deviation of the eight spatial samples, for the short range measurements, was calculated for each measurement location and the results are shown in Figure 6.32. For antenna heights below 15 cm there was no discernible spread. Normally, it is expected that the standard deviation would increase with increasing path length. However, when the antennas are placed at increasing heights from the surface, i.e. 15 cm and 20 cm, the transmission gain standard deviation increases along the distance as normal.

Figure 6.33 shows all the measurements obtained in this study (very short and short path lengths) for vertical polarisation.

A curious and unexplained observation is the deep fading close to a range of 1 m distance for an antenna height of 5 cm.

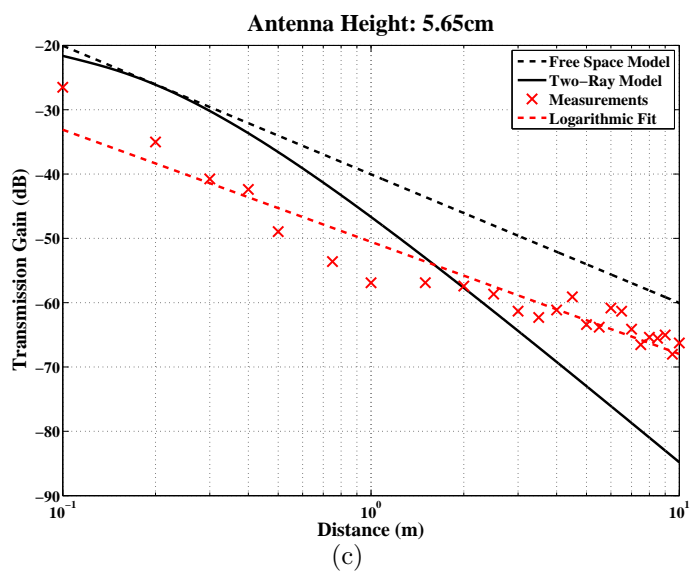
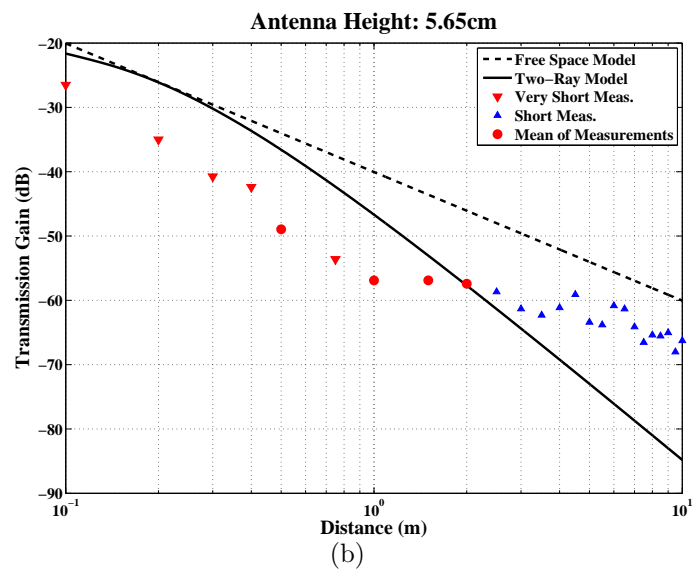
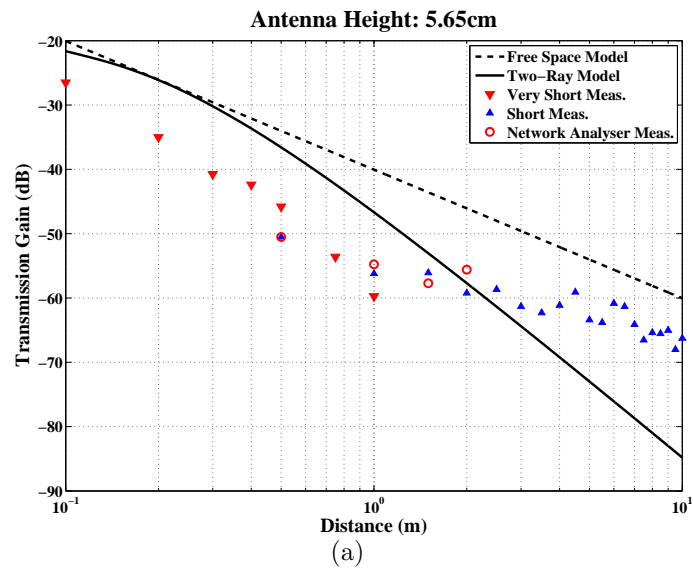


Figure 6.28: Measurements for antenna height 5.65 cm.

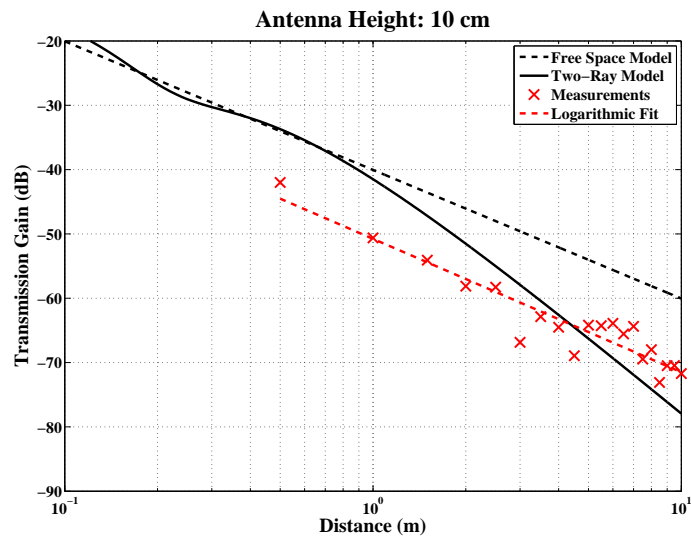


Figure 6.29: Transmission gain (dB) for antenna height 10 cm.

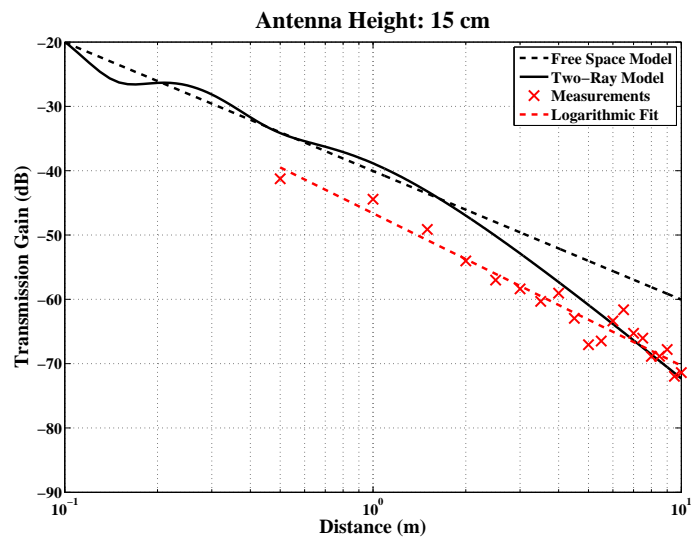


Figure 6.30: Transmission gain (dB) for antenna height 15 cm

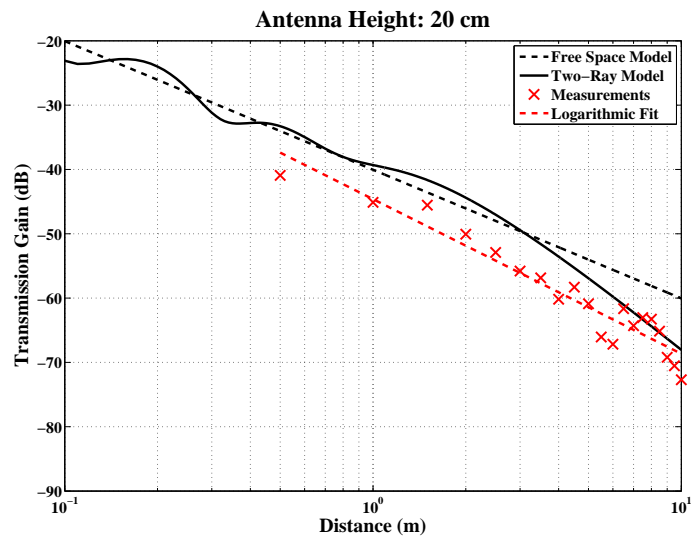


Figure 6.31: Transmission gain (dB) for antenna height 20 cm

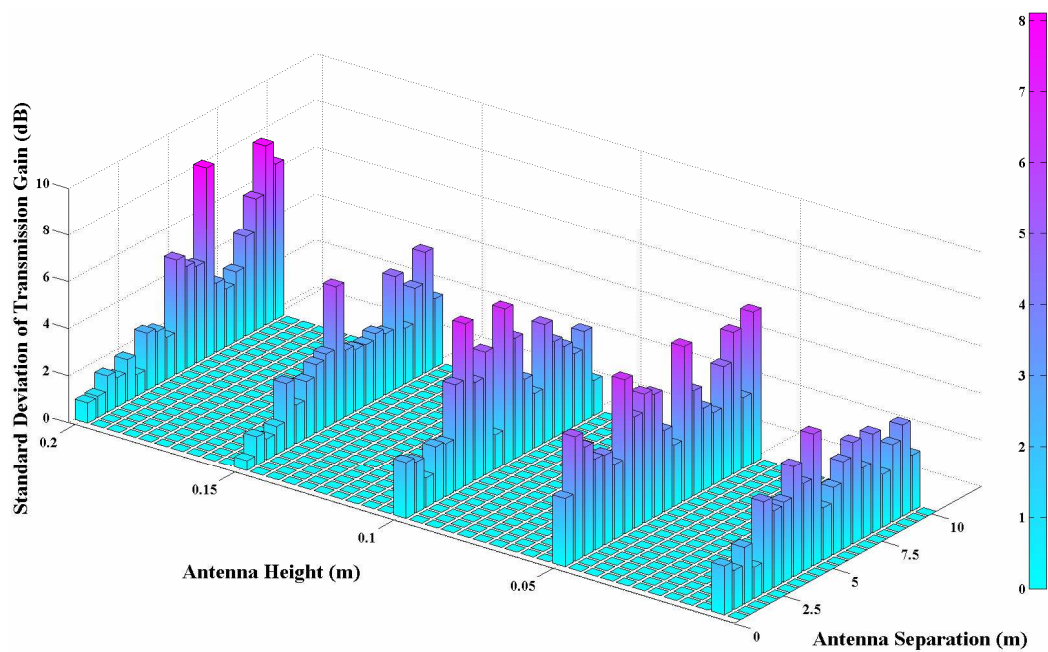


Figure 6.32: Standard deviation of transmission gain (dB) in respect of path length and antenna height for short distance measurements.

For small antenna separations (less than 0.4 m) the transmission gain increases with increasing the antenna height. On the contrary, however, for antenna separations greater than 0.5 m the transmission gain decreases when increasing the antenna height.

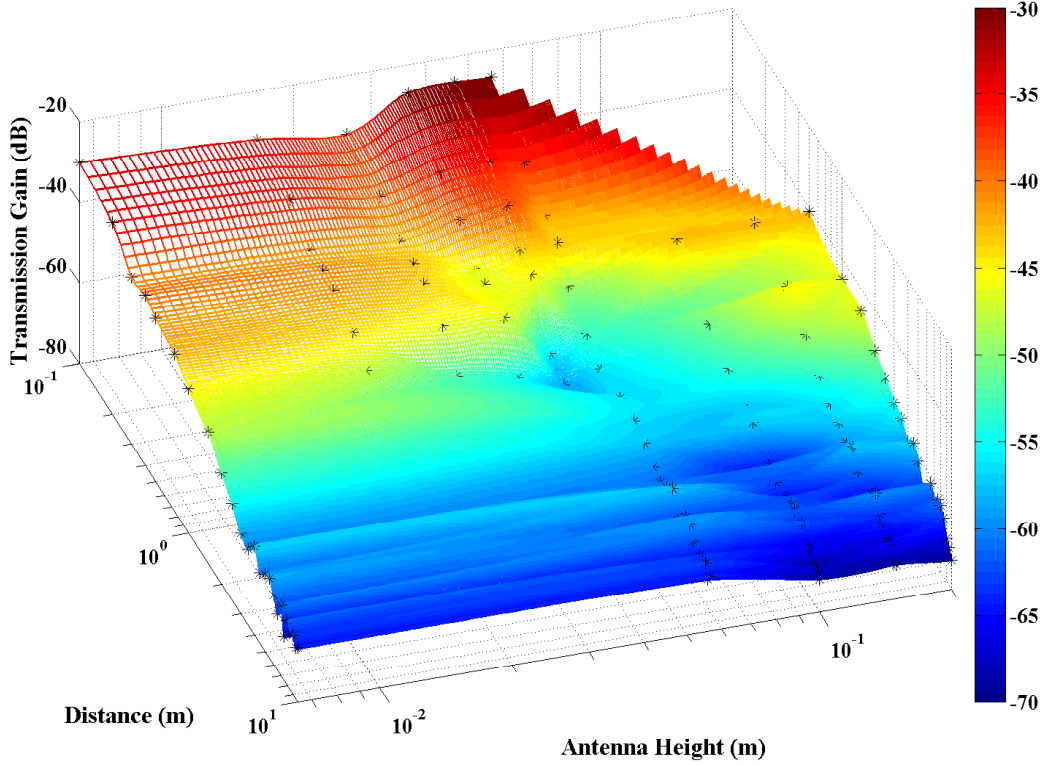


Figure 6.33: All available measurements for vertical polarisation.

6.6.2 Gradients and Path Loss Indices

Table 6.7 summarises all the gradients obtained from the vertical polarisation measurements for the entire span of ranges (0.1 to 10 m). Excluding the case where the antennas are attached on the surface (0.65 cm antenna height), the gradient seems to increase with increasing antenna height.

<i>Antenna Height (cm)</i>	<i>Gradient (dB/decade)</i>
0.65	-20.24
5.65	-17.43
10.00	-20.74
15.00	-23.68
20.00	-24.03

Table 6.7: Gradients of all measurements of Section 6.6.

Figure 6.34 shows the corresponding path loss indices for all the measurements obtained in the study.

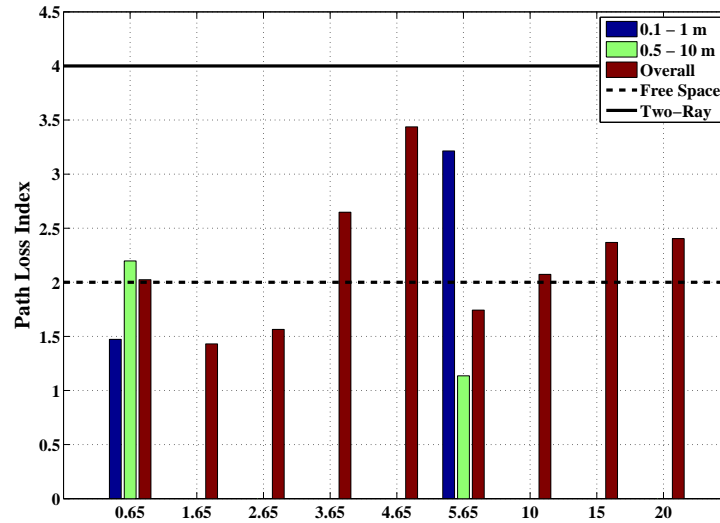


Figure 6.34: Path loss indices for all measurements (both very short and short range measurements).

6.7 Summary and Conclusions

Measurements of transmission loss at 2.45 GHz between pairs of rectaxial and patch antennas located on the interior wall of a building have been presented in Section 6.4. The measurements are intended to emulate links such as might be formed by pairs of nodes in a sensor network within smart buildings.

The conclusions of this study are:

- There is no significant dependence of received power on antenna-wall offset with the exception microstrip antenna with a reduced height of 30 cm.
- For vertically polarised rectaxial antennas the loss is lower for a reduced height of 30 cm compared to a reduced height of 0 cm.
- For horizontally polarised rectaxial antennas the reduced height has no significant impact on transmission loss.
- The path-loss index for the patch antennas with 0 cm reduced height is between 2.9 and 3.6 and for a 30 cm reduced height is between 1.4 and 1.6.
- The path-loss index for the vertically polarised rectaxial antenna with 0 cm reduced height is between 4.2 and 4.6.

- The path-loss index for the horizontally polarised rectaxial antenna lies between 2 and 2.1 for 0 cm reduced height and between 1.6 and 1.9 for 30 cm reduced height.

An additional study has related transmission loss to antenna height and polarisation for very short wireless links (< 1 m). Since wireless sensor nodes in future are small and are likely to be deployed close to surfaces, significant improvement in received power can be achieved by appropriate selection of antenna height. The conclusions of this study are:

For vertically polarised rectaxial antennas (Sets V1 and V2):

- Transmission gain decreases with increasing antenna height.
- Mean specific transmission loss is 14.5 dB/decade between 10 cm and 100 cm.
- Increasing antenna height above 2.65 cm has no significant effect on transmission gain.
- For antenna heights greater than 2.65 cm the gradient of the measured data (mean specific transmission loss) is approximately 30 dB/decade.

For horizontally polarised rectaxial antennas (Sets H1 and H2):

- There is no clear, systematic, dependence of transmission gain for antenna height less than 2.65 cm.
- For antenna height less than 2.65 cm, propagation loss is greater for horizontal polarisation than for vertical polarisation.
- For antenna height less than 2.65 cm, the mean loss gradient is 25.3 dB/decade.
- For antenna height less than 2.65 cm, the loss gradient is larger (more negative) than that for vertical polarisation indicating greater attenuation.
- The losses generally increase as transmit and receive antenna heights are reduced until 3.65 cm. This is not true for 10 cm antenna separation.
- For antenna heights greater than 2.65 cm and for distances further than R_{max} , the gradient (35.4 dB/decade) suggests a two-ray model.
- Propagation loss increases when decreasing height.
- The spread of transmission gain for various antenna heights decreases with increasing antenna separation.

Empirical channel models for short range communications pertinent to a range of wireless sensor network applications have also been presented. Best-fit logarithmic fits to the empirical data have been produced. The data available from the very short distance measurements have been merged, where appropriate (i.e. 0.65 cm and 5.65 cm antenna height), to obtain a single model for the range of interest (0.1 -10 m). Additional frequency response measurements were undertaken using a network analyser for validation purposes. The conclusions of this study are:

- Deviation of data points from the regression line is generally small.
- The loss gradient increases when the antenna height increases.
- Transmission gain generally increases with increasing antenna height.
- Unlike the theoretical models, for very low antenna heights (less than 3.65 cm), the gradients are low, i.e. either close to free space or lower.
- For antenna separations less than 0.4 m transmission gain increases with increasing antenna height.
- For antenna separations greater than 0.5 m transmission gain decreases with increasing antenna height.

The practical importance of this study relates to applications where antennas are located close to plane surfaces e.g. small, unmanned, vehicles used for exploration, monitoring or rescue purposes in confined spaces.

CHAPTER 7

Conclusions and Future Work

This section contains those conclusions that can be drawn from the work reported and makes some suggestions for extending this work.

7.1 Conclusions

The conclusions drawn from the work undertaken for the WIDAGATE project are:

- A simple theoretical model suggests that the minimum symbol rate for which a wideband propagation model is required for a gas turbine depends on engine radius. As engine radius increases this symbol rate decreases. For a Gnome engine, with mean radius 0.2 m, the expected minimum symbol rate is 70 Mbaud. Since this is sufficient to support the maximum foreseeable bit-rate for the WIDAGATE application, even assuming the minimum possible modulation order (i.e. two), it is concluded that a narrowband channel model is satisfactory.
- The 50% correlation bandwidth exceeded for 50% of links is at least 5.5 MHz and 25 MHz for ISM-band and UWB-band measurements, respectively.
- Mean transmission loss is sensitively dependant on path length and relatively insensitive to path curvature. It appears to be systematically lower in the presence of a cowling. It is concluded that this is due to a low-Q cavity resonator formed by the concentric cylinders of the engine and cowling.
- A channel model incorporating transmission loss, interference and noise has been presented for WSNs deployed in gas turbine engines. The model is scalable to engines of different size.

7.1. CONCLUSIONS

The conclusions drawn from the work undertaken for the animal husbandry project are:

- Fading is generally severe (20 - 30 dB).
- Received power in dBm is approximately normally distributed and RSSI in volts is therefore log-normally distributed.
- The correlation between signals received by two antennas on one collar is low suggesting useful antenna diversity can be realised.
- The correlation between signals received by two base-stations from a single antenna on a collar is low suggesting useful base-station diversity can be realised.
- Median diversity gain (averaged over four experiment instances) for antenna and base-station diversity is 2.8 dB and 4.8 dB, respectively. The 10% and 90% diversity gain exceedances averaged over the four instances for antenna and base-station diversity are 7.4 dB, 1.2 dB, 8.4 dB and 1.1 dB, respectively.
- Median diversity gain (averaged over four experiment instances) for two collars are 8.1 dB and 7 dB, respectively. The 10% exceedances averaged over all four instances are 14.3 dB and 11.2 dB for the first and second collar, respectively. The 90% exceedances are 4.1 dB for the first, and 3.5 dB for the second, collar.
- Median overall mean diversity for collar 1 and collar 2 is 7.9 dB. The 10% and 90% diversity gain exceedances are 11.6 dB and 5 dB, respectively.
- Optimisation of base-station height can coherently combine direct and ground-reflected signals and offer practical and useful reduction of transmission loss.

The conclusions drawn from the work relating to WSN nodes deployed over indoor plane surfaces for smart building applications are:

- Measurements of transmission loss at 2.45 GHz between pairs of rectaxial and patch antennas located on the interior wall of a laboratory have been presented. The measurements are intended to emulate links such as might be formed by pairs of nodes in a sensor network within smart buildings.
 - There is no systematic, significant, dependence of received power on antenna offset from the underlying surface.

- Transmission loss measurements versus antenna height for vertical and horizontal polarisation for very short wireless links (< 1 m) have been undertaken.
 - For antenna height less than 2.65 cm, propagation loss is greater for horizontal polarisation than for vertical polarisation and the loss gradient is larger (more negative) than that for vertical polarisation.
 - For vertically polarised rectaxial antennas:
 - * Transmission loss increases with increasing antenna height.
 - * Mean specific transmission loss is 14.5 dB/decade between 10 cm and 100 cm.
 - * Increasing antenna height above 2.65 cm has no significant effect on transmission loss, while for antenna heights in excess of 2.65 cm the gradient of the measured data (mean specific transmission loss) is approximately 30 dB/decade.
 - For horizontally polarised rectaxial antennas
 - * For antenna height less than 2.65 cm there is no clear dependence of transmission loss.
 - * For distance greater than R_{max} the gradient (35.4 dB/decade) suggests a two-ray model.
 - * Mean loss gradient is 25.3 dB/decade for antenna heights less than 2.65 cm.
 - * The losses generally increase as transmit and receive antenna heights are reduced until a height of 3.65 cm is reached.
 - * The spread of transmission loss decreases with increasing antenna separation irrespective of antenna height.
- Empirical channel models for short range communications pertinent to a range of wireless sensor network applications have been presented. Best-fit logarithmic curves have been derived from the empirical data. The data available from the very short distance measurements have been merged, where appropriate, to obtain a single model for the range 0.1 m to 10 m. Additional frequency response measurements were undertaken using a network analyser for validation purposes.
 - The spread of data around the regression line is generally small.
 - Specific loss (dB/octave) increases with increasing antenna height.

- In contrast to simple theoretical models specific loss gradient is close to free-space (or lower) for very low antenna heights (less than 3.65 cm).
- For antenna separations less than 0.4 m transmission loss decreases with increasing antenna height, while for antenna separations greater than 0.5 m transmission loss increases with increasing antenna height.

7.2 Discussion and Future Work

Further insight into the fundamental propagation physics for all the applications investigated could be gained by simulating the channel measurements using a finite element programme (e.g. COMSOL Multiphysics). Some attention has already been given to this but significant challenges remain. These are the adequate definition of boundary conditions and long run times with the currently available computing resources. The animal husbandry measurement present particular problems in this respect but useful insight would be possible using very simple models for the cattle (e.g. cuboids with the dielectric properties of an appropriate saline solution).

Comparison of the WIDAGATE channel measurements with analytical diffraction models for simple cylinders would yield insight into the practical significance of engine surface detail. Channel measurements using a model engine comprising a smooth cylinder would yield similar insight. Comparison of these measurements with simulations obtained using finite element calculations would provide validation of both.

A larger database of animal husbandry measurements in the environment already measured would increase the statistical significance of, and the confidence in, the existing measurements. Similar measurements in other environments would allow a model with greater portability to be developed.

A WSN network simulation (e.g. using OMNeT++ [81]) incorporating the physical channel models developed from the measurements would enable the evaluation of the entire WSN protocol stack allowing the comparison of proprietary technologies and/or the proposal of new (optimum) protocols for this application.

The measurements for smart building WSNs should be extended to many more plane surface commonly found in building interiors including, in the first instance, suspended ceilings and floors. (Investigation of propagation over, and under, floor coverings should be included in the latter.) The key academic question still not fully resolved is the significance of surface wave propagation for all these surfaces.

Appendix A: Complex Factor F (Equation Proof)

$$F = 1 + |\Gamma| e^{j\phi} e^{-j\theta} \quad (\text{A.1})$$

For the case that the reflecting surface is a perfect conductor:

$$|\Gamma| e^{j\phi} = -1 \quad (\text{A.2})$$

$$|F| = |1 - e^{-j\theta}| \quad (\text{A.3})$$

$$|F| = |1 - [\cos(\theta) - (j\sin(\theta))]| = |[1 - \cos(\theta)] + (j\sin(\theta))| \quad (\text{A.4})$$

$$|F|^2 = F \cdot \bar{F} \quad (\text{A.5})$$

where \bar{F} is the complex conjugate of F .

$$|F|^2 = [(1 - \cos(\theta)) + j\sin(\theta)] \cdot [(1 - \cos(\theta)) - j\sin(\theta)] \quad (\text{A.6})$$

$$|F|^2 = (1 - \cos(\theta))^2 + j\sin(\theta) \cdot (1 - \cos(\theta)) - j\sin(\theta) \cdot (1 - \cos(\theta)) - (j\sin(\theta))^2 \quad (\text{A.7})$$

$$|F|^2 = (1 - \cos(\theta))^2 + \sin^2(\theta) \quad (\text{A.8})$$

$$|F|^2 = 1 + \cos^2(\theta) - 2\cos(\theta) + \sin^2(\theta) \quad (\text{A.9})$$

$$|F|^2 = 2 - 2\cos(\theta) \quad (\text{A.10})$$

Using the trigonometric identity:

$$\sin\left(\frac{\theta}{2}\right) = \pm\sqrt{\frac{1 - \cos(\theta)}{2}} \quad (\text{A.11})$$

$$|F|^2 = \left(2\sin\left(\frac{\theta}{2}\right)\right)^2 \quad (\text{A.12})$$

We finally obtain:

$$|F| = 2\sin\left(\frac{\theta}{2}\right) \quad (\text{A.13})$$

Appendix B: UWB-band Measurements and Modelling for Measurements without Cowling (3 GHz to 11 GHz)

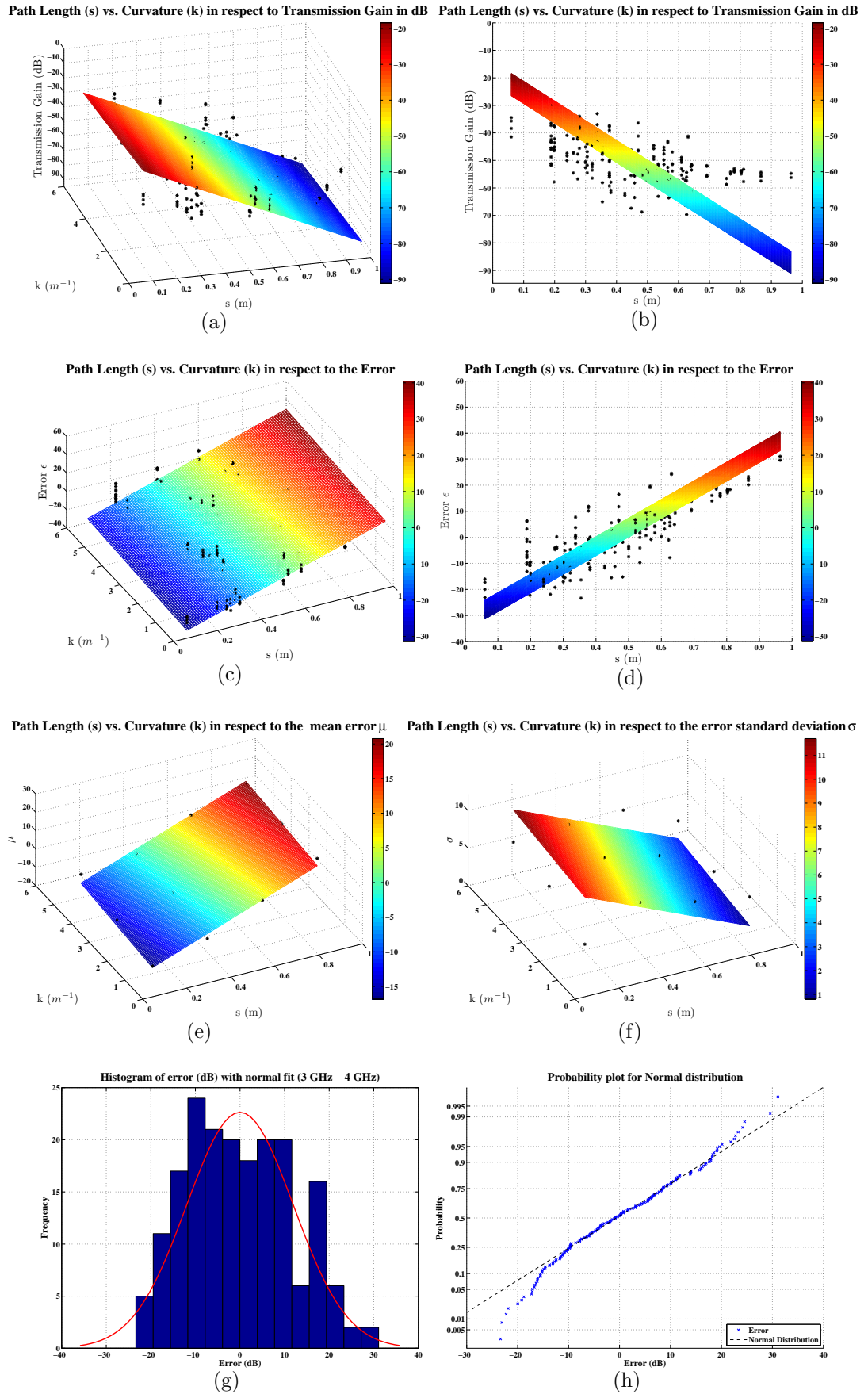


Figure B.1: Transmission gain and error modelling of measurements without cowling within 3 GHz to 4 GHz. 148

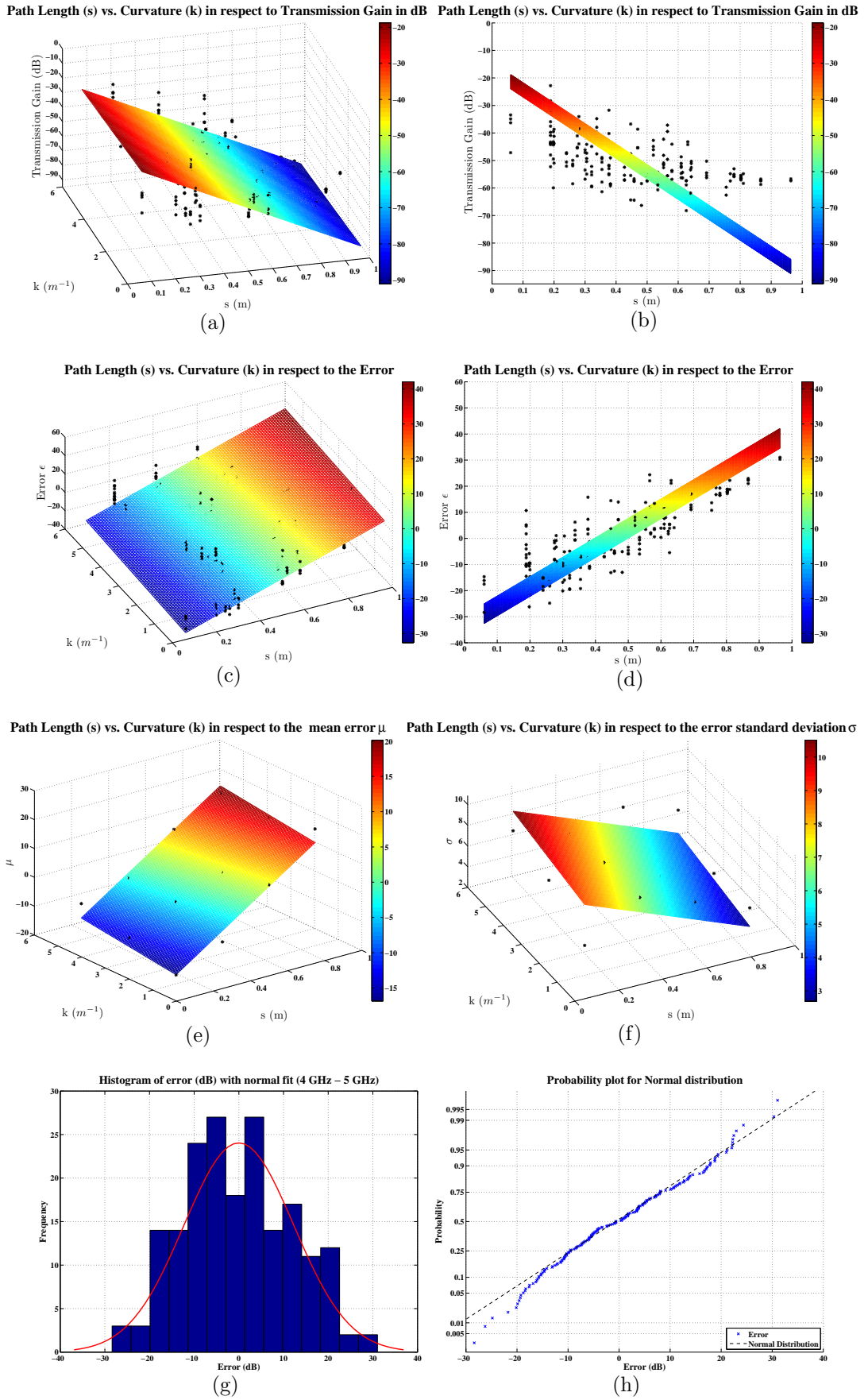


Figure B.2: Transmission gain and error modelling of measurements without cowling within 4 GHz to 5 GHz. 149

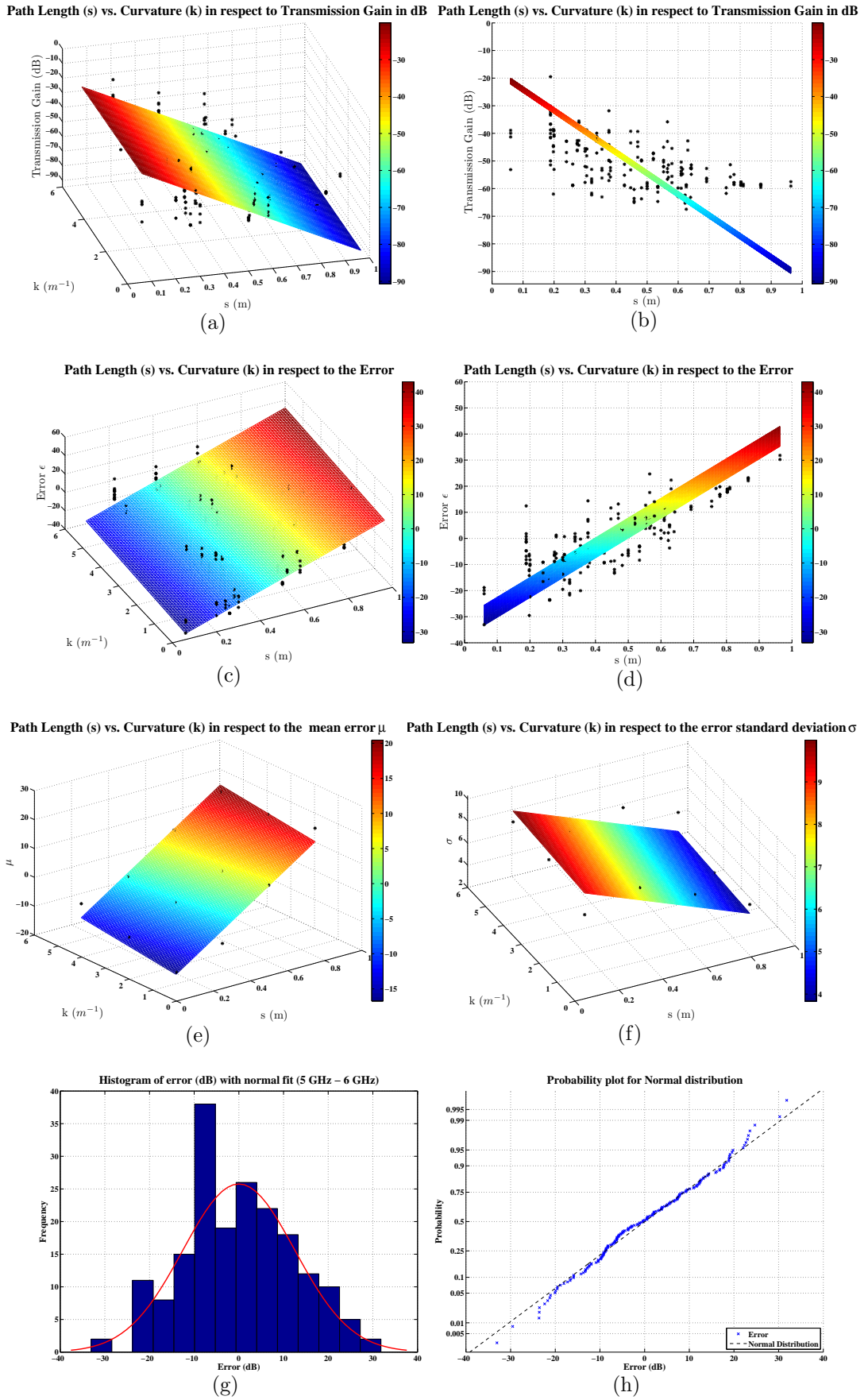


Figure B.3: Transmission gain and error modelling of measurements without cowling within 5 GHz to 6 GHz. 150

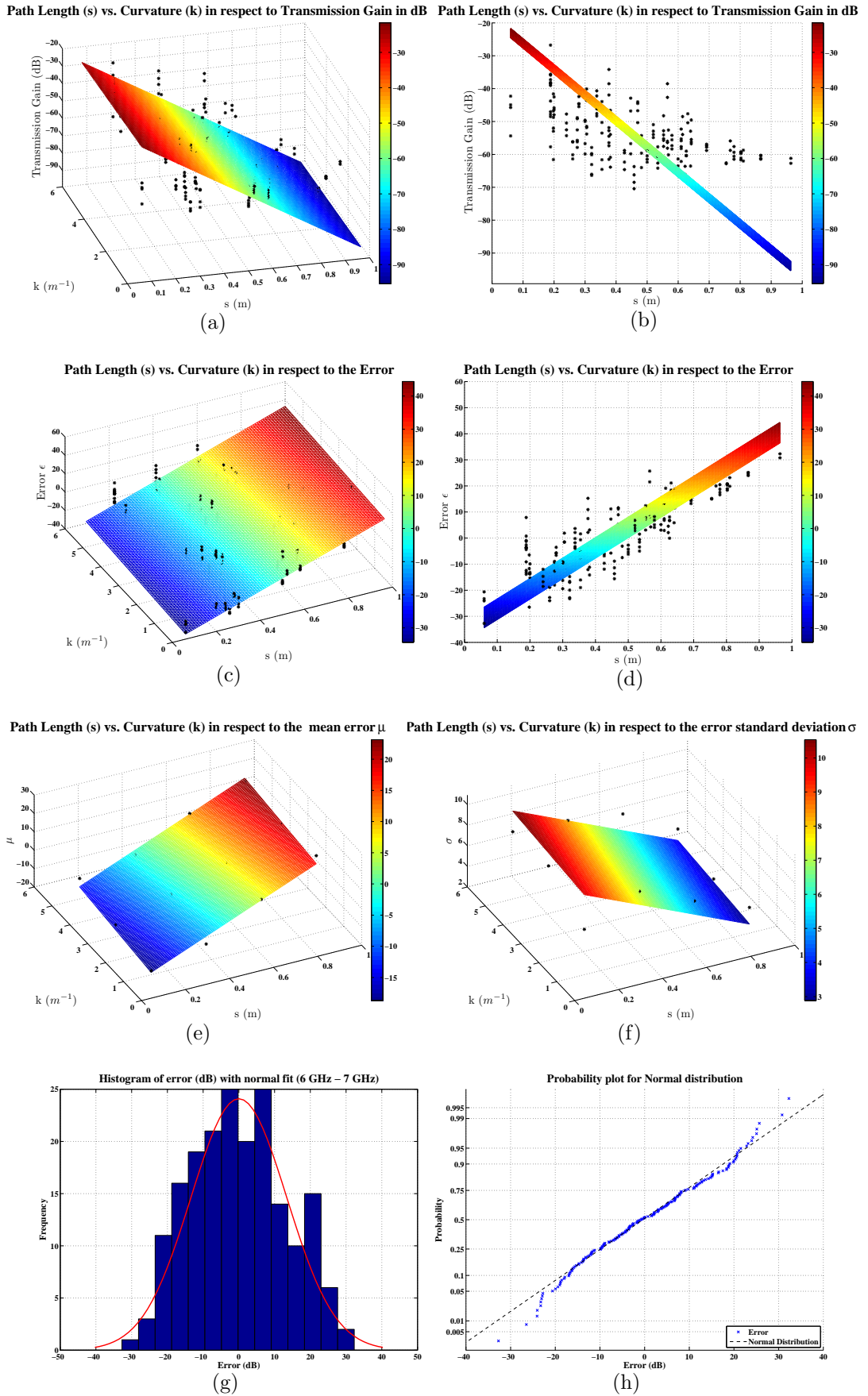


Figure B.4: Transmission gain and error modelling of measurements without cowling within 6 GHz to 7 GHz. 151

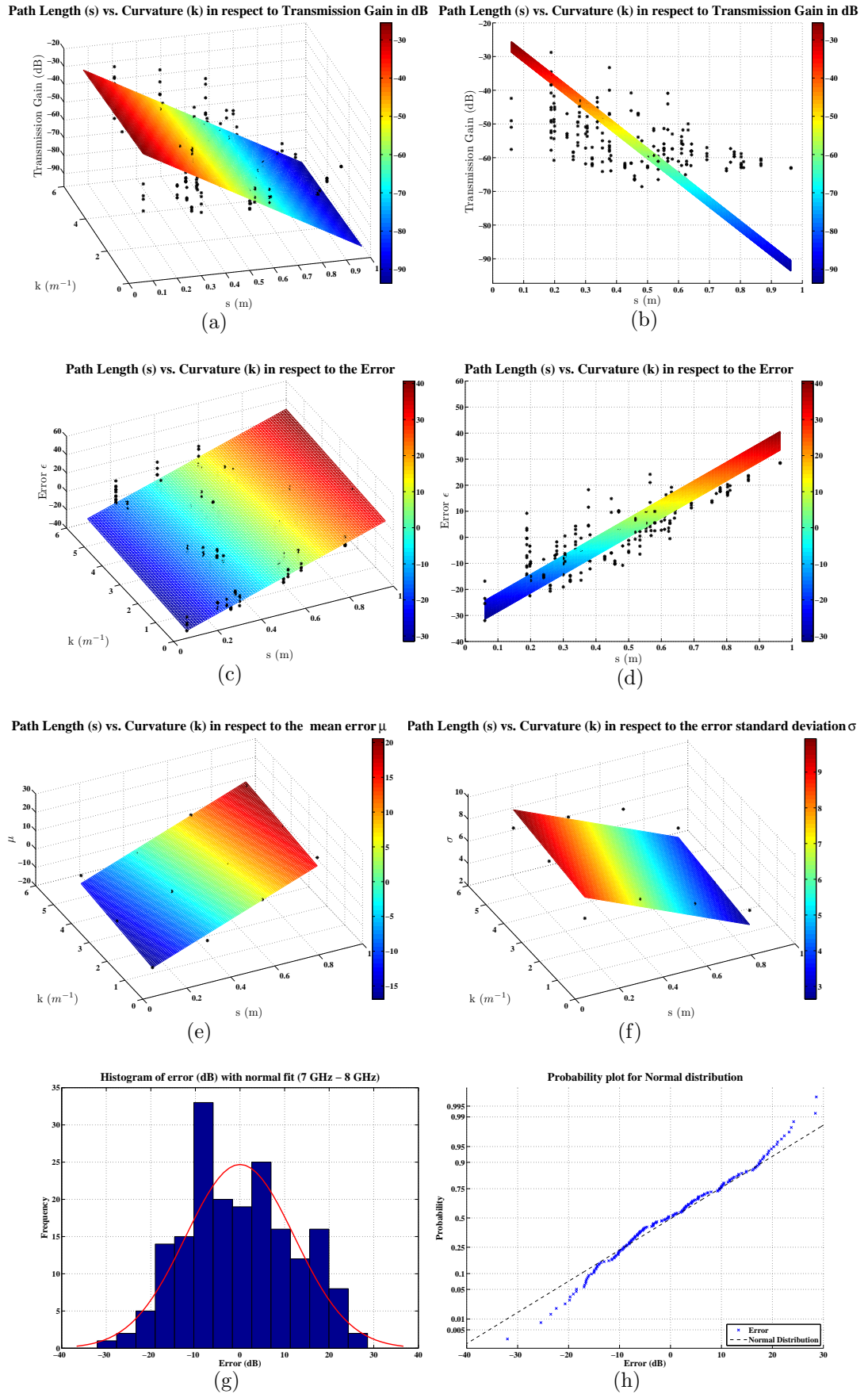


Figure B.5: Transmission gain and error modelling of measurements without cowling within 7 GHz to 8 GHz. 152

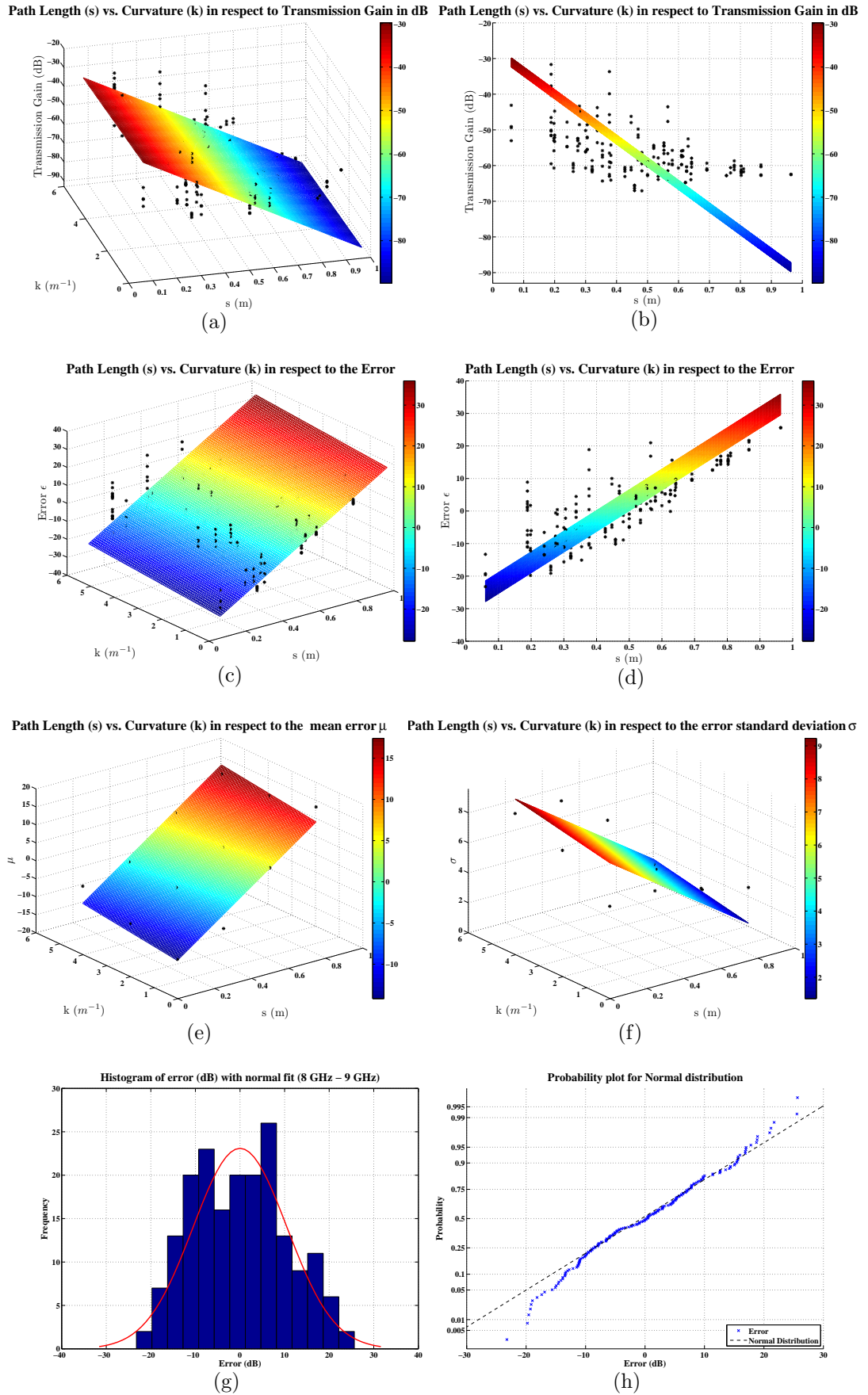


Figure B.6: Transmission gain and error modelling of measurements without cowling within 8 GHz to 9 GHz. 153

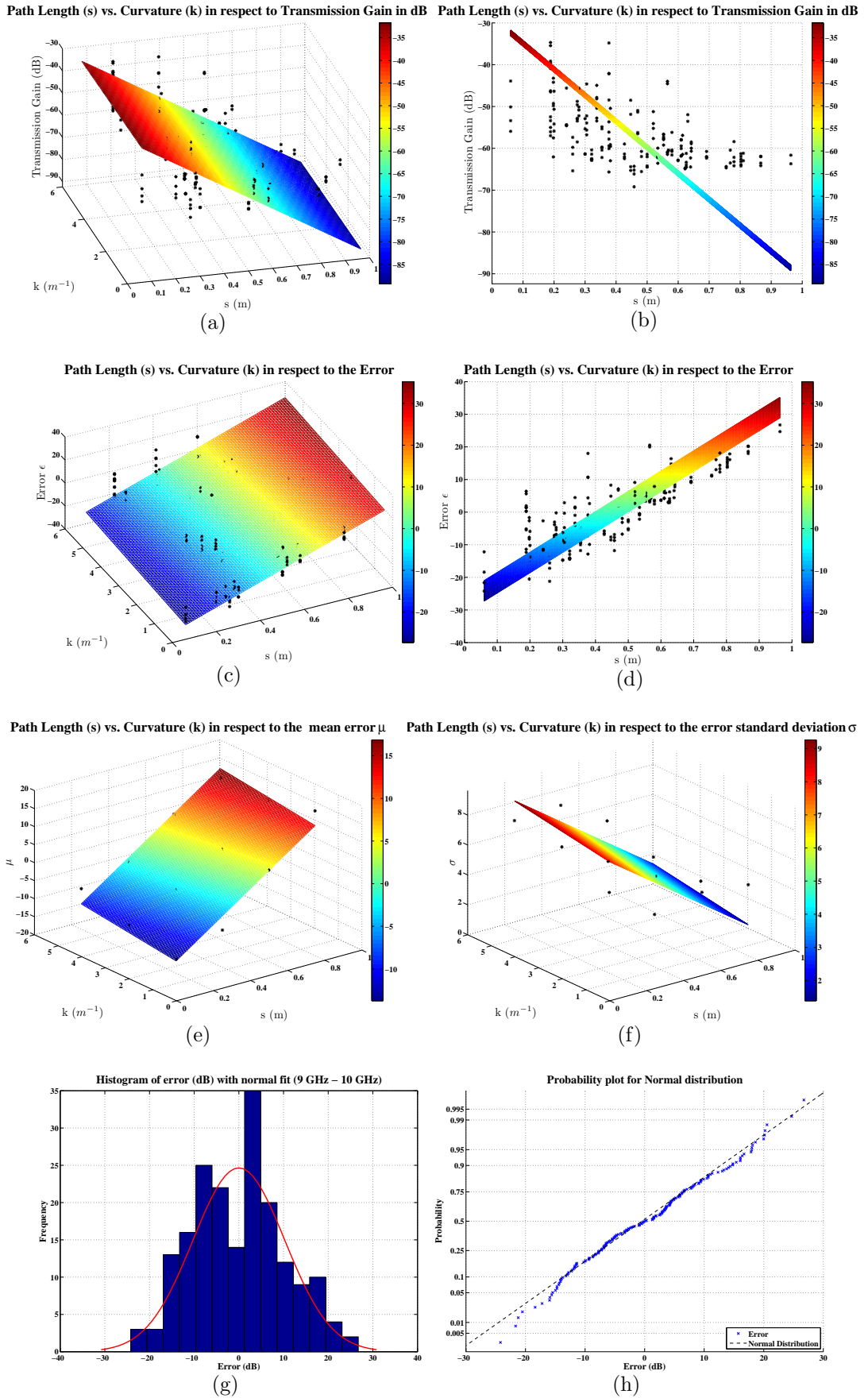


Figure B.7: Transmission gain and error modelling of measurements without cowling within 9 GHz to 10 GHz. 154

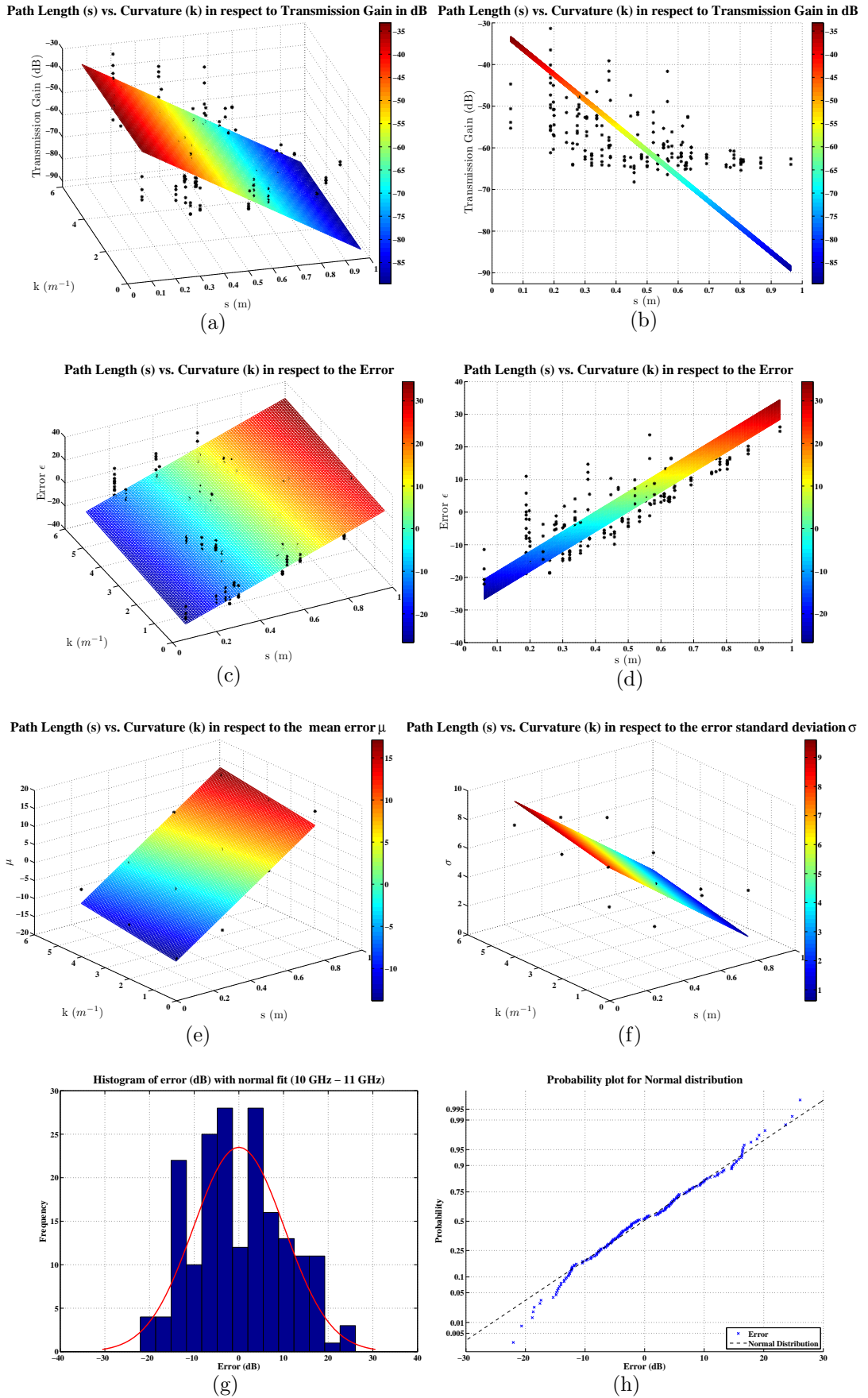


Figure B.8: Transmission gain and error modelling of measurements without cowling within 10 GHz to 11 GHz. 155

Appendix C: UWB-band Measurements and Modelling for Measurements with Cowling (3 GHz to 11 GHz)

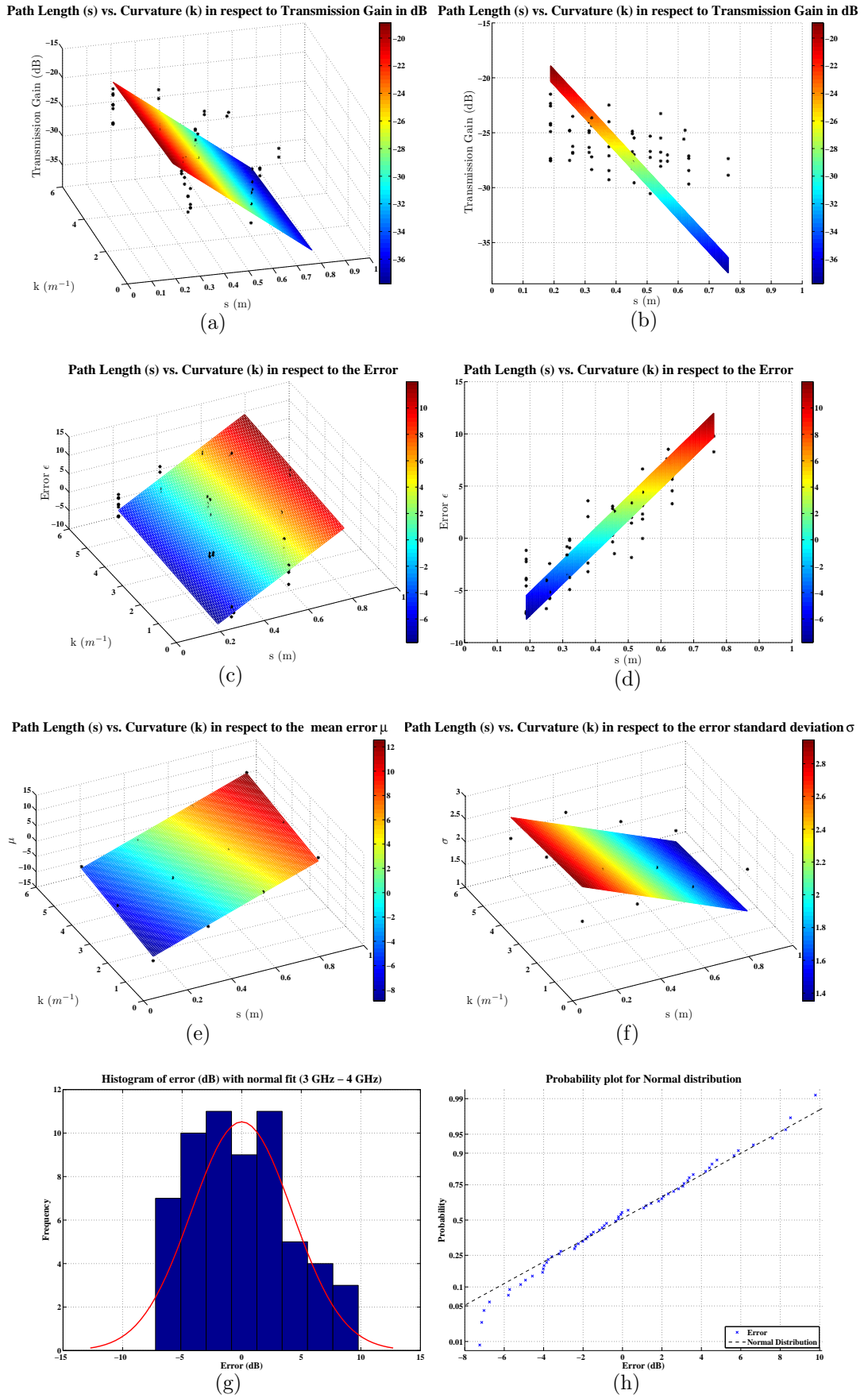


Figure C.1: Transmission gain and error modelling of measurements with cowling within 3 GHz to 4 GHz.

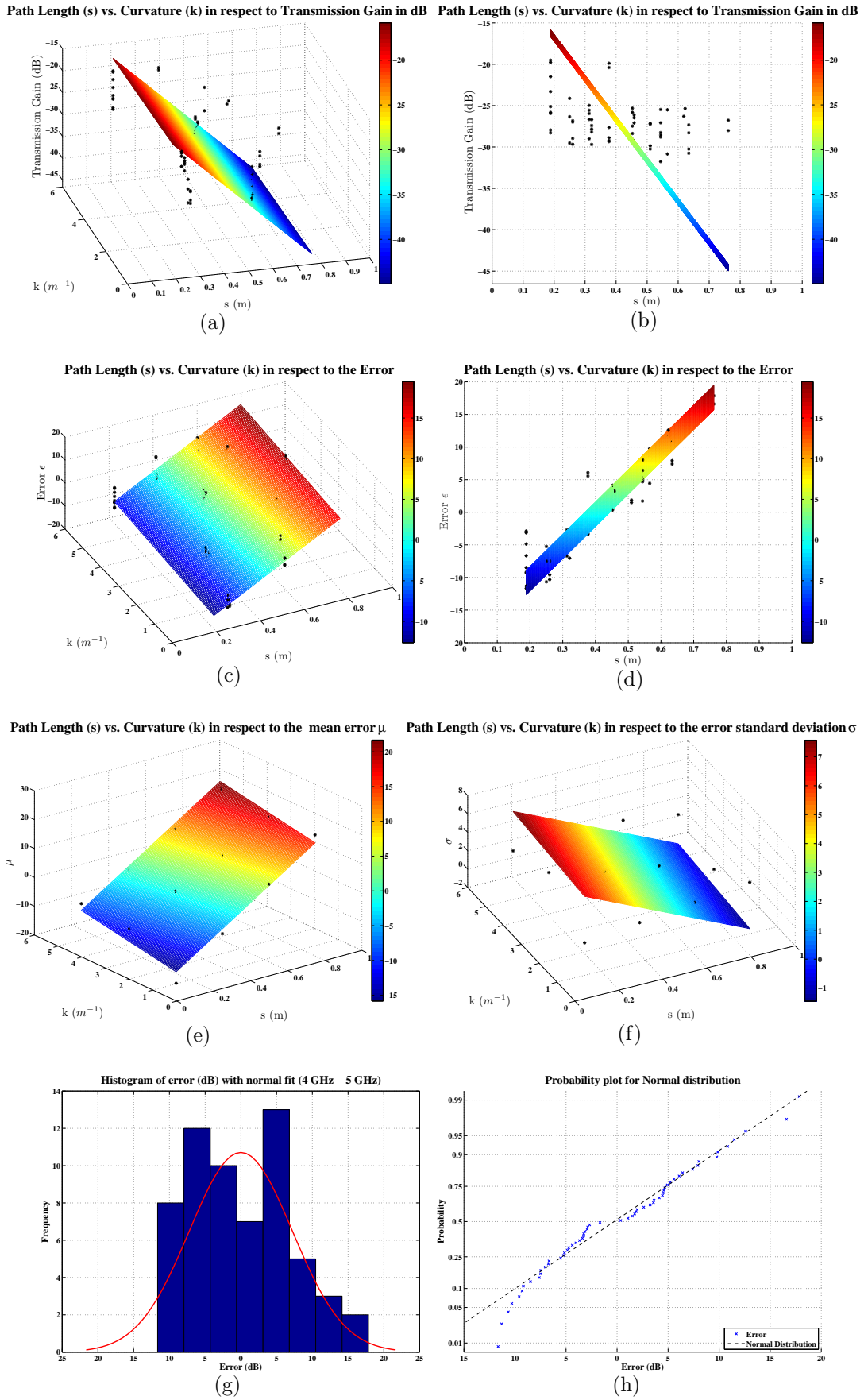


Figure C.2: Transmission gain and error modelling of measurements with cowling within 4 GHz to 5 GHz. 158

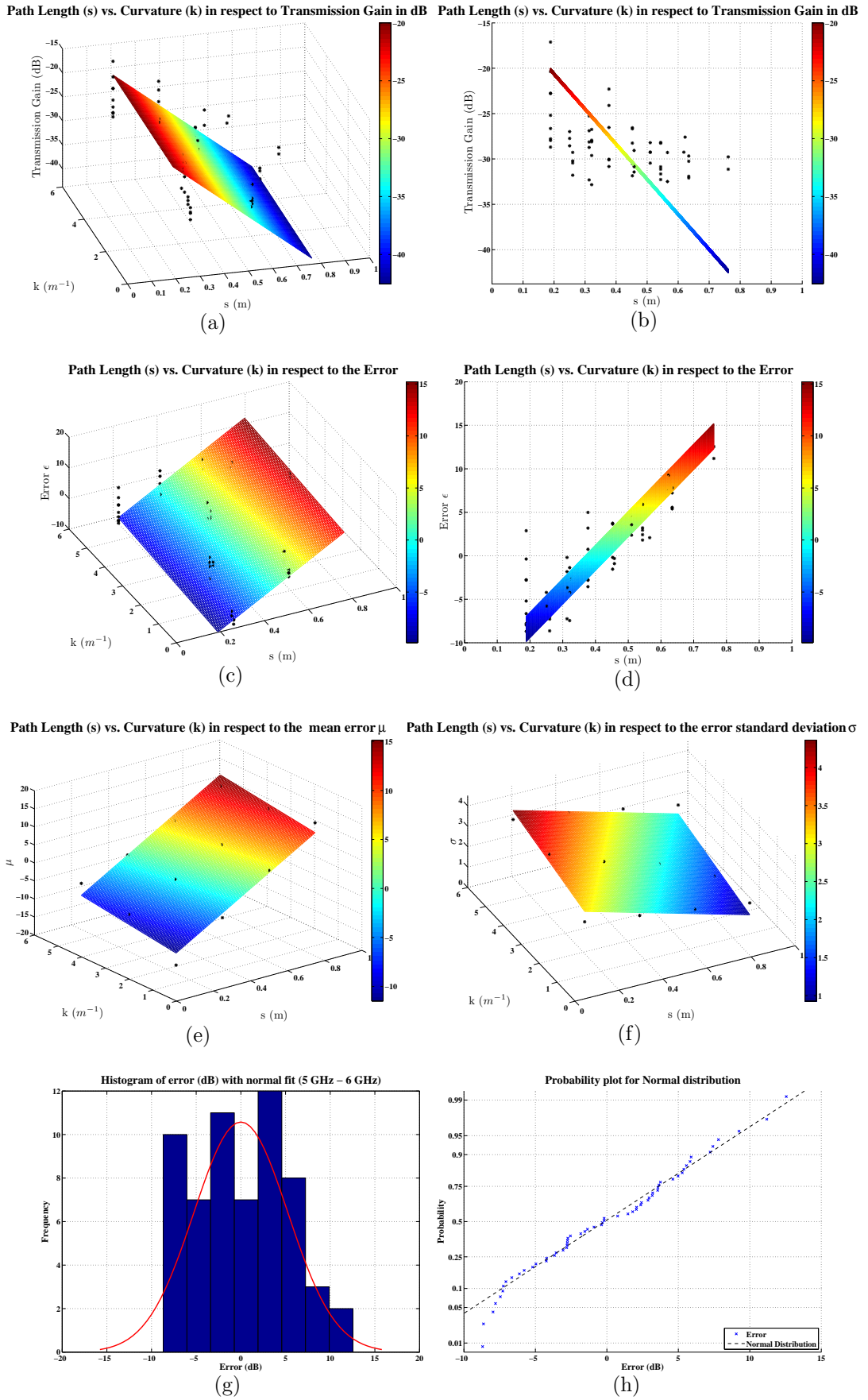


Figure C.3: Transmission gain and error modelling of measurements with cowling within 5 GHz to 6 GHz.

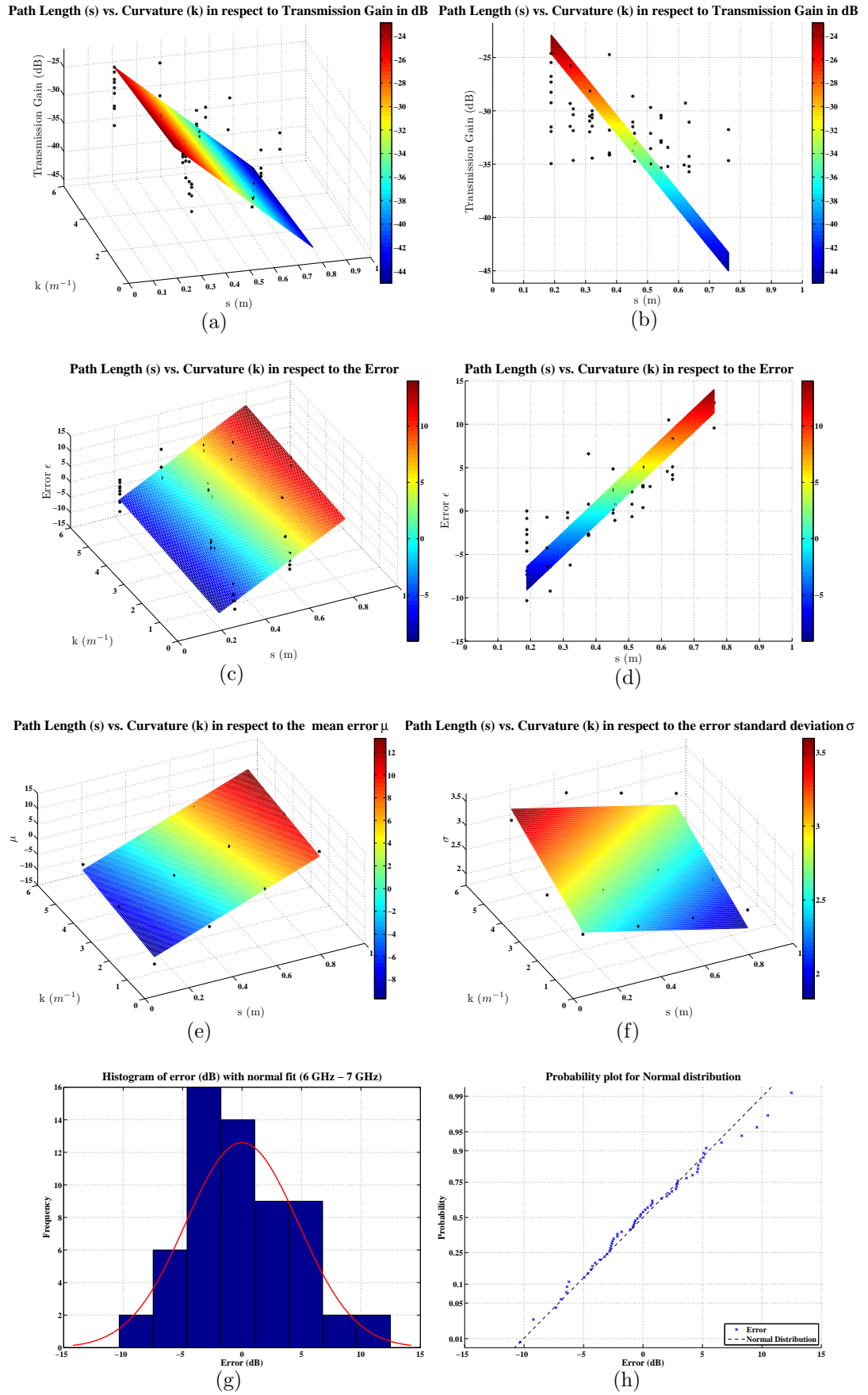


Figure C.4: Transmission gain and error modelling of measurements with cowling within 6 GHz to 7 GHz.

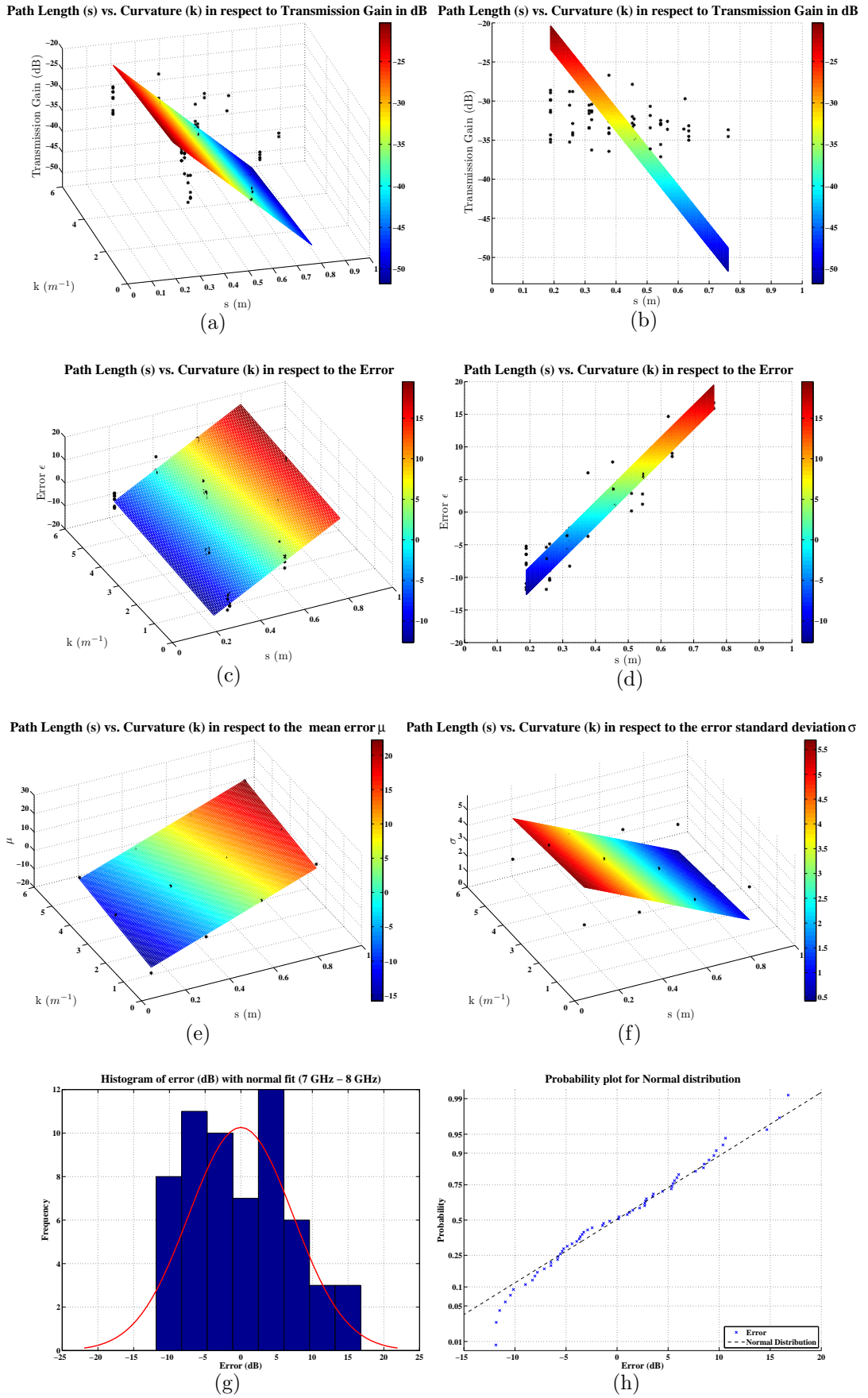


Figure C.5: Transmission gain and error modelling of measurements with cowling within 7 GHz to 8 GHz.

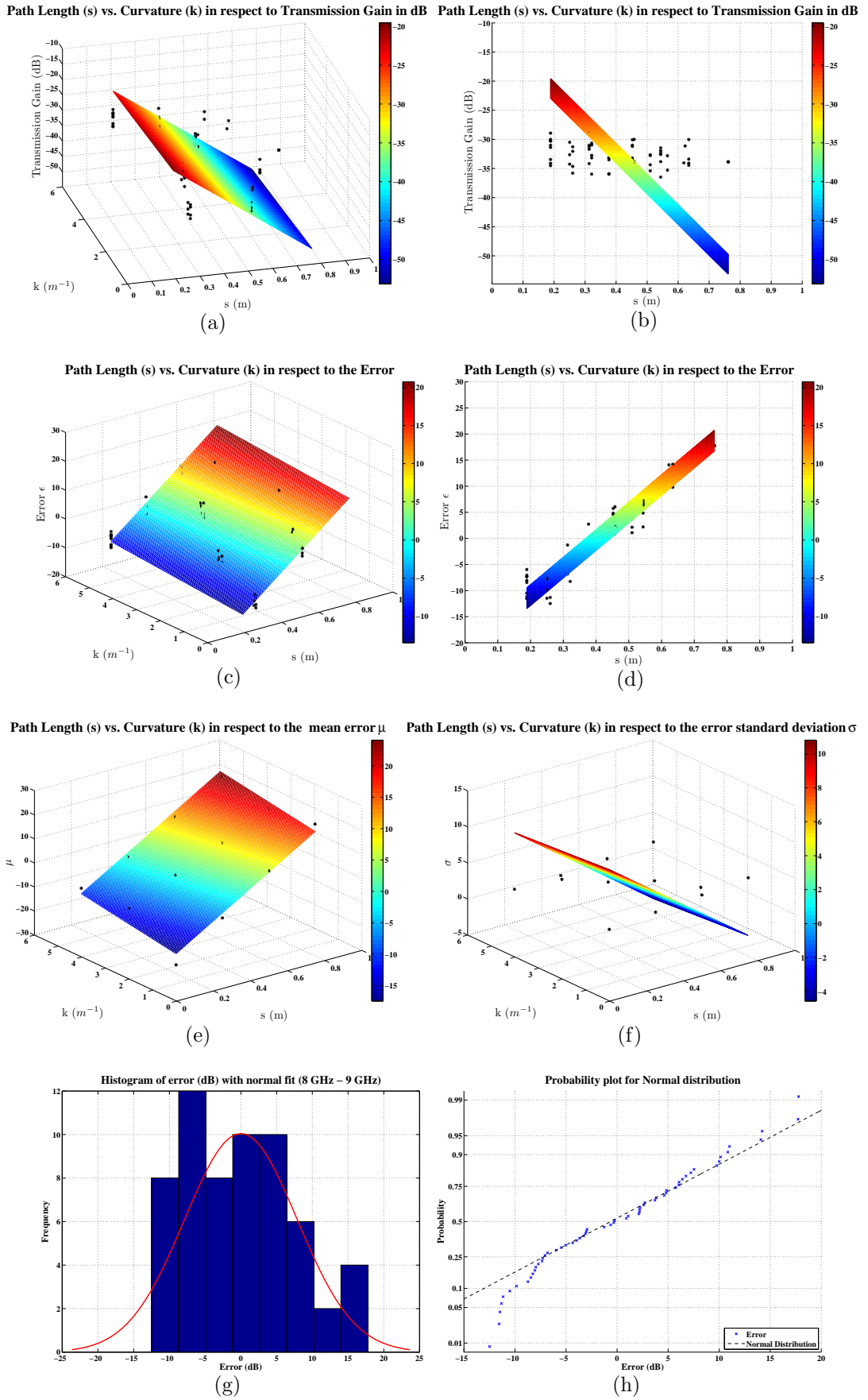


Figure C.6: Transmission gain and error modelling of measurements with cowling within 8 GHz to 9 GHz.

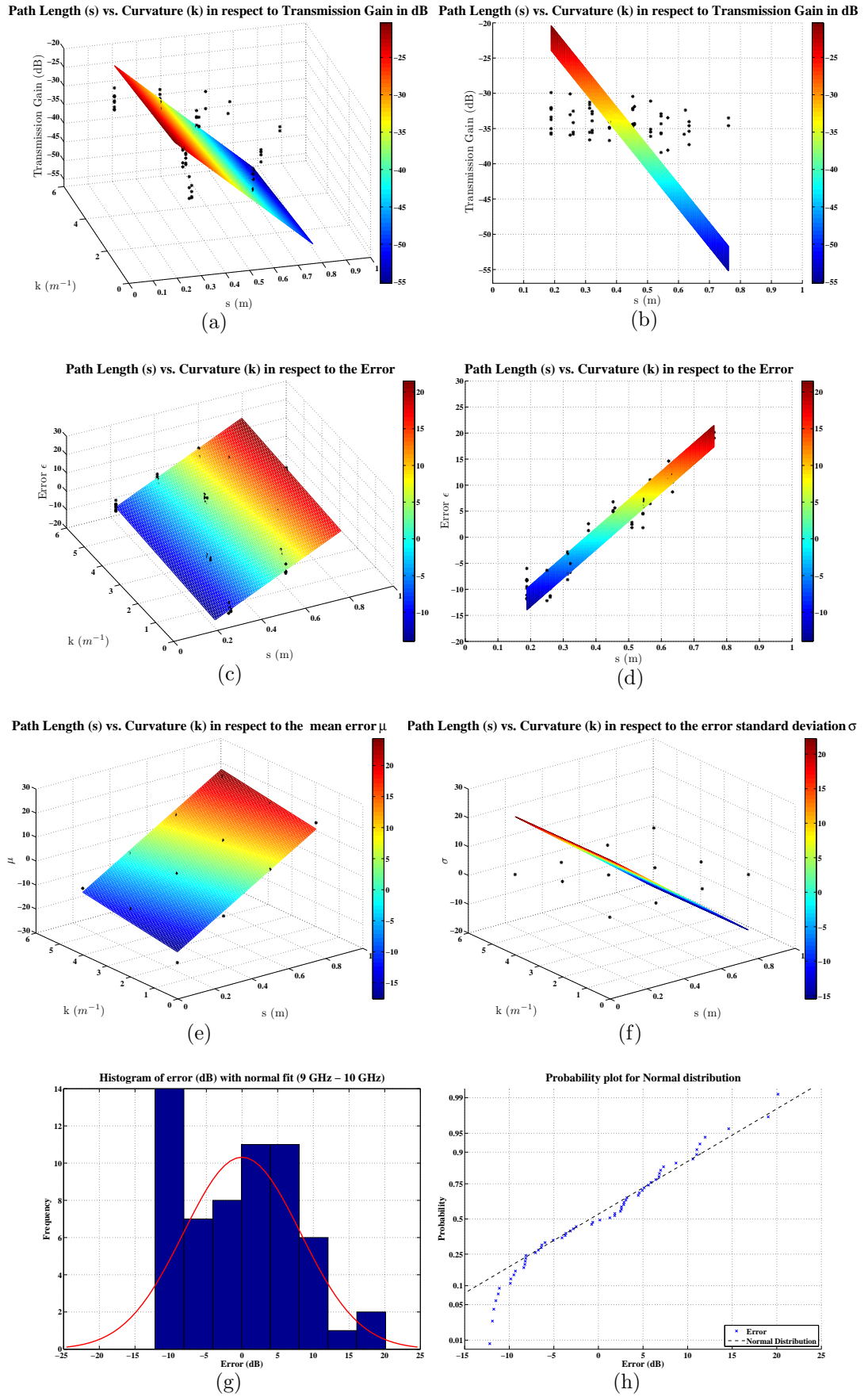


Figure C.7: Transmission gain and error modelling of measurements with cowling within 9 GHz to 10 GHz. 163

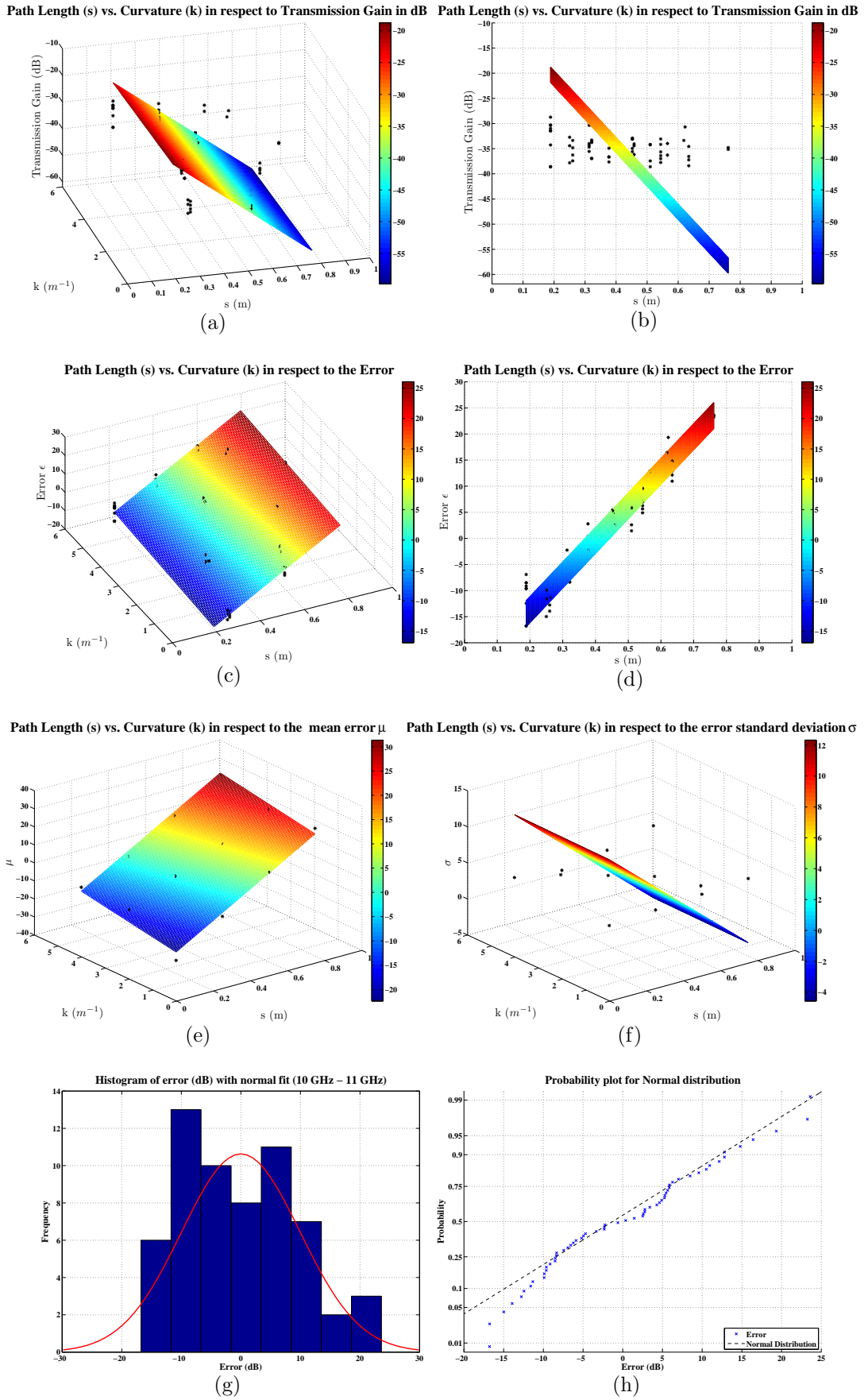


Figure C.8: Transmission gain and error modelling of measurements with cowling within 10 GHz to 11 GHz.



Appendix D: Rectaxial Antenna Radiation Pattern and Chipboard Reflection Coefficient

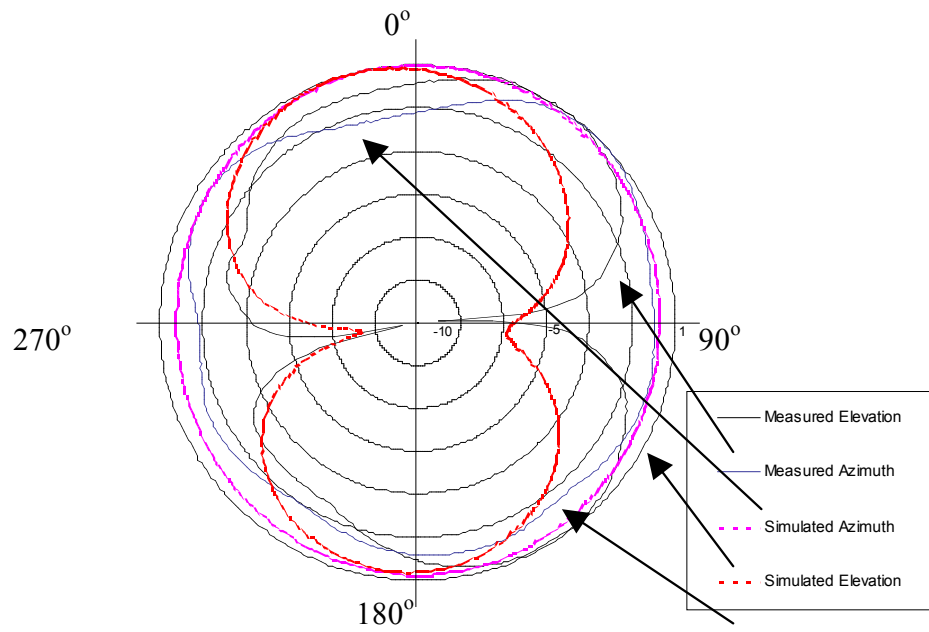


Figure D.1: Measured and simulated radiation pattern of rectaxial antenna. After [51].

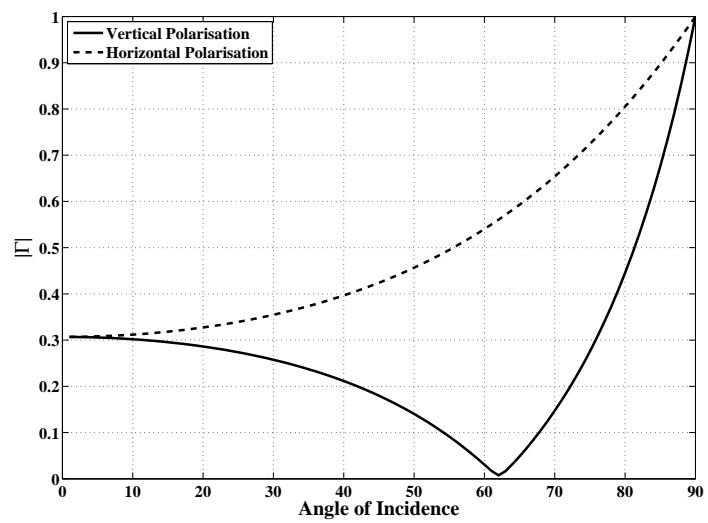


Figure D.2: Magnitude of the reflection coefficient for $\epsilon = 3.55$ and $\sigma = 0.02$.

Bibliography

- [1] WIDAGATE: Wireless Data Acquisition in Gas Turbine Engines. <http://gow.epsrc.ac.uk/ViewGrant.aspx?GrantRef=TS/G002681/1>, (Last assessed on 6th January 2010). (cited on page 2)
- [2] CBM: Condition Based Monitoring. <http://www.ititechmedia.com/defaultpage131abcde0.aspx?pageID=806>, (Last assessed on 6th January 2010). (cited on page 2)
- [3] SpeckNet. <http://www.specknet.org>, (Last assessed on 28th June 2008). (cited on pages 2, 7, 104, 105)
- [4] B. S. Manoj and C. Siva Ram Murthy. *Ad-Hoc Wireless Networks: Architectures and Protocols*. Prentice Hall PTR, 2004. (cited on pages x, 6, 8, 9, 11, 13)
- [5] E. H. Callaway Jr. *Wireless Sensor Network Architectures and Protocols*. Auerbach, 2004. (cited on pages 6, 7)
- [6] SMART DUST. <http://robotics.eecs.berkeley.edu/~pister/SmartDust/>, (Last assessed on 25th December 2009). (cited on page 7)
- [7] Bluetooth SIG. <http://www.bluetooth.com>, (Last assessed on 9th November 2009). (cited on pages 8, 34)
- [8] IEEE 802.11 WLAN. <http://standards.ieee.org/getieee802/802.11.html>. (cited on page 8)
- [9] IEEE 802.15.4-2006. <http://standards.ieee.org/getieee802/download/802.15.4-2006.pdf>, (Last assessed on 27th December 2009). (cited on page 8)
- [10] IEEE 802.15 WPAN High Rate Alternative PHY Task Group 3a (TG3a) Merged Proposal 1. (cited on page 8)
- [11] IEEE 802.15 WPAN High Rate Alternative PHY Task Group 3a (TG3a) Merged Proposal 2. (cited on page 8)

- [12] ECMA International Organisation. <http://www.ecma-international.org/publications/standards/Ecma-369.htm>. (cited on page 8)
- [13] Microwave Journal. http://www.mwjournal.com/Journal/article.asp?HH_ID=AR_478, February (Last assessed on 25th December 2009). (cited on page 8)
- [14] Chipcon CC2420. <http://focus.ti.com/docs/prod/folders/print/cc2420.html>, (Last assessed on 26th December 2009). (cited on pages x, 11)
- [15] Crossbow Technology Inc. <http://www.xbow.com/>, (Last assessed on 28th June 2008). (cited on pages 11, 72, 82, 84)
- [16] Telematica. http://www.telematica.polito.it/wsn/ppt/WSN1_Hardware.pdf, (Last assessed on 5th January 2010). (cited on page 11)
- [17] BT Node. <http://www.btnode.ethz.ch/Documentation/BTnodeRev3HardwareReference>, (Last assessed on 5th January 2010). (cited on page 11)
- [18] FireFly 2.2 Datasheet. http://www.nanork.org/attachment/wiki/Documentation/FireFly_datasheet.pdf?format=raw, (Last assessed on 5th January 2010). (cited on page 11)
- [19] VISHAY. <http://www.vishay.com/>, (Last assessed on 18th October 2009). (cited on page 11)
- [20] Decawave ScenSor. <http://www.decawave.com/scensor.html>, (Last assessed on 26th December 2009). (cited on page 11)
- [21] IEEE 802.15.4a-2007. <http://standards.ieee.org/getieee802/download/802.15.4a-2007.pdf>, (Last assessed on 27th December 2009). (cited on page 11)
- [22] A. S. Tanenbaum. *Computer Networks*. Prentice Hall PTR, 2003 Fourth Edition. (cited on page 11)
- [23] T. S. Rappaport. *Wireless Communications Principles and Practices*. Prentice Hall PTR, Second edition, 2002. (cited on pages xi, 15, 18, 20, 28, 29, 30, 31, 32, 87, 113)
- [24] S. R. Saunders. *Antennas and Propagation for Wireless Communication Systems*. John Wiley & Sons Ltd, 1999. (cited on pages x, 15, 16, 17, 18, 20, 24, 26, 29, 31, 33)
- [25] W. L. Stutzman. *Polarization in Electromagnetic Systems*. Artech Jouse, 1993. (cited on page 16)

- [26] I. A. Glover and P. M. Grant. *Digital Communications*. Pearson Education Limited, second edition, 2004. (cited on pages 23, 36, 65, 100)
- [27] P. Nobles and F. Halsall. Delay Spread Measurements within A Building at 2 GHz, 5 GHz and 17 GHz. In *Proc. IEE Colloquium on Propagation Aspects of Future Mobile Systems (Digest No: 1996/220)*, pages 8/1–8/6, October 25, 1996. (cited on page 30)
- [28] N. Moraitis, A. Kanatas, G. Pantos, and P. Constantinou. Delay Spread Measurements and Characterization in A Special Propagation Environment for PCS Microcells. In *Proc. 13th IEEE International Symposium on Personal, Indoor and Mobile Radio Communications*, volume 3, pages 1190–1194, September 15–18, 2002. (cited on page 30)
- [29] W. G. Newhall, K. J. Saldanha, and T. S. Rappaport. Propagation Time Delay Spread Measurements at 915 MHz in a Large Train Yard. In *Proc. IEEE 46th Vehicular Technology Conference 'Mobile Technology for the Human Race'*, volume 2, pages 864–868, April 28–May 1, 1996. (cited on page 30)
- [30] G. S. Prabhu and P. M. Shankar. Simulation of Flat Fading Using MATLAB for Classroom Instruction. Volume 45(1):19–25, February 2002. (cited on page 30)
- [31] V. M. Hinostroza. Frequency Selectivity Parameters for Broadband Signals. In *Proc. 7th International Conference on ITS Telecommunications ITST '07*, pages 1–6, June 6–8, 2007. (cited on page 31)
- [32] H. MacLeod, C. Loadman, and Z. Chen. Experimental Studies of the 2.4-GHz ISM Wireless Indoor Channel. In *Proc. 3rd Annual Communication Networks and Services Research Conference*, pages 63–68, May 16–18, 2005. (cited on page 31)
- [33] J. G. Proakis and M. Salehi. *Digital Communications*. McGraw-Hill, Fifth edition, 2008. (cited on page 32)
- [34] Recommendation ITU-R P.526-10: Propagation by diffraction. Recommendation ITU-R P.526-10, International Telecommunication Union, 2007. (cited on page 33)
- [35] T. Chiu and K. Sarabandi. Electromagnetic Scattering Interaction between a Dielectric Cylinder and a Slightly Rough Surface. 47(5):902–913, May 1999. (cited on page 33)
- [36] D. E. Eliades. Terrain Simulation for the Cascaded Cylinder Diffraction Model. *IEE Proceedings H Microwaves, Antennas and Propagation*, 140(4):285–291, August 1993. (cited on page 33)

- [37] D. E. Eliades. Alternative Derivation of The Cascaded Cylinder Diffraction Model. *IEE Proceedings H Microwaves, Antennas and Propagation*, 140(4):279–284, August 1993. (cited on page 33)
- [38] M. Ghaddar, L. Talbi, T. A. Denidni, and A. Sebak. A Conducting Cylinder for Modeling Human Body Presence in Indoor Propagation Channel. 55(11):3099–3103, November 2007. (cited on page 33)
- [39] M. C. Renken, S. Kim, K. W. Hollman, and C. M. Fortunko. Accuracy of Resonant Ultrasound Spectroscopy: An Experimental Study. In *Proc. IEEE Ultrasonics Symposium*, volume 1, pages 483–488, October 5–8, 1997. (cited on page 33)
- [40] V. N. Troitsky and L. M. Martynov. Comparison of Diffraction over Mountain Ridges-Experimental Results with Diffraction Loss Calculation by Different Theoretical Methods. In *Proc. Eleventh International Conference on (IEE Conf Antennas and Propagation Publ. No. 480)*, volume 1, pages 199–202, April 17–20, 2001. (cited on page 33)
- [41] C. Zhou and R. C. Qiu. Pulse Distortion Caused by Cylinder Diffraction and its Impact on UWB Communications. 56(4):2385–2391, July 2007. (cited on page 33)
- [42] C. Zhou and R. C. Qiu. Pulse Distortion Caused by Cylinder Diffraction and its Impact on UWB Communications. In *Proc. IEEE 2006 International Conference on Ultra-Wideband*, pages 645–650, September 24–27, 2006. (cited on page 33)
- [43] K. Sasloglou, I. A. Glover, P. Dutta, R. Atkinson, I. Andonovic, and G. Whyte. A Channel Model for Wireless Sensor Networks in Gas Turbine Engines. In *Proc. Loughborough Antennas & Propagation Conference (LAPC 2009)*, Loughborough, UK, pages 761–764, 16–17 Nov. 2009. (cited on page 34)
- [44] K. Sasloglou, I. A. Glover, P. Dutta, R. Atkinson, I. Andonovic, and G. Whyte. Empirical Modelling and Simulation of Transmission Loss between Wireless Sensor Nodes in Gas Turbine Engines. In *The 7th International Conference on Information, Communications and Signal Processing (ICICS 2009)*, 7–10 Dec. 2009. (cited on pages 34, 45)
- [45] IEEE 802.11b. http://standards.ieee.org/getieee802/download/802.11b-1999_Cor1-2001.pdf, (Last assessed on 9th November 2009). (cited on page 34)
- [46] IEEE 802.11g. <http://standards.ieee.org/getieee802/download/802.11g-2003.pdf>, (Last assessed on 9th November 2009). (cited on page 34)

- [47] Wireless Universal Serial Bus. <http://www.usb.org/developers/wusb/>, (Last assessed on 2nd November 2009). (cited on page 34)
- [48] Status of Project IEEE 802.11y. http://grouper.ieee.org/groups/802/11/Reports/tgy_update.htm, (Last assessed on 9th November 2009). (cited on page 34)
- [49] IEEE 802.11a. <http://standards.ieee.org/getieee802/download/802.11a-1999.pdf>, (Last assessed on 9th November 2009). (cited on page 34)
- [50] "G013. what is Meant by ISM Applications and How Are the Related Frequencies Used?". <http://www.itu.int/ITU-R/terrestrial/faq/index.html#g013>, (Last assessed on 30th October 2009). (cited on pages xviii, 36, 37)
- [51] G. Whyte, N. Buchanan, and I. Thayne. An Omnidirectional, Low Cost, Low Profile, 2.45 GHz Microstrip Fed Rectaxial Antenna for WSN Applications. IEE Conference on Propagation and Antennas, 2006. (cited on pages xvii, 37, 108, 116, 167)
- [52] Huber & Suhner. <http://www.hubersuhner.com>, (Last assessed on 18th October 2009). (cited on pages 37, 47)
- [53] Plextek. <http://www.plextek.co.uk/uwb.htm>, (Last assessed on 2nd November 2009). (cited on pages xi, 43)
- [54] EUROCAE ED-14E "A Joint EUROCAE RTCA Achievement" [Sections 19-21]. Technical report, The European Organisation for Civil Aviation Equipment, March 2005. (cited on pages xiii, xviii, 63, 64, 65, 70)
- [55] A. Mainwaring, J. Polastre, R. Szewczyk, D. Culler, and J. Anderson. Wireless Sensor Networks for Habitat Monitoring. In *Proceedings of the ACM International Workshop on Wireless Sensor Networks and Applications (WSNA'02)*, Atlanta, USA, 2002. (cited on page 79)
- [56] P. Zhang, C. M. Sadler, S. A. Lyon, and M. Martonosi. Hardware Design Experiences on ZebraNet. In *Proceedings of SenSys, Baltimore, Maryland, USA*, 2004. (cited on page 79)
- [57] I. McCauley, B. Matthews, L. Nugent, A. Mather, and J. Simons. Wired Pigs: Ad-hoc Wireless Sensor Networks in Studies of Animal Welfare. In *Proc. EmNetS-II Embedded Networked Sensors The Second IEEE Workshop on*, pages 29–36, 30–31 May 2005. (cited on page 79)
- [58] M. Radenkovic and B. Wietrzyk. Wireless mobile ad-hoc sensor networks for very large scale cattle monitoring. In *Proceedings of the 6th International Workshop on*

- Applications and Services in Wireless Networks (ASWN'06)*, pages 47–58, Berlin, Germany, Aug. 2006. (cited on page 79)
- [59] K. Mayer, K. Taylor, and K. Ellis. Cattle Health Monitoring Using Wireless Sensor Networks. In *The 2nd IASTED International Conference on Communication and Computer Networks*, November 2004. (cited on page 79)
- [60] Y. Guo, P. Corke, G. Poulton, T. Wark, G. Bishop-Hurley, and D. Swain. Animal Behaviour Understanding Using Wireless Sensor Networks. In *Local Computer Networks, Proceedings 2006 31st IEEE Conference on*, pages 607–614, Nov. 2006. (cited on page 79)
- [61] P. Corke and P. Sikka. Results from the Farm. <http://eecs.harvard.edu/emnets/papers/corkeEmnets06.pdf>. (Last visited on 24/02/08). (cited on page 79)
- [62] K. Sasloglou, I. A. Glover, K. H. Kwong, and I. Andonovic. Wireless Sensor Network for Animal Monitoring Using both Antenna and Base-station Diversity. In *Proc. 11th IEEE Singapore International Conference on Communication Systems ICCS 2008*, pages 27–33, 2008. (cited on page 80)
- [63] K. Sasloglou, I. A. Glover, H. G. Goh, K. H. Kwong, M. P. Gilroy, C. Tachtatzis, C. Michie, and I. Andonovic. Antenna and Base-station Diversity for WSN Livestock Monitoring. *Scientific Research Journal on Wireless Sensor Network*, Volume 1:p. 383–396, December 2009. (cited on page 80)
- [64] TDK. http://www.tdk.co.jp/tefe02/e821_cabpb1240.pdf, (Last assessed on 28th June 2008). (cited on pages xiii, 80, 81, 108, 110)
- [65] Hyperlinktech. <http://www.hyperlinktech.com>, (Last assessed on 28th June 2008). (cited on page 82)
- [66] A. Papoulis. *Probability, Random Variables, and Stochastic Processes*. Mc-Graw Hill, third edition, 1991. (cited on page 86)
- [67] K. H. Kwong, T. T. Wu, K. Sasloglou, B. Stephen, D. Cao, H. G. Goh, S. K. Goo, M. Gilroy, C. Tachtatzis, I. A. Glover, C. Michie, and I. Andonovic. Implementation of Herd Management System with Wireless Sensor Networks. In *Joint International Agricultural Conference (JIAC 2009), Wageningen, Netherlands*, 6–8 Jul. 2009. (cited on page 100)
- [68] J. F. LaFortune and M. Lecours. Measurement and Modeling of Propagation Losses in a Building at 900 MHz. 39(2):101–108, 1990. (cited on page 104)

- [69] D. J. Y. Lee and W. C. Y. Lee. Propagation Prediction in and through Buildings. 49(5):1529–1533, 2000. (cited on page 104)
- [70] A. Borrelli, C. Monti, M. Vari, and F. Mazzenga. Channel Models for IEEE 802.11b Indoor System Design. In *Proc. IEEE International Conference on Communications*, volume 6, pages 3701–3705 Vol.6, 2004. (cited on page 104)
- [71] S. Zvanovec, M. Valek, and P. Pechac. Results of Indoor Propagation Measurement Campaign for WLAN Systems Operating in 2.4 GHz ISM-band. volume 1 of *Antennas and Propagation*, pages Page(s): 63 – 66. ICAP 2003, 31 March-3 April 2003. (cited on page 104)
- [72] B. Sujak, D. K. Ghodgaonkar, B. M. Ali, and S. Khatun. Indoor Propagation Channel Models for WLAN 802.11b at 2.4 GHz ISM Band. In *Proc. Asia-Pacific Conference on Applied Electromagnetics APACE 2005*, pages 5 pp.–, 2005. (cited on page 104)
- [73] K. Siwiak. *Radiowave Propagation and Antennas for Personal Communications*. Artech House, 1995. (cited on pages 105, 106)
- [74] Integrated Publishing. <http://www.tpub.com/neets/book10/40c.htm>. (cited on page 105)
- [75] K. Bullington. Radio Propagation Fundamentals. *The Bell System Technical Journal*, Vol. 36(No.3):p. 593–625, 1957. (cited on page 105)
- [76] K. A. Norton. The Physical Reality of Space and Surface Waves in the Radiation Field of Radio Antennas. *Proceedings of the IRE*, 25(9):1192–1202, 1937. (cited on page 105)
- [77] G. Tesserault, N. Malhouroux, and P. Pajusco. Determination of Material Characteristics for Optimizing WLAN Radio. In *Proc. European Conference on Wireless Technologies*, pages 225–228, October 8–10, 2007. (cited on pages 106, 116)
- [78] K. Sasloglou, F. Darbari, I. A. Glover, I. Andonovic, and R. W. Stewart. Some Preliminary Short-range Transmission Loss Measurements for Wireless Sensors Deployed on Indoor Walls. In *Proc. 11th IEEE Singapore International Conference on Communication Systems ICCS 2008*, pages 129–132, 2008. (cited on page 108)
- [79] T. S. Rappaport. Indoor Radio Communications for Factories of the Future. 27(5):15–24, 1989. (cited on page 113)
- [80] F. Darbari, K. Sasloglou, R. W. Stewart, I. A. Glover, and I. Andonovic. Effect of Antenna Height and Polarisation on Short Wireless Links. In *16th European*

BIBLIOGRAPHY

Signal Processing Conference (EUSIPCO 2008), Lausanne, Switzerland, August 2008. (cited on page 116)

- [81] OMNeT++. <http://www.omnetpp.org/>. (Last assessed on 3rd January 2010). (cited on page 143)